UNIVERSIDADE FEDERAL DO RIO GRANDE DO SUL
INSTITUTO DE PESQUISAS HIDRÁULICAS
PROGRAMA DE PÓS-GRADUAÇÃO EM RECURSOS HÍDRICOS E SANEAMENTO AMBIENTAL

Matheus Henrique Tavares

Análise do impacto de mudanças ambientais na variação espaço-temporal da qualidade da água de lagos rasos costeiros brasileiros por sensoriamento remoto

Porto Alegre

2023

Matheus Henrique Tavares

Análise do impacto de mudanças ambientais na variação espaço-temporal da qualidade da água de lagos rasos costeiros brasileiros por sensoriamento remoto

Tese apresentada ao Programa de Pós-Graduação em Recursos Hídricos e Saneamento Ambiental da Universidade Federal do Rio Grande do Sul, como requisito parcial à obtenção do grau de Doutor.

Orientador: David da Motta Marques
Coorientador: Carlos Ruberto Fragoso Jr.

Porto Alegre

2023

CIP - Catalogação na Publicação

Tavares, Matheus Henrique
   Análise do impacto de mudanças ambientais na variação espaço-temporal da qualidade da água de lagos rasos costeiros brasileiros por sensoriamento remoto / Matheus Henrique Tavares. -- 2023.
   197 f.
   Orientador: David Manuel Lelinho da Motta Marques.

   Coorientador: Carlos Ruberto Fragoso Jr..

   Tese (Doutorado) -- Universidade Federal do Rio Grande do Sul, Instituto de Pesquisas Hidráulicas, Programa de Pós-Graduação em Recursos Hídricos e Saneamento Ambiental, Porto Alegre, BR-RS, 2023.

   1. sensoriamento remoto. 2. qualidade da água. 3. limnologia. 4. temperatura superficial da água. 5. clorofila-a. I. Marques, David Manuel Lelinho da Motta, orient. II. Fragoso Jr., Carlos Ruberto, coorient. III. Título.

Elaborada pelo Sistema de Geração Automática de Ficha Catalográfica da UFRGS com os dados fornecidos pelo(a) autor(a).

Matheus Henrique Tavares

Análise do impacto de mudanças ambientais na variação espaço-temporal da qualidade da água de lagos rasos costeiros brasileiros por sensoriamento remoto

Tese apresentada ao Programa de Pós-Graduação em Recursos Hídricos e Saneamento Ambiental da Universidade Federal do Rio Grande do Sul, como requisito parcial à obtenção do grau de Doutor.

Trabalho aprovado. Porto Alegre, 7 de março de 2023:

Prof. Dr. David da Motta Marques– UFRGS
Orientador

Prof. Dr. Carlos Ruberto Fragoso Jr.– UFAL
Co-orientador

Prof. Dr. Rodrigo Cauduro Dias de Paiva – UFRGS
Examinador

Prof. Dra. Marie-Paule Bonnet – IRD
Examinadora

Prof. Dr. Enner Herenio de Alcântara – UNESP
Examinador

Agradecimentos

Primeiramente gostaria de agradecer à CAPES e ao CNPQ pelo financiamento deste estudo por meio da bolsa de estudos e auxílios (embora tenham sido 4 anos de governo Bolsonaro, marcado por combate à informação e aos fatos, por ataques às universidades e centros de pesquisas, e por políticas públicas anticientíficas e negacionistas), e à UFRGS e ao IPH pela ótima infraestrutura e incentivo à pesquisa dos alunos.

Vou fazer alguns agradecimentos, mas destaco que foram muitas pessoas que contribuíram para este trabalho e para minha formação pessoal e profissional. Primeiro agradeço ao professor David pelo incrível entusiasmo pela pesquisa científica, e por sempre querer transmitir o seu conhecimento (nos mais diversos assuntos). Agradeço também ao professor Ruberto pela co-orientação, pela recepção no período que passei em Maceió, pelas caronas, e pelo incentivo a sempre buscar novas áreas e novos conhecimentos. Também agradeço aos outros colaboradores da pesquisa, Jean-Michel e Tristan Harmel pela colaboração nos trabalhos no CELMM, e à Angélica pelo entusiasmo com meteorologia e seus dados. Agradeço também a outros professores do IPH que foram importantíssimos tanto na minha formação quanto para o desenvolvimento deste trabalho: Lucia, Fernando Fan, Beatriz, Juan Martín, Olavo, Nilza, Walter, à banca de qualificação, Enner e Marie, pelas importantes contribuições, e especialmente ao Rodrigo Paiva e ao Anderson, por terem criado a disciplina de Sensoriamento Remoto no curso, o que foi essencial para eu iniciar meus estudos neste tema. Também agradeço aos técnicos e funcionários do IPH, em especial ao Ivanir e ao Antônio pelos esforços de campo, eles têm uma experiência incrível em todos os aspectos do monitoramento do sistema hidrológico do Taim. Este trabalho também apoio indireto de pesquisadores e colaboradores anônimos que contribuem em fóruns e blogs de ajuda, como os da NASA (OBPG, EOS Help, Earthdata), do ACOLITE (em que o Quinten Vanhellemont é muito ativo) e, principalmente, à comunidade do *R* que, em especial no Stack Overflow, contribuiu com muitas ideias (e códigos) às minhas rotinas de processamento de dados.

Gostaria de agradecer às pessoas que foram importantes no período que passei em Maceió e por me receberem tão bem, principalmente ao Hugo, Wal, Alania, Kleber e Léo pela convivência (principalmente na quarentena), Jess, Yan, Clebson, Chris e Denis, ao pessoal da Rhama, Rafa, Erik e Alain, ao pessoal do LabISA/INPE, principalmente o Daniel, ao pessoal do dia-a-dia do IPH, Itza, Carlos, Pedro, Clari, Lari e Karla, e a galera nordestina que há tanto tempo faz parte do meu convívio, Dani e Beni, João, Thiago e Hugo. Gostaria de agradecer à minha família em Curitiba, meus pais por sempre terem me incentivado a estudar, Isa e Allan, e meu irmão Marcos, e amigos, Gui, Gus, Luís, Brian e a Jacarezada. Gostaria de agradecer às pessoas que conviveram comigo durante o duro período que foi a pandemia, Douglas, Julio, Cayo e Mary, e principalmente à minha família em Porto Alegre, Clebinho, Dan, Bruno e Marina, e à minha parceira de Delmiro/Maceió/Porto Alegre, Blenda, por terem me apoiado e deixado mais leves esses últimos 3 anos em POA. Obrigado a todos!

"O mundo não foi feito em alfabeto.
Senão que primeiro
em água e luz.
Depois árvore."
(Manoel de Barros)

Resumo

Lagos e lagunas são ambientes aquáticos com alta produtividade, abrigando biodiversidade e provendo outros importantes serviços ecossistêmicos. Suas características os tornaram importantes sítios de ocupação humana, podendo ser bastante afetados por atividades antropogênicos, além de variação climática. O sensoriamento remoto é uma excelente ferramenta para fornecer dados espacializados que melhorem o entendimento dos impactos destas variações climáticas e não-climáticas nestes ecossistemas. Este trabalho buscou compreender como mudanças ambientais afetam a variação espaço-temporal de parâmetros de qualidade da água de lagos rasos costeiros brasileiros, para isto validando dados de sensoriamento remoto. A primeira parte avaliou os padrões de variação do fitoplâncton num complexo de lagunas tropicais rasas utilizando imagens Sentinel-2 MSI. Primeiramente, foi validado um conjunto de correção atmosférica e algoritmo de clorofila-a (chla) para todo o complexo, com a combinação do ACOLITE com um modelo semi-analítico de razão de bandas do vermelho e infravermelho próximo se mostrando a mais robusta para as duas lagunas. A partir disso, foi avaliada a série espaço-temporal de *chla* junto com o coeficiente de absorção por matéria orgânica dissolvida colorida (CDOM). Se observou que a Manguaba é mais eutrófica do que a Mundaú e afetada principalmente pela afluência de nutrientes da bacia hidrográfica, enquanto que a Mundaú mostrou um padrão de variação mais definido, também afetada pela precipitação e vazão dos rios. Durante a estação chuvosa, a afluência dos rios geralmente reduz a *chla* devido à limitação da luz por CDOM, e aumenta em outros pontos devido a lançamentos de esgoto e águas pluviais. A análise mostrou a importância da hidrodinâmica no sistema, destacando zonas de recicurlação na laguna Manguaba, a influência do ciclo da cana, e das marés na renovação ou retenção da água no sistema. A segunda parte avaliou o impacto da variação climática na temperatura superficial de um conjunto de lagoas subtropicais costeiras rasas utilizando o sensor MODIS. Primeiramente, foram validados algoritmos de correção de efeito de superfície, verificando-se redução do viés e melhoria de todas as métricas pelos modelos testados. Comparando os resultados sem a correção do efeito, se observou diferença principalmente nos cálculos das tendências de aquecimento das lagoas e de evaporação da água. A análise da série temporal mostrou que os impactos nestas lagoas são uma alta taxa de aquecimento regional na primavera e em menor escala de aquecimento no verão, com concordância com as tendências de temperatura do ar na região. O aquecimento na primavera se deve principalmente à uma antecipação do fim do inverno e início da primavera, e rápida resposta das lagoas rasas. Também se observou uma geral homogeneidade espacial nas tendências de aquecimento, porém com diferenças nas áreas de afluência dos rios tributários.

Palavras-chaves: sensoriamento remoto; lagos; qualidade da água; temperatura superficial da água; clorofila-a; correção atmosférica.

Abstract

Lakes and lagoons are highly productive aquatic environments, harbouring biodiversity and providing other important ecosystem services. Their characteristics make them important sites of human occupation, and they can be highly affected by anthropogenic activities, in addition to climatic variability. Remote sensing is an excellent tool to provide spatialized data to improve the understanding of the impacts of these climatic and non-climatic variations in these ecosystems. This thesis sought to understand how environmental changes affect the spatiotemporal variability of water quality parameters of Brazilian coastal shallow lakes, validating remote sensing data for this purpose. The first part evaluated the spatiotemporal variation patterns of phytoplankton in a shallow tropical lagoon complex using Sentinel-2 MSI imagery. First, a set of atmospheric correction and chlorophyll-*a* (*chla*) algorithm was validated for the entire complex, with the combination of ACOLITE with a semi-analytical model using red and near infrared band ratio showing more consistency for the two lagoons. With this set validated, we assessed spatiotemporal series of *chla* along with the coloured dissolved organic matter (CDOM) absorption coefficient. Manguaba is more eutrophic than Mundaú and is mainly affected by the inflow of nutrients from the watershed, while Mundaú showed a more defined pattern of variation, which is also affected by precipitation and river flows. During the rainy season the rivers' inflow generally causes a reduction in *chla* due to light limitation by CDOM, while increasing in other parts due to the effect of sewage and stormwater discharges. The analysis showed the importance of hydrodynamics and residence times in the system, highlighting areas of recirculation in Manguaba lagoon, the influence of the sugarcane cycle, and of the tides in the renewal or retention of water in the system. The second part assessed the impact of climate variability on the surface temperature of a set of subtropical shallow coastal lakes using MODIS imagery. First, we validated algorithms to correct for a surface effect, and we verified reduced bias and improvement of all metrics by the models. Comparing the results without correction for the effect, we observed differences mainly in the calculation of the lakes' warming trends and of water evaporation. The analysis of the time series showed that the impacts on these lakes are a high regional warming rate observed in spring and to a lesser extent warming in summer, with agreement with air temperature trends in the region. The warming in spring is mainly due to the anticipatation of the end of winter and beginning of spring, and quick response of the shallow lakes. We also observed a general homogeneity in the warming trends, but with differences in the tributary rivers' inflow areas.

Key-words: remote sensing; lakes; water quality; water surface temperature; chlorophyll-*a*; atmospheric correction.

Lista de ilustrações

Lista de tabelas

Lista de abreviaturas e siglas

AC	*Atmospheric correction* – correção atmosférica
AOP	*Apparent optical property* – propriedade óptica aparente
CAPES	Coordenação de Aperfeiçoamento de Pessoal de Nível Superior
CDOM	*Chromophoric (Colored) dissolved organic matter* – matéria orgânica dissolvida cromofórica (colorida)
CELMM	Complexo Estuarino-Lagunar Mundaú-Manguaba
Chla	Clorofila-*a*
COA	Constituinte opticamente ativo
CNPq	Conselho Nacional de Desenvolvimento Cientifico e Tecnológico
DOC	*Dissolved organic carbon* – carbono orgânico dissolvido
IOP	*Inherent optical property* – propriedade óptica inerente
LSWT	*Lake surface water temperature* – temperatura superficial da água do lago
LST	*Land surface temperature* – temperatura superficial continental
MAE	*Mean Absolute Error* – erro médio absoluto
MERIS	*MEdium Resolution Imaging Spectrometer*
MODIS	*MODerate-Resolution Imaging Spectroradiometer*
MSI	*MultiSpectral Imager*

NAP	*Non-algal particles* – partículas não-algais
NIR	*Near infrared* – infravermelho próximo
nRMSE	*normalized Root mean-square error* – Raiz do erro quadrático médio normalizado
OLCI	*Ocean and Land Colour Instrument*
OWT	*Optical water type* – tipo óptico de água
PC	Ficocianina
POC	*Particulate organic carbon* – carbono orgânico particulado
RMSE	*Root mean-square error* – Raiz do erro quadrático médio
SAM	*Spectral angle mapper* – mapeador do ângulo espectral
S2	Sentinel-2 MSI
S3	Sentinel-3 OLCI e SLSTR
SST	*Sea surface temperature* – temperatura superficial oceânica
ST	*Surface temperature* – temperatura da superfície
SWT	*Surface water temperature* – temperatura superficial da água
TIR	*Thermal infrared* – infravermelho termal
TOA	*Top of atmosphere* – topo da atmosfera
TSA	Temperatura superficial da água
TSS	*Total suspended solids* – sólidos suspensos totais
VIS	Visível

Lista de símbolos

$a_i(\lambda)$	Coeficiente de absorção do parâmetro i no comprimento de onda λ
$a_i^*(\lambda)$	Coeficiente de absorção específica do parâmetro i no comprimento de onda λ
b_b	Coeficiente de retroespalhamento
ε	Emissividade
K_d	Coeficiente de atenuação difusa
λ	Comprimento de onda
L	Radiância
L^{down}	Radiância emitida/refletida para baixo pela atmosfera (*downwelling radiance*)
L^{up}	Radiância emitida/refletida para cima pela atmosfera (*upwelling radiance*)
L_{sensor}	Radiância medida pelo sensor (*top of atmosphere radiance*)
L_{corr}	Radiância medida pelo sensor e corrigida dos efeitos atmosféricos
η	Eficiência de aquecimento
Q	Vazão
ρ	Reflectância
ρ_w	Reflectância da água
R_{rs}	Reflectância de sensoriamento remoto (acima da superfície da água)

σ	Desvio-padrão
τ_a	*Aerosol optical thickness* – carga óptica do aerossol
τ	Transmissividade atmosférica
T_a	Temperatura do ar
T_w	Temperatura da água
T_{sensor}	Temperatura de brilho medida pelo sensor
w	Conteúdo de vapor d'água colunar na atmosfera
z_{eu}	Profundidade da zona eufótica
z_{SD}	Profundidade do disco de Secchi

Sumário

ANEXOS 179

Capítulo 1

Introdução

Lagos e lagunas são ambientes aquáticos continentais com alta produtividade, abrigando biodiversidade e provendo outros importantes serviços ecossistêmicos, como ciclagem de nutrientes, abastecimento de água, pesca e recreação (Janssen et al., 2021). Recentes estudos também mostram a importância destes sistemas no balanço global de carbono (Dean e Gorham, 1998; Cole et al., 2007), processando carbono orgânico alóctone, podendo ser fontes ou sumidouros de carbono (Tranvik et al., 2009), além de importantes fontes de metano (Günthel et al., 2019).

As características destes corpos hídricos tornaram eles importantes sítios de ocupação humana, sendo conectados a cidades como Porto Alegre (lago Guaíba), Maceió (lagoa Mundaú) e Rio de Janeiro (lagoa Rodrigo de Freitas), por exemplo. Devido a esta proximidade e interação antrópica, estes corpos d'água podem ser bastante afetados por impactos antropogênicos como descarga de nutrientes e poluentes, sobrepesca e excesso de retirada d'água, podendo ter impactos significativos em sua estrutura e funcionamento (Jenny et al., 2020). Impactos antropogênicos indiretos, como mudanças na bacia hidrográfica também pode afetar estes ambientes; por exemplo, mudanças no aporte de carbono orgânico dissolvido (*dissolved organic carbon* – DOC) podem mudar a composição da biota de um lago, causando uma mudança de dominância de produtores primários e produtividade (Jansson et al., 2000; Kelly et al., 2018; Zhang et al., 2020), que por sua vez podem impactar os serviços ecossistêmicos providos por estes corpos d'água (Janssen et al., 2021).

Lagos e lagunas são ecossistemas sensíveis a mudanças ao seu redor, e por serem sistemas lênticos muitas vezes localizados no final de sua bacia hidrográfica, e terem ampla distribuição geográfica e distintas características geomorfológicas, químicas e biológicas, foram cunhados como "sentinelas" de mudanças no ambiente (Williamson et al., 2008; Adrian et al., 2009). As mudanças climáticas vêm causando e irão causar mudanças nestes ambientes (Woolway et al., 2020); O'Reilly et al. (2003), por exemplo, em um trabalho seminal, mostrou que há variação na produtividade primária do Lago Tanganyika em função de variações no clima local. Diversos estudos já mostraram que houve aumento na temperatura superficial de lagos (LSWT, do inglês *lake surface water temperature*) (Livingstone, 2003; Schneider e Hook, 2010; O'Reilly et al., 2015). Em muitos casos, a LSWT têm aumentado, inclusive, mais rapidamente do que a temperatura do ar local (O'Reilly et al., 2015; Woolway et al., 2019), causando impactos como redução do oxigênio dissolvido e de habitat relacionados a temperatura da água (Halverson et al., 2021; Hansen, 2021). O estudo destes impactos, contudo, está limitado a lagos no Hemisfério Norte, e pouco é conhecido dos efeitos das mudanças climáticas em lagos no Hemisfério Sul, principalmente lagos rasos, que possuem resposta mais rápida devido à menor inércia termal.

Diante desses impactos climáticos e não-climáticos, a união de monitoramento e modelagem se torna essencial para o entendimento de como estas alterações têm afetado e irão afetar os sistemas lênticos. Nesse sentido, o uso de sensoriamento remoto têm tido grande desenvolvimento e aplicações na limnologia nos últimos anos, relacionando a cor da água (reflectância da água, ρ_w, em diferentes comprimentos de onda do visível – VIS – ou infravermelho próximo – NIR) a variáveis limnológicas, podendo servir como fonte de dados para ambientes sem monitoramento de campo, ou em sinergia com dados *in situ*, provendo espacialização de dados limnológicos e, muitas vezes, aumento da frequência destes dados (Dörnhöfer e Oppelt, 2016).

O uso do sensoriamento remoto permite gerar apenas uma quantidade limitada de dados, que são os que têm comportamento opticamente ativo, como matéria orgânica dissolvida cromofórica (*chromophoric dissolved organic matter* – CDOM) e pigmentos algais, além de parâmetros físicos como temperatura superficial e nível. Estas séries temporais e espacializadas de dados auxiliam no entendimento da estrutura e funcionamento de sistemas lóticos e lênticos, avaliando os impactos de longo prazo físicos, químicos e biológicos de mudanças no clima e no uso e cobertura do solo, assim como observar a dinâmica de eventos curtos, como *blooms* de algas ou eventos extremos, como realizado em diversos estudos na literatura (Woolway et al., 2016; Kraemer et al., 2017; Woolway e Merchant, 2018).

Contudo, apesar do desenvolvimento da teoria e de ferramentas de sensoriamento remoto com foco na limnologia, como modelos bio-ópticos, a extração destes parâmetros a partir da reflectância da água é complexa devido aos constituintes opticamente ativos (*optically active constituents* – OACs) na água e suas interações, o que dificulta o desenvolvimento de modelos bio-ópticos e ocasiona uma precisão consideravelmente inferior às medições de campo (Gege, 2017). Além disso, este processo é ainda mais dificultado para sensores a bordo de satélites, em que além da limitação da quantidade de bandas (resolução espectral) e de outras resoluções inerentes aos sensores (resoluções espacial, temporal e radiométrica),há interferência no sinal refletido pela superfície da água pela atmosfera e seus componentes, além de reflexão especular pela superfície da água e efeitos de adjacência, necessitando de correção para estes efeitos (que podem chegar a representar 90% do sinal medido pelo sensor) no processo chamado na literatura de correção atmosférica (*atmospheric correction* – AC), para se extrair a reflectância da superfície corretamente (Moses et al., 2017; Pahlevan et al., 2021).

Existem recentes esforços para a construção de bases de dados, para uso público, de produtos padronizados de sensoriamento remoto, como o Cyanobacteria Assessment Network (CyAN) (Schaeffer et al., 2015), um esforço conjunto de diversas agências estadunidenses para prover dados de *blooms* de cianobactérias em lagos e reservatórios. O objetivo destas bases é prover produtos padronizados para lagos em todo o mundo, permitindo, assim, análises consistentes, entre diferentes lagos, de dinâmica e tendências. Estas bases, porém, ainda estão limitadas à estimativa dos parâmetros devido à complexidade dos OACs em sistemas lênticos, aos processos de correção atmosférica e aos modelos bio-ópticos (Pahlevan et al., 2021). No caso do sensoriamento remoto da temperatura da água, a etapa de correção atmosférica é simplificada, e produtos prontos são disponibilizados. Entretanto, esses produtos são designados como temperatura superficial da terra (*land surface temperature* – LST), e nesta generalização os produtos perdem precisão devido à questões como variabilidade da emissividade (Masuda et al., 1988), coeficientes de calibração (Hulley et al., 2011) e principalmente aos efeitos de superfície, os efeitos de *cool-skin* (*pele fria*) e o *warm layer* (*camada quente*), que afetam a medição de radiação termal medida pelos sensores orbitais. Estes efeitos não são corrigidos nestes produtos, causando diferença nas estimativas de temperatura que pode afetar, por exemplo, cálculos de tendência de temperatura epilimnética, comumente utilizadas para aferir o impactos das mudanças climáticas na temperatura de lagos (O'Reilly et al., 2015). Porém, embora haja diversos estudos na área para águas oceânicas (Donlon et al., 2002; Minnett et al., 2011, 2019), onde a correção deste efeito é essencial para modelos climáticos, por exemplo, poucos são os esforços em águas continentais (Prats et al., 2018).

1.1 Justificativa

Dado o limitado conhecimento de como são impactados os lagos brasileiros por forçantes como mudanças na bacia hidrográfica e no clima, o sensoriamento remoto serve como ferramenta para estudar estes impactos de maneira espacializada, com séries temporais a depender da disponibilidade de dados dos sensores orbitais. Ainda há limitações no conhecimento de correção atmosférica e algoritmos de estimativas dos COAs, no caso do

SR da cor da água, e da correção dos efeitos de superfície, no caso do SR da LSWT, e de como estes afetam a qualidade dos dados providos por SR. Assim, a motivação desta tese é contribuir com o conhecimento nestas áreas do sensoriamento remoto e, com os dados validados dos sensores utilizados, avaliar a variação espaço-temporal de clorofila-a num complexo de lagunas tropicais rasas impactado por atividades antropogênicas na bacia hidrográfica, e de temperatura superficial em um conjunto de lagoas subtropicais costeiras rasas impactas pelas mudanças climáticas. Além disso, esta tese também é motivada por estudar e gerar conhecimento e caracterização destes sistemas, para auxiliar em seu manejo e conservação.

1.2 Questões científicas

Esta tese pretende responder a seguinte questão científica:

- quais são os padrões de variação espaço-temporal de parâmetros da qualidade da água em dois conjuntos de lagoas costeiras rasas? Quais são as forçantes que mais influenciam estes padrões?

1.3 Objetivo

Esta tese possui dois objetivos principais:

- avaliar os padrões de variação espaço-temporal de parâmetros da qualidade da água e suas forçantes em dois conjuntos de lagoas costeiras rasas a partir de bases de dados de sensoriamento remoto validadas com dados de campo

Como objetivos específicos, tem-se:

- gerar um produto padronizado de concentração de clorofila-a derivado do sensor Sentinel-2 MSI para o Complexo Estuarino-Lagunar Mundaú-Manguaba (CELMM) a partir de validação de uma combinação de algoritmos de correção atmosférica e estimativa de concentração de clorofila-a
- melhorar a compreensão de como o tipo óptico da água influencia na correção atmosférica e na estimativa de concentração de clorofila-a por sensores a bordo de satélites
- avaliar a variação espaço-temporal do fitoplâncton neste complexo, quais são suas forçantes, e possíveis fatores limitantes na produtividade

- gerar um produto padronizado de temperatura superficial da água para um conjunto de grandes lagoas subtropicais costeiras rasas derivado do sensor MODIS a partir da validação de algoritmos de correção do efeito de *cool-skin* desenvolvidos para águas oceânicas
- avaliar o impacto desta correção no cálculo de tendências da temperatura superficial e no balanço de calor deste conjunto de lagoas
- analisar o efeito de duas décadas de variabilidade climática na temperatura superficial e no balanço de calor destas lagoas

1.4 Organização da tese

Esta tese tem uma divisão clara em duas partes, referentes às duas áreas de estudo deste trabalho. Os dois primeiros capítulos foram desenvolvidos no CELMM, e os dois últimos nas grandes lagoas do Rio Grande do Sul, e em cada área de estudo, este trabalho se propôs a avaliar diferentes parâmetros com diferentes ferramentas. Em ambos os casos, o primeiro capítulo refere-se a melhorias metodológicas (sensoriamento remoto), e o segundo capítulo refere-se a aplicação da ferramenta para entendimento de processos (limnologia). Após o Capítulo 2, que contém curto um referencial teórico para o trabalho que foi desenvolvido aqui, os estudos foram desenvolvidos e apresentados nos Capítulos 3 a 6 para responder a questões científicas, escritos na forma de artigos em inglês:

- Capítulo 3:

  Correção atmosférica e de sunglint para estimativa de clorofila-*a* num sistema estuarino-lagunar produtivo tropical usando imagens Sentinel-2 MSI

  Validação de correção atmosférica e sunglint e de algoritmos para estimativa de clorofila-*a* utilizando o Sentinel-2 no CELMM.

- Capítulo 4:

  Avaliação da dinâmica a curto-prazo do fitoplâncton em um antropisado sistema estuarino-lagunar eutrófico tropical utilizando série temporal do Sentinel-2 MSI

  Avaliação da dinâmica do sistema através da análise da série temporal validada no CELMM durante o período de funcionamento do sensor.

- Capítulo 5:

  Impacto da correção do efeito de *cool-skin* sobre as tendências da temperatura superficial da água e o balanço de calor de três grandes lagoas rasas subtropicais

  Estudo de melhoria de dados de temperatura superficial da água derivados do MODIS e seu efeito.

- Capítulo 6:

  Altas taxas de aquecimento na primavera em três grandes lagoas rasas subtropicais no sul do Brasil detectadas com imagens MODIS

  Análise de tendências de aquecimento e suas forçantes nestas três lagoas durante o período de funcionamento do sensor a partir do produto validado.

A primeira parte, composta pelos Capítulos 3 e 4, refere-se a melhorias na questão metodológica do sensoriamento remoto da clorofila-*a*, avaliando o impacto da correção atmosférica e da seleção/calibração de algoritmos na estimativa de *chla*, tendo como estudo de caso o Complexo Estuarino Lagunar Mundaú-Manguaba e os sensores Sentinel-2 MSI, e análise, com estes dados, da dinâmica a curto-prazo da comunidade de fitoplâncton durante a duração da série deste sensor.

A segunda parte, composta pelos Capítulos 5 e 6, estudou a temperatura das grandes lagoas rasas do Rio Grande do Sul, primeiro analisando a melhoria da precisão de dados de temperatura superficial da água derivados do sensor MODIS, e sua aplicação para estudar o impacto das mudanças climáticas recentes na temperatura superficial da água das lagoas Mangueira, Mirim e dos Patos.

Capítulo 2

Referencial teórico

2.1 Forçantes externas e impactos antropogênicos e climáticos em lagos

Lagos são considerados sentinelas das mudanças climáticas, pois variações climáticas afetando a bacia hidrográfica ou a atmosfera vão se refletir em alterações nestes ecossistemas (Adrian et al., 2009; Williamson et al., 2008). Além disso, o aporte de substâncias carreadas pelos rios tributários de lagos afetam diretamente a estrutura e funcionamento dos ecossistemas. Estes aportes influenciam as taxas de aporte de nutrientes, matéria orgânica e sedimentos, que por sua vezes afetam diretamente a produção primária e os produtores (Wetzel, 2001).

Pesquisas recentes mostram, por exemplo, que a variabilidade das origens e quantidade de matéria orgânica dissolvida (DOM) vinda da bacia têm uma ligação direta e não-linear com a produção primária destes corpos hídricos, pois a variabilidade na estequiometria de nutrientes:carbono (disponibilidade de nutrientes) na DOM e a cromoforicidade (redução da quantidade de luz) do DOC (carbono orgânico dissolvido) criam diferentes relações entre produtividade e DOM (Kelly et al., 2018; Olson et al., 2020). Outros trabalhos mostram que mudanças no aporte de DOC também podem mudar a composição da biota de um lago, causando uma mudança de dominância de produtores primários (Jansson et al., 2000; Zhang et al., 2020), e a variação na disponibilidade de nutrientes, pode impactar os serviços ecossistêmicos providos por estes corpos d'água (Janssen et al., 2021).

O clima local afeta diretamente os ecossistemas aquáticos. As trocas de energia que ocorrem nestes ecossistemas são, em sua maioria, dependentes de reações químicas cuja velocidade depende da temperatura (lei de Arrhenius), e esta é, por isso, uma variável chave nestes ambientes, controlando, por exemplo, a solubilidade de gases, taxas de predação e distribuição de espécies (Wetzel, 2001). A temperatura da água (T_w) depende sobretudo do balanço de calor na superfície, que é determinado pelas condições atmosféricas: radiação incidente na superfície da água, velocidade do vento, e, principalmente, da temperatura do ar (Piccolroaz et al., 2013). Outras características do corpo hídrico também moldam como o clima afeta a variação física do lago, como a sua morfologia, que molda a superfície de troca de calor entre a água e a atmosfera (Ptak et al., 2018; González-Ávila et al., 2021), e turbidez, que influencia o albedo (razão entre a radiação refletida e a radiação incidente sobre a superfície) da água e, portanto, mudanças na turbidez podem influenciar o balanço de calor e a estratificação térmica (Heiskanen et al., 2015; Rose et al., 2016; Richardson et al., 2017).

Além destas, outras variáveis ambientais também alteram diretamente o regime de lagos, influenciando diretamente a sua hidrodinâmica, que têm relação direta com a disponibilidade de nutrientes, a temperatura e a produtividade (Cavalcanti et al., 2016). Em lagos rasos, por exemplo, a velocidade do vento pode ser determinante na hidrodinâmica, promovendo mistura e prevenindo estratificação térmica, que tem grande influência na comunidade fitoplânctonica, além de poderem ser mais afetados por ressuspensão de sedimentos, reduzindo a transparência da água (Crossetti et al., 2014). Padrões de precipitação e vazão afluente também tem papel importante na hidrodinâmica de certos lagos, pois além do aporte de substâncias vinda da bacia, aumentam o nível da água e podem causar diluição de nutrientes. Oleksy et al. (2021) mostrou que parâmetros como tempo de residência, razão área da bacia:área do lago e conectividade hidrológica influenciam a variação do metabolismo de lagos em razão de variabilidade de chuvas. Eventos extremos de precipitação também podem alterar significativamente o estado destes ecossistemas, podendo ser causadores de floração de algas pelo aporte súbito de nutrientes (Yang et al., 2016).

Dada a grande influência das forçantes externas sobre as condições destes ecossistemas aquáticos, se evidencia a necessidade de quantificar ou estabelecer relações entre estas forçantes e a qualidade da água destes sistemas, e estudar os impactos de mudanças nestas forçantes. Numa revisão bibliográfica sobre as pressões sobre grandes lagos ao redor do globo, Jenny et al. (2020) mostrou a devido a proximidade a grandes populações, mudanças de uso do solo e sinergia entre diversos estressores têm deteriorado a qualidade da água de grandes lagos. A Figura 2.1 mostra uma panorama das principais mudanças exercendo pressão sobre grandes lagos em cada continente ao redor do globo, como eutrofização (principalmente por aumento de fósforo), mudanças na dinâmica do DOC, sobrepesca, excesso de retirada d’água, e aquecimento, deteriorando a qualidade da água destes ecossistemas.

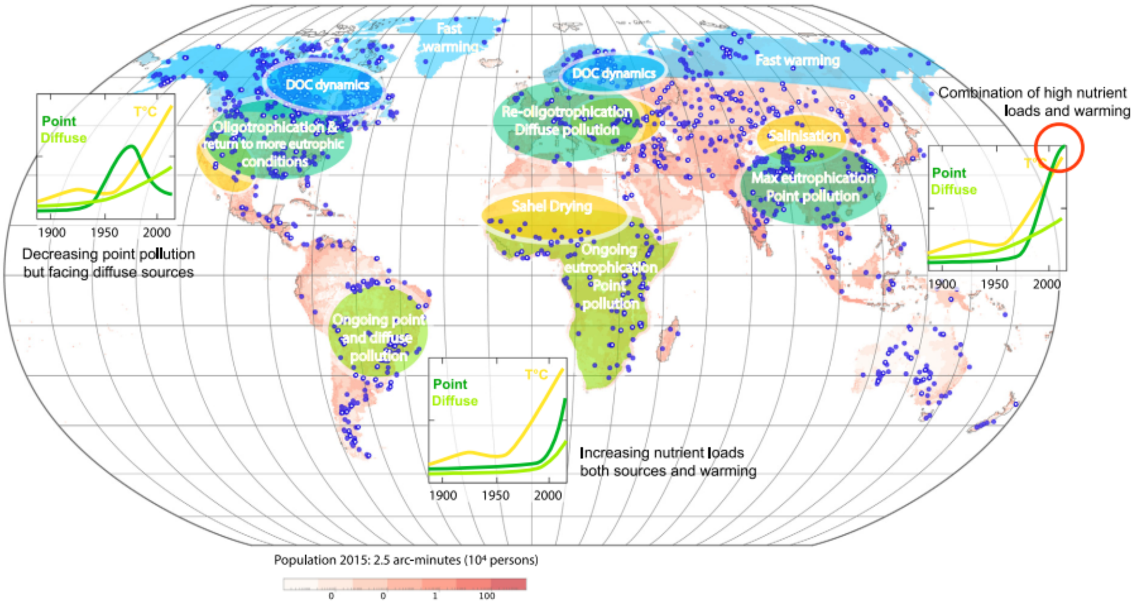

Figura 2.1 – Principais mudanças exercendo pressão sobre grandes lagos em cada continente, ressaltando a pressão por aumento de poluição pontual e difusa e aquecimento nos grandes corpos d'água brasileiros. (Fonte: Jenny et al. 2020)

Mudanças na bacia ou no aporte de nutrientes têm efeitos diretos na composição e distribuição de espécies, redução da transparência da água, aumento de anoxia, perda de biodiversidade, e aumento de eventos de floração de algas, que podem deteriorar ainda mais a qualidade da água (Jenny et al., 2020; Amorim e Moura, 2021). Além disso, as mudanças no aporte de DOM também afetam diretamente a produção primária e a disponibilidade de oxigênio, como já afirmado acima (Olson et al., 2020).

As mudanças climáticas vêm causando e irão causar mudanças nestes ambientes (Woolway et al., 2020); O'Reilly et al. (2003), por exemplo, em um trabalho seminal, mostrou que houve variação na produtividade primária do Lago Tanganyika em função de variações no clima local. Diversos estudos já mostraram que houve aumento na temperatura superficial de lagos (LSWT, do inglês *lake surface water temperature*) (Livingstone, 2003; Schneider e Hook, 2010; O'Reilly et al., 2015). Em muitos casos, a LSWT têm aumentado, inclusive, mais rapidamente do que a temperatura do ar local, mostrando a sinergia entre as mudanças de componentes atmosféricas afetando lagos (Lenters et al., 2005), principalmente devido ao aumento de radiação solar (O'Reilly et al., 2015; Schmid e Köster, 2016) ou diminuição sistêmica da velocidade do vento na superfície (Woolway et al., 2019). Estes parâmetros, junto com a temperatura, afetam diretamente o balanço de calor e a hidrodinâmica de lagos (Woolway et al., 2018), e o impacto destas mudanças nestes fluxos de calor são complexas (Fink et al., 2014; Woolway et al., 2019).

Estas mudanças, na maioria das vezes, não são constantes ao longo do ano, mas sim apresentam uma forte componente sazonal em função da variação sazonal da temperatura (Winslow et al., 2017; Kelleher et al., 2021) ou de aumento acentuado em função de acentuada estratificação térmica, que reduz a camada d'água interagindo com a atmosfera e modifica os padrões de balanço de calor quando a estratificação ocorre (Lee et al., 2012; Woolway e Merchant, 2018; Toffolon et al., 2020). A estratificação térmica também é diretamente afetada por características como morfologia (Kraemer et al., 2015) e velocidade do vento, e mudanças no vento podem resultar em variação mais acentuada no balanço de calor superficial (Woolway et al., 2019). Além disso, estas variações sazonais tem impacto adicional sobre o funcionamento dos ecossistemas, como modificações na fenologia dos produtores primários (Deng et al., 2014).

Um resumo dos impactos das mudanças climáticas sobre lagos pode ser visto na Figura 2.2. Estes incluem mudanças no balaço térmico, redução da cobertura de gelo, aumento da estratificação térmica e do balanço hídrico (Woolway et al., 2020). Como resposta a estas mudanças ocorre, por exemplo, redução do oxigênio dissolvido (a sua solubilidade diminui com a temperatura), podendo aumentar a hipoxia de águas profundas, alterações na produtividade primária, e modificações no habitat relacionados a temperatura da água (tanto vertical como horizontalmente) (Jenny et al., 2020; Halverson et al., 2021; Hansen, 2021).

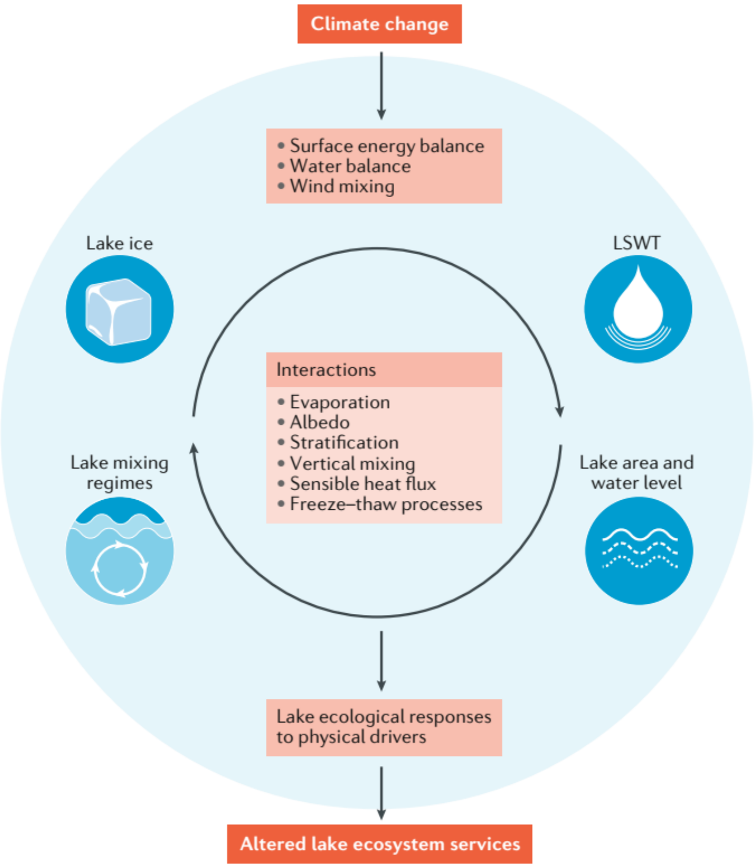

Figura 2.2 – Fluxograma ilustrando os impactos físicos das mudanças climáticas em lagos, como mudanças nos fluxos de energia, balanço hídrico, e mistura por vento. (Fonte: Woolway et al. 2020)

Assim, o entendimento de quais mudanças estão ocorrendo, com qual intensidade, e como estas afetam os ecossistemas aquáticos é essencial. Nesse sentido, o sensoriamento remoto se mostra como uma excelente ferramenta para esta tarefa, provendo dados consistentes e espacializados de alguns parâmetros limnológicos que têm grande valor nestes estudos, como por exemplo para estimar a taxa de aumento da temperatura superficial de lagos (Woolway e Merchant, 2018; Toffolon et al., 2020) e como estas afetam o habitat e a distribuição espacial de espécies (Halverson et al., 2021; Hansen, 2021). A sessão a seguir faz um resumo de como esta ferramenta pode ser utilizada na limnologia.

2.2 Sensoriamento remoto de variáveis limnológicas

O sensoriamento remoto é uma grande ferramenta para ajudar a compreender a variação espaço-temporal de variáveis resposta de ecossistemas aquáticos, e tem sido cada vez mais tanto estudado e desenvolvido para fornecer melhores produtos, como em aplicações para o entendimento de impactos antrópicos e climáticos sobre ambientes aquáticos lóticos e, principalmente, lênticos. Isto se deve não só ao crescimento do número de sensores com características ótimas para o sensoriamento da cor da água, como também às limitações do monitoramento contínuo quanto à acurada descrição espaço-temporal de processos que ocorrem nestes ambientes (Dörnhöfer e Oppelt, 2016). Esta revisão mostra um pequeno panorama do sensoriamento remoto de águas continentais, mostrando as principais variáveis que podem ser estimadas, o procedimento, as limitações e os erros geralmente associados à estas estimativas.

O sensoriamento remoto de águas continentais ou interiores (em inglês *inland waters*) também é conhecido como sensoriamento remoto da qualidade da água ou da cor da água (*water colour*), neste último caso quando considerando apenas a radiação de ondas curtas, que inclui a região do visível. Como considerarei também o espectro de ondas longas, para estimativas de temperatura da água, usarei então a terminologia de sensoriamento remoto de águas continentais, que é mais geral. Além disto, aqui trataremos mais especificamente do SR da água por sensores orbitais (a bordo de satélites), e quando tratarmos de medições de campo, por espectroradiômetros, isto será especificado.

O SR da cor da água se baseia na interação entre a radiação eletromagnética e a matéria, que neste caso não apenas os constituintes da água – incluindo a água – como também a atmosfera. Isto foi, inicialmente, aplicado para estudos de águas oceânicas, que proveu uma base inicial de conhecimento para o SR de águas interiores. Este é comparativamente muito mais recente do que o da terra ou águas oceânicas (Topp et al., 2020). Isto porque, além do fato da limnologia ser uma área mais restrita e recente, também apresenta maior complexidade por a cor da água ser, em geral, muito mais escura (sinal mais baixo) do que a da superfície terrestre, e muito mais diversificada do que águas oceânicas (Topp et al., 2020). A exemplo de curiosidade, a primeira missão orbital com diferentes bandas espectrais, o Landsat 1, lançado em 1972, foi designado principalmente para estudos de recursos naturais terrestres, com poucas aplicações nas relativamente escuras águas oceânicas e interiores.

Desde então, as bandas dos sensores foram consideravelmente modificadas para incorporar aplicações do SR da cor da água. A Figura 2.4 e a Tabela 2.1 resumem todas as variáveis limnológicas que podem ser estimadas por SR. São muitas as propriedades da água cuja informação pode ser obtida por SR, o que provêm uma potencial base de dados imensa para se melhor compreender os ecossistemas aquáticos e o impacto de forçantes externas sobre eles. Contudo, ressalta-se que o SR de ecossistemas aquáticos é relativamente recente, como mencionado anteriormente, e ainda há muitos desafios para expandir sua aplicabilidade na limnologia, principalmente para os sensores mais recentes.

Tabela 2.1 – Lista das propriedades de lagos, as suas variáveis-resposta, e os indicadores estimáveis por sensoriamento remoto (adaptado de Adrian et al., 2009 e Dörnhöfer e Oppelt, 2016).

Propriedade	**Variável**	**Indicador estimável**
Transparência	DOC Turbidez Disco de Secchi	CDOM material particulado suspenso (SPM) turbidez coeficiente de atenuação difusa (K_d) profundidade de disco de Secchi (z_{SD}) profundidade da zona eufótica (z_{eu})
Biota	Biomassa de fitoplâncton Fenologia Composição de espécies	*Chla* Ficocianina *Bloom* de algas Macrófitas submersas Macrófitas emersas Sedimento de fundo
Hidrologia	Nível	Nível (altimetria) Batimetria Área inundada
Temperatura	Temperatura epilimnética	Temperatura superficial

Inicialmente, nesta seção vou dar uma introdução ao sensoriamento remoto de águas interiores, e então, as subseções seguintes focarão apenas nas três variáveis estimadas neste trabalho, clorofila-a, matéria orgânica cromofórica dissolvida (CDOM), e temperatura, além do processo de remoção da influência da atmosfera no sinal medido pelos sensores orbitais, conhecido como correção atmosférica.

É sabido que a luz solar entra na água, interage com as moléculas de água e outros materiais que interagem com a luz, e parte desta luz é retroespalhada para fora da água, denotando sua cor, o que provém informações sobre o corpo d'água e os materiais ali presentes (Gordon, 2019). Portanto, a informação da relação entre a luz incidente e a luz

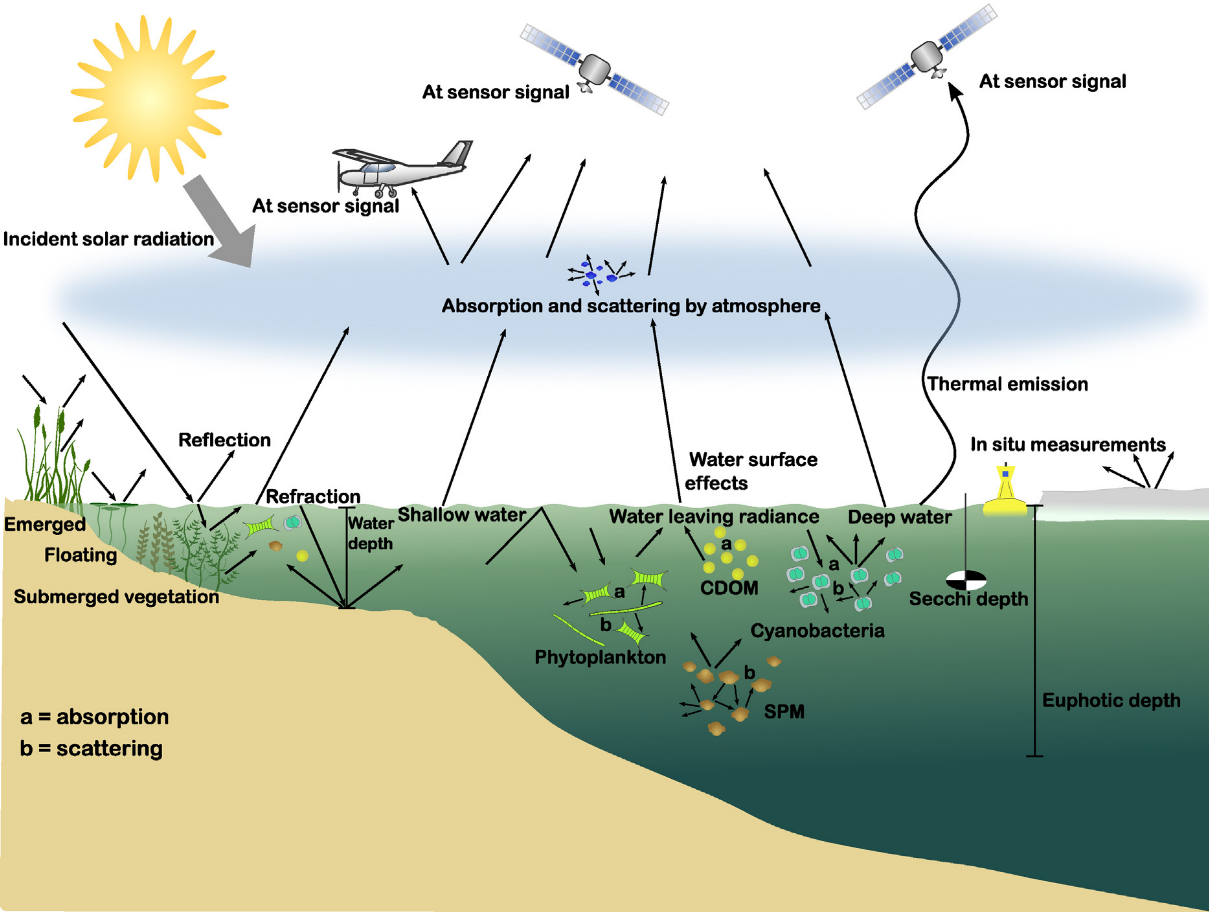

Figura 2.3 – Figura ilustrando a interação da radiação solar com a matéria após a entrada na atmosfera e seu caminho até atingir os sensores, e as propriedades de águas interiores que podem ser estimadas por sensoriamento remoto. (Fonte: Dörnhöfer e Oppelt 2016)

retroespalhada, e de como os materiais presentes na água interagem com a luz, formam o princípio básico de funcionamento do SR da cor da água. Os materiais que interagem com água são conhecidos como constituintes opticamente ativos (COAs), e são 4: pigmentos fotossintetizantes, principalmente a clorofila-a, presentes no fitoplâncton; material orgânico dissolvido na água e que interage com a luz, conhecido como cromofórico ou colorido; partículas não-algais suspensas, ou material particulado suspenso; e a própria água. Estes 4 componentes possuem propriedades ópticas inerentes e interagem com a luz de maneira complexa, e as diferentes concentrações entre si levam a diferentes comportamentos de interação com a luz, interferindo entre si. Águas que contém os 3 componentes (além da água) são chamadas de opticamente complexas pela dificuldade na quantificação das concentrações destes constituintes por conta desta interação (Gordon, 2019). Esta interação gera tantas possibilidade de cores de água, que levou à criação de subgrupos de tipos ópticos da água (*optical water types*, OWTs), com o objetivo de se definir possíveis simplificações para cada grupo, assim como os melhores modelos biofísicos de estimativas dos COAs. Spyrakos et al. (2018), por exemplo, propôs 13 grupos de OWTs para águas continentais, e mais 9 grupos de OWTs para águas costeiras. Subsequentes trabalhos utilizaram esta divisão para propôr os melhores algoritmos para cada grupo (Neil et al., 2019; Pahlevan et al., 2021).

Estas subdivisões mostram como as águas possuem diferentes cores em função da interação dos constituintes com a luz. Estes interagem de dois modos: por absorção ou espalhamento. A cor que observamos é o resultado da luz solar que é retroespalhada pela superfície observada, num comprimento de onda aproximado de 400 a 700 nm, como mostrado na Figura 2.3. Portanto, uma superfície azul como a água do oceano absorve a luz nos comprimentos de onda do verde até o vermelho, e espalha a luz no azul. Nesse sentido, o CDOM possui um comportamento de absorção principalmente no azul e verde, o que faz com que águas ricas em CDOM tenham uma coloração azul escura. Fitoplâncton absorve a luz principalmente no azul e vermelho, tendo uma coloração geralmente esverdeada, embora haja grande variação dentre grupos e espécies de indivíduos fotossintetizantes e pigmentos. O sedimento inorgânico espalha muita luz, aparecendo claro na maior parte do espectro, principalmente do verde ao vermelho, tornando as águas marrons. Este conhecimento de como os COAs interagem com a luz ao longo do espectro, isto é, suas curvas de absorção e retroespalhamento, formam a base dos algoritmos para sua quantificação.

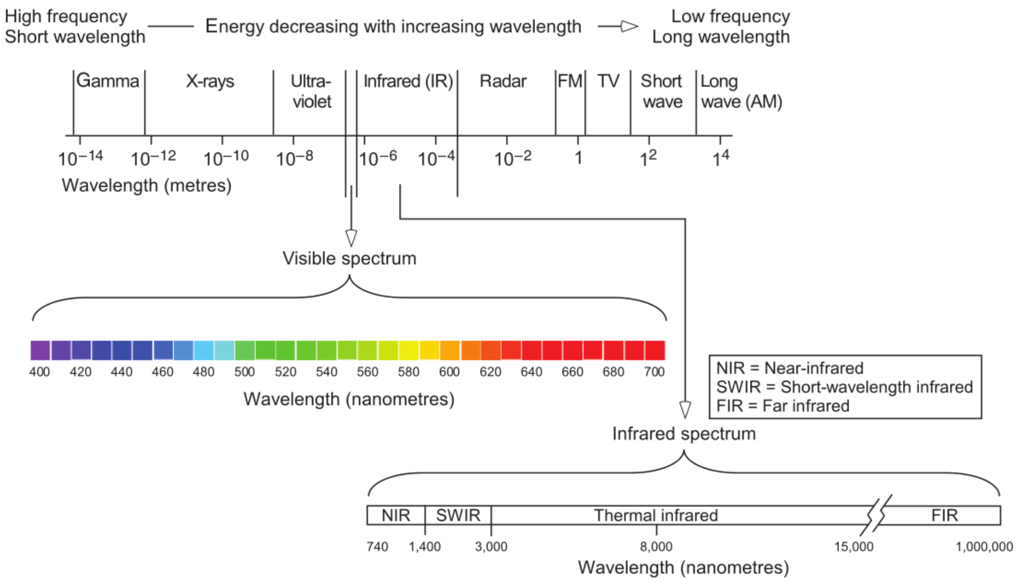

Figura 2.4 – Espectro da radiação eletromagnética. (Fonte: Purkis e Klemas 2011)

Devido à complexidade da interação dos COAs com a luz, nos algoritmos de quantificação dos constituintes geralmente são utilizados os picos de absorção e espalhamento da luz pelos COAs, principalmente aqueles que são únicos àquele COA. A Figura 2.5 mostra um exemplo do padrão de absorção da luz pelos COAs, neste caso em águas eutróficas, com grande presença de fitoplâncton. Por exemplo, em águas oceânicas onde há a presença apenas de água e fitoplâncton, são utilizadas bandas do verde (560 nm) e do azul (440 nm) para estimar a concentração de clorofila-a, contudo para águas produtivas com presença de

CDOM, que absorve luz nestas faixas, se utilizando modelos nas faixas do verde e *red-edge* (700 nm), onde há pico de espalhamento e absorção da luz pelo pigmento (Gitelson e Kondratyev, 1991; Dall'Olmo et al., 2003).

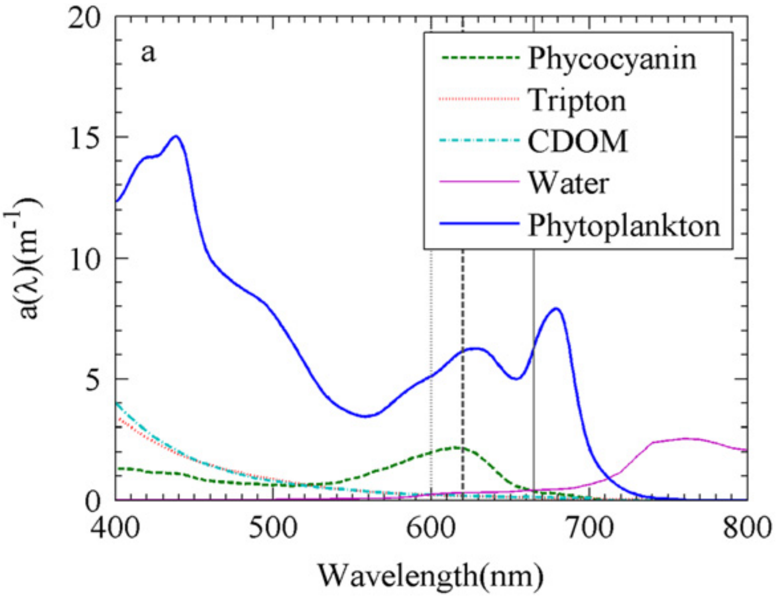

Figura 2.5 – Exemplo de coeficiente de absorção, $a(\lambda)$, dos COAs ao longo do espectro medidos em um conjunto de 15 tanques de aquacultura no Delta Research Extension Center. (Fonte: Mishra e Mishra 2014)

A partir do conhecimento dos COAs e da cor da água, se faz possível também estimar outras variáveis limnológicas. A turbidez (transparência) da água, por exemplo, é o resultado da interação entre estes 4 COAs, e é estimado a partir de modelos de turbidez ou outros indicadores de transparência da água, por exemplo com o disco de Secchi, muito utilizado por sua facilidade de medição e bons resultados, além de existirem relações para se estimar a profundidade da zona eufótica e o coeficiente de atenuação difuso (Lee et al., 2015; Ji, 2017).

Para quantificar parâmetros por sensores orbitais, se faz necessário primeiro corrigir a intensidade da luz que é medida pelo sensor (conhecido como radiação de topo da atmosfera, *top of atmosphere* – TOA) para a superfície (conhecido como radiação de fundo da atmosfera, *bottom of atmosphere* – BOA). Este procedimento, conhecido como correção atmosférica, é bastante complexo, envolve várias variáveis, e é sucintamente descrito a seguir.

2.2.1 Correção atmosférica

O processo de compensação pelo espalhamento e absorção da atmosfera e dos efeitos de reflexão na superfície da água (*skyglint* and *sunglint*) do sinal medido no topo da atmosfera (TOA) é conhecido como o processo de correção atmosférica (AC – *atmospheric correction*). Este processo é essencial para uma correta extração da reflectância da superfície da água (ρ_w) e de todos os produtos que dela derivam. Este processo é bem sucedido sobre águas oceânicas, porém em águas continentais e costeiras ainda há bastante incerteza e erros, em especial em sensores mais recentes, e isto limita a geração de produtos derivados destes dados (Pahlevan et al., 2021).

O processo de correção atmosférica é bastante complexo por haver muita interferência da atmosfera no sinal medido pelos sensores, principalmente na faixa do visível, sendo mais intenso no azul e decaindo com o comprimento de onda, podendo representar mais de 90% do sinal medido no TOA (Barbosa et al., 2019). Além disso, o reflexão da luz na superfície, conhecida como glint, em que a reflexão do céu, conhecida como skyglint, e do disco solar, conhecida como sunglint, afetam diretamente a medição correta da cor da água, influenciam não apenas o sinal medido por sensores orbitas como também medições de campo, utilizando espectroradiômetros, que devem ser cuidadosamente coletados de maneira a compensar por estas duas reflexões. A Figura 2.6 resume como a água e a atmosfera interagem com a luz até esta chegar no sensor. As substâncias presentes na água (COAs) interagem com a luz e são responsáveis pela cor da água, mas a radiação medida pelo sensor também inclui as componentes da atmosfera e de glint. Cada um destes componentes são resumidos pela equação de transferência radiativa (sem considerar efeitos de adjacência):

$$\rho_t(\lambda) = t\rho_w(\lambda) + [\rho_r(\lambda) + \rho_a(\lambda) + \rho_{ar}(\lambda)] + t_g\rho_g(\lambda) \tag{2.1}$$

em que ρ_t é a reflectância no topo da atmosfera, t é transmitância difusa da atmosfera, ρ_r é a reflectância de Rayleigh, ρ_a é a reflectância dos aerossóis, ρ_{ar} é o espalhamento por aerossóis e espalhamento Rayleigh, ρ_g é a reflectância por glint, e t_g é a transmitância da radiação especular pela atmosfera. Em certos algoritmos de correção, os componentes entre colchetes podem ser calculados juntos como ρ_{path}.

A transmissividade difusa é computada conhecendo as transmissões por moléculas na atmosfera e aerossóis. A componentes dos aerossóis é a mais difícil de ser estimada, e pequenos erros nesta componente podem levar à grandes erros em ρ_w, principalmente em função do baixo sinal da reflectância da água (absorve muita luz) (Gordon e Wang, 1994; Barbosa et al., 2019). Por isto, esta é a componente que apresenta maior diversidade de métodos de estimativa (Pahlevan et al., 2021). Em águas oceânicas, sua estimativa é facilitada por haver quase nenhuma radiação da água no NIR (suposição de pixel-negro) e haver homogeneidade espacial de aerossóis com pouca absorção de luz. Em águas continentais ou costeiras, a reflectância da água no NIR é muitas vezes significativa em função de sedimento que espalha luz nesta faixa, além de haver presença de múltiplos aerossóis com variabilidade espacial e espalhamento por aerossóis de superfícies terrestres que afetam ρ_{path} (efeito de adjacência) (Moses et al., 2017; Bulgarelli e Zibordi, 2018).

O trabalho de Pahlevan et al. (2021) realizou um grande estudo de revisão e

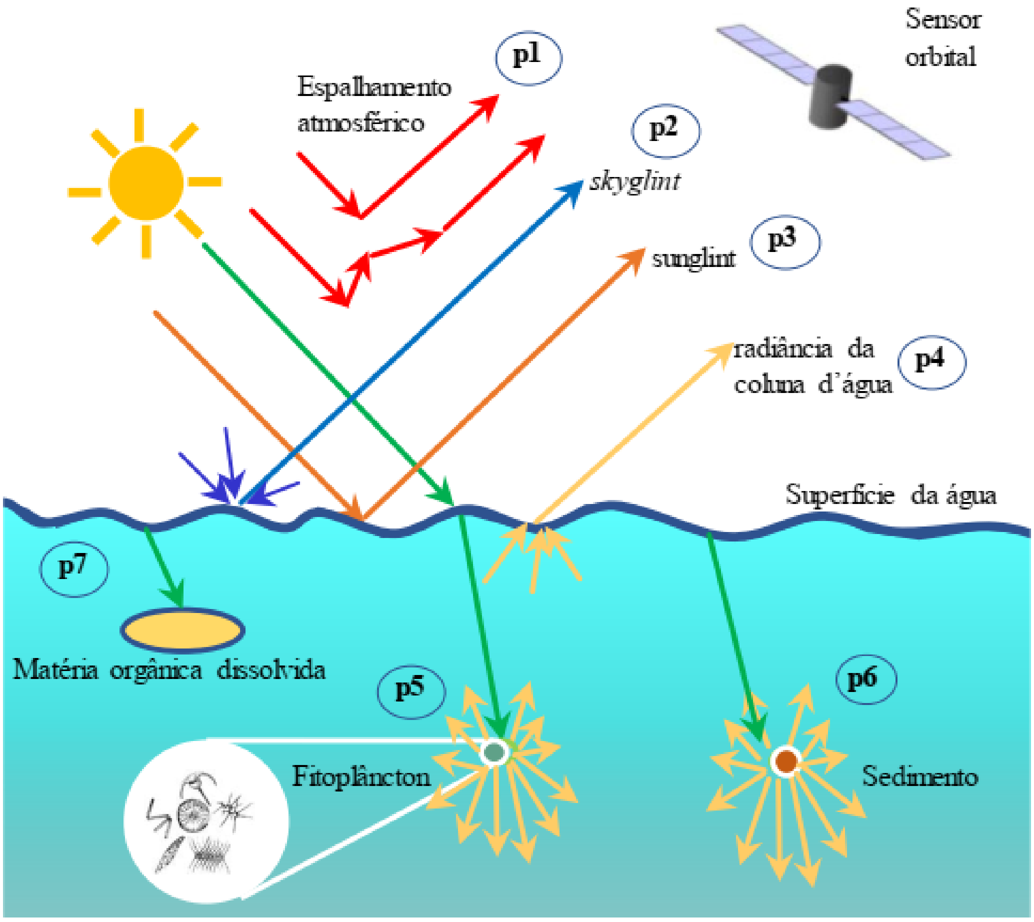

Figura 2.6 – Imagem mostrando como a luz interage com a atmosfera e a água até chegar ao sensor orbital. Os p's indicam os componentes que interagem com a luz e influenciam no sinal medido pelo sensor. (Fonte: Barbosa et al. 2019)

comparação dos principais processadores de AC para os dois principais sensores de média-resolução com usabilidade em águas interiores, Sentinel-2 MSI e Landsat 8 OLI. Em geral, os processadores podem ser divididos em duas grandes categorias, modelo de duas etapas e modelos de aprendizado de máquina. No primeiro, os efeitos de absorção são removidos primeiro e então a contribuição por aerossol é estimada. Esta contribuição, como dito anteriormente, é a que apresenta maior variabilidade de métodos, podem ser de abordagens terrestres ou oceânicas adaptadas à águas continentais, ou abordagens espectrais. Já os modelos de aprendizado de máquina são redes neurais artificiais que foram calibradas com dados medidos de reflectância de campo e de satélite, informações de geometria de visada, e parametrizações atmosféricas e de constituintes da água para a estimativa da reflectância da água (Doerffer e Schiller, 2007). Este estudo testou 8 processadores de AC, e mostrou que há grande variabilidade de desempenho entre os vários processadores de acordo com a banda e o OWT, além do impacto disso nas estimativas de clorofila-a e sólidos suspensos totais, principalmente considerando como os diferentes desempenhos nas bandas afetam a forma espectral de ρ_w. Mais informações sobre o funcionamento dos processadores de AC estão incluídos no Capítulo 3 desta tese, em que é apresentada uma pequena descrição de como cada processador testado funciona, suas simplificações e suposições.

Além destes desafios relacionados à composição atmosférica, os efeitos de superfície também tem considerável efeito na estimativa de ρ_w. A Figura 2.7 mostra a ocorrência de sunglint numa imagem do Sentinel-2 MSI sobre as lagoas Mangueira e Mirim, áreas de estudo desta tese. Esta reflexão direta do disco solar causa uma grande mudança na reflectância da água medida pelo sensor, podem até ocasionar saturação das bandas. Ela afeta a superfície da água principalmente quando o ângulo zenital solar é alto, que ocorre durante o verão, mas em regiões próximas ao Equador pode ocorrer ao longo do ano (Harmel et al., 2018). Para a sua correção, uma das abordagens é considerar que a radiação residual medida no infravermelho de ondas curtas (SWIR) após a correção atmosférica é toda devido ao sunglint, e então utilizar um modelo espectral linear para corrigi-lo nas demais bandas (Barbosa et al., 2019). O modelo do GRS (Glint Removal for Sentinel-2), utilizado no Capítulo 3, se baseia nisso, porém a correção espectral é feita utilizando uma estimativa da função de distribuição de reflectância bidireccional (BRDF) no SWIR e da t_g (Harmel et al., 2018).

Figura 2.7 – Imagem do Sentinel-2 MSI sem correção atmosférica mostrando a ocorrência de sunglint sobre a parte sul da lagoa Mangueira, e em algumas área da lagoa Mirim, mais à oeste.

Além do sunglint, os efeitos de adjacência também podem ter grande efeito na estimativa da reflectância da água, principalmente em corpos d'água próximos à superfícies brilhantes como áreas urbanas (Bulgarelli e Zibordi, 2018). A sua correção é complexa e ainda incipiente na literatura para águas interiores, mas este tema não foi abordado nesta tese.

A interação da atmosfera com a luz decai do azul para comprimentos de onda maiores, com variações. No infravermelho termal, a correção dos efeitos atmosféricos é bastante simplificada pois, além de a radiação medida ser emitida pela superfície, ou seja, interagir apenas uma vez com a atmosfera (“up”), os sensores geralmente estão localizados em janelas atmosféricas, isto é, a interação entre os compostos da atmosfera e a luz é minimizada. Como comparação, da radiação medida por sensores na faixa do azul, até 90% pode ser devido a efeitos atmosféricos (Moses et al., 2017), enquanto que os efeitos atmosféricos correspondem a erros de cerca de 1 K da temperatura superficial (Jiménez-Muñoz e Sobrino, 2006; Coll et al., 2012). A correção atmosférica no infravermelho termal geralmente é feita juntamente com a transformação de temperatura de brilho (medida pelo sensor) para temperatura de superfície, e este processo é melhor explicado na seção sobre o sensoriamento remoto da temperatura.

2.2.2 Clorofila-*a*

O fitoplâncton é o conjunto de organismos aquáticos microscópicos fotossintetizantes que não consegue se mover na água, apenas verticalmente controlando a sua flutuação, e vivem portanto dispersos na água. Eles formam a base da cadeia alimentar dos ecossistemas aquáticos, iniciando o fluxo de energia do sol para a teia trófica, e produzindo aproximadamente metade do oxigênio terrestre (considerando também o fitoplâncton oceânico). Seu entendimento é essencial para a compreensão de ecossistemas aquáticos terrestres ou oceânicos, sua estrutura e funcionamento, e como as mudanças climáticas irão impactar estes ecossistemas.

A necessidade de mapear fitoplâncton por sensoriamento remoto é antiga (Gordon, 2019), porém a forma como o fitoplâncton interage com a luz é bastante complexo. O efeito medido é o de milhões de células interagindo com a luz através de suas diferentes células fotossintetizantes, com diversos fatores que afetam esta interação (absorção e espalhamento) como o tamanho e formato das células, a variedade de grupos de organismos, a pigmentação (conjunto de pigmentos que absorvem luz), e a sua estrutura celular (Matthews, 2017).

O pigmento clorofila-a (chla) tem sido amplamente utilizado como *proxy* da biomassa de fitoplâncton não apenas no sensoriamento remoto como na limnologia em geral. Este é quase sempre o principal pigmento de absorção de luz, e tem comportamento espectral bem conhecido. Como afirmado anteriormente, contudo, a contração de chla varia entre os diferentes grupos de fitoplâncton, com diferentes configurações de luz, e até com o tamanho das células destes organismos (efeito de empacotamento), o que, somada à variabilidade na coluna d’água (múltiplos grupos ao mesmo tempo), aumenta a complexidade das estimativas de chla por sensoriamento remoto (Matthews, 2017).

A base de algoritmos de estimativa de chla são o seu comportamento espectral, *i.e.*, picos de absorção e espalhamento de luz. Como mostrado na Figura 2.5, a chla apresenta picos de absorção no azul (440 nm) e vermelho (670 nm), e picos de retroespalhamento no verde (560 nm) e infravermelho próximo (a partir de 700 nm). Logo, uma maior biomassa de fitoplâncton na água provavelmente terá (esta relação não é linear e depende de uma série de fatores, como dito anteriormente) uma maior concentração de chla, com maior absorção no azul e vermelho e reflexão no verde, resultando em águas mais esverdeadas. Esta relação é a base de algoritmos semi-empíricos relacionando a razão da luz azul e a verde com a chla. Um dos algoritmos mais conhecidos é o desenvolvido para o MERIS (OC4Me) (O'Reilly et al., 1998):

$$chla = 10\hat{}(a_0 + a_1x + a_2x^2 + a_3x^2 + a_4x^4) \tag{2.2}$$

em que

$$x = \log_{10}\left(\frac{R_{rs1}}{R_{rs2}}\right) \tag{2.3}$$

$$R_{rs1} = \max[R_{rs}(443), R_{rs}(489), R_{rs}(510)] \tag{2.4}$$

$$R_{rs2} = R_{rs}(560) \tag{2.5}$$

Este algoritmo é a base de algoritmos de cor do oceano e ele e suas derivações são utilizadas até hoje para estimativas de chla em lagos de águas claras.

Para águas opticamente complexas com quantidades significativas de material suspenso e, principalmente, CDOM, a absorção é a soma destes 3 componentes. Por exemplo, no pico de absorção do fitoplâncton em 440 nm, a absorção da luz por CDOM é bastante alta (Figura 2.5), e em águas com bastante detrito e CDOM o uso de algoritmos no azul se torna inviável devido a soma disto ao baixo sinal resultante nesta faixa, e aos efeitos atmosféricos, que são mais altos no azul (Moses et al., 2017). Nestes casos, outras informações são utilizadas para se estimar chla nestas condições.

De maneira análoga, muitos algoritmos utilizam o outro pico de retroespalhamento da chla, em 700 nm em diante para concentrações acima de 10 mg m^{-3}, como mostrado na Figura 2.5, que geralmente tem alta correlação com a concentração de chla (Gons et al., 2002). Enquanto em águas apenas com ou dominadas por fitoplâncton a banda do verde é utilizada, em águas com concentrações significativas de CDOM e NAP a banda de 700 nm (*red-edge*) é preferível por conta da influência maior destes dois COAs no verde. Algoritmos semi-empíricos semelhantes ao OC4 são utilizados, porém utilizando as bandas do vermelho (alta absorção da luz) e *red-edge* (alto retroespalhamento da luz), em vez do azul e verde (Gitelson e Kondratyev, 1991; Dall'Olmo et al., 2003). Esta é a base de muitos algoritmos desenvolvidos para águas interiores mesoeutróficas, como mostrado em Neil et al. (2019). Alguns exemplos são o modelo de razão de bandas (Gitelson e Kondratyev, 1991; Moses et al., 2009):

$$chla \propto \frac{R_{rs}(708)}{R_{rs}(665)} \tag{2.6}$$

O modelo de três bandas (Gitelson et al., 2003; Dall'Olmo et al., 2003; Moses et al., 2009):

$$chla \propto \left[R_{rs}(753) \times (R_{rs}^{-1}(665) - R_{rs}^{-1}(708))\right] \tag{2.7}$$

E o modelo de índice de bandas (*Band Index*) (Dall'Olmo e Gitelson, 2005; Gitelson et al., 2008; Le et al., 2009; Yang et al., 2010):

$$chla \propto \left(\frac{R_{rs}^{-1}(665) - R_{rs}^{-1}(708)}{R_{rs}^{-1}(753) - R_{rs}^{-1}(708)}\right) \tag{2.8}$$

Outro grupo de algoritmos são os semi-analíticos, que utilizam alguma forma de relação entre as propriedades ópticas inerentes (*inherent optical properties*, IOPs) e a reflectância, para estimar o coeficiente de absorção do fitoplâncton (a_{phy}) e, então, a chla. Estes métodos de inversão semi-analíticos geralmente utilizam pressupostos, simplificações, parametrizações empíricas ou aproximações para as IOPs, ou relações empíricas entre a reflectância e a IOP desejada (Mouw et al., 2015). Um exemplo bastante conhecido deste tipo de modelo é o desenvolvido por Gons et al. (2002), que utiliza bandas do vermelho e NIR e é parametrizado em função do coeficiente de absorção e simplificações no coeficiente de retroespalhamento. Ele assume que a absorção da luz na faixa do *red-edge* se deve principalmente à água devido ao alto espalhamento pela chla e pouca influência do CDOM e NAP, e na faixa do vermelho é principalmente pela água e chla. O coeficiente de retroespalhamento é assumido como independente do comprimento de onda, e é calculado analiticamente a partir da radiância no infravermelho próximo (Gons et al., 2002, 2005, 2008):

$$b_b = 1.61 \times \frac{\pi R_{rs}(778)}{0,082 - 0,6\pi R_{rs}(778)} \tag{2.9}$$

e a chla é calculada como:

$$chla = \frac{\frac{R_{rs}(708)}{R_{rs}(665)} \times (a_{água}(708) + b_b) - a_{água}(665) - b_b^{c_1}}{c_2} \tag{2.10}$$

em que $a_{água}(665) = 0,4$ m^{-1} e $a_{água}(708) = 0,7$ m^{-1} (Buiteveld et al., 1994) são valores aproximados do coeficiente de absorção da água nas faixas do vermelho e NIR, respectivamente, e c são as constantes de calibração.

Além dos modelos semi-empíricos e semi-analíticos, algoritmos de aprendizado de máquina têm ganhado espaço recentemente na literatura. O mais conhecido deles é o MDN (Mixture Density Networks), desenvolvido por Pahlevan et al. (2020) para os sensores Sentinel-2 MSI e Sentinel-3 Ocean and Land Color Imager (OLCI) para estimar chla para uma grande variedade de águas continentais. A MDN é uma classe de redes neurais combinadas com modelos de mistura (mixture models), que estima funções de densidade de probabilidade, utilizando o método de máxima verossimilhança, para extrai o valor ótimo de dada variável baseado num conjunto de dados de treinamento. Este conjunto consiste em 1000 dados pareados de R_{rs} e chla medidos em campo em águas continentais diversas no globo. Para o MSI, os dados de entrada são as R_{rs} das bandas entre 400–800 nm range (B1 a B7). O algoritmo foi desenvolvido especialmente para sensores orbitais, porém ele tem certa sensibilidade à correção atmosférica, isto é, à qualidade dos dados de entrada de radiância (Pahlevan et al., 2020).

Outros modelos de chla também utilizam o comportamento da fluorescência dos fotossistemas (principalmente do PSII, em 685 nm), que resulta do descarte de energia não usada na fotossíntese e é emitida em comprimento de onda maior (menor energia) do que a absorvida (Matthews, 2017), mas este tema não será abordado aqui por não ter sido utilizado neste trabalho.

Dada a grande gama de algoritmos disponíveis na literatura e a complexidade das águas continentais, há uma alta variabilidade de erros associados a estas estimativas. Um valor desejável de erro estipulado para estimativas de chla por sensores orbitais é de 30% (Gordon, 2019), mas estes valores também variam devido à amplitude de concentração de chla encontrada em águas interiores. O estudo de Neil et al. (2019), utilizando uma grande quantidade de dados com diferentes concentrações de chla, e variados modelos, encontrou RMSE de 1,8 a até 251 mg/m³, e quando utilizando os melhores modelos, um valor de RMSE de 1,8 mg/m³ e $r = 0{,}89$. Há também um esforço recente para se entender qual a melhor escolha para cada caso. Neste mesmo estudo de Neil et al. (2019), os autores utilizaram a divisão das águas continentais em OWT feita por Spyrakos et al. (2018) para testar os melhores modelos em cada OWT. Como resultado foi mostrado que há grande variabilidade para a maioria dos OWT, e que ainda há necessidade de mais estudos neste tema para delinear as melhores opções.

2.2.3 CDOM

A matéria orgânica dissolvida colorida, também conhecida como matéria orgânica dissolvida cromofórica (ou *gelbstoff* ou *yellow substance*) é a porção da matéria orgânica dissolvida que interage com a luz. É uma mistura complexa de carbono, nitrogênio, fósforo e enxofre com grande variabilidade de composição, peso molecular e biodisponibilidade, e é importante nos ciclos biogeoquímicos e de fluxo de energia em ecossistemas aquáticos (Zhang et al., 2020). Recentemente têm atraído mais atenção devido à necessidade de se mapear e quantificar as fontes e sumidouros de carbono, para melhor compreender o balanço de carbono no planeta, levando em consideração trabalhos recentes que mostram a importância de ecossistemas aquáticos como processadores de carbono (“active pipe”, Cole et al., 2007; Tranvik et al., 2009). Em relação à produtividade primária, especificamente o CDOM é importante não apenas pela disponibilidade de nutrientes, mas também por atuar a luz na água, controlando a produtividade do fitoplâncton pela disponibilidade de luz, assim como por atenuar a radiação ultravioleta (UV), nociva a estes organismos (Seekell et al., 2015).

O CDOM entra em ambientes aquáticos de forma alóctone, vindo da bacia por rios tributários e lançamento de esgotos industriais e domésticos, ou autóctone, por decomposição de fitoplâncton e plantas macrófitas, e tem altas variação espacial e temporal, o que dificulta a identificação de sua origem. Neste sentido, o tempo de residência do corpo d'água, junto com o que as fontes de CDOM no corpo d'água, definem a taxa e o fluxo de geração e consumo de CDOM (Wetzel, 2001). O monitoramento de CDOM por sensoriamento remoto é relativamente mais recente, tendo mais desafios para ser estimado com acurácia de forma global, e tanto no caso do carbono orgânico dissolvido (DOC) como do DOM, apenas o CDOM pode ser estimado, e este também é então utilizado como um indicador destas outras variáveis, embora esta relação ainda não seja bem conhecida (Griffin et al., 2018).

O CDOM interage com a luz apenas por absorção, não havendo espalhamento da luz. Seu espectro de absorção é próximo a uma exponencial, com pico no UV e azul e decaimento até o NIR, como mostrado na Figura 2.5. O espectro de absorção do CDOM no azul coincide tanto com a absorção da clorofila-a do fitoplâncton quanto a de material particulado não-algal (NAP), o que dificulta a sua quantificação. Por isso, estimativas de CDOM geralmente usam o coeficiente de absorção (aCDOM) como medida, que pode ser analisado no espectro do ultravioleta ao visível (Barbosa et al., 2019). Em águas continentais, se usa o aCDOM em um comprimento de onda específico no azul, em função de ser o pico de absorção.

Os modelos de estimativa de aCDOM estabelecem uma relação direta entre o aCDOM e a Rrs, utilizam modelos semi-empíricos de razão de bandas, ou modelos semi-analíticos de águas continentais, como feito para a chla (Barbosa et al., 2019). Por ser mais recente na literatura (Kutser et al., 2015), a maior parte dos modelos são empíricos ou semi-empíricos, estando estes, então, com aplicação limitada a área de estudo onde o modelo foi treinado (Zhang et al., 2020). Além disso, nenhum sensor orbital contém bandas designadas especificamente para a estimativa de CDOM em águas continentais, e sua acurácia está limitada devido a absorção concomitante de CDOM e chla (Brezonik et al., 2015). Devido à esta característica empírica dos modelos de aCDOM, seus erros típicos variam na literatura, de 0,19 m^{-1} a 0,73 m^{-1}, mas com valores de aCDOM que vão desde $0{,}13^{-1}$ a até $\sim 10^{-1}$, dificultando a comparação de métricas entre estudos.

Os modelos semi-empíricos de razão de bandas geralmente seguem a seguinte formulação:

$$\text{aCDOM}(\lambda) \propto \frac{Rrs(\lambda_1)}{Rrs(\lambda_2)}$$

em que λ_1 e λ_2 são comprimentos de onda onde há grande e baixa absorção por CDOM, de preferência com pouca influência dos demais COAs.

2.2.4 Temperatura

Ao contrário do SR da cor da água, que se baseia na luz solar refletida pela superfície, o SR da temperatura superficial se baseia na emissão de radiação pela superfície do planeta. Pela lei de Planck, todo corpo emite radiação eletromagnética em todos os comprimentos de onda, e a energia irradiada total e o pico, no espectro, em que esta emissão ocorre dependem da temperatura do corpo. Para a superfície do planeta, a uma temperatura média de 25°C (300 K), este pico ocorre próximo a 10000 nm (10 µm), na região conhecida como infravermelho termal (Figura 2.3), que corresponde também a uma janela atmosférica nesta região, o que faz que a maioria dos sensores termais seja na faixa de 10 a 12 µm.

Visto que os sensores medem a radiação medida pelos corpos, a sua medição é chamada de temperatura radiométrica, e difere de sua temperatura de fato, esta medida por um termômetro e chamada de temperatura cinética. Para superfícies isotérmicas e homogêneas, em equilíbrio térmico, essas temperaturas são iguais; como estes casos quase nunca são encontrados, estas temperaturas quase sempre são diferentes (Li et al., 2013), usualmente na faixa de décimos ou centésimos de diferença (Handcock et al., 2012).

As relações entre radiação emitida e temperatura de uma superfície são formuladas matematicamente pelas leis de Planck, lei do deslocamento de Wien (derivada da lei de Planck), lei de Stefan-Boltzmann e pela lei de Kirchhoff (Jensen, 2009). Estas leis são enunciadas para um corpo negro, um corpo teórico (idealizado) que, em equilíbrio térmico com o ambiente, emite radiação eletromagnética na maior taxa (energia por tempo) possível. A partir desta definição, define-se também a emissividade, que é a razão entre a emissão de radiação eletromagnética de um corpo e um corpo negro; em outras palavras, um corpo negro possui emissividade 1, e todas superfícies reais possuem emissividade entre 0 e 1, a depender de sua temperatura e da faixa espectral observada (Purkis e Klemas, 2011). A lei de Planck, base do sensoriamento remoto termal, relaciona a temperatura de um objeto com a radiância espectral por ele emitida nos diferentes comprimentos de onda. Para um corpo negro, ela é dada por (Schott, 2007):

$$B_\lambda(\lambda, T) = \frac{c_1}{\lambda^5 \exp\left(\frac{c_2}{\lambda T}\right) - 1} \tag{2.11}$$

em que B é a radiância espectral emitida pelo corpo, no comprimento de onda λ e a uma temperatura T, e c_1 e c_2 são as constantes de Planck, e valem $c_1 = 1,191 \times 10^8$ W µm^4/m^2 sr e $c_2 = 1,439 \times 10^4$ Kµm, respectivamente.

A lei de Stefan-Boltzmann, derivada da lei de Planck, determina que a energia total irradiada por um corpo negro é proporcional à quarta potência da sua temperatura absoluta. Também derivada a partir da lei de Planck, a lei do deslocamento de Wien determina o comprimento de onda em que ocorre o pico de emissão de radiação eletromagnética por um corpo. A lei de Kirchhoff enuncia que, para um objeto em equilíbrio termodinâmico, sua emissividade é igual a sua absortividade. Isso significa que, para objetos com alta emissividade na faixa do infravermelho termal, grande parte da radiação emitida pelo Sol e que chega à superfície é absorvida, e o restante é refletida para o ambiente. Isto também contribui que o sensoriamento da temperatura seja realizado na faixa do TIR, considerando apenas a energia emitida pela superfície e captada pelo sensor, a partir da inversão da lei de Planck, obtendo-se o que é chamado de temperatura de brilho da superfície. Conhecendo a emissividade do corpo, esta temperatura é transformada então em temperatura da superfície.

A temperatura da superfície é, ao contrário da temperatura de brilho, uma variável cinética independente do comprimento de onda, e representa a temperatura termodinâmica da camada mais superficial ("skin"), também sendo chamada de *skin temperature* na literatura (Guillevic et al., 2018). Quando utilizando sensores orbitais para a estimativa da temperatura, dois efeitos precisam ser corrigidos para transformar a temperatura de brilho em temperatura de superfície: a emissividade da superfície e os efeitos atmosféricos (Ottlé e Stoll, 1993; Schott, 2007). Diferentes maneiras foram propostas pra lidar com estas correções de formas distintas, para os diferentes sensores, em vários estudos na literatura, como revisado por Li et al. (2013).

Como descrito em Li et al. (2013), a estimativa da LST e da emissividade ao mesmo tempo é impossível utilizando sensoriamento remoto. Contudo, ela é essencial para a correção da emissão de radiação pela superfície em temperatura; estudos mostraram que erros na emissividade estão associados em erros na estimativa da temperatura superficial da água (WST) de 0,2 a 0,7°C (Friedman, 1969; Jiménez-Muñoz e Sobrino, 2006; Hulley et al., 2011). Para contornar isto, há duas opções: o uso de valores fixos de emissividade, ou modelos que usem informações de outras bandas para a estimativa desta, como propostos por Sobrino et al. (2004) e Sobrino et al. (2008) para diversos tipos de usos do solo, por exemplo. No caso da água, esta se aproxima a um corpo negro nos comprimentos de onda de 10–12 μm, mas sua emissividade varia com condições da água, como a temperatura, a salinidade, a turbidez e a quantidade de ácido húmico (Wenyao et al., 1987 *apud* Dugdale, 2016; Handcock et al., 2012), além de condições de geometria, variando com o ângulo de visada (Masuda et al., 1988). Por isto, há grande dificuldade de se estimar um valor de emissividade para cada corpo d'água, pois além da demanda de trabalho de campo e de laboratório para sua aferição, pode variar no tempo e no espaço. Por isso, em estudos de WST o que se faz é assumir um valor fixo de emissividade.

A emissão de radiação também interage com a atmosfera, cujos efeitos devem ser corrigidos. A radiação emitida pela atmosfera não é a mesma que chega ao sensor (topo da atmosfera – TOA, do inglês *top of atmosphere*), mas esta é afetada pela atmosfera, principalmente em função do vapor d'água, que possui alta variabilidade espacial e temporal (Jiménez-Muñoz e Sobrino, 2003). De fato, apesar do espectro do TIR utilizada pelos sensores (10 a 12 µm, geralmente) se situar em uma janela atmosférica, ainda há considerável influência da atmosfera nesta região do espectro, que atua tanto emitindo radiação (em todas as direções, portanto na direção do sensor e também em direção à superfície) quanto absorvendo e refletindo parte da radiação emitida pela superfície. A não-remoção destes efeitos, isto é, calcular a temperatura de brilho diretamente utilizando a radiação TOA medida pelo sensor pode acarretar em erros de até 2°C, em casos de rios e lagos (Kay et al., 2005). A correção destes efeitos é feita apenas com o conhecimento dos perfis verticais da temperatura e da quantidade de vapor d'água atmosféricos (Perry e Moran, 1994 *apud* Li et al., 2013).

Estes efeitos são dados por três variáveis: τ, a transmissividade da atmosfera (sem unidade), que é uma medida da interação entre a atmosfera e a radiação em dado comprimento de onda e varia de 0 (totalmente opaca) a 1 (totalmente transparente), L_{up} (*upwelling radiance*), que é a quantidade de radiação emitida pela atmosfera na direção do sensor, e L_{down} (*downwelling radiance*), que é a quantidade de radiação emitida ou refletida pela atmosfera na direção da superfície, cujas unidades são as mesmas da radiação absorvida pelo sensor. Para cada pixel, a radiação TOA medida pelo sensor é dada por (Schott, 2007):

$$L_{\text{sensor}} = [\varepsilon B + (1 - \varepsilon) L^{\text{down}}]\tau + L^{\text{up}} \tag{2.12}$$

em que L_{sensor} é a radiação medida pelo sensor (TOA, em W/(m^2 sr µm), e ε é a emissividade da superfície.

Com o uso de modelos de transferência radiativa, como os modelos MODTRAN e Lowtran, é possível fazer a estimativa destas variáveis usando os perfis de temperatura e vapor d'água da atmosfera para se chegar ao valor corrigido de radiação emitida pela superfície imageada. A correção da radiação é feita usando a seguinte equação (Schott, 2007):

$$L_{\text{corr}} = \frac{L_{\text{sensor}} - L^{\text{up}} - \tau L^{\text{down}}(1 - \varepsilon)}{\varepsilon \tau} \tag{2.13}$$

Com o valor corrigido de L e da emissividade da água, é possível, então, se calcular a temperatura de superfície invertendo a lei de Planck (Equação 2.11).

Contudo, esses valores de correção dependem de perfis acurados da atmosfera, que nem sempre estão disponíveis, e dos modelos de transferência radiativa, que são softwares privados e caros (Li et al., 2013). Por isso, outros modelos foram desenvolvidos com este intuito, e que podem ser divididos em três grandes grupos, considerando que a emissividade da superfície seja conhecida (Li et al., 2013): com uma banda termal, com várias bandas termais, ou uma aproximação multi-ângulo.

Aqui, trataremos apenas do segundo grupo, que inclui o MODIS. Há dois produtos de temperatura de superfície disponibilizados pelo MODIS, o MOD11, que é o produto de LST, e o MOD28, que é o produto de temperatura superficial dos oceanos (SST, sigla para *sea surface temperature*). Estes produtos também usam algoritmos diferentes para calcular a temperatura, mas ambos usam o que é chamado de *split-window* (janela dividida), que usa informação das duas bandas termais e dados complementares para fazer a estimativa. Esses algoritmos usam a diferença de radiância que é medida por cada banda termal (com comprimentos de onda adjacentes) para fazer a correção atmosférica e estimar a temperatura. A correção atmosférica é, geral, feita com base em parametrizações da quantidade de vapor d'água atmosférico.

O produto MOD11 LST usa um algoritmo *split-window* linear, chamado de generalizado, desenvolvido por Wan e Dozier (1996) especificamente para o MODIS. Ele é baseado em uma relação linear entre as temperaturas de brilho nas bandas 31 e 32, e considera a diferença de emissividade em cada banda, que é um valor tabelado (Zhang, 1999) e calculado com base no uso de solo utilizando outras bandas (*e.g.,* vermelho e NIR), cuja equação é:

$$\mathrm{LST} = b_0 + \left(b_1 + b_2\frac{1-\bar{\varepsilon}}{\bar{\varepsilon}} + b_3\frac{\Delta\varepsilon}{\bar{\varepsilon}^2}\right)\frac{T_i + T_j}{2} + \left(b_4 + b_5\frac{1-\bar{\varepsilon}}{\bar{\varepsilon}} + b_6\frac{\Delta\varepsilon}{\bar{\varepsilon}^2}\right)\frac{T_i - T_j}{2} \qquad (2.14)$$

em que T_i e T_j são as temperaturas de brilho, $\bar{\varepsilon}$ é a emissividade média das duas bandas, $\Delta\varepsilon$ é a diferença de emissividade entre as duas bandas, e b_n, $n = 0, 1, ..., 6$ são constantes calibradas usando dados medidos de temperatura, e variam conforme a emissividade, o ângulo de visada do sensor, o vapor d'água atmosférico e a temperatura do ar (calculados no produto MOD07 de perfis atmosféricos do MODIS). Estes coeficientes estão em constante revisão e calibração pela equipe do MODIS (*e.g.* Hulley et al., 2011), de modo a melhorar a acurácia da estimativa da LST pelo produto MOD11, que é de cerca de 1°C (Wan e Dozier, 1996).

Contudo, especificamente para a água, outra limitação aparece: os efeitos de superfície. A radiação medida pelos sensores é emitida por uma fina camada superficial ($\sim$10–20 μm), que na maioria das condições é mais fina do que a camada superficial da água interagindo na atmosfera (Wong e Minnett, 2018), devido ao fluxos de calor superficiais (fluxo de radiação de onda longa e fluxos turbulentos de calor – condução e evaporação) (Schluessel et al., 1990), esta camada superficial, chamada na literatura de *skin layer*, é quase sempre mais fria que a água imediatamente abaixo. Essa diferença de temperatura, que é medida por sensores radiométricos mas não pelos termômetros, que medem a temperatura da camada d'água (*bulk temperature*), é chamada de efeito *cool-skin* ("pele fria") e afeta as estimativas de temperatura superficial da água por sensores no infravermelho termal, causando um viés negativo nas estimativas da temperatura epilimnética da ordem de 0,1 a 1,0°C (Schluessel et al., 1990; MacCallum e Merchant, 2012; Wilson et al., 2013; Alappattu et al., 2017; Prats et al., 2018), como mostrado por exemplo com dados medidos por Alappattu et al. (2017) na Figura 2.8. O efeito de *warm layer* ("camada quente") também pode ocorrer, mas apenas durante o dia, quando há radiação solar o suficiente para causar estratificação térmica superficial, causando um gradiente superficial de temperatura que pode suprimir o efeito *cool-skin*. O efeito é menos comum (Alappattu et al., 2017, por exemplo, identificou viés positivo em apenas 1,5% das medições em águas costeiras e oceânicas), dependendo de estratificação térmica, mas pode causar um viés positivo nas estimativas da temperatura de até 6°C (Fairall et al., 1996a).

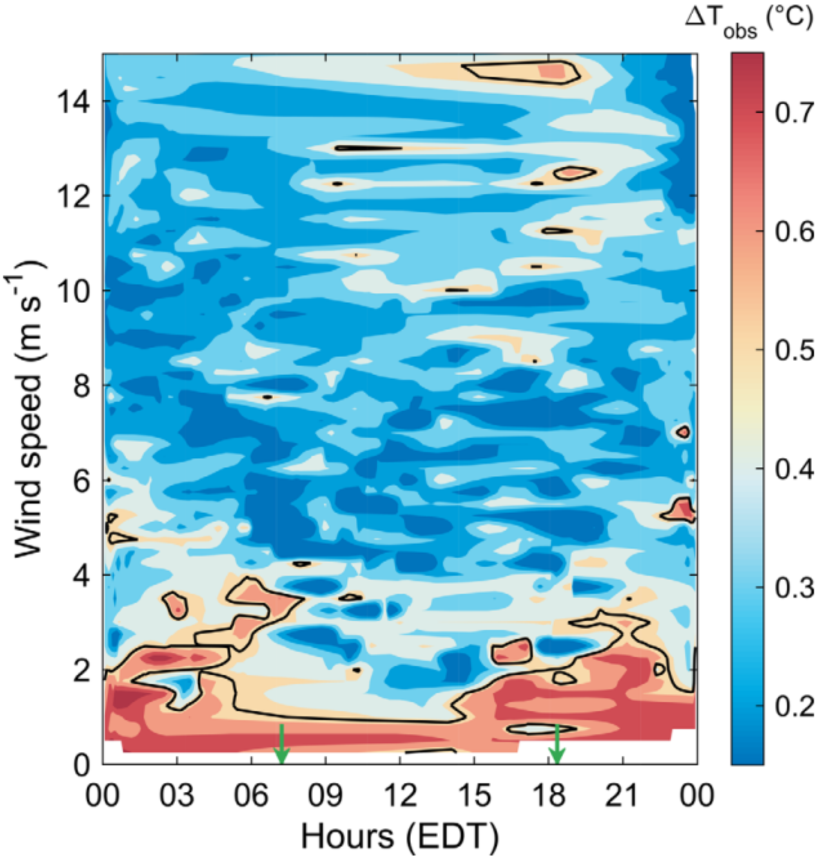

Figura 2.8 – Gráfico das diferenças entre a temperatura da camada d'água (*bulk*) e na camada mais superficial (*skin*) da água medidas por boias com termômetro e sensor radiométrico. (Fonte: Alappattu et al., 2017)

O efeito *cool-skin* tem sido extensivamente estudado em águas oceânicas (Robinson et al., 1984; Schluessel et al., 1990; Fairall et al., 1996a; Donlon et al., 2002; Minnett et al., 2011; Alappattu et al., 2017), contudo, poucos foram os estudos sobre como isto afeta as medições de LSWT (Oppenheimer, 1997; Wilson et al., 2013; Prats et al., 2018). Muitos modelos foram desenvolvidos para quantificar o efeito de *cool-skin* em águas oceânicas, tanto empíricas (Donlon et al., 2002; Alappattu et al., 2017) quanto determinísticas (Fairall et al., 1996b), dependendo principalmente da velocidade do vento, que regula tanto a mistura turbulenta e o fluxo de calor quanto a renovação do ar, com ventos mais fortes resultando em uma camada menor e, portanto, em uma diferença de temperatura inferior (Fairall et al., 1996a; Donlon et al., 2002). Em águas continentais, entretanto, estudos se limitaram a investigar o efeito (Wilson et al., 2013), Riffler et al. (2015) aplicando um modelo empírico desenvolvido por Minnett et al. (2011) para águas oceânicas, e Prats et al. (2018) avaliando a aplicação de um modelo determinístico adaptado para águas continentais.

O efeito *cool-skin* pode ter impactos em cálculos de tendências pois sua amplitude depende principalmente da velocidade do vento, e portanto tendências de variação de velocidade do vento (Woolway et al., 2019) vão impactar vieses sistemáticos na temperatura estimada por sensores orbitais. Além disso, a temperatura na camada mais superficial da água, sob o efeito *cool-skin* (na maioria das condições), é a que interage com a atmosfera na troca de gases e calor (Minnett et al., 2019), e por isso deve ser utilizada nos cálculos destes fluxos (Oppenheimer, 1997). Oppenheimer (1997) mostrou que usar temperaturas da camada d'água sem o efeito *cool-skin* para o cálculo de fluxos de calor latente e sensível em lagos resultam em uma superestimativa de $\sim$10%. Esta correção também tem sido utilizadas para melhoras as estimativas de trocas entre ar e oceanos, por exemplo, em modelos de previsão do tempo (Brodeau et al., 2017; Zhong et al., 2019). Os modelos de correção do efeito *cool-skin* mais utilizados são modelos empíricos, principalmente em função da velocidade do vento. Eles geralmente relacionam o efeito com uma função exponencial da seguinte forma (Donlon et al., 2002; Minnett et al., 2011):

$$T_{skin} = c - b\exp(-a \times u_{10}) \tag{2.15}$$

em que T_{skin} é a diferença de temperatura causada pelo efeito *cool-skin*, e a, b e c são coeficientes calibrados com dados de campo.

Outros modelos também incluem mais variáveis como fluxo de radiação de onda longa (Alappattu et al., 2017) e salinidade (Fairall et al., 1996a; Prats et al., 2018).

2.2.5 Sensores utilizados neste trabalho

Como mostrado acima, modelos bio-ópticos em geral precisam de informação em picos de absorção ou espalhamento dos COAs para estimar concentrações, e isto depende de configurações de sensores (resoluções radiométrica e espectral) para obter um valor acurado da radiação que está sendo reflectida pela água nestes comprimentos de onda específicos. Além disso, os sensores orbitais necessitam de boa resolução espacial para mapear pequenos lagos, rios e reservatórios com suficiente delineamento espacial, e com boa resolução temporal para mapear as variáveis com significativa frequência para o entendimento da variação temporal destas variáveis. Devido à esta limitação, são poucos os sensores configurações ótimas para serem aplicados de forma geral na limnologia, principalmente os sensores mais recentes.

Neste trabalho, foram utilizados dois sensores orbitais, com características bastante diferentes. O primeiro deles é o MSI (MultiSpectral Instrument), sensor da ESA (Agência Espacial Europeia) a bordo dos satélites Sentinel-2A, lançado em 23 de junho de 2015, e 2B, lançado em 7 de março de 2017. Os satélites têm um tempo de revisita no Equador de 10 dias, sendo então uma revisita a cada 5 dias a partir de 2017. O sensor MSI possui 13 bandas espectrais com resolução espacial variando de 10 a 60 m, dependendo do comprimento de onda, do visível até o SWIR (infravermelho de ondas curtas), utilizadas, por exemplo, para a correção atmosférica em águas turvas (Pahlevan et al., 2017). Suas configurações permitem uma série de aplicações na limnologia, como estimativa de chla, CDOM, e mapeamento de macrófitas (Pahlevan et al., 2017). Uma de suas limitações, como mostrado no Capítulo 3, é a correção atmosférica, que tem sido bastante estudada e discutida na literatura (Pahlevan et al., 2021). Quanto a sua usabilidade, as imagens são disponibilizadas gratuitamente pela Copernicus em sua plataforma SciHub (`https://scihub.copernicus.eu/dhus/`). Aqui, o download das imagens foi realizado com auxílio do pacote *sentinelsat* (Valgur et al., 2019).

O outro sensor utilizado nesta tese foi o MODIS (Moderate Resolution Imaging Spectroradiometer), a bordo dos satélites Terra, lançado em 18 de dezembro de 1999, e o Aqua, lançado em 4 de maio de 2002. Este sensor da NASA possui 36 bandas espectrais, desde o visível até o infravermelho termal, com resolução de 250 m a 1 km, a depender da banda, e com um tempo de revisita de no máximo 2 dias. Além disso, devido à sua órbita e grande ângulo de visada, na maioria das regiões os satélites passam duas vezes por dia pela mesma área, o Terra aproximadamente às 10h30 da manhã e da noite, e o Aqua aproximadamente às 1h30 da tarde e da madrugada. Considerando a grande durabilidade dos sensores, se destaca a grande série gerada, com mais de 23 anos de dados diários coletados até o momento.

A grande quantidade de bandas do sensor, junto com os produtos prontos disponibilizados pela equipe do MODIS (como de índices espectrais, evapotranspiração e cor do oceano) resulta num grande número de aplicações, principalmente no monitoramento da vegetação, solos e oceanos. Contudo, na limnologia suas aplicações são mais limitadas, se comparadas ao Sentinel-2, principalmente devido as suas resoluções espaciais e radiométricas e ao decaimento do funcionamento de algumas bandas, embora, ainda assim, muitos são os estudos de qualidade utilizando MODIS na literatura.

A maioria destes trabalho utilizam os dados de temperatura da água do MODIS, que se destaca devido à sua resolução espectral (duas bandas termais, 31 e 32) e radiométrica (diferença de temperatura equivalente ao ruído, do inglês *"noise equivalent temperature difference"* – NEΔT, de 0,05°C a 27°C) (Barnes et al., 1998), e consistência da série de dados. O produto de temperatura do MODIS é o MOD11, em que o produto MOD11A1 é o diário com resolução de $\sim$1 km, e inclui informações da temperatura diurna e noturna, a qualidade dos pixels, a emissividade em cada banda, e o ângulo de visada.

As imagens de temperatura do MODIS foram baixadas da plataforma da NASA *AppEEARS* (*Application for Extracting and Exploring Analysis Ready Samples*, `https://appeears.earthdatacloud.nasa.gov/`), que disponibiliza a opção de download de camadas de imagens de sensores da NASA, que podem ser recortadas apenas para uma região delimitada, reduzindo o tamanho dos dados a serem baixados.

2.3 Lagos rasos brasileiros

Embora o Brasil seja o “país das águas”, a maior parte desta água está distribuída entre seus grandes rios e áreas alagadas, havendo poucos lagos naturais no país, em comparação a outras regiões (Tundisi e Tundisi, 2016). Por outro lado, há muitos barramentos nestes rios, como os conhecidos reservatórios nos rios Tietê, Paraná e São Francisco, criando lagos artificiais profundos. Lagos naturais, no entanto, são na sua maioria pequenos e rasos, e no Brasil os lagos naturais também são (Pi et al., 2022). As regiões mais conhecidas que abrigam lagos são a Região dos Lagos, com lagoas como a hipersalina Lagoa de Araruama, com 200 km^2, e a região dos Pampas, bioma que cobre também Uruguai e Argentina e abriga uma grande quantidade de lagos devido ao seu relevo plano. Apenas na província de Buenos Aires, na Argentina, há uma quantidade aproximada de 14000 lagos rasos maiores que 10 ha (O’Farrell et al., 2021). No Brasil, o Pampa está presente apenas no estado do Rio Grande do Sul, que concentra alguns dos principais e mais conhecidos lagos do Brasil: lago Guaíba e a Lagoa dos Patos, além das grandes lagoas Mirim e Mangueira, no extremo sul do Brasil. Estes lagos costeiros têm origem no processo de aumento e redução do nível do mar e ação do vento criando depressões no solo e dunas de areia num relevo plano que resultaram numa grande quantidade de lagos rasos que vão desde o sul de Santa Catarina até o sul do Uruguai, sendo lagos como a lagoa Itapeva outro exemplo desta região (Schwarzbold e Schäfer, 1984). Além disto, também em função deste relevo plano, esta região abriga algumas áreas úmidas extremamente ricas em biodiversidade, sendo importantes refúgios de aves migratórias e para reprodução de peixes (Bridgewater e Kim, 2021). As seguintes áreas na região são áreas úmidas Ramsar: a Lagoa do Peixe, entre o Oceano Atlântico e a Lagoa dos Patos; a Estação Ecológica do Taim, no norte da lagoa Mangueira, e os Bañados del Este, localizados a sudeste da Lagoa Mirim.

Além destes, o estado do Alagoas também abriga uma grande quantidade de lagos costeiros, tendo este nome justamente por este motivo (Pereira, 2023). O principal sistema é o Complexo Estuarino Lagunar Mundaú Manguaba (CELMM), formados pelas lagunas Manguaba e Mundaú (a título de curiosidade, cujos nomes antigamente eram referenciados como Alagoa do Sul e Alagoa do Norte, respectivamente), que têm origem na deposição de sedimento pelos rios Mundaú, Paraíba do Meio e Sumaúma, gerando um sistema de canais e ilhas entre os rios e o oceano e aprisionando a água no complexo, criando uma condição de águas salobra que, atualmente, é mais doce, principalmente na lagoa Manguaba. Curiosamente, o nome Maceió, a capital do estado que se desenvolveu ao largo da lagoa Mundaú e dela depende econômica e socialmente, vêm do tupi "Maçayó", que significa "o que tapa o alagadiço", ou seja, a localização onde ocorreu a deposição do sedimento "tapando" o leito antigo dos rios.

Embora sejam lagos rasos e costeiros, estas lagoas possuem características bastante distintas. Além da diferente gênese e características geográficas, as lagoas estudadas nesta tese também possuem diferentes características limnológicas. As lagoas alagoanas recebem uma contribuição grande de nutrientes e sedimentos vinda de sua grande bacia, e associadas ao depósito de esgotos sem tratamento e de fertilizantes utilizados na agricultura, principalmente da cana, criando condições para proliferação de algas grande, com grande ocorrência de florações que talvez não sejam maiores por conta da cor da água, que é escura pela combinação de CDOM e sedimentos (Oliveira e Kjerfve, 1993; Melo-Magalhães et al., 2009; Lins et al., 2018). Já as lagoas gaúchas são em geral oligomesotróficas, com turbidez que se deve mais a ressuspensão do sedimento pela ação do vento do que por contribuição da bacia (Fragoso Jr et al., 2008; Crossetti et al., 2014; Cavalcanti et al., 2016). A ação do vento também contribui para a oxigenação do sedimento, que ocasiona o sequestro de fósforo e reduz o efeito da eutrofização na disponibilidade de nutrientes nestes lagos. Destes lagos, provavelmente apenas o lago Guaíba tem um processo mais avançado de eutrofização em função dos rios que fazem parte de sua bacia e da área urbana de Porto Alegre, em sua margem leste, com deterioração da qualidade da água e ocorrência de floração de algas nas margens em que a água é mais parada.

Capítulo 3

Correção atmosférica e de sunglint para estimativa de clorofila-a num sistema estuarino-lagunar produtivo tropical usando imagens Sentinel-2 MSI

Matheus Henrique Tavares
Regina Camara Lins
Tristan Harmel
Carlos Ruberto Fragoso Jr.
Jean-Michel Martínez
David Motta-Marques

Artigo publicado no periódico "ISPRS Journal of Photogrammetry and Remote Sensing", DOI: `https://doi.org/10.1016/j.isprsjprs.2021.01.021`

Atmospheric and sunglint correction for retrieving chlorophyll-*a* in a productive tropical estuarine-lagoon system using Sentinel-2 MSI imagery

Matheus Henrique Tavares[a,*], Regina Camara Lins[a], Tristan Harmel[b], Carlos Ruberto Fragoso Jr.[c], Jean-Michel Martínez[b], David Motta-Marques[a]

[a] *Instituto de Pesquisas Hidráulicas, Universidade Federal do Rio Grande do Sul, 91501-970 Porto Alegre, Brazil*
[b] *Géosciences Environnement Toulouse (GET), UMR5563, Institut de Recherche pour le Développement (IRD)/Centre National de la Recherche Scientifique (CNRS)/Université Toulouse 3, 14 Avenue Edouard Belin, 31400 Toulouse, France*
[c] *Centro de Tecnologia, Universidade Federal de Alagoas, 57072–970 Maceió, Brazil*

Abstract

Remote monitoring of chlorophyll-*a* (*chla*) has been widely used to evaluate the trophic state of inland and coastal waters, however, there is still much uncertainty in the algorithms applied in different optical water types. The influence of different atmospheric correction (AC) processors, which can also provide correction for sunglint and adjacency effects, on the retrieved *chla* is poorly understood. In this study, state-of-the-art atmospheric correction and *chla* algorithms are evaluated using Sentinel-2 MSI imagery in the Mundaú-Manguaba Estuarine-Lagoon System (MMELS), a productive tropical system that consists of two turbid lagoons of different optical water types (OWT). We compared the performance of six different AC processors, with the addition of sunglint correction for two of them, with measured water reflectance. There was difficulty in correcting for the atmospheric effects, especially for bands 2, 3 and 8A. Overall, C2X showed the best performance over MMELS, but with sunglint correction, ACOLITE and GRS provided the most consistent water reflectance (ρ_w). Sunglint correction might be essential for retrieving accurate ρ_w in most low-latitude water bodies. We also found that in Mundaú, the dense urban area surrounding it likely caused heavy adjacency effects in the satellite-retrieved reflectance, and thus correction for it is necessary. We also compared the performance of six *chla* algorithms recommended for the OWTs present in MMELS in addition to a widely applied and a global chla algorithm in retrieving this variable using both field and satellite reflectance, in this case corrected with the three best performing processors. For the *in situ* data, most algorithms performed well in Manguaba lagoon, while in Mundaú lagoon the semi-analytical NIR-red ratio (2SAR) algorithm was the most consistent model, and in both cases the locally calibrated algorithms outperformed the global algorithm. When retrieving *chla* with the satellite-derived ρ_w, considerably poorer results were produced, especially in Mundaú lagoon. The global algorithm was found to be especially sensitive to the atmospheric effects. We also found that the quality of AC provided by the algorithms is not a general predictor of the performance of the *chla* models, even when analysing individual bands separately, while the relationship between *chla* concentration and the ratio of bands used by most algorithms can be. Despite containing distinct water characteristics, *chla* can be modelled using a single algorithm, 2SAR, calibrated for MMELS as a whole, with r^2 of 0.77 and nRMSE of 38.7%, and we consider that 2SAR has the potential to be a global algorithm for this OWT, provided that it is recalibrated for a large dataset of satellite-derived BOA reflectance. We recommend that further studies explore the impacts of AC, sunglint and adjacency effects on the performance of *chla* algorithms, in order to delineate the most suitable combinations of AC + *chla* algorithms for the variable OWTs, in an effort to provide the basis for global-scale retrievals of this pigment using medium-resolution sensors such as MSI and OLI.

Keywords: Chlorophyll-*a* (chl-*a*), Sentinel-2 MSI, Turbid productive waters, Algorithm validation, Optical water type, Water quality

---

[*] Correspondence author.

1. Introduction

Estuarine systems are complex transitional zones between the continent and the ocean. Due to their unique characteristics, they can be very productive, harbouring high biodiversity and providing essential ecosystem services such as fisheries, habitat provision, and sediment retention (Barbier et al., 2011). These systems generally exhibit spatial variability and distribution of organisms influenced by environmental factors, mainly a variable salinity gradient, and seasonal river inflow and nutrient discharge, which are also associated with the hydrodynamics of the water body (Mitchell et al., 2015). However, for being at the end of the watershed and commonly associated with socio-economic development in its surroundings, these ecosystems can be impacted by anthropogenic effects such as increased nutrient discharge, pollution, and unrestrained fishing, which in turn can undermine their ecological status and ecosystem services provision (*e.g.*, Courrat et al., 2009). This, associated with the limited water exchange and high retention times, can enhance the harmful effects of these activities, resulting in increased water turbidity, algal blooms, and fish kills (Orive et al., 2002).

Monitoring of chlorophyll-*a* (*chla*), a phytoplankton biomass indicator, has been frequently used to evaluate the trophic state of inland and coastal waters due to their sensitivity and quick response to multiple environmental factors (Carlson, 1977; Baban, 1996; Boyer et al., 2009). Due to its spatio-temporal variability and limited representation of field monitoring, associated with the difficult and laborious field campaigns, remote sensing of *chla* has been widely used to complement this monitoring (Gitelson and Kondratyev, 1991; Matthews, 2017; Giardino et al., 2019). Considering its known spectral characteristics, different algorithms have been developed to maximise sensitivity to *chla* while minimising the effects of other optically active water constituents, mainly chromophoric dissolved organic matter (CDOM), detritus, also known as non-algal particles (NAP), and water itself (Mouw et al., 2015; Gege, 2017). However, there is still much uncertainty related to the retrieval of *chla* due to the high variability of water spectral response as a function of different concentrations of the optically active water constituents (Mouw et al., 2015).

Recently, Spyrakos et al. (2018) proposed a classification system for inland and coastal waters based on their spectral response, as well as taking into account the main optically active water constituents, dividing inland waters into 13 categories of optical water types (OWT). Based on this, Neil et al. (2019) analysed how a large number of *chla* algorithms performed considering the different inland OWT using an extensive dataset of measured *chla* and water reflectance. The results show a large variability in the performance of the algorithms even when considering each OWT, also noted in other studies considering OWT classification (Cui et al., 2020), especially for turbid waters, where the absorption and scattering by CDOM and NAP have higher relative importance in relation to *chla*. Therefore, further validation of these algorithms is still needed to provide a better understanding of the strengths and limitations of each algorithm, in order to produce more accurate results.

In addition to the algorithms, another challenge in retrieving *chla* from satellite-borne sensors is that the radiance measured by these sensors can be highly influenced by the atmosphere. The gaseous molecules and aerosols in the atmosphere can both absorb and scatter light reflected from the surface, especially smaller wavelengths, influencing the signal received by the sensor (Moses et al., 2017). Therefore, correcting for these effects is essential in order to retrieve water-leaving radiance accurately. However, atmospheric correction (AC) is a complex process, as there are difficulties associated not only with atmospheric modelling (*e.g.*, aerosol modelling, diffusive sky reflectance and heterogeneous atmospheric conditions over a scene) (Gordon et al., 1988; Wang and Gordon, 1994), but also with the air-water interface itself, which is potentially roughened by steady or gusty winds. From a remote sensing point-of-view, the water surface produces undesirable effects such as reflection of the direct sunlight toward the sensor field of view. That reflection of the Sun disk, called sunglint, can be highly unpredictable precluding proper remote sensing of the in-water constituents. On the other hand, the sunglint signal becomes more pronounced when the Sun is high on the horizon, which is mostly the case for space observation in the tropical regions (Harmel and Chami, 2013).

Atmospheric correction methods commonly used for water applications separate the water and atmospheric signals using different approaches (Jamet et al., 2011). Particularly in inland waters, methods designed to correct for the atmospheric effects over open ocean waters can not be used as some assumptions, such as the altitude at mean sea level and the NIR black-pixel assumption, are not valid as a consequence of elevation, suspended solids and adjacency effects (Jamet et al., 2011; Vanhellemont and Ruddick, 2015; Moses et al., 2017). Furthermore, water reflects only a small portion of the incident light, and thus a stronger influence of the atmosphere occurs due to low signal-to-noise-ratio (SNR), and additional noise signals such as adjacency effects and the aforementioned sunglint, adding more complexity to the process (Moses et al., 2017; Bulgarelli and Zibordi, 2018; Harmel et al., 2018). There has been a recent effort in developing and testing AC algorithms for coastal and inland waters, but as in the case of the *chla* models, there is high uncertainty in the strengths and limitations of these algorithms (Doxani et al., 2018; Pereira-Sandoval et al., 2019; Warren et al., 2019). Besides the uncertainty in the AC itself, there is also uncertainty in the impacts of the AC methods in retrieving biophysical parameters such as *chla*, which also needs to be addressed (Maciel et al., 2019; Molkov et al., 2019). Exploring these questions, in this study we evaluated state-of-the-art atmospheric correction processors, in addition of a sunglint correction method, and chlorophyll-*a* algorithms are evaluated using Sentinel-2 MSI imagery in a productive tropical coastal system in Northern Brazil.

2. Methodology

2.1. Study area

The study area is the Mundaú-Manguaba Estuarine-Lagoon System, a shallow (maximum depth of 3.5 m) tropical lagoon system located in the metropolitan area of Maceió, state of Alagoas, northeastern Brazil, between 9°35’ S and 9°46’ S latitude and 35°34’ W and 35°58’ W longitude (Figure 1). The MMELS is composed of two lagoons, the Mundaú Lagoon (surface area of 27 km^2), located in the Northern part of the system, which receives freshwater mainly from the Mundaú river basin (annual average discharge of 35 m^3/s); and the Manguaba Lagoon (surface area of 42 km^2), which is located in the Southern part of the system and receives freshwater from two basins, the Paraíba do Meio and the Sumaúma river basins (annual average discharge of 28 m^3/s). The MMELS exhibits a tropical semi-humid climate with well-defined wet (from May to July) and dry (from October to December) seasons. Temperature varies little throughout the year, with an average annual mean temperature of 25°C, and the winds blow predominantly from a southeasterly direction (Oliveira and Kjerfve, 1993). A more detailed description of the MMELS can be found in Lins et al. (2018).

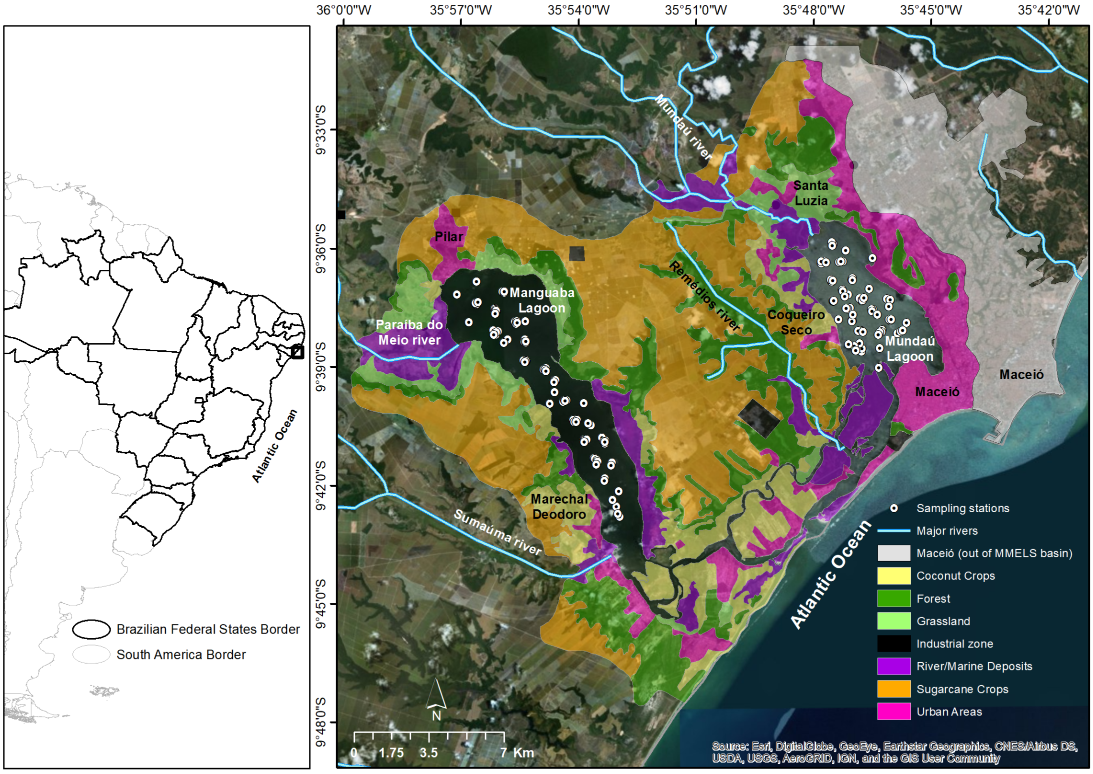

Figure 1: Location map showing the MMELS, the sampling stations in Mundaú and Manguaba lagoons, and land cover surrounding the system, highlighting the extensive urban area of Maceió city (capital of Alagoas state).

Although they are connected, the lagoons have distinct characteristics, as described in Lins et al. (2017). Both lagoons are characterised by eutrophic conditions and are dominated by phytoplankton, but Manguaba lagoon is larger, has a higher retention time, and is less affected by the tides, which makes it generally less saline than Mundaú lagoon. Additionally, there is a small water flow between the lagoons through the connecting channel system, which creates different conditions of nutrients and hydrodynamics in each lagoon due to their different geometries and tributary rivers. In terms of the water constituents, Manguaba lagoon has higher chlorophyll-*a* concentration and lower total suspended solids (TSS) concentration, while also exhibiting less spatial variability than Mundaú lagoon (Lins et al., 2017).

Furthermore, despite being shallow, the high turbidity observed in both lagoons, with Secchi disk values ranging between 0.58–0.95 m, implies that bottom sediment has little or no effect on water reflectance as the photic zone depth is lower than water depth in MMELS, and so measurements of reflectance can be considered as water reflectance only (Lins et al., 2017).

2.2. *Field measurements*

Shipboard data were collected during ten field campaigns conducted between March 2017 and March 2019 (Table 1), however, there were only six match-ups between these campaigns and Sentinel-2 MSI images, considering a window of one day between satellite overpass. During each field campaign, a set of sampling stations, well-distributed across MMELS, was established (Figure 1). At each sampling station, above-water optical measurements and water sample collection for laboratory analysis were carried out. In total, 152 (97 considering only dates with satellite overpass) field water quality and corresponding water reflectance data were collected.

Table 1: Data of each field campaign and the number of collected optical measurements and water samples in MMELS, and information about match-up with Sentinel-2 MSI images

Date	Lagoon site	Sampling stations	Satellite match-up	Sensor	Image Date
03/24/2017	Mundaú	15	No	NA	NA
03/22/2018	Manguaba	14	No	NA	NA
05/22/2018	Mundaú	12	Yes	S2B	05/23/2018
05/23/2018	Manguaba	14	Yes	S2B	05/23/2018
08/06/2018	Manguaba	5	No	NA	NA
10/25/2018	Mundaú	18	No	NA	NA
02/26/2019	Mundaú	18	Yes	S2B	02/27/2019
02/27/2019	Manguaba	17	Yes	S2B	02/27/2019
03/23/2019	Manguaba	18	Yes	S2A	03/24/2019
03/24/2019	Mundaú	18	Yes	S2A	03/24/2019

In each station, a 2-litre bottle collected water 0.2 m below the water surface immediately after optical measurements. The samples were stored in a cooler with ice in the dark, and taken back to the laboratory for analysing the concentration of *chla* and total suspended solids (TSS). All samples were filtered on land, no later than 12 h after sampling, using Whatman GF/F glass fibre filters (pore size of 0.45 µm). The filters were wrapped in aluminium foil and kept frozen until analysis. For each water sample, *chla* was extracted from the filters and left into a solution of 90% ethanol for 18h in an amber flask and measured by the spectrophotometric trichromatic method (Rice et al., 2005). For TSS determination, Whatman GF/F filters (pore size of 0.47 µm) were dried before and after water filtering to a constant weight at 103 to 105°C, and measured gravimetrically (Rice et al., 2005).

Above-water hyperspectral reflectance measurements were performed using TriOs RAMSES radiometers (operating in the range 320–950 nm), with a spectral resolution of approximately 3.3 nm, following the ocean optics protocols recommended by NASA (Mueller et al., 2003). All of the radiometers were mounted in an aluminium pole vertically positioned on the top of the boat. An irradiance sensor was used to measure downwelling irradiance above the water surface, $E_d(\lambda)$, and two radiance sensors (with a 7°field of view) were used to measure upwelling radiance above the surface water, as well as the incident sky radiance, $L_s(\lambda)$, that was used to correct for the skylight reflection effect at the air-water interface.

The remote sensing reflectance, $R_{rs}(\lambda)$, was calculated as follows:

$$R_{rs}(\lambda) = \frac{L_w(\lambda)}{E_d(\lambda)} = \frac{L_u(\lambda) - \rho L_s(\lambda)}{E_d(\lambda)} \tag{1}$$

The total radiance measured above surface, $L_u(\lambda)$, is composed of the water-leaving radiance, $L_w(\lambda)$, and the portion of the L_s that is reflected by water surface, $L_r(\lambda)$. Because only $L_u(\lambda)$ is directly measurable, and $L_w(\lambda)$ and $L_r(\lambda)$ are not measured, and $L_r(\lambda)$ is assessed as $\rho L_s(\lambda)$, where ρ is a proportionality factor, as provided by Mobley (1999).

2.3. Atmospheric correction

We tested six algorithms for the atmospheric correction, we tested six algorithms, considering the ones most used and that produced the best results for inland and coastal water bodies in the literature (*e.g.*, Doxani et al., 2018, Ilori et al., 2019, Maciel et al., 2019): ACOLITE, C2RCC, GRS, iCOR, SeaDAS and Sen2Cor. We considered only bands 2 to 8A (except for B8) in the analysis, for being the bands considered in the chlorophyll-*a* algorithms (Section 2.5.1), and also the most commonly used bands in remote sensing applications in general. We did not consider B1, the aerosol band, for being the most sensitive to atmospheric effects, as it is difficult to remove these effects to retrieve surface reflectance, and also due to its coarse resolution of 60 m, which can produce mixed pixels.

In addition, sunglint correction was also applied to the best performing AC methods, using the algorithm developed for GRS (Harmel et al., 2018). In the following sections we broadly describe each tested algorithm, and in Section 2.4 we describe the algorithm for sunglint correction. There were 51 match-ups between *in situ* and Sentinel-2 MSI reflectance data, 25 in the Mundaú and 26 in the Manguaba lagoon. For the comparison with measured water reflectance, *in situ* reflectance was resampled to the Sentinel-2 bands (S2A and S2B according to Table 1) using the sensors' Relative Spectral Responses (RSR):

$$R_{rs}(\lambda_0) = \frac{\int_{\lambda_i}^{\lambda_f} R_{rs}(\lambda) RSR(\lambda) d\lambda}{\int_{\lambda_i}^{\lambda_f} RSR(\lambda) d\lambda} \tag{2}$$

where λ_0 is the centre wavelength of each S2 band, λ_i and λ_f are the lower and upper wavelengths of each band, and λ represents each wavelength in this range according to the spectral resolution of the radiometers.

The nomenclature of the AC algorithms is described in Table 2. For the assessment of performance of these algorithms, we used the coefficient of determination (r^2), the slope of the linear regression, root-mean-squared error (RMSE), bias, mean absolute error (MAE) and the spectral angle mapper (SAM). Due to the low data values, we calculated normalised bias and MAE using a normalised approach:

$$\text{nBias} = 10^{\left[\frac{\sum_{i=1}^{N}(log_{10}(E_i) - log_{10}(M_i))}{n}\right]} \tag{3}$$

$$\text{nMAE} = 10^{\left[\frac{\sum_{i=1}^{N}|log_{10}(E_i) - log_{10}(M_i)|}{n}\right]} \tag{4}$$

where E and M are the retrieved and measured reflectance, and n is the number of data points. For both metrics, a value of 1 indicates a perfect fit, and variations are in percent and indicate an over or underestimation, for nBias, and overall error, for nMAE.

SAM is a metric to assess the spectral similarity between two spectra. It considers the retrieved and measured reflectance spectra as vectors, and the similarity is based on the angle between these two vectors in a vector space with b dimensions, where b is the number of bands analysed. It is calculated as:

$$\mathrm{SAM} = \arccos\left(\frac{\vec{E}\cdot\vec{M}}{\left\|\vec{E}\right\|\cdot\left\|\vec{M}\right\|}\right) = \arccos\left(\frac{\sum_{i=1}^{b} E_i M_i}{\sqrt{\sum_{i=1}^{b} E_i^2}\sqrt{\sum_{i=1}^{b} M_i^2}}\right) \tag{5}$$

Table 2: Nomenclature of the algorithms applied for atmospheric and sunglint correction of the Sentinel-2 MSI images

Name	Description
Aco	ACOLITE processor
Aco-SG	ACOLITE with GRS-sunglint correction
C2RCC	Regular C2RCC
C2X	C2RCC calibrated for turbid waters
GRS-AC	GRS – atmospheric correction
GRS-SG	GRS – atmospheric and sunglint correction
iCOR	iCOR processor
SDS	SeaDAS processor
S2C	Sen2Cor processor

2.3.1. ACOLITE

The Atmospheric Correction for OLI “lite” (ACOLITE) processor was applied to correct for atmospheric effects using the *dark spectrum fitting* (DSF) proposed by Vanhellemont and Ruddick (2018) and Vanhellemont (2019), over the previous implemented SWIR-based exponential extrapolation (EXP) (Vanhellemont and Ruddick, 2014, 2015, 2016). The DSF algorithm is based on two assumptions: a homogeneous atmosphere over the satellite scene (or subscene used) and the black-pixel assumption. For the latter, however, instead of assigning a determined band with zero reflectance for estimating atmospheric path reflectance (ρ_{path}), such as the SWIR bands in the EXP method, for each scene, the band with the lowest reflectance pixels is chosen for determining ρ_{path}. To retrieve this, for each band, a linear regression using ordinary least squares is fitted to the darkest thousand pixels in the reflectance histogram, and the darkest object, that is, the “dark spectrum”, ρ_{dark}, is estimated as the offset of this regression.

In this process, a few values (such as water vapour transmittance, Rayleigh optical thickness, and the atmospheric path reflectance) are used from a Look-Up Table (LUT) generated using 6SV (Kotchenova et al., 2006). A base

LUT was generated for various atmospheric transmittance windows for different atmospheric conditions. It was then interpolated to create a dataset from 0.39 to 2.40 µm, with a 1 nm resolution. Then, for Sentinel-2 MSI, a specific LUT was generated by interpolating it to the sensor bands' relative spectral response (RSR).

For the range of bands and each aerosol model, aerosol optical thickness (derived at 550 nm, τ_a) is estimated based on this LUT. Then, for each aerosol model, the band giving the lowest positive value of τ_a is used, and an aerosol model is chosen based on the lowest RMSE between ρ_{dark} and the retrieved ρ_{path}. With the estimated τ_a, ρ_{path}, two-way diffuse atmospheric transmittance (t_{du}) and the spherical albedo of the atmosphere (s_a) are retrieved from the specific LUT and the surface reflectance ρ_s is estimated as:

$$\rho_s = \frac{\rho_t/t_g - \rho_{path} - \rho_{sky}}{t_{du} + s_a(\rho_t/t_g - \rho_{path} - \rho_{sky})} \tag{6}$$

where ρ_t is the top-of-atmosphere (TOA) reflectance, t_g is the atmospheric gas transmittance, which is estimated using an average transmittance of water vapour and ozone, and ρ_{sky} is the diffusive sky reflectance, which is calculated analytically (Gordon et al., 1988).

The ACOLITE processor can also remove sunglint, as it has implemented GRS (Harmel et al., 2018; Vanhellemont, 2019), which is described in Section 2.4.

2.3.2. C2RCC

The Case 2 Regional processor, originally developed by Doerffer and Schiller (2007) and updated by Brockmann et al. (2016) as the Case 2 Regional Coast Colour (C2RCC), is an AC processor based on sets of neural networks that related TOA water reflectance to radiative transfer simulations of water-leaving radiances.

Atmospheric characteristics are modelled based on radiative transfer model SOS (Chami et al., 2001; Lenoble et al., 2007), and aerosol optical properties are derived from AERONET-OC data. Water characteristics are modelled using Hydrolight (Mobley, 1994) and a bio-optical model (described in Doerffer and Schiller, 2007) considering absorption of phytoplankton, CDOM and non-algal particles, and sediment scattering as a white scatterer (for calcareous sediment). These water characteristics are all parameterised considering only ρ_w in the deep blue spectrum (B1/aerosol – 443 nm), based on bio-optical databases (Werdell and Bailey, 2005; Nechad et al., 2015). The neural networks were then trained based on TOA reflectance, these modelled water characteristics and environmental variables (such as ozone concentration). Additionally, a special set of networks was also trained for extreme ranges of absorption and scattering, that is, for very turbid waters. Both the regular, hereafter called C2RCC, and the high turbidity-focused network, hereafter called C2X (both names in reference to their designation in SNAP, ESA's Sentinel toolbox) were used in this work to correct for atmospheric effects. Although this model also retrieves IOPs, these were not tested here.

The algorithm is available in ESA's SNAP and was applied after resampling to 20 m for all bands and considering fixed values of water salinity (15 PSU), temperature (25°C), and ozone concentration (280 ppm).

2.3.3. GRS

The GRS (Glint Removal for Sentinel-2) processor was proposed by Harmel et al. (2018) as a coupled atmospheric–sunglint correction algorithm. The overall processing enables to handle gas absorption, molecule scattering and radiation imputed to weakly absorbing aerosols along with the direct light reflected on the rough air-water interface (*i.e.*, the spectral sunglint signal). For the sake of clarity, we divide the two modalities of the GRS algorithm: *(i)* GRS-AC, the component dealing with the atmospheric correction only, and *(ii)* GRS-SG, the coupled AC-sunglint removal process. In this section, the GRS-AC is described, while the sunglint removal of GRS-SG is detailed in Section 2.4.

First, the gaseous absorption (mainly CO_2, H_2O and O_3) correction is performed with the SMAC software (Rahman and Dedieu, 1994), which is based on parameterizations of the gas transmittances from full radiative transfer computations using 6S (Kotchenova et al., 2006). Atmospheric pressure and gas concentrations are retrieved from bilinear interpolation within the grid of the Copernicus Atmosphere Monitoring Service dataset (CAMS). Then, spectral radiances are corrected for the diffuse sky light and its reflection on the air-water interface. For each pixel, the diffuse radiance component is reconstructed for the given viewing geometry (*i.e.*, sensor and Sun viewing angles and relative azimuth) from pre-computed LUTs. Those LUTs were generated based on the radiative transfer model OSOAA (Chami et al., 2015) for typical fine and coarse mode aerosol models (Levy et al., 2009), including the specific spectral response of the sensor bands (Bodhaine et al., 1999). The atmosphere diffuse radiance coupled with surface reflection, L_{sky}, is obtained considering a bimodal aerosol model (Wang and Gordon, 1994) as follows:

$$L_{sky}(\lambda, \tau_a) = \gamma L_{sky}^{fine}(\lambda, \tau_a) + (1-\gamma) L_{sky}^{coarse}(\lambda, \tau_a) \tag{7}$$

where L_{sky}^{fine} and L_{sky}^{coarse} are the radiances for the fine and coarse aerosol modes, respectively, for τ_a; γ is the mixing coefficient corresponding to the relative amount of each mode in the atmosphere. Note that τ_a is obtained from the CAMS dataset (Benedetti et al., 2009; Morcrette et al., 2009) and γ is retrieved from non-linear fitting including the LUT aerosol parameters with the spectral values of τ_a provided by CAMS. If no sunglint correction is applied (case of GRS-AC), the water-leaving component is eventually obtained after subtraction of L_{sky} and division by the total transmittance (*i.e.*, diffuse + total transmittances) calculated for the bimodal aerosol model from the LUT.

2.3.4. iCOR

iCOR is an algorithm developed by De Keukelaere et al. (2018) to correct for atmospheric effects in both land and water (except open ocean) environments. In addition to the atmosphere, it also corrects for adjacency effects, using different approaches for land and water pixels. It depends on ancillary data, mainly a digital elevation model (DEM), viewing geometry and information of the atmosphere, which are inputted based on an aerosol model (a fixed rural model) and pre-generated LUTs (providing parameters such as aerosol density, aerosol type, and water vapour content) derived with MODTRAN5 (Moderate-Resolution Atmospheric Radiance and Transmittance Model – version 5) (Berk et al., 2006).

Initially, τ_a is retrieved based on land pixels using a technique developed by Guanter et al. (2005). First, cloud pixels are retrieved using VNIR bands, then the scene is subdivided into tiles, and for each tile, the darkest pixels for each band are selected. The radiance of these pixels, the corresponding ρ_{path}, and MODTRAN5 LUT are used to estimate an upper boundary of τ_a, and then τ_a is retrieved using an endmember inversion technique based on NDVI and band centre wavelength.

The correction of adjacency effects for water pixels is applied using the SIMilarity Environmental Correction (SIMEC) developed by (Sterckx et al., 2015). The method assumes the NIR similarity (the shape of ρ_w in the NIR is regular) and that pixels for which this assumption is invalid are affected by adjacency reflectance. For these pixels, the corrected reflectance is estimated based on the surrounding water pixels using bands 5 (red-edge) and 7 (NIR). The number of pixels used in this process is determined iteratively based on a maximum value of reflectance stipulated by the NIR similarity.

Finally, the pixels are corrected for the adjacency effects, and the atmospheric effects are corrected by solving the radiative transfer equation using ancillary data and MODTRAN5 LUTs (Kaufman, 1984; Sterckx et al., 2011). In this study, we used the SNAP plugin to apply iCOR using default settings. For dates 02/27/2019 and 03/24/2019, the algorithm could not retrieve u_{H_2O} for the estimation of τ_a, and values of τ_a derived from Sen2Cor were used instead.

2.3.5. SeaDAS

The SeaWiFS (Sea-viewing Wide Field-of-view Sensor) Data Analysis System is an algorithm originally developed by Gordon and Wang (1994) to correct TOA reflectance data from the SeaWiFS sensor. The algorithm has since been updated by NASA's Ocean Color Biology Processing Group (OBPG) to perform atmospheric correction of most ocean colour sensors (Mobley et al., 2016), such as MODIS, the Landsat missions, and Sentinel-2 (Pahlevan et al., 2017a,b). In this algorithm, the TOA radiance is expressed as:

$$L_{tot} = tL_w + L_r + L_a + L_{ar} \tag{8}$$

where t is the diffuse atmospheric transmittance, L_w is the water-leaving radiance, L_r is the radiance from scattering by air molecules in the absence of aerosol, L_a is the aerosol radiance, and L_{ar} is the radiance resulting from multiple scattering by air molecules and aerosol.

Rayleigh scattering is assumed known and corrected using ancillary data (such as O_3 and NO_2 concentration and wind speed), observing geometry and LUTs (Mobley et al., 2016). Aerosol particle size distribution is divided into fine and coarse particles, and this distribution is estimated at two bands where reflectance is assumed zero (black-pixel assumption) (Gordon and Wang, 1994). Aerosol radiance is then estimated from aerosol LUTs and relative humidity (Ahmad et al., 2010) and extrapolated for the other bands. Diffuse atmospheric transmission is estimated based on LUTs calculated for the retrieved aerosol type and Rayleigh optical thickness (Yang and Gordon, 1997).

Here, the function *l2gen* (version 9.5.0) was used to correct for atmospheric effects using the algorithm developed by Gordon and Wang (1994) with two configurations: the NIR/SWIR switching algorithm proposed by Wang and Shi

(2007) using the 740–865 nm combination for the NIR bands and the 1613–2200 nm combination for the SWIR bands, and the iterative NIR-signal removal method (Bailey et al., 2010) with the 865–1609 nm band combination suggested by Pahlevan et al. (2017a) and Mobley et al. (2016) for turbid waters.

2.3.6. Sen2Cor

Sen2Cor is the default atmospheric correction algorithm for Sentinel-2 MSI in SNAP (Müller-Wilm et al., 2016). It is a simple algorithm based on LUTs generated with a large dataset and the atmospheric radiative transfer model libRadtran (Mayer and Kylling, 2005; Emde et al., 2016) for different aerosol models, elevation, viewing geometries, and atmospheric conditions (such as visibility, ozone concentration, aerosol optical thickness, and water vapour content) generated specifically for Sentinel-2 MSI.

τ_a is retrieved based on the Dark Dense Vegetation method (Kaufman and Sendra, 1988), which assumes that the behaviour of the reflectance of dark vegetation (dark soil and water may also be used) pixels is known and that the ratio of reflectance between the SWIR (B12) and the blue (B2) and red (B4) bands is constant, and then different ratios are a result of atmospheric scattering. u_{H_2O} is retrieved using the Atmospheric Precorrected Differential Absorption algorithm (Schläpfer et al., 1998), which uses a band in an atmospheric absorption spectrum (B9) and a band in an atmospheric window (B8A) and, assuming that the reflectance in both bands is equal, estimates the absorption by the atmosphere and then, the columnar water vapour content. Both variables are pixel-derived and generated for the whole scene.

With the parameters, the image is corrected for all bands using the LUTs. We used the Sen2Cor SNAP plugin with default settings, except the aerosol type, which was set as maritime, and ozone content, which was set as 290 Dobson Units.

2.4. Sunglint correction

The GRS algorithm Harmel et al. (2018) was specifically developed to handle and correct for the sunglint signal for Sentinel-2-like sensors, that is, nadir or near-nadir viewing sensors with SWIR bands. The main principle is to estimate the bidirectional reflectance distribution function (BRDF) of the rough air-water interface from the SWIR bands (*i.e.*, ~1610 and ~2200 nm). The sunglint signal obtained in the SWIR is then propagated toward the NIR and visible bands.

Estimation of the sunglint radiance is based on the fact that water body is virtually totally absorbing; the water absorption coefficient in the SWIR is several orders of magnitude greater than that in the NIR. It is worth remembering that more than 99.99% of the light radiation in the SWIR is absorbed within the first millimetre. The authors also highlighted that atmosphere interferes less with light in this part of the spectrum, improving the accuracy of the sunglint estimation in relation to NIR approaches. Once corrected for atmosphere signal (from the AC processor), the remaining radiance in the SWIR is interpreted as the pure surface component of the signal and then translated into BRDF. This BRDF in the SWIR is extrapolated to the other bands considering the spectral variation of the refractive index of water and its important consequences onto the spectral sunglint signal (see Harmel et al., 2018 for details). The sunglint radiance is eventually retrieved from the spectral BRDF and the atmosphere direct transmittance computed from the spectral aerosol optical thickness.

The version used here accounts for the spectral response of each band of Sentinel-2 A and B. Practically, the AC processor is first applied, then the sunglint correction is performed based on the aerosol parameters retrieved by the AC processor. Finally, the sunglint radiation is calculated for each pixel, for each band, considering the estimated BRDF, atmosphere direct transmittance, and the extraterrestrial sun radiance reaching the atmosphere, and the water-leaving radiance is then corrected by removing this value.

2.5. *Chlorophyll-a retrieval*

To retrieve chlorophyll-*a*, we used reflectance data from both the atmospheric-corrected satellite images and *in situ* measurements. The algorithms used to retrieve *chla* are described in the following section. The algorithms were processed in *R* (R Core Team, 2020), with the help of packages *minpack.lm* (Elzhov et al., 2016) for implementation of the non-linear least-squares algorithm and *openair* (Carslaw and Ropkins, 2012) for plotting the Taylor diagrams.

2.5.1. *Algorithms*

The selection of the most suitable algorithms was based on the results provided by Neil et al. (2019). Since the lagoons have distinct water optical characteristics, the selected models were fit to each lagoon separately and also considering MMELS as a whole. To select the algorithms, we first classified each lagoon according to Spyrakos et al. (2018), and since there is no phycocyanin or NAP data available, this classification was based solely on chlorophyll-*a* concentrations and a visual comparison of the reflectance curves (Figure 2).

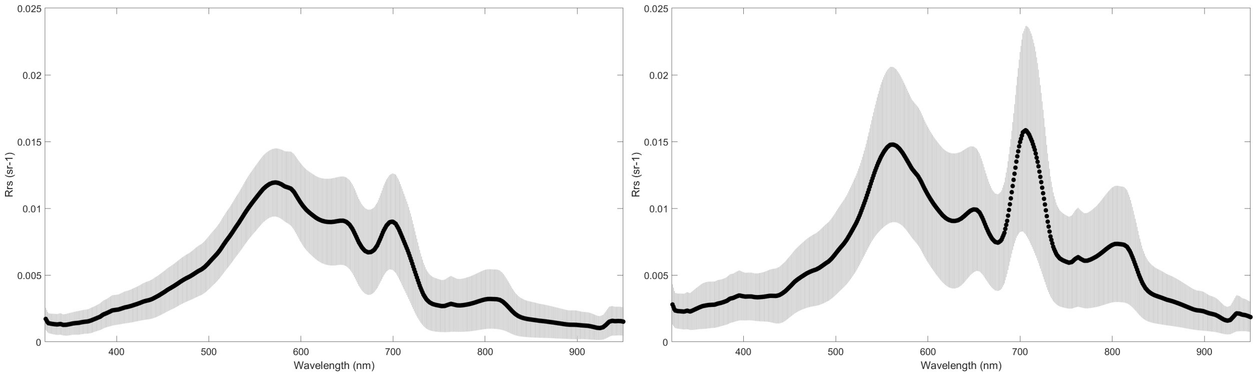

(a) Mundaú lagoon

(b) Manguaba lagoon

Figure 2: Mean (black dots) and standard deviation (grey ranges) of the remote sensing reflectance measured in **(a)** Mundaú and **(b)** Manguaba lagoons in the 10 field campaigns.

According to Spyrakos et al. (2018), Mundaú lagoon is classified as optical water type (OWT) 6 due to medium values of *chla* (μ = 12.9 mg/m^3), a higher peak in the green spectrum, and lower peaks in the red and red-edge spectra (Figure 2a). Waters of this type are characterised by a balanced effect of CDOM, NAP, and phytoplankton to absorption, and usually high content of cyanobacteria (although this may not be the case for Mundaú, since the trough at 620 nm is not as apparent as in Manguaba, for example). Manguaba lagoon is classified as OWT 8 due to high values of *chla* (μ = 42.8 mg/m^3) and near equally high peaks in the green and red-edge spectrum. Phytoplankton is generally the dominant absorbing pigment, as it is likely the case for Manguaba since it is less turbid than Mundaú despite having consistently much higher concentrations of *chla*, and also due to the high peaks in the red-edge spectrum, which are generally higher than in the green spectrum (Figure 2b).

As identified by Neil et al. (2019), the best-performing algorithms (following their nomenclature) were, for OWT 6, models A, C, H, I, J, L, M, N, and R, and, for OWT 8, models A, C, H, J, L, and R, while when considering any OWT, the recommended algorithms were A, C, J, L, M, and R. However, since Model R (Quasi-analytical algorithm) (Mishra et al., 2013) needs bands centred at 411 nm and 620 nm (which are not present in MSI), it was not considered here. Additionally, since Sentinel-2 MSI lacks a band centred at 520 nm, we used model N instead of L, considering only the 490 nm blue band. Therefore, here we selected models A, C, H, I, J, and N, which are described below. In addition, we also tested the widely applied three-band algorithm (Gitelson et al., 2003; Dall'Olmo et al., 2003; Moses et al., 2009) and the recently released Mixture Density Network algorithm, developed by Pahlevan et al. (2020) to be a global algorithm, which can be applied over a large range of OWT. The nomenclature of these algorithms is described in Table 3.

The input data for the algorithms is the remote sensing reflectance (R_{rs}) for the selected bands, which is derived by dividing surface reflectance by π (units of 1/sr). For the calibration of the models, data were selected randomly from all dates available, and we used 2/3 of the data for the calibration of the models and 1/3 for validation, except for the MDN algorithm, which is a global algorithm and is already calibrated. To remove possible effects of the dataset in the calibration, this process was repeated 100 times for each algorithm, resampling the datasets in every run and the mean values of the metrics were used. For the assessment of performance, we used r^2, bias, RMSE and RMSE normalised to the *chla* concentration (nRMSE), using the mean values of the metrics calculated for each run of each algorithm.

Table 3: Nomenclature of the chlorophyll-*a* algorithms tested in this study.

Acronym	**Model in Neil et al. (2019)**	**Description**
2BLR	Model A	Two-band linear NIR-red ratio algorithm
2BQR	Model C	Two-band quadratic NIR-red ratio algorithm
2SAR	Model H	Semi-analytical NIR-red ratio algorithm
3BR	Model B	Three-band NIR-red ratio algorithm
BI	Model I	Band index algorithm
MDN	NA	Mixture Density Network
NDCI	Model J	Normalised Difference Chlorophyll Index
OC2	Model N	Two-band blue-green ratio algorithm

Two-band linear NIR-red ratio algorithm – 2BLR. In the two-band linear NIR-red ratio (2BLR) algorithm (Gitelson and Kondratyev, 1991; Moses et al., 2009), *chla* is estimated based on the ratio:

$$chla_{\mathrm{2BLR}} = a \times \left(\frac{R_{rs}(708)}{R_{rs}(665)} \right) + b \tag{9}$$

This algorithm is based on the high absorption in the red spectrum and high peak in the red-edge by chlorophyll pigments, which is also the basis of algorithms used for the mapping of terrestrial vegetation (*e.g.*, NDVI) (Dall'Olmo et al., 2003).

Two-band quadratic NIR-red ratio algorithm – 2BQR. The two-band quadratic NIR-red ratio (2BQR) algorithm (Gurlin et al., 2011) is similar to the 2BLR algorithm, but it uses a second-order polynomial instead of a linear regression:

$$chla_{\mathrm{2BQR}} = a \times \left(\frac{R_{rs}(708)}{R_{rs}(665)} \right)^2 + b \times \left(\frac{R_{rs}(708)}{R_{rs}(665)} \right) + c \tag{10}$$

The second-order polynomial was proposed due to the non-linear relationship between the ratio of MERIS (MEdium Resolution Imaging Spectrometer) red-edge and red bands and measured *chla* data (Gurlin et al., 2011).

Semi-analytical NIR-red ratio algorithm – 2SAR. In the semi-analytical NIR-red ratio (2SAR) algorithm (Gons et al., 2002, 2005, 2008), *chla* is estimated based on water absorption and backscattering. It assumes that the absorption in the red-edge spectrum is mainly due to water, and in the red spectrum it is due to *chla* and water combined. The backscattering coefficient is assumed to be wavelength-independent and is calculated from radiance in the NIR region as:

$$b_b = 1.61 \times \frac{\pi R_{rs}(778)}{0.082 - 0.6\pi R_{rs}(778)} \tag{11}$$

and *chla* as:

$$chla_{\mathrm{2SAR}} = \frac{\frac{R_{rs}(708)}{R_{rs}(665)} \times (a_w(708) + b_b) - a_w(665) - b_b^a}{b} \tag{12}$$

where $a_w(665) = 0.4\ \mathrm{m}^{-1}$ and $a_w(708) = 0.7\ \mathrm{m}^{-1}$ (Buiteveld et al., 1994) are approximated values of water absorption coefficients in the red and red-edge bands, respectively.

Three-band NIR-red ratio algorithm – 3BR. The three-band NIR-red ratio (3BR) algorithm was proposed by Gitelson et al. (2003) to estimate *chla* from terrestrial vegetation, and then applied by Dall'Olmo et al. (2003) to retrieve phytoplankton *chla* in turbid waters. The algorithm was further developed by Dall'Olmo and Gitelson (2005) and Moses et al. (2009) and is calculated as:

$$chla_{\mathrm{3BR}} = a \times \left[R_{rs}(753) \times (R_{rs}^{-1}(665) - R_{rs}^{-1}(708)) \right] + b \tag{13}$$

In this algorithm, the third band was added to reduce the effect of backscattering on the retrieved *chla*. This band is located in a spectral region where the absorption by CDOM, NAP and *chla* is negligible.

Band index algorithm – BI. The band index (BI) algorithm was developed by Yang et al. (2010) based on Dall'Olmo and Gitelson (2005), Gitelson et al. (2008) and Le et al. (2009):

$$chla_{\mathrm{BI}} = a \times \left(\frac{R_{rs}^{-1}(665) - R_{rs}^{-1}(708)}{R_{rs}^{-1}(753) - R_{rs}^{-1}(708)} \right) + b \tag{14}$$

where the term multiplying *a* is termed index, based on the band sensitivities of phytoplankton and CDOM.

The three optimal wavelengths for the estimation of *chla* concentrations in turbid waters were identified in the 3BR algorithm (Dall'Olmo and Gitelson, 2005), and Yang et al. (2010) modified it by adding another term subtracting in the denominator, to compensate for non-negligible absorption and scattering by suspended particles around 750 nm in turbid waters, but removing the need of another band in the algorithm developed by Le et al. (2009).

Mixture Density Network – MDN. This algorithm was developed by Pahlevan et al. (2020) for both Sentinel-2 MSI and Sentinel-3 Ocean and Land Color Imager (OLCI) to be able to retrieve *chla* over a wide range of different OWT. The MDN is a class of neural networks (NN) that estimates probability density functions (PDF) to retrieve the optimal value of a variable based on the training dataset, in this case using the maximum likelihood. For this algorithm, a five-layer NN with 100 neurons per layer was trained, outputting the parameters (mean, standard deviation and the mixing coefficient) of five PDFs. The training dataset consisted of 1000 co-located *in situ* R_{rs} and *chla* pairs from a wide range of different typically optical waters. For MSI, the input R_{rs} data consists of the seven bands within the 400–800 nm range (B1–B7). As this is a global algorithm, no calibration was applied, and the results were generated only for the global (entire) dataset.

Normalised Difference Chlorophyll Index – NDCI. The Normalised Difference Chlorophyll Index (NDCI) was developed by Mishra and Mishra (2012) and is based on the best adjust (a second-order polynomial) of a normalised index, varying between -1 and +1 (similar to NDVI), of a relationship between red and red-edge bands. The algorithm, based on this index, retrieves *chla* as:

$$chla_{\mathrm{NDCI}} = a + b \times \left(\frac{R_{rs}(708) - R_{rs}(665)}{R_{rs}(708) + R_{rs}(665)} \right) + c \times \left(\frac{R_{rs}(708) - R_{rs}(665)}{R_{rs}(708) + R_{rs}(665)} \right)^2 \tag{15}$$

Two-band ratio algorithm – OC2. The NASA Ocean Colour two-band ratio (OC2) algorithm (O'Reilly et al., 1998; O'Reilly et al., 2000; O'Reilly and Werdell, 2019) is based on the ratio of blue to green R_{rs}:

$$chla_{\mathrm{OC2}} = 10^{a+bX+cX^2+dX^3+eX^4} \tag{16}$$

where

$$X = log_{10} \left(\frac{R_{rs}(490)}{R_{rs}(560)} \right) \tag{17}$$

It is based on the selection of the blue band with higher reflectance (OC4 was recommended by Neil et al. 2019), but in light of the issues mentioned above with B1, here only B2 (490 nm – blue band) was used. Although this algorithm was designed for Case-I waters only and has been shown to perform poorly in turbid inland waters due to the absorption of CDOM and NAP in the blue and green spectra, we included it in our analysis for comparison.

2.5.2. In situ models

For the semi-empirical algorithms using *in situ* reflectance data, we considered all field campaigns, including those without satellite match-ups (Table 1). In total, there were 152 data points in MMELS, 81 in the Mundaú lagoon, and 71 in the Manguaba lagoon.

2.5.3. Satellite data models

For the satellite data, we applied the algorithms to the images after correction using the three best AC algorithms. The bands used in Neil et al. (2019), from MERIS, were adapted to the Sentinel-2 MSI bands: the red-edge band (B5), which is centred at 705 nm instead of 708 nm, B6, which is centred at 740 nm instead of 753 nm, and B7, which is centred at 783 nm instead of 778 nm. We also considered that differences between the spectral response of S2A and S2B were negligible. For these match-up data, there were 49 chlorophyll data points, 24 in the Mundaú lagoon, and 25 in the Manguaba lagoon.

3. Results

3.1. Atmospheric correction

Due to the large amount of results, only metrics for MMELS and Mundaú and Manguaba lagoons, considering all bands, were included here (Table 4). The plots of the results for each band individually are seen in Figure 3, while the metrics for each band were included in the Supplementary material.

The results show that there is difficulty in retrieving ρ_w using the satellite data, with elevated errors and low r^2, especially bands 2 (blue), 3 (green) and 8A (NIR) (Tables S1, S2 and S7). For bands 4 (red), 5 (red-edge), 6 (NIR), and 7 (NIR) (Tables S3 to S6), most algorithms performed reasonably well, except for C2RCC. Without considering sunglint removal, C2X showed the best performance (Table 4), with r^2 of 0.60, nBias of 1.2, nMAE of 1.61, RMSE of 0.0117, and SAM of 3.8°, when considering all bands for MMELS.

We note that SeaDAS failed to accurately retrieve water reflectance across the three dates (Figures S1 and S2) using both configurations, estimating negative reflectances for many points (and providing no results for 20 of the 51 data points). In the case of Manguaba, even the mean value of the retrieved reflectances was negative for all but bands 4, 5 and 6. This huge variation of performance between the two lagoons might be related to the different water optical characteristics found in the scene (Mundaú, Manguaba and ocean waters), where the reflectance in Mundaú lagoon may be used for the calculation of Rayleigh-corrected radiance and determination of the aerosol type, and the extrapolation to Manguaba causes the negative ρ_w (as seen in the metrics in Table S10); the low signal-to-noise ratio of the SWIR band, as observed by Pahlevan et al. (2017a) or the adjacency effects in Mundaú lagoon. However, as done in the study conducted by Molkov et al. (2019) where a similar problem occurred, we did not consider this processing tool in our study.

As C2X is a neural network which estimates water reflectance from a measured database, without the influence of sunglint, this effect cannot be removed from the retrieved reflectance, only if applied before the AC, which is not

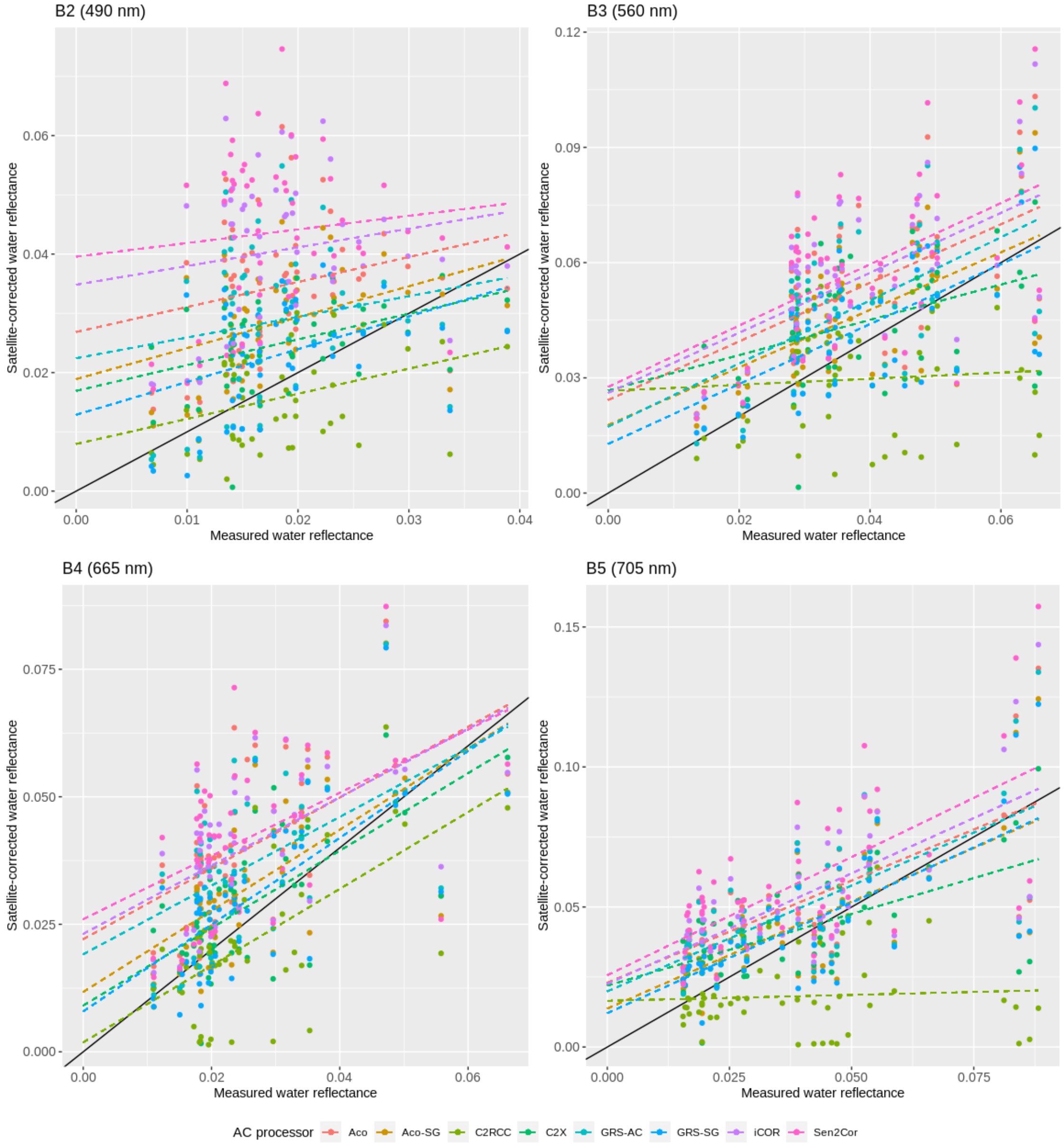

Figure 3: Comparison of the *in situ* with satellite-derived water reflectance corrected by each algorithm for bands 2 to 8A. The black lines represent the 1:1 line, and the colour dashed lines represent the regression lines for each AC processor for each band.

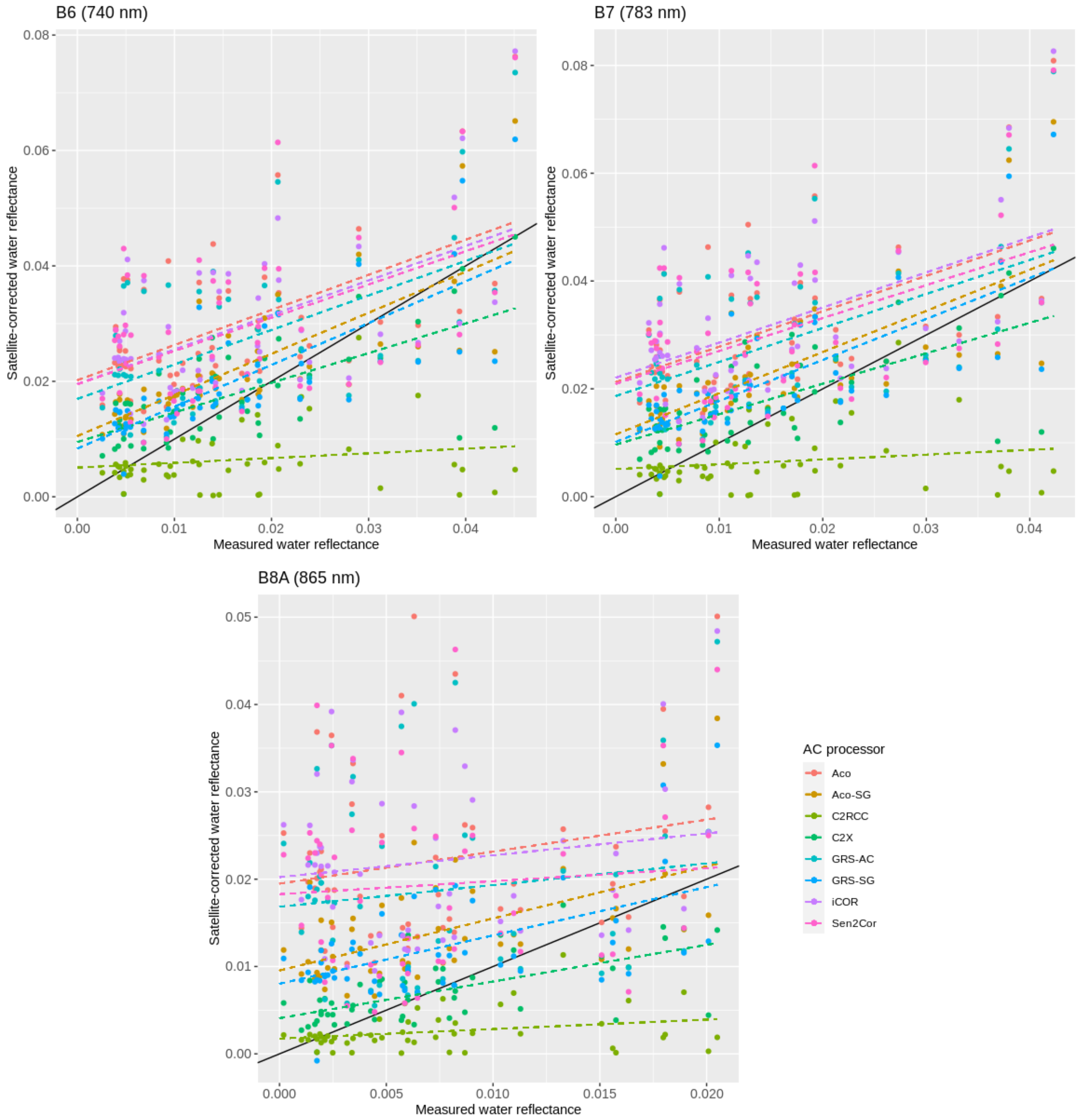

Figure 3: Cont.

Table 4: Metrics calculated for each atmospheric correction algorithm between *in situ* and satellite-derived water reflectance for MMELS and Mundaú and Manguaba lagoons (values in bold represent the best result in each case)

Algorithm		**Raw***	**Aco**	**Aco-SG**	**C2RCC**	**C2X**	**GRS-AC**	**GRS-SG**	**iCOR**	**S2C**
r^2	MMELS	0.27	0.54	0.64	0.26	0.60	0.51	**0.65**	0.52	0.49
	MUD	0.24	0.48	0.68	0.67	**0.70**	0.41	0.69	0.44	0.38
	MAG	0.30	0.60	0.63	0.14	0.61	**0.64**	0.60	0.60	0.60
Slope	MMELS	0.83	0.80	0.85	0.41	0.79	0.81	0.86	0.84	**0.92**
	MUD	0.86	0.71	0.85	0.85	**0.98**	0.64	0.85	0.70	0.76
	MAG	0.83	0.90	0.86	0.19	0.70	**0.96**	0.88	**0.96**	1.08
nBias	MMELS	3.29	2.03	1.55	0.47	**1.20**	1.74	1.36	2.10	2.07
	MUD	3.88	2.47	1.79	**0.87**	1.37	2.20	1.60	2.54	2.55
	MAG	2.80	1.68	1.34	0.26	**1.05**	1.38	1.17	1.75	1.69
nMAE	MMELS	3.31	2.11	1.70	2.45	**1.61**	1.92	1.63	2.18	2.19
	MUD	3.90	2.55	1.93	**1.48**	1.78	2.37	1.79	2.63	2.71
	MAG	2.82	1.76	1.52	3.98	**1.45**	1.57	1.49	1.83	1.78
RMSE	MMELS	0.0438	0.0194	0.0128	0.0172	**0.0117**	0.0174	**0.0116**	0.0211	0.0234
	MUD	0.0462	0.0211	0.0126	**0.0090**	0.0116	0.0190	0.0110	0.0227	0.0254
	MAG	0.0414	0.0176	0.0130	0.0224	**0.0118**	0.0157	**0.0121**	0.0194	0.0212
SAM	MMELS	22.3°	10.5°	7.0°	15.0°	**3.8°**	8.7°	4.9°	11.0°	9.4°
	MUD	19.6°	10.4°	5.8°	7.1°	4.8°	8.8°	**3.8°**	10.1°	8.8°
	MAG	25.0°	11.2°	8.2°	22.2°	**5.7°**	9.1°	6.2°	12.1°	10.2°

*no atmospheric correction

possible as GRS corrects for sunglint after AC, based on the retrieved aerosol parameters. Therefore, this correction was applied to the two best performing algorithms besides C2X, ACOLITE and GRS-AC. With the addition of the sunglint removal, the performance of both ACOLITE and GRS greatly improved, with r^2 increasing from 0.54 to 0.64 and from 0.51 to 0.65, RMSE decreasing from 0.0194 to 0.0128 and from 0.0174 to 0.0126, and SAM decreasing from 10.5°to 7.0°and from 8.7°to 4.9°, respectively (Table 4). It is also interesting to note that the results were bettered in every band for both algorithms. Analysing each band individually, the best results were achieved using:

- B2: GRS-SG (best metrics except for RMSE)
- B3: GRS-SG (best metrics except for slope)
- B4: C2X (best metrics except for slope)
- B5: GRS-SG (best metrics except for slope)

- B6: GRS-SG (best metrics except for nBias)
- B7: GRS-SG (highest r^2 and slope) and C2X (lowest nBias, nMAE and RMSE)
- B8A: C2X (best metrics except for slope)

The performance of the algorithms showed a considerable variation between each lagoon, except for the algorithms with sunglint removal. Most algorithms showed better results for Manguaba, except for C2RCC. For C2X, r^2 and slope were higher for Mundaú, while nBias, nMAE and RMSE were lower for Manguaba. Figure 4 shows a comparison of the mean ρ_w measured at both Mundaú and Manguaba lagoons and the mean reflectances retrieved from S2 images after AC. While most algorithms retrieved the reflectance at Manguaba lagoon quite well, for Mundaú, there is a considerable overestimation of the reflectance over all bands, more pronounced in bands 2 (blue), 3 (green), 7 (NIR), and 8A (NIR).

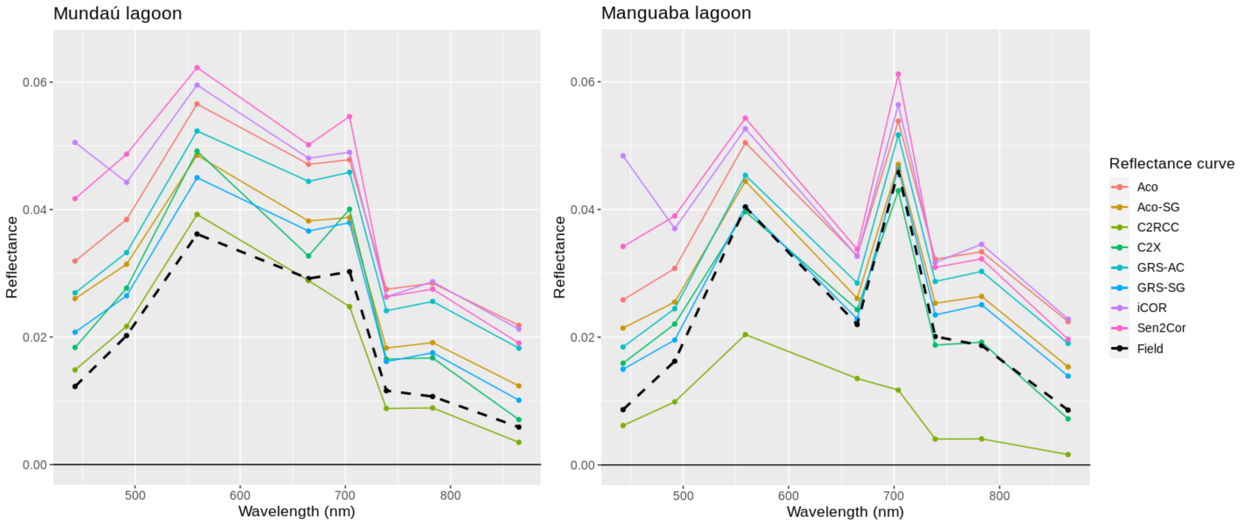

Figure 4: Mean reflectance curves measured at Mundaú and Manguaba lagoons (thicker lines), and the reflectances retrieved by Sentinel-2 MSI images after atmospheric correction. The curves of the measured data are plotted only for the central wavelength of Sentinel-2 MSI bands 1 to 8A.

Despite GRS-SG consistently showing better metrics than Aco-SG, these differences were only marginal, and their performances were similar (Table 4 and Figure 4), although these small differences can be significant for the *chla* models. Both GRS and ACOLITE with sunglint correction were the most consistent algorithms, which is needed in analysing the performance of the *chla* algorithms applied in this study since they use all bands (except for B8A) evaluated here. Furthermore, C2X showed the best results for B4, which is widely used in *chla* models. Therefore, due to the large number of analyzed algorithms, we chose to use reflectances corrected with these three methods, GRS-SG, Aco-SG and C2X, to properly evaluate *chla* retrieval procedures. Note that the first two algorithms exemplify the "physically-based approach" whereas the latter enables us to evaluate the "machine-learning" approach.

3.2. *Chlorophyll-a*

3.2.1. *In situ data*

There was a high variation in chlorophyll-*a* concentration across dates in MMELS as a whole and in each lagoon. In MMELS, it varied from a mean of 64.4 mg/m^3 in 05/22-23/2018 to 110.7 mg/m^3 in 03/23-24/2019 (Table 5), and showed a higher variation across the sampling points in 05/22-23, when the standard deviation was almost 50%, also found in Manguaba lagoon, and slightly higher than what was found in Mundaú lagoon (39%). It also showed a high standard deviation in 03/23-24 due to the large difference of *chla* content between each lagoon.

Table 5: Mean (Standard Deviation) chlorophyll-*a* (mg/m^3) measured on each field campaign

Site	**03/24/2017**	**03/22/2018**	**05/22-23/2018**	**08/06/2018**	**10/25/2018**	**02/26-27/2019**	**03/23-24/2019**
Mundaú	23.7 (7.6)	NA	51.1 (20.1)	NA	52.2 (19.5)	16.7 (5.6)	24.3 (6.1)
Manguaba	NA	64.2 (28.2)	68.0 (24.5)	46.5 (11.1)	NA	101.2 (23.1)	197.0 (17.9)
MMELS	NA	NA	60.3 (24.3)	NA	NA	57.7 (45.8)	110.7 (88.5)

*NA: no field measurements on this date

Mundaú showed a steady increase, considering a calendar year, from February, when it showed a mean concentration of 16.7 mg/m^3 of *chla*, to May, when it showed 51.1 mg/m^3, also showing high *chla* (52.2 mg/m^3) in October, while Manguaba showed high variability between 2018 and 2019, with large values in February (101.2 mg/m^3) and March (197.0 mg/m^3) 2019, but smaller, more constant values in 2018 (64.2 mg/m^3 in March to 46.5 mg/m^3 in August).

Most models showed an efficient performance (Figure 5, Table S11) for MMELS. The performance for MMELS and Manguaba was similar, with all algorithms showing consistent performances, except for the OC2 algorithm. In both cases (MMELS and Manguaba), the BI, 3BR and 2SAR algorithms produced the best results (r^2 of 0.95–0.97, nRMSE of 10.2–19.2%), with very consistent performances in both calibration and validation. The global algorithm, MDN, showed a consistent performance for MMELS and Manguaba, with $r^2 > 0.90$ in both cases, although the nRMSE was high, comparable to OC2, due to a large bias. In the case of Mundaú, the 2SAR algorithm produced relatively consistent results, with r^2 of 0.79–0.82 and nRMSE of 25.9-28.0%. The other algorithms also showed a decent performance, except again for the OC2 model, while nRMSE was higher for MDN.

3.2.2. *Satellite-derived reflectance models*

Using satellite reflectance corrected with Aco-SG, GRS-SG and C2X, for MMELS, 2BRL, 2BQR, 2SAR, 3BR, and NDCI models (r^2 of 0.75–0.81, nRMSE of 33.3–43.2%) performed well with Aco-SG (Figure 6, Table S12), while for C2X and GRS-SG (Figure 7, Table S13), performance decreased considerably for most algorithms in comparison with the *in situ* models, with the 2SAR algorithm presenting the best results for GRS-SG (r^2 of 0.75, nRMSE of 39.8%), and 2BQR and NDCI algorithms presenting the best results for C2X (r^2 of 0.61–0.63, nRMSE of 45.8–52.9%). Considering each lagoon separately, the results are very different, and as with the *in situ* models, most algorithms

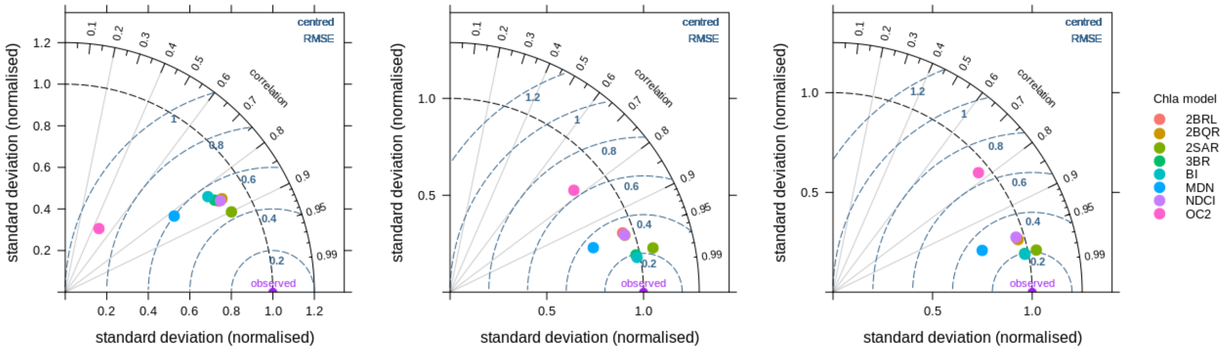

a) Mundaú lagoon b) Manguaba lagoon c) MMELS

Figure 5: Taylor diagrams for the chlorophyll-*a* retrieved from algorithms using *in situ* measured reflectance.

performed well in Manguaba but not in Mundaú. For the former, the results are similar to MMELS when using Aco-SG (although slightly poorer), with 2BRL, 2BQR, 2SAR and NDCI algorithms (r^2 of 0.67–0.70, nRMSE of 23.3–29.5%) producing the best results (Figure 9). For C2X, all models showed relatively similar performances except for the OC2 algorithm, and 2BRL, 2BQR and NDCI algorithms showed the best results (r^2 of 0.65–0.71, nRMSE of 22.9–26.5%). For GRS-SG, performance decreased considerably when compared to Aco-SG and C2X, with the 2SAR algorithm producing the best results (r^2 of 0.59, nRMSE of 28.7%). For Mundaú, all algorithms showed low performance, and the best results were produced using C2X with the OC2 algorithm (r^2 of 0.33–0.55, nRMSE of 48.4–72.4%) (Figure 9). In all cases, the performance of MDN greatly decreased, showing a very inconsistent performance.

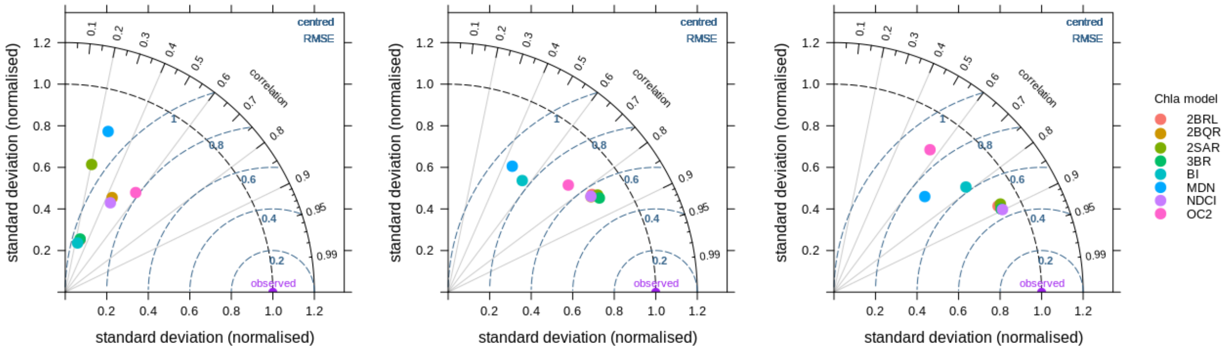

a) Mundaú lagoon b) Manguaba lagoon c) MMELS

Figure 6: Taylor diagrams for the chlorophyll-*a* retrieved from algorithms using Sentinel-2 MSI images corrected using ACOLITE with sunglint correction.

Figure 9 shows a comparison of measured and modelled *chla* in different scenarios, considering the best model in different cases, while Figure 10a) shows the comparison of the same model, the 2SAR algorithm, in MMELS when

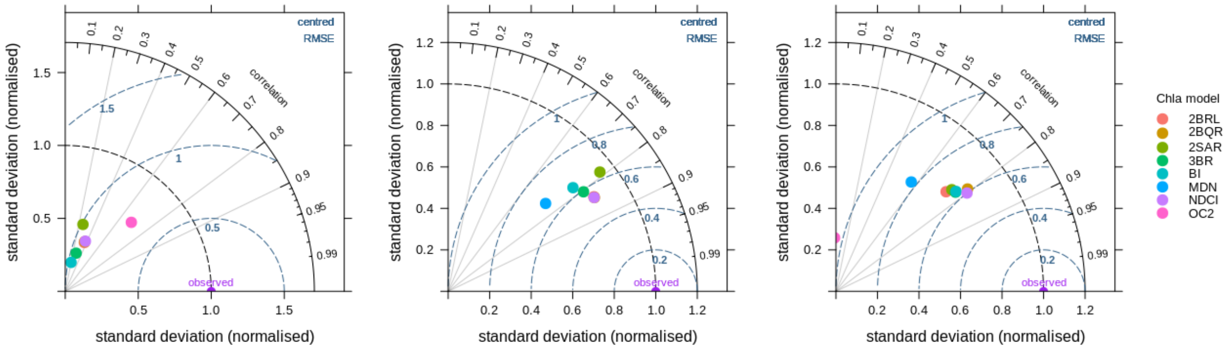

a) Mundaú lagoon b) Manguaba lagoon c) MMELS

Figure 7: Taylor diagrams for the chlorophyll-*a* retrieved from algorithms using Sentinel-2 MSI images corrected using C2X.

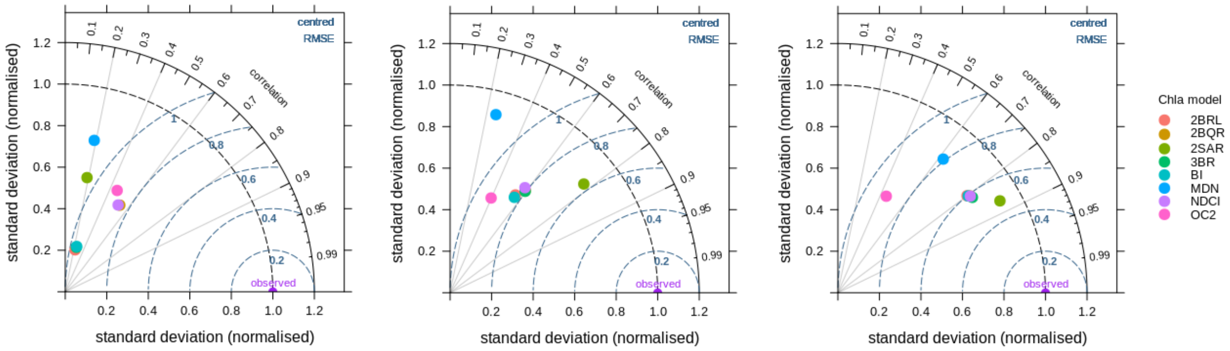

a) Mundaú lagoon b) Manguaba lagoon c) MMELS

Figure 8: Taylor diagrams for the chlorophyll-*a* retrieved from algorithms using Sentinel-2 MSI images corrected using GRS with sunglint correction.

locally calibrated (mean values of the coefficients over the 100 runs) considering *in situ* and Aco-SG-corrected satellite reflectance and with the coefficients provided by Neil et al. (2019) when calibrated for OWT 8 (hereafter named Cluster, as in their study), the class of Manguaba lagoon, and Figure 10b) also compares the effect of the different calibrated coefficients (Field, Satellite and Cluster). Although the *in situ* model (Figure 9a) presents more data points, the loss of performance is evident when modelling *chla* using satellite-derived reflectance. It also shows that most algorithms performed better using reflectance corrected with Aco-SG, and that unsatisfactory results were generated for Mundaú in all scenarios. In addition to this difference in performance, when using satellite-derived reflectance, there is also a tendency in overestimating small *chla* and underestimating very high *chla* concentrations, which was not observed when using *in situ* data.

In addition, the metrics in Table 6 show that although the Cluster calibration provides consistent results, with high r^2 in both cases (in situ and satellite reflectance), the bias and errors are high, almost doubling for the field data, and

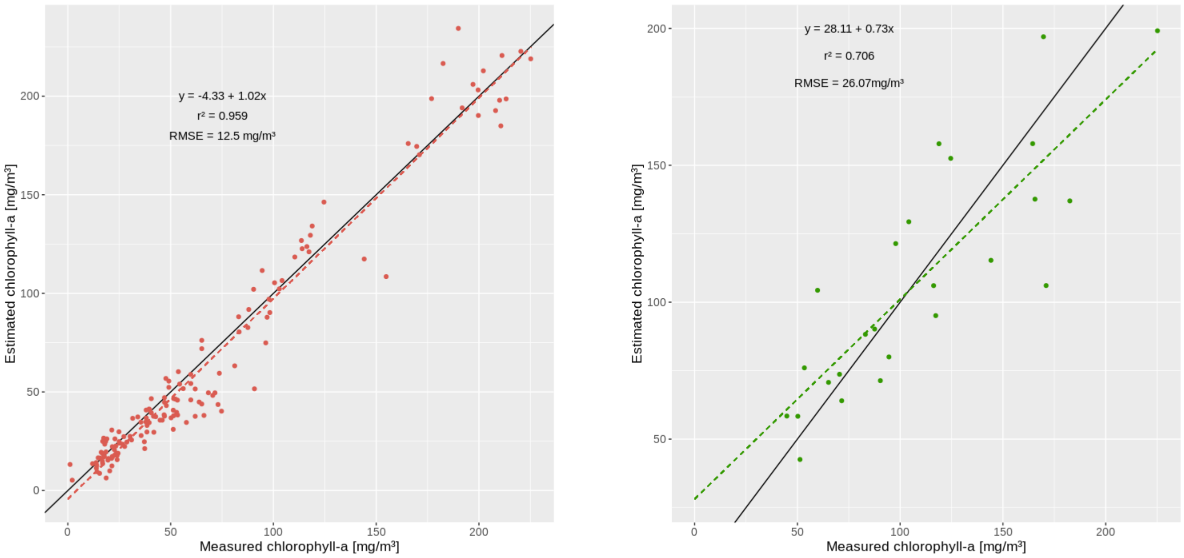

(a) 2SAR–in situ–MMELS

(b) 2SAR–Aco-SG–Manguaba

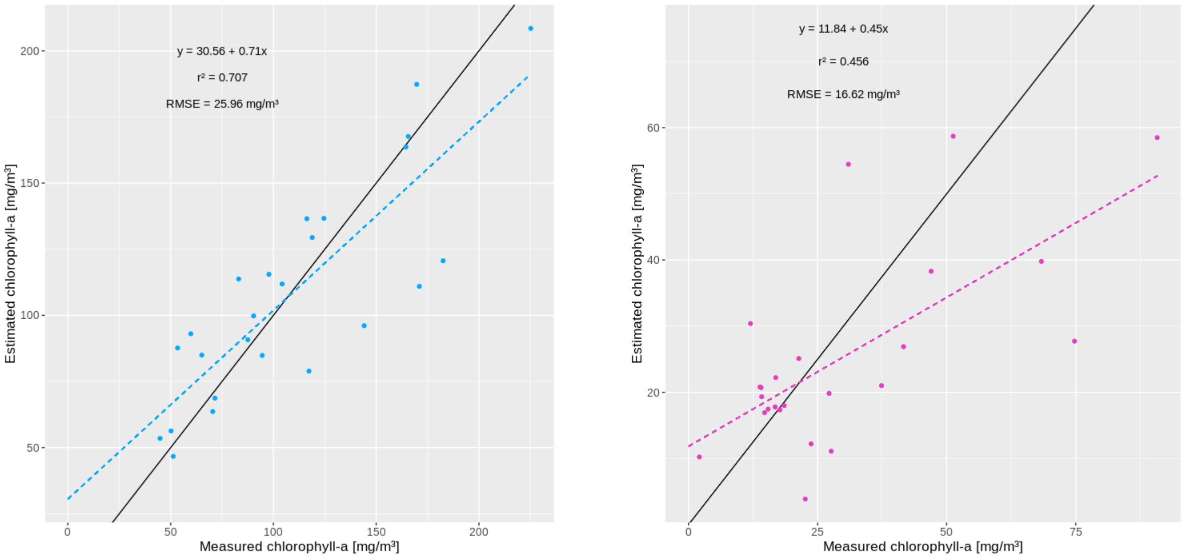

(c) NDCI–C2X–Manguaba

(d) OC2–C2X–Mundaú

Figure 9: Plots of measured *vs.* estimated chlorophyll-*a* using Sentinel-2 MSI images for (**a**) MMELS, using the NDCI algorithm with Aco-SG, (**b**) Manguaba, using the 2SAR algorithm with Aco-SG, (**c**) using the NDCI algorithm with C2X, and (**d**) Mundaú, using the OC2 algorithm with C2X. The models were generated using the mean values of each coefficient obtained in the calibration procedure.

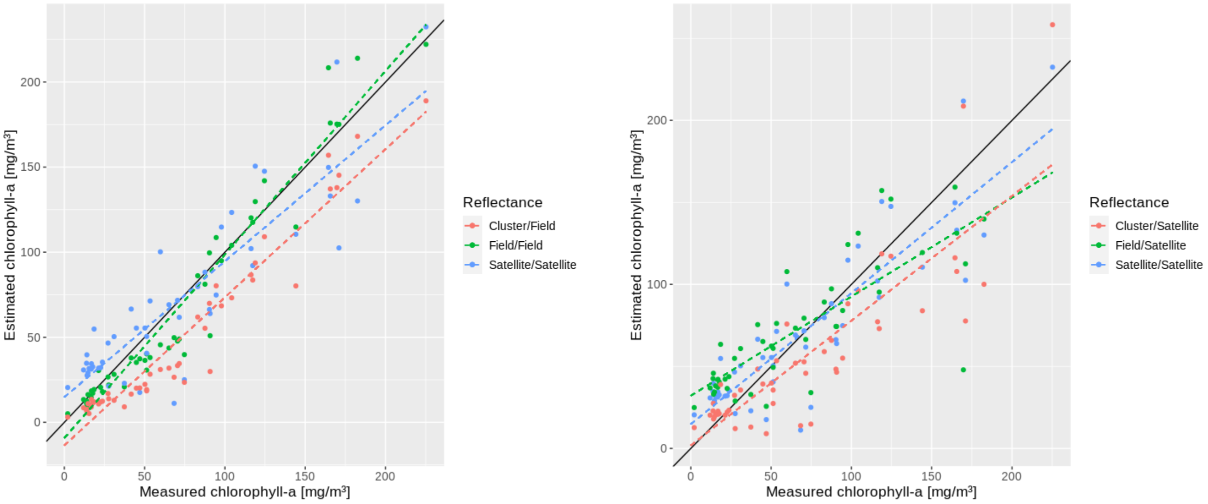

Figure 10: Plots of measured *vs.* estimated chlorophyll-*a* in MMELS using the 2SAR algorithm with the coefficients calibrated using Field and Satellite (Aco-SG corrected MSI) reflectance, and provided by the Cluster calibration (OWT 8 in Neil et al., 2019) (the first name refers to the coefficients used, and the second to the water reflectance data used in the model).

increasing by almost 25% for satellite data. However, for the latter, the results are similar to the produced by the model when using the coefficients calibrated for field data, although these coefficients are very divergent.

Table 6: Metrics for the 2SAR algorithm with the coefficients (**a** and **b**) calibrated using Field and Satellite (Aco-SG corrected MSI) reflectance, and provided by the Cluster calibration (OWT 8 in Neil et al., 2019) (the first name refers to the coefficients used, and the second to the water reflectance data used in the model)

Model	a	b	r^2	Bias (mg/m^3)	RMSE (mg/m^3)	nRMSE (%)
Field/Field	2.50	0.0142	0.95	-3.7	15.2	21.6
Cluster/Field	1.25	0.0174	0.93	-22.7	26.9	38.3
Satellite/Satellite	1.67	0.0141	0.78	0.7	25.5	36.2
Field/Satellite	2.50	0.0142	0.65	2.4	30.7	43.7
Cluster/Satellite	1.25	0.0174	0.73	-15.0	31.9	45.3

Lastly, chlorophyll-*a* maps were created from S2 corrected reflectance using the most consistent algorithm, the 2SAR algorithm. Figure 11 shows the map on the date with less cloud cover, 05/23/2018. This is also the date with the smaller differences found in *chla* in the *in situ* measurements (Table 5), which is uncommon since the higher values of *chla* in Manguaba lagoon are generally found in the rainy season (April to July), whereas in Mundaú lagoon they are found in the dry season (October to March) (Lins et al., 2018). In Mundaú, the higher values are found in the Southeastern part of the lake, closer to the urban area, and this is probably caused by organic load due to point and non-point sources from this area, from where urban stormwater and untreated sewage discharge flow (Costa et al., 2011). The lowest values of *chla* are concentrated in the Southern area, likely due to the influence of saltwater from the flood tide, since the lagoons are dominated by freshwater phytoplankton, while diatom marine species have a lower growth rate in the lagoon due to high turbidity (Melo-Magalhães et al., 2009). The effect of tide is minimised in Manguaba, hence the higher values even in points close to the connecting channels (Oliveira and Kjerfve, 1993). The higher values found in Manguaba are in the Western margin, close to the mouth of river Paraíba do Meio and along this margin, following the hydrodynamics of the lake. This is a result of the high retention time in this lagoon and the organic loading by the river, carrying fertiliser and nutrient loading, probably coming from sugarcane crops, in addition to minor wastewater discharge from urban areas (Costa et al., 2011).

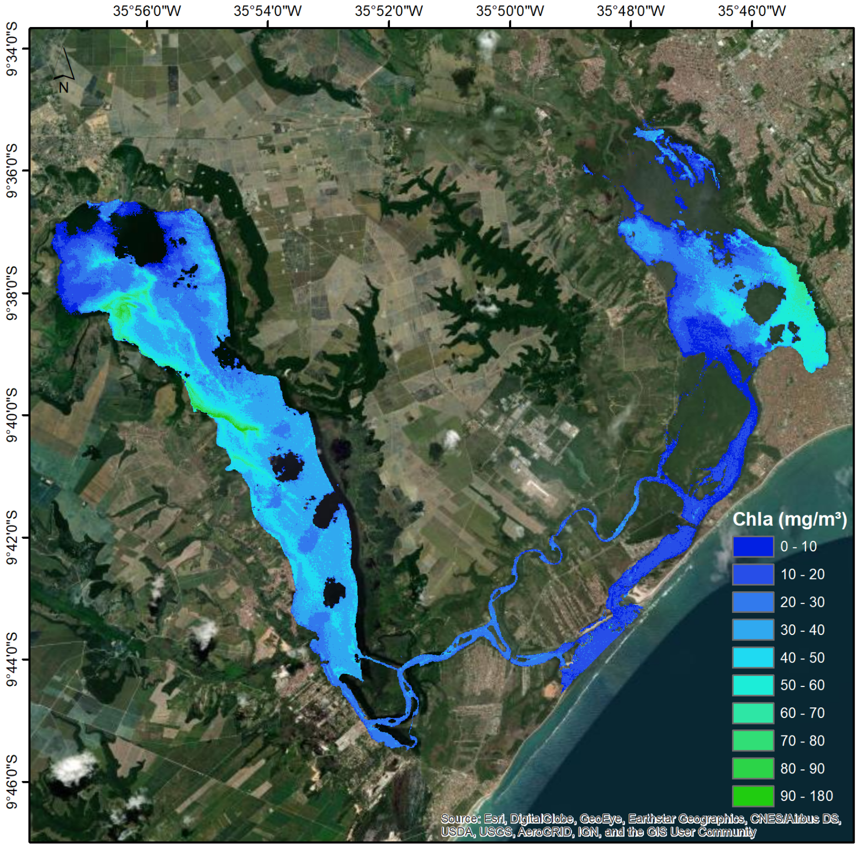

Figure 11: Map of concentration of chlorophyll-*a* in MMELS, created with the locally calibrated 2SAR algorithm using reflectance derived from the Sentinel-2 MSI image on 05/23/2018 and corrected with Aco-SG.

4. Discussion

4.1. Atmospheric correction

The results show that all algorithms reduced the error between surface and satellite reflectance (Table 4); however, in some cases, the r^2 decreased after the AC, in comparison with the uncorrected reflectance. For Sen2Cor, for example, r^2 decreased in all cases, although the other metrics were improved. Bands 2 (blue) and 3 (green), being the most affected by Raleigh and aerosol scattering and thus the most influenced by the atmosphere (Mouw et al., 2015), were the most difficult for correction, and even though errors decreased substantially using all algorithms, the highest r^2 for B2 was 0.14, for example. For B5 (red-edge), most AC algorithms showed slight improvement, when raw reflectance showed the highest r^2 (0.45) and one of the lowest errors. Molkov et al. (2019), for example, found r^2 and RMSE of 0.87 and 0.0169 for this band, although mean reflectance values were smaller in the Gorky Reservoir. Poorer results were also expected for B8A (NIR) due to higher atmospheric absorption in this spectrum, while better results were expected for B4 (red), when r^2 was lowest than 0.5 for all algorithms. Vanhellemont (2019), for example, found, for this band, r^2 of 0.71 and RMSE of 0.0068 when applying ACOLITE to S2 and validating it with AERONET-OC data, while the best result found in MMELS was using C2X, with r^2 and RMSE, respectively, of 0.48 and 0.0098.

The main issue in accurately correcting for atmospheric effects is the retrieval of aerosol optical thickness (aerosol contribution to radiance measured in each band) (Moses et al., 2017). Due to the different sources of aerosols in the study area (urban area, crops and marine aerosols, for example), not only the complexity in retrieving τ_a is increased, but aerosol types and load can also have large spatial variability, further reducing the accuracy of this estimation over the system, especially for the processors that assume atmosphere homogeneity over each scene, such as ACOLITE and C2RCC.

C2X showed a consistent performance, and although r^2 was not high for any specific band, it was higher than 0.60 when considering all data and for each lagoon separately, while also showing consistently low errors for all bands, and it is recommended for studies in turbid waters (Pereira-Sandoval et al., 2019; Warren et al., 2019). When not considering sunglint removal, its performance was considerably better than the other algorithms applied here, and this consistency has been shown in other studies (*e.g.*, C2RCC in Ansper and Alikas, 2019; Molkov et al., 2019; Pereira-Sandoval et al., 2019). Among the two options for C2RCC, C2X is clearly the best for MMELS for being designed for turbid waters, which was expected. Its consistent performance was likely due to the minimisation of adverse effects that limit the quality of the AC, *i.e.*, the strong influence of the atmosphere (aerosols), and sunglint and adjacency effects. This efficiency was achieved despite its simplified methodology, consisting of a neural network calibrated to TOA reflectance and atmospheric data. As a result, these adverse effects had reduced importance since the final output, ρ_w, is not a “corrected” bottom-of-atmosphere (BOA), but rather a value of “expected” water reflectance given the atmospheric conditions and the TOA reflectance (Doerffer and Schiller, 2007). Limitations in this algorithm might also be related to uncertainty in the determination of the IOPs (variability of the absorption of each IOP) (Brockmann et al., 2016), assumption of a rough water surface caused by a constant wind with a speed of 3 m/s (Doerffer and Schiller, 2007), the use of B1 (deep blue) for the derivation of the IOPs which, although being commonly used for this retrieval (since CDOM is more optically active in the blue and green bands) (Babin et al., 2003), is the most affected by atmospheric aerosols (Kutser, 2012), and the sunglint and adjacency effects that indirectly affect the estimated ρ_w.

Algorithms that are not specific for water bodies showed lower efficacy. iCOR is based on two assumptions that are not valid for MMELS (and for many other aquatic environments): the absence of sunglint and moderate or low turbidity. The first assumption is for the adjacency correction, and as shown by the improvement of the results when using GRS, sunglint affects most pixels on most dates. Even though adjacency correction is necessary for coastal and inland water bodies (Martins et al., 2017; Bulgarelli and Zibordi, 2018; Ansper and Alikas, 2019), this assumption, and the inflexibility of this algorithm as to whether or not to apply this adjacency correction, limits its application to the AC of images in aquatic environments. It also could not retrieve u_{H_2O} in two dates, which might be due to the elevated values and that may not be present in the LUTs used by the AC method. Because of this, iCOR did not show considerable correction of the atmospheric effects in terms of r^2 (Table 4), although errors were substantially reduced. Sen2Cor also provided poor results, in contrast to other lake studies (Martins et al., 2017; Maciel et al., 2019). This can be due to its simplified methodology and the effects of sunglint and adjacency, as well as to the retrieval of τ_a and u_{H_2O}, resulting in miscorrection of the atmospheric contribution to ρ_t.

ACOLITE performed relatively better than iCOR, likely due to its interesting approach in not selecting bands before analysing the image. Switching reflectance thresholds have been proposed to switch from NIR–SWIR-based AC (Wang et al., 2009; Liu et al., 2019), but an image-based selection of the best bands to retrieve τ_a can result in lower errors in the estimation of ρ_{path}, particularly in waters with sunglint, with high adjacency effect or very turbid waters (Ilori et al., 2019; Maciel et al., 2019; Vanhellemont, 2019), which are all existing conditions in MMELS, especially in Mundaú lagoon. Its limitations are likely related to the assumption of a homogeneous atmosphere over the whole scene (due to high variability in the aerosol load and type, considering the proximity to the dense urban area), and the adjacency effects, as observed in Pereira-Sandoval et al. (2019). GRS-AC showed the best performance among the physically-based algorithms, which is related to the robustness of the algorithms it is based on (SMAC and OSOAA). It may also reduce the uncertainty in retrieving τ_a by using gridded values provided by CAMS, which have been shown to be consistent (Cesnulyte et al., 2014), improving the accuracy of the modelling of aerosols and thus, L_{sky}. Limitations of GRS are related to the resolution of the CAMS dataset (~80 km) and its consequent loss of accuracy in retrieving more accurate aerosol optical properties. To our knowledge, this is the first study that directly compares the AC of GRS with other processors, and the results show potential for broad applicability.

Considering the application of sunglint correction, Vanhellemont (2019) did not find a substantial improvement in ACOLITE's performance with S2 data (decrease of RMSE but little variation of r^2). Here, on the other hand, sunglint showed to be essential in the AC of satellite images when using physically-based algorithms. The sunglint correction algorithm improved the results produced by both ACOLITE and GRS-AC for all bands, which was also observed by Harmel et al. (2018), testing GRS with AERONET data for a large number of S2 images, when r^2 increased from 0.56 to 0.87 and RMSE decreased from 0.78 to 0.32 mW/(cm^2 sr um), considering all bands, and especially for B4 (red), r^2 increased from 0.19 to 0.88.

The influence of sunglint is probably relevant for most water bodies in low latitudes (Harmel et al., 2018; Maciel et al., 2019). Figure 12 shows the values of sun zenith angle, sensor viewing angle and the incident angle of the light at the water surface through the year for Sentinel-2 overpass times in 2019. Although an estimate of the probability of sunglint to occur takes into account wind and surface rugosity (that is, when not considering the actual measured radiance data), this probability is greater for smaller incident angles. Since sunglint mainly affects water surface when the sun zenith angle is high on the horizon and for sensor viewing angles close to nadir (which is the case for Sentinel-2 viewing configuration), the contribution of sunglint signal to the sensor measurements can be high throughout the year in MMELS and any other water bodies in the tropical region (Harmel and Chami, 2013). Thus, we recommend the usage of sunglint corrections in all studies dependent on ρ_w under such circumstances. It would also be interesting to test whether the performance of other algorithms would also improve with the application of this technique. In this sense, it is important to highlight that this sunglint algorithm cannot be applied to C2X since it retrieves ρ_w based on a large measured dataset, and thus the sunglint has influence only on TOA reflectance, which are input to the neural network, and not on the outputted ρ_w, but the implementation of a sunglint correction method for this algorithm is in development (Pereira-Sandoval et al., 2019).

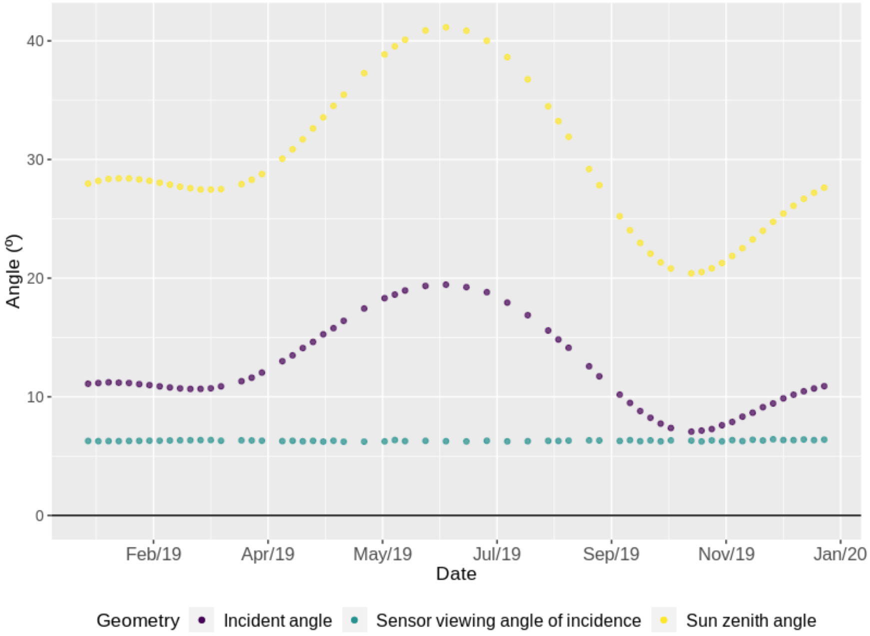

Figure 12: Sun zenith, sensor viewing and incident angles for Sentinel-2 overpass times in MMELS for 2019.

A considerable difference in performance between each lagoon was observed. Most algorithms showed better results for Manguaba lagoon, and even C2X, Aco-SG and GRS-SG, which showed a higher r^2 for Mundaú, showed high errors (Figure 4) for this lagoon. This poor retrieval of Mundaú reflectances is most likely due to adjacency effects on water reflectance since Mundaú lagoon is close to a highly anthropised area in Maceió city (Figure 1), with a large urban area, which covers most of its Northeastern margin, as well as coconut and sugarcane crops surrounding the other parts of the lagoon. The urban area is the most important adjacency affecting the water reflectance, since it typically has higher reflectance in all bands, as verified by examining different pixels in this area. Forest and grasslands, which cover most of the area surrounding Manguaba lagoon, and lagoon waters have fairly similar spectral responses, except for bands 7 and 8A, and thus a larger error was expected for these bands in the AC of reflectance for Manguaba lagoon as well, as observed (Figure 4). Accordingly, this is a possible reason for the overestimation of ρ_w in these bands by both Aco-SG and GRS-SG. Adjacency correction has been shown to be required for accurate retrieval of reflectance of inland waters using satellite imagery (Martins et al., 2017; Bulgarelli and Zibordi, 2018; Ansper and Alikas, 2019), and this is likely the case for MMELS as well, especially Mundaú lagoon. iCOR, which could have shown an improved performance due to its adjacency correction model, also retrieved poor results for Mundaú due to the sunglint effect (Sterckx et al., 2015), as discussed above. The variability of τ_a can also be of importance since the aerosol load is likely higher in Mundaú due to the dense urban area in its vicinity, further reducing the accuracy of the AC.

Another aspect that could have influenced the AC in Mundaú lagoon is the fact that most match-up data had one day of difference between *in situ* measurements and satellite overpass (Table 1). However, due to the high retention times in this lagoon (*ca.* 16 days), especially in the dry season (Oliveira and Kjerfve, 1993), the temporal variability of its optical properties is small, thus this effect is minimised, and other effects, as discussed above, are responsible for the inadequate correction of atmospheric effects in this lagoon.

4.2. Chlorophyll-a

4.2.1. Retrieval using measured reflectance data

In general, all NIR-red algorithms produced consistent results in all three datasets of *in situ* reflectances (MMELS, Manguaba, and Mundaú) (Figure 5, Table S11), with the best results always found for Manguaba, with 2SAR, 3BR and the BI algorithm showing particularly consistent results with RMSE of ~10–14%. In Neil et al. (2019), the mean values of r^2 and the slope of the regression line for OWT 8 (Manguaba), considering all recommended algorithms, were 0.66–0.71 and 0.84–0.89, respectively, while for OWT 6 (Mundaú), these values were ~0.50 and ~0.60, considerably lower than found here. For MDN, the results were very consistent in terms of r^2, however, the bias was very high and negative in all cases, resulting in high nRMSE. This might be related to the low percentage of the dataset in hypereutrophic water (*chla* > 90 mg/m^3) used for calibration (~5%), and a poor identification of the OWT of the lagoons, leading to OWT with possibly higher concentrations of CDOM and NAP, resulting in this wide underestimation of the *chla* concentrations.

For Mundaú, the performance decreased considerably for all models (which is expected as performance varies across OWTs, Neil et al., 2019, 2020), with the best results provided by the 2SAR algorithm (r^2 of 0.81 and nRMSE of ~27%). The performance of the models for Mundaú was better than the mean found in Neil et al. (2019) but poorer than other similar studies. For example, Moses et al. (2009) found r^2 of 0.95 and RMSE of 3.7 mg/m^3 when applying the 2BRL algorithm with MERIS in waters with a reflectance curve similar to Mundaú and *chla* concentrations of 0–65 mg/m^3, although Mundaú reflectance curves have a higher peak at 700 nm. The high turbidity of Mundaú is likely influencing the performance of the algorithms, as the absorption by CDOM and NAP or backscattering by suspended particles might be comparable to the absorption coefficient by *chla* (a_ϕ), especially in low *chla* concentrations, affecting the modelling by the algorithms (Gitelson et al., 2008; Kutser et al., 2016). In Gitelson et al. (2008), the 3BR algorithm performed better since it removed the influence of backscattering in higher wavelengths, but here the BI and the 3BR algorithms produced results similar to the two-band models, which means that the absorption by CDOM and NAP likely has more influence on the results than backscattering. The same applies to the NDCI algorithm, which also assumes that CDOM and NAP absorption do not vary in the red and red-edge spectra (Mishra and Mishra, 2012).

By combining the reflectance of both lagoons, the resulting performance of the models appeared to mask the fairly poorer performance for Mundaú, since Manguaba shows higher *chla* concentrations, and thus, the nRMSE is lower for Mundaú. When combining the modelled *chla* in Manguaba and Mundaú lagoons separately, the resulting r^2 and nRMSE are 0.96 and 17.8%, showing only marginal difference from the metrics for the MMELS dataset (r^2 of 0.96 and nRMSE of 18.8%, Table S11). Therefore, *chla* can be modelled in MMELS as a whole without loss of accuracy, when considering measured ρ_w. Additionally, a few studies (*e.g.*, Dall'Olmo and Gitelson, 2005; Huang et al., 2014) found limitations in NIR-red algorithms for *chla* <20 mg/m^3, however here this difference was not observed for 2SAR (Figure 9), when considering MMELS or Mundaú separately, showing that this algorithm is more robust in lower *chla* concentrations, which can be the reason for its consistency in Mundaú lagoon (Figure 5).

4.2.2. Retrieval using satellite data

For the satellite reflectance models, there was a substantial loss of performance in the results, when compared with the *in situ* models, due not only to the differences between the satellite-derived and the measured *in situ* water reflectance, but also to the influence of the difference of efficiency in removing the atmospheric influence across the satellite bands: a disproportionate increase or decrease in reflectance, especially at the red and red-edge bands, causes inaccurate estimations of *chla* (Mishra and Mishra, 2012). Dall'Olmo et al. (2005) found that NIR-red models are reasonably resistant to these errors due to AC for SeaWiFS and MODIS; however, here we notice a much stronger influence of the AC in the results, especially when comparing the different results produced by each model when using Aco-SG (Figure 6, Table S12) or C2X (Figure 7, Table S13). This also agrees with the results recently found by Pahlevan et al. (2020), where they found that the *chla* retrieved using the MDN algorithm varied greatly when using ACOLITE, POLYMER or SeaDAS. We also highlight that MDN is highly dependant on the quality of the AC, as its performance strongly decreased for tested AC methods (Tables S11 to S13), impairing its applicability to our study area. The low number of data points used may also decrease its performance by constraining the identification of the OWT and thus the retrieval of IOPs.

Despite the loss of performance, the results produced by most locally calibrated algorithms were reasonably consistent for Manguaba and MMELS when using Aco-SG, and compare well with the literature. When simulating the reflectance of S2 bands from *in situ* data measured in MMELS, Lins et al. (2017) found r^2 of 0.78 and RMSE of 10.4 mg/m^3 using the 2BLR algorithm, which is fairly similar to the results found here using Aco-SG (r^2 of 0.78 and RMSE of 25.5 mg/m^3), if considering the atmospheric effects. Watanabe et al. (2018) also simulated S2 bands, finding r^2 of 0.82–0.85 and nRMSE of 45.3–52.5% when applying the 2BRL algorithm, the three-band algorithm, and the NDCI algorithm in a hypereutrophic reservoir, with little variation in the results produced by each model. Here, the best results were found for MMELS when using Aco-SG, with considerable difference in the results for Manguaba and

Mundaú for Aco-SG (Table S12), C2X (S13) and GRS-SG (Table S14).

Another example of the influence of the AC is the inconsistency of algorithms when using *in situ* and satellite data. For MMELS and Manguaba, the NDCI algorithm, for example, was very consistent with Aco-SG and C2X, although it did not produce the best results with *in situ* reflectance. On the other hand, the BI algorithm showed the best results for Manguaba with *in situ* reflectance but a poor performance with satellite data for all three AC algorithms. The 3BR also showed a loss of performance, although not as pronounced as observed for BI. This can be due to the lower signal-to-noise ratio of B6, which makes this band more sensitive to the uncertainties in the AC (Moses et al., 2009). However, the 2SAR algorithm was not as sensitive to the AC using Aco-SG and GRS-SG despite using reflectance at B7, which showed considerable deviation from the measured water reflectance (Figure 4).

Interestingly, for Manguaba, with C2X, the 2SAR algorithm produced considerably poorer results, while the BI algorithm produced better results than when using Aco-SG and GRS-SG. For the BI algorithm, this can be due to the relation between bands 4, 5 and 6: while both Aco-SG and GRS-SG greatly overestimated $R_{rs}(740)$, C2X provided much closer values for this band (Figure 4), thus providing more consistency for the values in the ratio of bands. For the 2SAR algorithm, although C2X provided much closer values than Aco-SG and GRS-SG (Table S8), r^2 and Slope are lower for C2X, resulting in similar errors for all three algorithms. In the case of the MDN algorithm, as it depends on the identification of the OWT to retrieve *chla*, this wide variation of AC across bands is greatly detrimental to its performance, possibly more relevant than retrieving water reflectance with lower bias. Another significant drawback of this algorithm is the consideration of B1 as input data. Although we did not consider this band in our analysis of the performance of the AC methods, in Figure 4, it is clear that reflectance in this band was considerably overestimated. It is also important to consider that it has a resolution of 60 m, which can substantially reduce its accuracy, further contributing to the poor performance observed here.

Despite being an interesting metric to assess the performance of AC, the SAM is not a good predictor of the performance of *chla* models. Even though C2X showed the lowest SAM when considering only the bands used in the red-NIR models (Table S8), with angles close to 1°, it produced similar results for the algorithms using only bands 4 and 5, but poorer results when using the 2SAR algorithm (bands 4, 5 and 7), for example. It is probably because SAM considers the mean values of retrieved reflectance, when the uncertainty associated with these mean values is also of great importance in the resulting *chla* model. Even an analysis of individual bands is not a good predictive of the performance, as GRS-SG produced consistent reflectance data for both bands 4 and 5 (Tables S3 and S4), low values of SAM (Table S8), but performance of most algorithms was relatively poor. Comparing the values in Table S9 with those in Tables S11 to S14, there is a clear relationship between the r^2 for *chla* and the ratio $R_{rs}(705)/R_{rs}(665)$ (which is first order sensitive to *chla* concentration) and the r^2 for the *chla* models based on this ratio in all cases. GRS-SG showed lower performance for the linear regression between measured *chla* and this ratio than Aco-SG and C2X, which is reflected in the poorer results produced by the *chla* models. Therefore, the set of metrics used here, in addition to the r^2 for the regression between measured *chla* and the ratio of bands used in the *chla* models, might provide a more reliable basis for the prediction of the performance of *chla* models than a smaller set or individual metrics alone, such as r^2 and

RMSE only.

Considering Mundaú lagoon alone, all models produced poor results for both Aco-SG and C2X, even the 2SAR algorithm, which showed reasonably good results when considering *in situ* reflectance data (Figure 5, Table S11). Chen et al. (2017) found similar limitations in Lake Huron, which has a spectral response and water parameters similar to Mundaú lagoon, using S2 data corrected with Sen2Cor and Hydrolight, finding the best performance applying the 2BRL algorithm, with r^2 of 0.49 and nRMSE of 48.5%. Here, the OC2 algorithm showed the best performance, when it should have been the opposite, considering the poor performance of the AC algorithms in the blue and green bands, and especially since it showed the poorer results with *in situ* data in all cases (as expected, as the waters in Mundaú are turbid and have a high content of dissolved organic matter and particulate material, which have a high absorption coefficient in smaller wavelengths, especially blue) (Gons et al., 2002; Gurlin et al., 2011). It is possible that this inadequate correction of the atmospheric effects (high RMSE in all bands for both Aco-SG and C2X) somehow reduced the errors in retrieving *chla*. Nevertheless, all algorithms are very inconsistent and unreliable when considering Mundaú alone. This is a direct consequence of the poor AC, especially in the red and red-edge bands, which is likely caused by the adjacency effects in Mundaú, as discussed in Section 4.1. Therefore, to accurately retrieve *chla* in Mundaú, atmospheric, sunglint, and adjacency effects have to be corrected for, and this might be the case for other urban lakes.

As in the AC, the difference of one day between *chla* data and satellite reflectance could also be reducing the performance of the models in Mundaú lagoon. However, as discussed before, the retention time of this lagoon is high and this effect is minimised, if compared to the importance of AC, as seen in other studies (Kutser, 2012). Additionally, the tide is the most important driver of hydrodynamic variability in the system (Oliveira and Kjerfve, 1993), but the effect of tide is more relevant, in this short period of time, only in the region closer to the channel, where *chla* concentrations are lower (Figure 11). This variability could be the reason for the higher errors observed for very low concentrations of *chla*, but has a low impact in the metrics calculated between field and modelled *chla*, if compared to other effects such as due to adjacency.

When combining the datasets of both Mundaú and Manguaba, the algorithms also show great improvement in the r^2 when using satellite reflectance, especially Aco-SG and GRS-SG, which might be not only due to the larger amplitude of *chla* values but also to the higher number of points. Considering MMELS, the 2SAR algorithm showed the most consistent performance considering *in situ* and satellite results (for all three AC algorithms tested, although for C2X it produced slightly poorer results, as already discussed for Manguaba), as found in other results in turbid and productive waters (Gurlin et al., 2011; Neil et al., 2019). Moreover, as with the *chla* modelling using measured ρ_w, the combination of Manguaba and Mundaú datasets did not reduce the performance of the model (the mean value of r^2 decreased from 0.79 to 0.77, and nRMSE increased from 35.2 to 38.7), showing that *chla* can be modelled in MMELS with a single calibrated 2SAR algorithm, using satellite reflectance corrected with Aco-SG. Using the coefficients calibrated for the cluster of OWT 8, the class of Manguaba, the 2SAR algorithm was able to retrieve *chla* with a certain consistency (high r^2) however, the errors increased by about 25% (Table 6), a considerable increase. The possibility of using 2SAR as a global algorithm for this OWT is further discussed in Section 4.3.

Although Gurlin et al. (2011) highlighted that the assumption of the insensitivity of $R_{rs}(753)$ to any water constituents might not be valid in very turbid waters due to scattering by suspended solids, here this did not affect the modelling of *chla* even in Mundaú, where the 2SAR algorithm produced the best results using *in situ* reflectance. The limitations of the NIR-red for low *chla* concentrations affected the modelling of *chla* using satellite reflectance (Figure 10), however, this is a limitation of the AC algorithms and not the *chla* models, as discussed in Section 4.2.1. Since there was a great overestimation of reflectance in Mundaú (with lower *chla* concentrations) for all AC processors (Figure 4), this directly affected the modelling of *chla*, reducing the r^2 for the regression between measured *chla* and the ratio $R_{rs}(705)/R_{rs}(665)$ (Table S9).

Also relating to the 2SAR algorithm, Gons et al. (2005) changed the absorption coefficient of water from $a_w(704) = 0.63$ m^{-1} to $a_w(708) = 0.70$ m^{-1} when updating it to be used with MERIS (Buiteveld et al., 1994). Since B5 is centred at 705 nm, both values were tested here, and although this band has a higher spectral response to 704 nm than to 708 nm, the model using $a_w(708)$ showed the best results and was used here. There is difficulty in estimating the value of a_w for B5 since it varies considerably in the range of wavelengths to which this band is sensitive to, from 696 nm (0.524 m^{-1}) to 714 nm (0.844 m^{-1}) (Buiteveld et al., 1994). An integration of S2 RSR to the water absorption coefficients provided by Buiteveld et al. (1994) results in 0.64 m^{-1}, while when also considering the absorption increment due to temperature (a difference between water and reference temperatures of 5°C), $a_w(B5) = 0.65$ m^{-1}, a marked difference from 0.70 m^{-1}. Although testing the sensitivity of the 2SAR algorithm to this value was not in the scope of this study, this limitation has to be taken into account when applying this model with satellite-derived reflectance data.

4.3. Perspective for future studies

Our study showed that locally calibrated algorithms outperformed a global *chla* algorithm, MDN (Pahlevan et al., 2020), in all tests over two turbid lagoons. Although MDN was consistent, it largely underestimated *chla* concentrations, which is likely due to the small dataset of *chla* > 90 mg/m^3 used in the algorithm's calibration, hampering its applicability over eutrophic waters such as those found in MMELS. Although performance varied across the two OWTs, the 2SAR algorithm produced consistent results when calibrated for both OWT and when combining the datasets, providing a reliable model to retrieve *chla* in this system. When using the coefficients calibrated by Neil et al. (2019) for OWT 8, which includes Manguaba lagoon, it showed a very high r^2 but high bias, which resulted in an increase of 100% in the nRMSE, so further refinement of this calibration is still needed in order to be applied broadly. When considering only measured reflectance, calibrating algorithms for the same OWT might provide more general applicable algorithms and reduce the need to locally adjust models to retrieve *chla*, but the magnification of errors caused by this approach must be further investigated.

Furthermore, studies of distinct OWT rarely consider the impact of the atmospheric effects on the radiance measured by the satellite sensor and its major effect on the performance of *chla* models, as identified in several studies (*e.g.* Ansper and Alikas 2019; Molkov et al. 2019; Pahlevan et al. 2020). Although *chla* algorithms have been relatively well tested over different OWTs, few studies have tested the performance of different AC methods and made recommendations according to these criteria (Warren et al., 2019). To effectively and operationally retrieve *chla* using satellite data, the most suitable AC processors must be selected beforehand, in combination with the *chla* algorithm (as we showed that quality of AC provided by the algorithms is not a general predictor of the performance of the *chla* models), and this might be done according to OWTs (Spyrakos et al., 2018; Pereira-Sandoval et al., 2019), also taking into account other characteristics such as environmental conditions at the moment of image acquisition (Ilori et al., 2019).

When applying *chla* models using satellite imagery, recalibrating them using satellite-derived – instead of field measured – reflectance enhances performance, as observed here. The 2SAR model parameters, and thus the retrieved *chla* concentrations, showed a considerable difference for the calibration using our dataset of *in situ* and satellite data, as well as those calibrated in Neil et al. (2019). Although the latter coefficients produced elevated errors (an increase of 25%), the model showed remarkable efficiency in retrieving *chla* in MMELS using Aco-SG-corrected reflectance, when considering that it was calibrated for ρ_w data based on MERIS bands. We consider that 2SAR has the potential to be a global algorithm for this OWT (or larger groups of OWTs, Spyrakos et al., 2018), provided that it is recalibrated for satellite-derived BOA reflectance, reinforcing the need for further studies on the suitability of AC processors for each OWT (Pahlevan et al., 2020). The same applies to MDN: although it showed promising results for *in situ* reflectance data, it lost much performance when applied with satellite data, which was already observed in Pahlevan et al. (2020). We also highlight that a more consistent calibration for productive waters is needed, as it largely underestimated *chla* in both lagoons. Additionally, the removal of $R_{rs}(B1)$ as input data for MDN, when retrieving *chla* in turbid waters, might also be considered, as it has a lower resolution (60 m) and is the most sensitive to atmospheric effects, generally being corrected with the lowest accuracy by the AC processors (*e.g.*, Ansper and Alikas 2019; Ilori et al. 2019).

Based on our results and other studies (Pereira-Sandoval et al., 2019; Warren et al., 2019), we infer that ACOLITE and C2X might be the best AC processors over meso and hypereutrophic complex waters (Pereira-Sandoval et al., 2019; Warren et al., 2019). We also highlight that GRS provided very consistent atmospheric and sunglint correction, as also shown in Harmel et al. (2018), however, this algorithm has not been extensively tested yet, and further studies are needed to access it robustly. As studies in productive water in tropical regions are scarce, we also highlight that sunglint correction may be necessary to accurately retrieve *chla* (Maciel et al., 2019) for the sensors that cannot be tilted to avoid specular reflection, as is the case for Sentinel-2 MSI and Landsat 8 OLI, for example, and for MSI, technical limitations should be addressed, such as lack of bands and the time difference between the bands' measurements, which can hinder the correction of this effect in very windy conditions. More generally, correction of adjacency effects is also important (Martins et al., 2017; Bulgarelli and Zibordi, 2018; Ansper and Alikas, 2019; Pereira-Sandoval et al., 2019), considering aerosol scattering and directional reflectance of the surrounding area (such as clouds and vegetation), especially in smaller water bodies, since they might affect radiance for over 20 km, depending on atmospheric conditions (Bulgarelli and Zibordi, 2018). We reinforce that further studies are needed to better understand the impacts of AC, sunglint and adjacency effects on the performance of *chla* algorithms, in order to delineate the most suitable combinations of AC + *chla* algorithms for each OWT, in an effort to provide the basis for global-scale retrievals of this pigment using medium-resolution sensors such as MSI and OLI.

5. Conclusions

In this study, we aimed to find the best combination of atmospheric correction and chlorophyll-*a* algorithms to model this parameter in a productive tropical estuarine-lagoon system using Sentinel-2 MSI images. For this, we considered a few of the most commonly used AC algorithms applied to coastal and inland water bodies, and the *chla* models recommended by Neil et al. (2019) for the optical water types (Mundaú lagoon was identified as OWT 6 and Manguaba lagoon as OWT 8) present in MMELS, in addition to a widely applied and a global *chla* algorithm (MDN, Pahlevan et al., 2020). First, we compared *in situ* with satellite radiance corrected with the selected AC algorithms and found that C2X (C2RCC calibrated to turbid waters) (r^2 of 0.60, nBias of 1.2, RMSE of 0.0117, SAM of 5.7°), and ACOLITE (r^2 of 0.64, nBias of 1.55, RMSE of 0.0128, SAM of 8.2°) and GRS (r^2 of 0.65, nBias of 1.36, RMSE of 0.0116, SAM of 9.1°), both with sunglint correction, provided the most consistent surface water reflectance, when considering all bands analysed (bands 2, 3, 4, 5, 6, 7 and 8A). Sunglint correction was essential in deriving consistent water reflectance from remote sensing data, which is likely the case for most low-latitude water bodies, and thus we recommend the correction of this effect under such circumstances. In Mundaú, where surrounding land, mainly the dense urban area, can greatly influence the satellite-retrieved reflectance, we also verified that adjacency correction is necessary for accurate retrievals of water reflectance.

Secondly, we used *in situ* radiance and *chla* data to assess the performance of the *chla* models using measured water radiance. Most selected models showed consistent performances for both calibration and validation, especially for MMELS and Manguaba, with the 2SAR (Gons et al., 2002, 2005) and the BI (Yang et al., 2010) algorithms producing the best results (r^2 of 0.95–0.97, nRMSE of 10.2–19.2%), while for Mundaú, the 2SAR algorithm was the most consistent model (r^2 of 0.81, nRMSE of 26.8%). The higher turbidity and lower *chla* concentrations observed in this lagoon are likely the cause for the loss of efficiency of the models due to higher absorption by CDOM and NAP, which might be comparable to that by *chla*. We also showed that the locally calibrated algorithms outperformed the global algorithm, however, its performance might be enhanced by increasing the proportion of eutrophic waters in the dataset for the calibration procedure.

Lastly, when retrieving *chla* with the satellite-derived water reflectance, considerably poorer results were produced, especially for Mundaú, where the adjacency effects substantially affected water reflectance. We also found that the quality of AC provided by the algorithms is not a general predictor of the performance of the *chla* models, even when analysing individual bands separately, while the relationship between chlorophyll-*a* concentration and the ratio of bands used in the *chla* models might be. The combination of both Manguaba and Mundaú data increased both r^2 and nRMSE in relation to Manguaba in most cases. This is not only a consequence of the higher number of data points but also of the increase of the amplitude of *chla* concentrations. We showed that there is no significant difference in the results produced when modelling Manguaba or Mundaú lagoons separately or MMELS as a whole, and thus *chla* can be modelled in this system with the 2SAR algorithm, which showed the most consistent performance, using Sentinel-2 MSI images corrected with Aco-SG (r^2 of 0.78, nRMSE of 36.2%). The MDN algorithm was very susceptible to the influence of AC in the reflectance, impairing its applicability in MMELS. We also compared our calibration with the derived by Neil et al. (2019) for OWT 8 (which includes Manguaba), and r^2 was similar but nRMSE increased by 25%. We consider that 2SAR has the potential to be a global algorithm for this OWT (or larger groups of similar OWTs), provided that it is recalibrated for a large dataset of satellite-derived BOA reflectance.

We recommend that further studies explore the impacts of AC, sunglint and adjacency effects on the performance of *chla* algorithms, in order to delineate the most suitable combinations of AC + *chla* algorithms for the variable OWTs, in an effort to provide the basis for global-scale retrievals of this pigment using medium-resolution sensors such as MSI and OLI.

Acknowledgements

This research was funded by CAPES (Coordenação de Aperfeiçoamento de Pessoal de Nível Superior) through the project "Qualidade e circulação de água em ecossistemas costeiros: monitoramento e modelagem para tomada de decisão", and by CNPq (Conselho Nacional de Desenvolvimento Científico e Tecnológico) through the scholarship number 150600/2018-6. The GRS development was funded through the French National Spatial Agency (CNES) TOSCA program and data processing was performed at the ECLA center, INRAE, Aix-en-Provence, France thanks to Nathalie Reynaud and Thierry Tormos. T. H. fellowship was funded by the CNES/TOSCA OBS2CO project. We would like to thank the providers of the atmospheric correction algorithms integrated to SNAP (C2RCC, iCOR and Sen2Cor), NASA's Ocean Color Biology Processing Group for SeaDAS and Quinten Vanhellemont for providing ACOLITE for free. The GRS-AC and GRS-SG processing were partly based on data generated using Copernicus Atmosphere Monitoring Service Information [2019]; neither the European Commission nor ECMWF is responsible for any use that may be made of the information it contains. We are also grateful for the AQUASENSE/FINEP project for providing resources to attend a joint research meeting on the use of remote sensing images for water quality monitoring, and for the Global Lake Ecological Observatory Network (GLEON) for providing a venue for the discussion on lakes. Lastly, we would like to thank the reviewers for their contributions, which substantially improved the manuscript.

References

Ahmad, Z., Franz, B.A., McClain, C.R., Kwiatkowska, E.J., Werdell, J., Shettle, E.P., Holben, B.N., 2010. New aerosol models for the retrieval of aerosol optical thickness and normalized water-leaving radiances from the SeaWiFS and MODIS sensors over coastal regions and open oceans. Applied Optics 49, 5545–5560.

Ansper, A., Alikas, K., 2019. Retrieval of chlorophyll a from Sentinel-2 MSI data for the European Union water framework directive reporting purposes. Remote Sensing 11, 64. doi:`10.3390/rs11010064`.

Baban, S.M.J., 1996. Trophic classification and ecosystem checking of lakes using remotely sensed information. Hydrological Sciences Journal 41, 939–957. doi:`10.1080/02626669609491560`.

Babin, M., Stramski, D., Ferrari, G.M., Claustre, H., Bricaud, A., Obolensky, G., Hoepffner, N., 2003. Variations in the light absorption coefficients of phytoplankton, nonalgal particles, and dissolved organic matter in coastal waters around Europe. Journal of Geophysical Research: Oceans 108. doi:`10.1029/2001JC000882`.

Bailey, S.W., Franz, B.A., Werdell, P.J., 2010. Estimation of near-infrared water-leaving reflectance for satellite ocean color data processing. Optics Express 18, 7521–7527.

Barbier, E.B., Hacker, S.D., Kennedy, C., Koch, E.W., Stier, A.C., Silliman, B.R., 2011. The value of estuarine and coastal ecosystem services. Ecological Monographs 81, 169–193. doi:`10.1890/10-1510.1`.

Benedetti, A., Morcrette, J.J., Boucher, O., Dethof, A., Engelen, R., Fisher, M., Flentje, H., Huneeus, N., Jones, L., Kaiser, J., Kinne, S., Mangold, A., Razinger, M., Simmons, A.J., Suttie, M., 2009. Aerosol analysis and forecast in the European centre for medium-range weather forecasts integrated forecast system: 2. Data assimilation. Journal of Geophysical Research: Atmospheres 114. doi:`https://doi.org/10.1029/2008JD011235`.

Berk, A., Anderson, G.P., Acharya, P.K., Bernstein, L.S., Muratov, L., Lee, J., Fox, M., Adler-Golden, S.M., Chetwynd Jr., J.H., Hoke, M.L., Lockwood, R.B., Gardner, J.A., Cooley, T.W., Borel, C.C., Lewis, P.E., Shettle, E.P., 2006. MODTRAN5: 2006 update, in: Proceedings of SPIE 6233, Algorithms and Technologies for Multispectral, Hyperspectral, and Ultraspectral Imagery XII, International Society for Optics and Photonics. p. 62331F. doi:`10.1117/12.665077`.

Bodhaine, B.A., Wood, N.B., Dutton, E.G., Slusser, J.R., 1999. On Rayleigh optical depth calculations. Journal of Atmospheric and Oceanic Technology 16, 1854–1861. doi:`10.1175/1520-0426(1999)016<1854:ORODC>2.0.CO;2`.

Boyer, J.N., Kelble, C.R., Ortner, P.B., Rudnick, D.T., 2009. Phytoplankton bloom status: Chlorophyll *a* biomass as an indicator of water quality condition in the southern estuaries of Florida, USA. Ecological Indicators 9, S56–S67. doi:`10.1016/j.ecolind.2008.11.013`.

Brockmann, C., Doerffer, R., Peters, M., Stelzer, K., Embacher, S., Ruescas, A., 2016. Evolution of the C2RCC neural network for Sentinel 2 and 3 for the retrieval of ocean colour products in normal and extreme optically complex waters, in: Proceedings of the Living Planet Symposium, p. 54.

Buiteveld, H., Hakvoort, J., Donze, M., 1994. Optical properties of pure water, in: Ocean Optics XII, pp. 174–183. doi:`10.1117/12.190060`.

Bulgarelli, B., Zibordi, G., 2018. On the detectability of adjacency effects in ocean color remote sensing of mid-latitude coastal environments by SeaWiFS, MODIS-A, MERIS, OLCI, OLI and MSI. Remote Sensing of Environment 209, 423–438.

Carlson, R.E., 1977. A trophic state index for lakes 1. Limnology and Oceanography 22, 361–369. doi:`10.4319/lo.1977.22.2.0361`.

Carslaw, D.C., Ropkins, K., 2012. openair — an R package for air quality data analysis. Environmental Modelling & Software 27–28, 52–61. doi:`10.1016/j.envsoft.2011.09.008`.

Cesnulyte, V., Lindfors, A., Pitkänen, M., Lehtinen, K., Morcrette, J.J., Arola, A., 2014. Comparing ECMWF AOD with AERONET observations at visible and UV wavelengths. Atmospheric Chemistry & Physics 14, 593–608. doi:`10.5194/acp-14-593-2014`.

Chami, M., Lafrance, B., Fougnie, B., Chowdhary, J., Harmel, T., Waquet, F., 2015. OSOAA: a vector radiative transfer model of coupled atmosphere-ocean system for a rough sea surface application to the estimates of the directional variations of the water leaving reflectance to better process multi-angular satellite sensors data over the ocean. Optics Express 23, 27829–27852. doi:`10.1364/OE.23.027829`.

Chami, M., Santer, R., Dilligeard, E., 2001. Radiative transfer model for the computation of radiance and polarization in an ocean–atmosphere system: polarization properties of suspended matter for remote sensing. Applied Optics 40, 2398–2416. doi:`10.1364/AO.40.002398`.

Chen, J., Zhu, W., Tian, Y.Q., Yu, Q., Zheng, Y., Huang, L., 2017. Remote estimation of colored dissolved organic matter and chlorophyll-a in Lake Huron using Sentinel-2 measurements. Journal of Applied Remote Sensing 11, 036007. doi:`10.1117/1.JRS.11.036007`.

Costa, T.L., Araújo, M.P., Knoppers, B.A., Carreira, R.S., 2011. Sources and distribution of particulate organic matter of a tropical estuarine-lagoon system from NE Brazil as indicated by lipid biomarkers. Aquatic Geochemistry 17, 1–19. doi:`10.1007/s10498-010-9104-1`.

Courrat, A., Lobry, J., Nicolas, D., Laffargue, P., Amara, R., Lepage, M., Girardin, M., Le Pape, O., 2009. Anthropogenic disturbance on nursery function of estuarine areas for marine species. Estuarine, Coastal and Shelf Science 81, 179–190. doi:`10.1016/j.ecss.2008.10.017`.

Cui, T., Zhang, J., Wang, K., Wei, J., Mu, B., Ma, Y., Zhu, J., Liu, R., Chen, X., 2020. Remote sensing of chlorophyll *a* concentration in turbid coastal waters based on a global optical water classification system. ISPRS Journal of Photogrammetry and Remote Sensing 163, 187–201. doi:`10.1016/j.isprsjprs.2020.02.017`.

Dall'Olmo, G., Gitelson, A.A., Rundquist, D.C., 2003. Towards a unified approach for remote estimation of chlorophyll-a in both terrestrial vegetation and turbid productive waters. Geophysical Research Letters 30. doi:`10.1029/2003GL018065`.

Dall'Olmo, G., Gitelson, A.A., Rundquist, D.C., Leavitt, B., Barrow, T., Holz, J.C., 2005. Assessing the potential of SeaWiFS and MODIS for estimating chlorophyll concentration in turbid productive waters using red and near-infrared bands. Remote Sensing of Environment 96, 176–187.

doi:10.1016/j.rse.2005.02.007.

Dall'Olmo, G., Gitelson, A.A., 2005. Effect of bio-optical parameter variability on the remote estimation of chlorophyll-a concentration in turbid productive waters: experimental results. Applied Optics 44, 412–422. doi:10.1364/AO.44.000412.

De Keukelaere, L., Sterckx, S., Adriaensen, S., Knaeps, E., Reusen, I., Giardino, C., Bresciani, M., Hunter, P., Neil, C., Van der Zande, D., Vaiciute, D., 2018. Atmospheric correction of Landsat-8/OLI and Sentinel-2/MSI data using iCOR algorithm: validation for coastal and inland waters. European Journal of Remote Sensing 51, 525–542. doi:10.1080/22797254.2018.1457937.

Doerffer, R., Schiller, H., 2007. The MERIS Case 2 water algorithm. International Journal of Remote Sensing 28, 517–535. doi:10.1080/01431160600821127.

Doxani, G., Vermote, E., Roger, J.C., Gascon, F., Adriaensen, S., Frantz, D., Hagolle, O., Hollstein, A., Kirches, G., Li, F., et al., 2018. Atmospheric correction inter-comparison exercise. Remote Sensing 10, 352. doi:10.3390/rs10020352.

Elzhov, T.V., Mullen, K.M., Spiess, A.N., Bolker, B., 2016. minpack.lm: R Interface to the Levenberg-Marquardt Nonlinear Least-Squares Algorithm Found in MINPACK, Plus Support for Bounds. URL: https://CRAN.R-project.org/package=minpack.lm. r package version 1.2-1.

Emde, C., Buras-Schnell, R., Kylling, A., Mayer, B., Gasteiger, J., Hamann, U., Kylling, J., Richter, B., Pause, C., Dowling, T., Bugliaro, L., 2016. The libRadtran software package for radiative transfer calculations (version 2.0.1). Geoscientific Model Development 9, 1647–1672. doi:10.5194/gmd-9-1647-2016.

Gege, P., 2017. Radiative transfer theory for inland waters, in: Mishra, D.R., Ogashawara, I., Gitelson, A.A. (Eds.), Bio-optical Modeling and Remote Sensing of Inland Waters. Elsevier, pp. 25–67. doi:10.1016/B978-0-12-804644-9.00002-1.

Giardino, C., Brando, V., Gege, P., Pinnel, N., Hochberg, E., Knaeps, E., Reusen, I., Doerffer, R., Bresciani, M., Braga, F., Foerster, S., Champollion, N., Dekker, A., 2019. Imaging spectrometry of inland and coastal waters: state of the art, achievements and perspectives. Surveys in Geophysics 40, 401–429. doi:10.1007/s10712-018-9476-0.

Gitelson, A.A., Dall'Olmo, G., Moses, W., Rundquist, D.C., Barrow, T., Fisher, T.R., Gurlin, D., Holz, J., 2008. A simple semi-analytical model for remote estimation of chlorophyll-a in turbid waters: Validation. Remote Sensing of Environment 112, 3582–3593. doi:10.1016/j.rse.2008.04.015.

Gitelson, A.A., Gritz, Y., Merzlyak, M.N., 2003. Relationships between leaf chlorophyll content and spectral reflectance and algorithms for non-destructive chlorophyll assessment in higher plant leaves. Journal of Plant Physiology 160, 271–282.

Gitelson, A.A., Kondratyev, K.Y., 1991. Optical models of mesotrophic and eutrophic water bodies. International Journal of Remote Sensing 12, 373–385. doi:10.1080/01431169108929659.

Gons, H.J., Auer, M.T., Effler, S.W., 2008. Meris satellite chlorophyll mapping of oligotrophic and eutrophic waters in the Laurentian Great Lakes. Remote Sensing of Environment 112, 4098–4106. doi:10.1016/j.rse.2007.06.029.

Gons, H.J., Rijkeboer, M., Ruddick, K.G., 2002. A chlorophyll-retrieval algorithm for satellite imagery (Medium Resolution Imaging Spectrometer) of inland and coastal waters. Journal of Plankton Research 24, 947–951. doi:10.1093/plankt/24.9.947.

Gons, H.J., Rijkeboer, M., Ruddick, K.G., 2005. Effect of a waveband shift on chlorophyll retrieval from MERIS imagery of inland and coastal waters. Journal of Plankton research 27, 125–127. doi:10.1093/plankt/fbh151.

Gordon, H.R., Brown, J.W., Evans, R.H., 1988. Exact Rayleigh scattering calculations for use with the Nimbus-7 coastal zone color scanner. Applied Optics 27, 862–871. doi:10.1364/AO.27.000862.

Gordon, H.R., Wang, M., 1994. Retrieval of water-leaving radiance and aerosol optical thickness over the oceans with SeaWiFS: a preliminary algorithm. Applied Optics 33, 443–452.

Guanter, L., Alonso, L., Moreno, J., 2005. A method for the surface reflectance retrieval from PROBA/CHRIS data over land: application to ESA SPARC campaigns. IEEE Transactions on Geoscience and Remote Sensing 43, 2908–2917. doi:10.1109/TGRS.2005.857915.

Gurlin, D., Gitelson, A.A., Moses, W.J., 2011. Remote estimation of chl-a concentration in turbid productive waters — return to a simple two-band NIR-red model? Remote Sensing of Environment 115, 3479–3490. doi:10.1016/j.rse.2011.08.011.

Harmel, T., Chami, M., 2013. Estimation of the sunglint radiance field from optical satellite imagery over open ocean: Multidirectional approach and polarization aspects. Journal of Geophysical Research: Oceans 118, 76–90. doi:10.1029/2012JC008221.

Harmel, T., Chami, M., Tormos, T., Reynaud, N., Danis, P.A., 2018. Sunglint correction of the Multi-Spectral Instrument (MSI)-SENTINEL-2 imagery over inland and sea waters from SWIR bands. Remote Sensing of Environment 204, 308–321. doi:`10.1016/j.rse.2017.10.022`.

Huang, C., Zou, J., Li, Y., Yang, H., Shi, K., Li, J., Wang, Y., Chena, X., Zheng, F., 2014. Assessment of NIR-red algorithms for observation of chlorophyll-a in highly turbid inland waters in China. ISPRS Journal of Photogrammetry and Remote Sensing 93, 29–39. doi:`10.1016/j.isprsjprs.2014.03.012`.

Ilori, C.O., Pahlevan, N., Knudby, A., 2019. Analyzing performances of different atmospheric correction techniques for Landsat 8: application for coastal remote sensing. Remote Sensing 11, 469. doi:`doi:10.3390/rs11040469`.

Jamet, C., Loisel, H., Kuchinke, C.P., Ruddick, K., Zibordi, G., Feng, H., 2011. Comparison of three SeaWiFS atmospheric correction algorithms for turbid waters using AERONET-OC measurements. Remote Sensing of Environment 115, 1955–1965. doi:`10.1016/j.rse.2011.03.018`.

Kaufman, Y.J., 1984. Atmospheric effect on spatial resolution of surface imagery. Applied Optics 23, 3400–3408. doi:`10.1364/AO.23.003400`.

Kaufman, Y.J., Sendra, C., 1988. Algorithm for automatic atmospheric corrections to visible and near-IR satellite imagery. International Journal of Remote Sensing 9, 1357–1381. doi:`10.1080/01431168808954942`.

Kotchenova, S.Y., Vermote, E.F., Matarrese, R., Klemm Jr, F.J., 2006. Validation of a vector version of the 6S radiative transfer code for atmospheric correction of satellite data. part I: Path radiance. Applied Optics 45, 6762–6774. doi:`10.1364/AO.45.006762`.

Kutser, T., 2012. The possibility of using the Landsat image archive for monitoring long time trends in coloured dissolved organic matter concentration in lake waters. Remote Sensing of Environment 123, 334–338. doi:`10.1016/j.rse.2012.04.004`.

Kutser, T., Paavel, B., Verpoorter, C., Ligi, M., Soomets, T., Toming, K., Casal, G., 2016. Remote sensing of black lakes and using 810 nm reflectance peak for retrieving water quality parameters of optically complex waters. Remote Sensing 8, 497. doi:`10.3390/rs8060497`.

Le, C., Li, Y., Zha, Y., Sun, D., Huang, C., Lu, H., 2009. A four-band semi-analytical model for estimating chlorophyll-a in highly turbid lakes: The case of Taihu Lake, China. Remote Sensing of Environment 113, 1175–1182. doi:`10.1016/j.rse.2009.02.005`.

Lenoble, J., Herman, M., Deuzé, J., Lafrance, B., Santer, R., Tanré, D., 2007. A successive order of scattering code for solving the vector equation of transfer in the earth's atmosphere with aerosols. Journal of Quantitative Spectroscopy and Radiative Transfer 107, 479–507. doi:`10.1016/j.jqsrt.2007.03.010`.

Levy, R.C., Remer, L.A., Tanré, D., Mattoo, S., Kaufman, Y.J., 2009. Algorithm for remote sensing of tropospheric aerosol over dark targets from MODIS: Collections 005 and 051: Revision 2; feb 2009. MODIS algorithm theoretical basis document URL: `http//modisatmos.gsfc.nasa.gov/_docs/ATBD_MOD04_C005_rev2.pdf`.

Lins, R.C., Martinez, J.M., Motta-Marques, D., Cirilo, J.A., Fragoso Jr., C.R., 2017. Assessment of chlorophyll-a remote sensing algorithms in a productive tropical estuarine-lagoon system. Remote Sensing 9, 516. doi:`10.3390/rs9060516`.

Lins, R.C., Martinez, J.M., Motta-Marques, D., Cirilo, J.A., Medeiros, P.R.P., Fragoso Jr, C.R., 2018. A multivariate analysis framework to detect key environmental factors affecting spatiotemporal variability of chlorophyll-a in a tropical productive estuarine-lagoon system. Remote Sensing 10, 853. doi:`10.3390/rs10060853`.

Liu, H., Zhou, Q., Li, Q., Hu, S., Shi, T., Wu, G., 2019. Determining switching threshold for NIR-SWIR combined atmospheric correction algorithm of ocean color remote sensing. ISPRS Journal of Photogrammetry and Remote Sensing 153, 59–73. doi:`10.1016/j.isprsjprs.2019.04.013`.

Maciel, D., Novo, E., Sander Carvalho, L.S., Barbosa, C., Flores Júnior, R., Lobo, F.L., 2019. Retrieving total and inorganic suspended sediments in Amazon floodplain lakes: a multisensor approach. Remote Sensing 11, 1744. doi:`10.3390/rs11151744`.

Martins, V., Barbosa, C., Carvalho, L., Jorge, D., Lobo, F., Novo, E., 2017. Assessment of atmospheric correction methods for Sentinel-2 MSI images applied to Amazon floodplain lakes. Remote Sensing 9, 322. doi:`10.3390/rs9040322`.

Matthews, M.W., 2017. Bio-optical modeling of phytoplankton chlorophyll-*a*, in: Mishra, D.R., Ogashawara, I., Gitelson, A.A. (Eds.), Bio-optical Modeling and Remote Sensing of Inland Waters. Elsevier, pp. 157–188. doi:`10.1016/B978-0-12-804644-9.00006-9`.

Mayer, B., Kylling, A., 2005. The libRadtran software package for radiative transfer calculations – description and examples of use. Atmospheric Chemistry and Physics 5, 1855–1877. doi:`10.5194/acp-5-1855-2005`.

Melo-Magalhães, E., Medeiros, P., Lira, M., Koening, M., Moura, A., 2009. Determination of eutrophic areas in Mundaú/Manguaba lagoons, Alagoas-Brazil, through studies of the phytoplanktonic community. Brazilian Journal of Biology 69, 271–280. doi:`10.1590/`

S1519-69842009000200006.

Mishra, S., Mishra, D.R., 2012. Normalized difference chlorophyll index: A novel model for remote estimation of chlorophyll-a concentration in turbid productive waters. Remote Sensing of Environment 117, 394–406. doi:`10.1016/j.rse.2011.10.016`.

Mishra, S., Mishra, D.R., Lee, Z., Tucker, C.S., 2013. Quantifying cyanobacterial phycocyanin concentration in turbid productive waters: A quasi-analytical approach. Remote Sensing of Environment 133, 141–151. doi:`10.1016/j.rse.2013.02.004`.

Mitchell, S.B., Jennerjahn, T.C., Vizzini, S., Zhang, W., 2015. Changes to processes in estuaries and coastal waters due to intense multiple pressures–an introduction and synthesis. Estuarine, Coastal and Shelf Science 156, 1–6. doi:`10.1016/j.ecss.2014.12.027`.

Mobley, C.D., 1994. Light and water: radiative transfer in natural waters. Academic Press.

Mobley, C.D., 1999. Estimation of the remote-sensing reflectance from above-surface measurements. Applied Optics 38, 7442–7455. doi:`10.1364/AO.38.007442`.

Mobley, C.D., Werdell, J., Franz, B., Ahmad, Z., Bailey, S., 2016. Atmospheric correction for satellite ocean color radiometry. Technical Report. NASA Goddard Space Flight Center, Greenbelt, MD United States.

Molkov, A.A., Fedorov, S.V., Pelevin, V.V., Korchemkina, E.N., 2019. Regional models for high-resolution retrieval of chlorophyll a and TSM concentrations in the Gorky Reservoir by Sentinel-2 imagery. Remote Sensing 11, 1215. doi:`10.3390/rs11101215`.

Morcrette, J.J., Boucher, O., Jones, L., Salmond, D., Bechtold, P., Beljaars, A., Benedetti, A., Bonet, A., Kaiser, J., Razinger, M., Schulz, M., Serrar, S., Simmons, A.J., Sofiev, M., Suttie, M., Tompkins, A.M., Untch, A., 2009. Aerosol analysis and forecast in the European centre for medium-range weather forecasts integrated forecast system: Forward modeling. Journal of Geophysical Research: Atmospheres 114. doi:`10.1029/2008JD011235`.

Moses, W.J., Gitelson, A.A., Berdnikov, S., Povazhnyy, V., 2009. Satellite estimation of chlorophyll-a concentration using the red and NIR bands of MERIS—the Azov sea case study. IEEE Geoscience and Remote Sensing Letters 6, 845–849. doi:`10.1109/LGRS.2009.2026657`.

Moses, W.J., Sterckx, S., Montes, M.J., De Keukelaere, L., Knaeps, E., 2017. Atmospheric correction for inland waters, in: Mishra, D.R., Ogashawara, I., Gitelson, A.A. (Eds.), Bio-optical Modeling and Remote Sensing of Inland Waters. Elsevier, pp. 69–100. doi:`10.1016/B978-0-12-804644-9.00003-3`.

Mouw, C.B., Greb, S., Aurin, D., DiGiacomo, P.M., Lee, Z., Twardowski, M., Binding, C., Hu, C., Ma, R., Moore, T., Moses, W., Craig, S.E., 2015. Aquatic color radiometry remote sensing of coastal and inland waters: Challenges and recommendations for future satellite missions. Remote Sensing of Environment 160, 15–30. doi:`10.1016/j.rse.2015.02.001`.

Mueller, J.L., Davis, C., Arnone, R., Frouin, R., Carder, K., Lee, Z., Steward, R., Hooker, S., Mobley, C.D., McLean, S., 2003. Above-water radiance and remote sensing reflectance measurements and analysis protocols, in: Mueller, J.L., Fargion, G.S. (Eds.), Ocean Optics Protocols for Satellite Ocean Color Sensor Validation Revision 4. Goddard Space Flight Space Center: Greenbelt, MD, USA, pp. 21–31.

Müller-Wilm, U., Devignot, O., L, P., 2016. Sen2Cor Configuration and User Manual. Technical Report. S2-PDGS-MPC-L2ASUM-V2.5.5, Telespazio VEGA Deutschland GmbH: Darmstadt, Germany.

Nechad, B., Ruddick, K.G., Schroeder, T.A., Oubelkheir, K., Blondeau-Patissier, D., Cherukuru, N.R.C., Brando, V.E., Dekker, A.G., Clementson, L.A., Banks, A.C., Maritorena, S., Werdell, P.J., Sá, C., Brotas, V., Caballero De Frutos, I., Ahn, Y.H., Salama, S., Tilstone, G.H., Martínez-Vicente, V., Foley, D., McKibben, M., Nahorniak, J.S., Peterson, T.D., Siliό-Calzada, A., Röttgers, R., Lee, Z., Peters, M., Brockmann, C.W., 2015. CoastColour Round Robin data sets: a database to evaluate the performance of algorithms for the retrieval of water quality parameters in coastal waters. Earth System Science Data Discussions 8, 173–258. URL: `http://hdl.handle.net/10902/7934`.

Neil, C., Spyrakos, E., Hunter, P., Tyler, A., 2020. Corrigendum to "A global approach for chlorophyll-a retrieval across optically complex inland waters based on optical water types" [Remote Sens. Environ., 229: 159–178]. Remote Sensing of Environment 246, 111837.

Neil, C., Spyrakos, E., Hunter, P.D., Tyler, A.N., 2019. A global approach for chlorophyll-a retrieval across optically complex inland waters based on optical water types. Remote Sensing of Environment 229, 159–178. doi:`10.1016/j.rse.2019.04.027`.

Oliveira, A.M., Kjerfve, B., 1993. Environmental responses of a tropical coastal lagoon system to hydrological variability: Mundaú-Manguaba, Brazil. Estuarine, Coastal and Shelf Science 37, 575–591. doi:`10.1006/ecss.1993.1074`.

O'Reilly, J.E., Maritorena, S., Mitchell, B.G., Siegel, D.A., Carder, K.L., Garver, S.A., Kahru, M., McClain, C., 1998. Ocean color chlorophyll algorithms for SeaWiFS. Journal of Geophysical Research: Oceans 103, 24937–24953. doi:`10.1029/98JC02160`.

O'Reilly, J.E., Werdell, P.J., 2019. Chlorophyll algorithms for ocean color sensors-OC4, OC5 & OC6. Remote Sensing of Environment 229, 32–47.

Orive, E., Elliott, M., de Jonge, V., 2002. Nutrients and eutrophication in estuaries and coastal waters. Springer Netherlands.

O'Reilly, J.E., Maritorena, S., O'Brien, M., Siegel, D., Toole, D., Menzies, D., Smith, R., Mueller, J., Mitchell, B.G., Kahru, M., et al., 2000. SeaWiFS postlaunch calibration and validation analyses, part 3. NASA Technical Memo 206892, 3–8.

Pahlevan, N., Sarkar, S., Franz, B., Balasubramanian, S., He, J., 2017a. Sentinel-2 MultiSpectral Instrument (MSI) data processing for aquatic science applications: Demonstrations and validations. Remote Sensing of Environment 201, 47–56.

Pahlevan, N., Schott, J.R., Franz, B.A., Zibordi, G., Markham, B., Bailey, S., Schaaf, C.B., Ondrusek, M., Greb, S., Strait, C.M., 2017b. Landsat 8 remote sensing reflectance (Rrs) products: Evaluations, intercomparisons, and enhancements. Remote Sensing of Environment 190, 289–301.

Pahlevan, N., Smith, B., Schalles, J., Binding, C., Cao, Z., Ma, R., Alikas, K., Kangro, K., Gurlin, D., Hà, N., Matsushita, B., Moses, W., Greb, S., Lehmann, M.K., Ondrusek, M., Oppelt, N., Stumpf, R., 2020. Seamless retrievals of chlorophyll-a from Sentinel-2 (MSI) and Sentinel-3 (OLCI) in inland and coastal waters: A machine-learning approach. Remote Sensing of Environment , 111604.

Pereira-Sandoval, M., Ruescas, A., Urrego, P., Ruiz-Verdú, A., Delegido, J., Tenjo, C., Soria-Perpinyà, X., Vicente, E., Soria, J., Moreno, J., 2019. Evaluation of atmospheric correction algorithms over Spanish inland waters for Sentinel-2 Multi Spectral Imagery data. Remote Sensing 11, 1469. doi:`10.3390/rs11121469`.

R Core Team, 2020. R: A Language and Environment for Statistical Computing. R Foundation for Statistical Computing. Vienna, Austria. URL: `https://www.R-project.org/`.

Rahman, H., Dedieu, G., 1994. SMAC: a simplified method for the atmospheric correction of satellite measurements in the solar spectrum. International Journal of Remote Sensing 15, 123–143. doi:`10.1080/01431169408954055`.

Rice, E., Baird, R., Eaton, A., Clesceri, L., 2005. Standard methods for the examination of water and wastewater. American Public Health Association: Washington, DC, USA.

Schläpfer, D., Borel, C.C., Keller, J., Itten, K.I., 1998. Atmospheric precorrected differential absorption technique to retrieve columnar water vapor. Remote Sensing of Environment 65, 353–366. doi:`10.1016/S0034-4257(98)00044-3`.

Spyrakos, E., O'Donnell, R., Hunter, P.D., Miller, C., Scott, M., Simis, S.G., Neil, C., Barbosa, C.C., Binding, C.E., Bradt, S., Bresciani, M., Dall'Olmo, G., Giardino, C., Gitelson, A.A., Kutser, T., Li, L., Matsushita, B., Martinez-Vicente, V., Matthew, M.W., Ogashawara, I., Ruiz-Verdú, A., Schalles, J.F., Tebbs, E., Zhang, Y., Tyler, A.N., 2018. Optical types of inland and coastal waters. Limnology and Oceanography 63, 846–870. doi:`10.1002/lno.10674`.

Sterckx, S., Knaeps, E., Ruddick, K., 2011. Detection and correction of adjacency effects in hyperspectral airborne data of coastal and inland waters: the use of the near infrared similarity spectrum. International Journal of Remote Sensing 32, 6479–6505. doi:`10.1080/01431161.2010.512930`.

Sterckx, S., Knaeps, S., Kratzer, S., Ruddick, K., 2015. SIMilarity Environment Correction (SIMEC) applied to MERIS data over inland and coastal waters. Remote Sensing of Environment 157, 96–110. doi:`10.1016/j.rse.2014.06.017`.

Vanhellemont, Q., 2019. Adaptation of the dark spectrum fitting atmospheric correction for aquatic applications of the Landsat and Sentinel-2 archives. Remote Sensing of Environment 225, 175–192. doi:`10.1016/j.rse.2019.03.010`.

Vanhellemont, Q., Ruddick, K., 2014. Turbid wakes associated with offshore wind turbines observed with Landsat 8. Remote Sensing of Environment 145, 105–115. doi:`10.1016/j.rse.2014.01.009`.

Vanhellemont, Q., Ruddick, K., 2015. Advantages of high quality SWIR bands for ocean colour processing: Examples from Landsat-8. Remote Sensing of Environment 161, 89–106. doi:`10.1016/j.rse.2015.02.007`.

Vanhellemont, Q., Ruddick, K., 2016. Acolite for Sentinel-2: Aquatic applications of MSI imagery, in: Proceedings of the 2016 ESA Living Planet Symposium, Prague, Czech Republic, pp. 9–13.

Vanhellemont, Q., Ruddick, K., 2018. Atmospheric correction of metre-scale optical satellite data for inland and coastal water applications. Remote Sensing of Environment 216, 586–597. doi:`10.1016/j.rse.2018.07.015`.

Wang, M., Gordon, H.R., 1994. Radiance reflected from the ocean–atmosphere system: synthesis from individual components of the aerosol size distribution. Applied Optics 33, 7088–7095. doi:`10.1364/AO.33.007088`.

Wang, M., Shi, W., 2007. The NIR-SWIR combined atmospheric correction approach for MODIS ocean color data processing. Optics Express 15, 15722–15733.

Wang, M., Son, S., Shi, W., 2009. Evaluation of MODIS SWIR and NIR-SWIR atmospheric correction algorithms using SeaBASS data. Remote Sensing of Environment 113, 635–644. doi:`10.1016/j.rse.2008.11.005`.

Warren, M.A., Simis, S.G., Martinez-Vicente, V., Poser, K., Bresciani, M., Alikas, K., Spyrakos, E., Giardino, C., Ansper, A., 2019. Assessment of atmospheric correction algorithms for the Sentinel-2A MultiSpectral Imager over coastal and inland waters. Remote Sensing of Environment 225, 267–289. doi:`10.1016/j.rse.2019.03.018`.

Watanabe, F., Alcantara, E., Rodrigues, T., Rotta, L., Bernardo, N., Imai, N., 2018. Remote sensing of the chlorophyll-a based on OLI/Landsat-8 and MSI/Sentinel-2a (Barra Bonita reservoir, Brazil). Anais da Academia Brasileira de Ciências 90, 1987–2000. doi:`10.1590/0001-3765201720170125`.

Werdell, P.J., Bailey, S.W., 2005. An improved in-situ bio-optical data set for ocean color algorithm development and satellite data product validation. Remote Sensing of Environment 98, 122–140. doi:`10.1016/j.rse.2005.07.001`.

Yang, H., Gordon, H.R., 1997. Remote sensing of ocean color: assessment of water-leaving radiance bidirectional effects on atmospheric diffuse transmittance. Applied Optics 36, 7887–7897.

Yang, W., Matsushita, B., Chen, J., Fukushima, T., Ma, R., 2010. An enhanced three-band index for estimating chlorophyll-a in turbid case-II waters: case studies of Lake Kasumigaura, Japan, and Lake Dianchi, China. IEEE Geoscience and Remote Sensing Letters 7, 655–659. doi:`10.1109/LGRS.2010.2044364`.

Capítulo 4

Avaliação da dinâmica a curto-prazo do fitoplâncton em um antropisado sistema estuarino-lagunar eutrófico tropical utilizando série temporal do Sentinel-2 MSI

Matheus Henrique Tavares

Artigo a ser submetido.

Assessment of short-term phytoplankton dynamics in an anthropised eutrophic tropical estuarine-lagoon system using Sentinel-2 MSI time series

Matheus Henrique Tavares[a,*], David Motta-Marques[a], Carlos Ruberto Fragoso Jr.[b], Regina Camara Lins[b]

[a] *Instituto de Pesquisas Hidráulicas, Universidade Federal do Rio Grande do Sul, 91501-970 Porto Alegre, Brazil*
[b] *Centro de Tecnologia, Universidade Federal de Alagoas, 57072–970 Maceió, Brazil*

Abstract

Estuarine systems are complex transitional zones between the continent and the ocean. They can be very productive, harbouring high biodiversity and providing essential ecosystem services such as fisheries, habitat provision, and sediment retention. These systems generally exhibit spatial variability and distribution of organisms influenced by a salinity gradient, and seasonal river inflow and nutrient discharge, but for being at the end of the watershed and commonly associated with socioeconomic development in its surroundings, can be heavily impacted by anthropogenic activities, which in turn can undermine their ecological status and ecosystem services provision. In this study, we assessed the spatiotemporal patterns of chlorophyll-*a* (chla) in a heavily anthropised system using a validated Sentinel-2 MSI-derived time series. We also used a remote sensing-derived series of the absorption coefficient of coloured dissolved organic matter (aCDOM) to explore the chla-CDOM relationship and evaluated the impact of environmental forcings on chla. The results showed that Manguaba is more eutrophic than Mundaú and has a less defined variation throughout the year, mostly due the nutrient influx from the basin due to sugarcane crops. Mundaú shows a more defined pattern and pronounced variation along the year, affected by the sugarcane crop cycle and precipitation. The chla maps showed the impact of the river inflows on the system, typically decreasing chla due to light limitation, as well as the point sources of pollution, which increased chla during the wet season. A clustering technique divided the two lagoons into four homogeneous spatial groups, where in Mundaú they show a distinct longitudinal gradient of chla, while in Manguaba the gradient showed an increase of chla from the extremities to the centre of the lagoon. This most productive cluster, at the centre of the lagoon, included areas of recirculation, highlighting the importance of hydrodynamics and water residence times in this system. A canonical correspondence analysis determined each cluster's most important drivers of chla. The short-term analysis also allowed for assessing the relative importance of the tides on the system. Our results point to a further degradation of the water quality in the system, with possible increase in algal bloom and fish kill events reported near Manguaba lagoon.

Keywords: Chlorophyll-*a* (chla), Sentinel-2 MSI, Turbid productive waters, Coloured dissolved organic matter, Water quality

---

[*] Correspondence author.
Email address: `tavaresmatheush@gmail.com` (Matheus Henrique Tavares)

Manuscript to be submitted to Environmental Monitoring and Assessment *March 27, 2023*

1. Introduction

Estuarine systems are complex transitional zones between the continent and the ocean. Due to their unique characteristics, they can be very productive, harbouring high biodiversity and providing essential ecosystem services such as fisheries, habitat provision, and sediment retention (Barbier et al., 2011). These systems generally exhibit spatial variability and distribution of organisms influenced by environmental factors, mainly a variable salinity gradient and seasonal river inflow and nutrient discharge, which are also associated with the hydrodynamics of the water body (Mitchell et al., 2015). However, for being at the end of the watershed and commonly associated with socioeconomic development in its surroundings, these ecosystems can be impacted by anthropogenic activities such as increased nutrient discharge, pollution, and unrestrained fishing, which in turn can undermine their ecological status and ecosystem services provision (*e.g.*, Courrat et al., 2009). This, associated with the limited water exchange and high retention times, can enhance the harmful effects of these activities, resulting in increased water turbidity, algal blooms, and fish kills (Orive et al., 2002).

Monitoring of chlorophyll-*a* (*chla*), a phytoplankton biomass indicator, has been frequently used to evaluate the trophic state of inland and coastal waters due to their sensitivity and quick response to multiple environmental factors (Carlson, 1977; Baban, 1996; Boyer et al., 2009), and remote sensing of *chla* has been widely used to complement this monitoring (Gitelson and Kondratyev, 1991; Matthews, 2017; Giardino et al., 2019). The recently launched constellation of satellites Sentinel-2A and B, carrying the Multispectral Instrument (MSI), provided the suite of resolutions (spatial, temporal, spectral and radiometric) able to monitor many limnological variables to better comprehend the effects of watershed inputs into smaller waterbodies with high spatial (10 to 20 m) and temporal (repeat cycle of 5 days) resolutions (Pahlevan et al., 2017). Despite the limited variables that can be estimated via remote sensing, it is a very powerful tool, especially in poorer regions with limited financial and human resources to monitor degraded aquatic ecosystems, and compared with other satellite-bourne sensors, Sentinel-2 provides more spatially detailed observations that allows for better comprehension of spatial variability of limnological parameters.

One of the optically active constituents, which can be mapped via remote sensing, is coloured dissolved organic matter (CDOM), the organic matter that interacts with light. Research has shown that it is an important driver of productivity with a non-linear relationship with primary production, which in larger concentrations the effects of nutrient input (positive relationship) are superseded by light limitation (negative relationship) (Kelly et al., 2018; Olson et al., 2020). In addition, changes in the watershed, along with climate change and eutrophication of the waterbodies, resulted in generally increased inputs of CDOM to receiving aquatic ecosystems, directly affecting the nutrient content and light absorption of DOM, altering the structure and function of these systems (Zhang et al., 2020). The different stoichiometric ratios of nutrients in the DOM (Olson et al., 2020) can, for example, influence the occurrence of cyanobacterial blooms, which can further degrade water quality (Fulweiler and Nixon, 2012; Amorim and Moura, 2021).

In this study, we used satellite-derived chla data and the effects of CDOM, also derived from satellite, to assess the drivers of short-term phytoplankton dynamics and environmental forcings over an anthropised eutrophic tropical estuarine-lagoon system for the period between 2016 and 2021, to better understand the spatiotemporal functioning of the system with high-to-moderate resolution satellite data.

2. Methodology

2.1. Study area

The study area is the Mundaú-Manguaba Estuarine-Lagoon System (MMELS), a shallow (maximum depth of 3.5 m) tropical lagoon system located in the metropolitan area of Maceió, state of Alagoas, northeastern Brazil, between 9°35' S and 9°46' S latitude and 35°34' W and 35°58' W longitude (Figure 1). The MMELS is composed of two lagoons, the Mundaú lagoon (surface area of 27 km^2), located in the Northeastern part of the system, which receives freshwater mainly from the Mundaú river basin (surface area of 4127 km^2, annual average discharge of 35 m^3/s); and the Manguaba lagoon (surface area of 42 km^2), which is located in the Southwestern part of the system and receives freshwater from two basins, the Paraíba do Meio (surface area of 3145 km^2, annual average discharge of 25 m^3/s) and the Sumaúma (surface area of 404 km^2, annual average discharge of 3 m^3/s) river basins. The tides are semidiurnal, with an average amplitude of $\sim$1.45 m, but the direct influence of the tides in this choked lagoon system is small due to the complex system of channels connecting the lagoons to the ocean (Brito Jr et al., 2018). The MMELS exhibits a tropical semi-humid climate, while the most inward areas of its basin are semi-arid, with the whole basin showing well-defined wet (from May to July) and dry (from October to December) seasons. Over MMELS, temperature varies little throughout the year, with an average annual mean temperature of 25°C, mean precipitation of $\sim$1700 mm per year, and the winds blow predominantly from a southeasterly direction.

The margins of Mundaú lagoon are mainly occupied by the urban area of Maceió city (Figure 1) and other small urban areas, and coconut and sugarcane crops, while the margins of Manguaba lagoon are intensively used for agriculture (mainly sugarcane crops), grassland, and vegetation fragments (forest and mangrove areas). A substantial part of the large areas used for agriculture, particularly the Sumaúma river basin, are covered by sugarcane crops that withdraw water from the rivers to wash the sugarcane stalks. Most producers do not treat the effluents, which are carried to the rivers with added fructose (high biochemical oxygen demand and nutrients), and are a major source of pollutants and nutrients for the lagoons, especially Manguaba lagoon (Oliveira and Kjerfve, 1993). Additional sources of nutrient loading and organic matter deposit into the lagoons are untreated sewage from the urban areas, industrial effluents, and other untreated effluents (mainly from agriculture) from the Mundaú and Paraíba do Meio river basins. As a result, both lagoons are characterised by eutrophic conditions and dominated by phytoplankton (Melo-Magalhães et al., 2009; Lins et al., 2018), with frequent algal blooms that can cause water anoxia and reported fish kill events. Figure 2 shows point sources of sanitary and industrial effluents mapped by Luz et al. (2022) according to the Maceió Sanitation Plan and high-resolution satellite imagery.

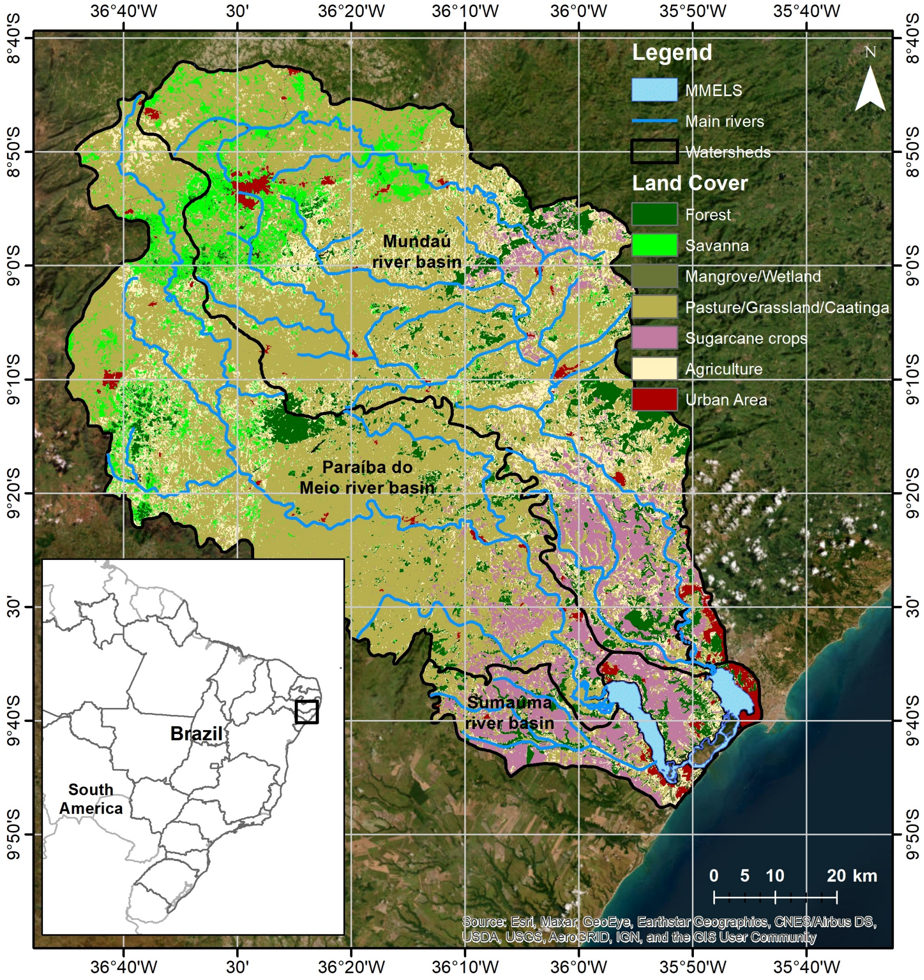

Figure 1: Location map showing the MMELS watershed, land cover, and main hydrography. Source: Agência Nacional de Águas, MapBiomas (Souza Jr et al., 2020).

Although they are connected, the lagoons have distinct characteristics, as described in Lins et al. (2017). Both lagoons are characterised by eutrophic conditions and are dominated by phytoplankton, but Manguaba lagoon is larger, has a much higher retention time, and is less affected by the tides, which makes it generally less saline than Mundaú lagoon. Additionally, the water flow between the lagoons through the connecting channel system is small, which creates different conditions of nutrients and hydrodynamics in each lagoon due to their different geometries and tributary rivers. Regarding the water constituents, Manguaba lagoon has higher chlorophyll-*a* concentration and lower total suspended solids (TSS) concentration (Lins et al., 2017). Furthermore, despite being shallow, the high turbidity observed in both lagoons, with Secchi disk values ranging between 0.58 and 0.95 m, implies that bottom sediment has little or no effect on water reflectance as the photic zone depth is lower than water depth in MMELS, and only the shallower part of Mundaú lagoon (northeastern-most margin) was removed from processing due to possible bottom effects on water

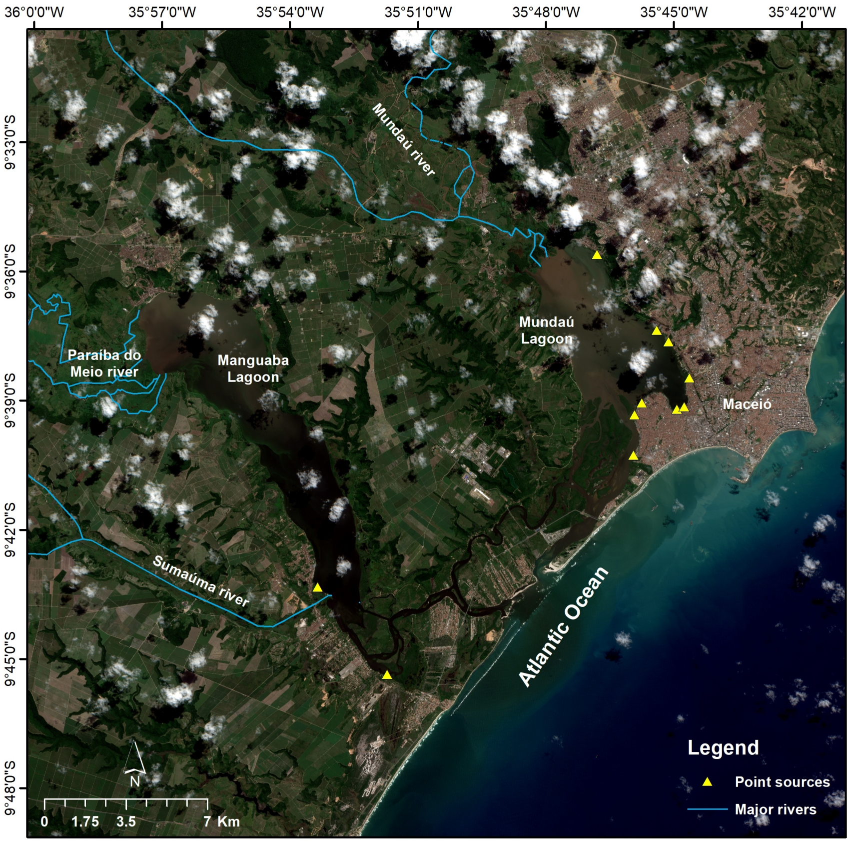

Figure 2: Sentinel-2 MSI image from 05/23/2018 showing the MMELS, the main tributary rivers, and point sources of sanitary and industrial effluents (Luz et al., 2022).

reflectance.

2.2. *Sentinel-2 MSI imagery processing*

The Multispectral Instrument (MSI) is a high-to-moderate-resolution, multi-spectral imaging sensor aboard two satellites, the Sentinel-2A (S2A) and Sentinel-2B (S2B) satellites, launched by the European Space Agency (ESA) on June 23, 2015 and March 7, 2017, respectively. The satellites have a revisit time of 10 days, and the sensor samples 13 spectral bands, ranging from the visible to the shortwave infrared (SWIR) bands, with 10 m to 60 m spatial resolution. The Sentinel-2 mission, along with Landsat 8 OLI (Operational Land Imager), has provided high-quality aquatic science products over continental waters, with spatial, temporal, and spectral resolutions that considerably enhanced the applications of remote sensing to inland waters (Pahlevan et al., 2017).

In this study, atmospheric and sunglint-corrected Sentinel-2 MSI imagery was processed using a combination of ACOLITE (Atmospheric Correction for OLI "lite") and GRS (Glint Removal for Sentinel-2), as previously validated (Tavares et al., 2021), to derive chlorophyll-a concentration and coloured dissolved organic matter absorption coefficient (aCDOM) at 400 nm for the Mundaú-Manguaba Estuarine-Lagoon System from 2016 to 2021 using algorithms that were previously validated (Tavares et al., 2021; Lima Filho et al., 2022).

The ACOLITE processor was applied to correct for atmospheric effects using the *dark spectrum fitting* (DSF) proposed by Vanhellemont and Ruddick (2018), and GRS (Harmel et al., 2018; Vanhellemont, 2019) was used to correct for the sunglint signal (reflection of the sun disc on the water). A brief description of the processes, challenges, and uncertainties regarding atmospheric correction (AC) of Sentinel-2 MSI imagery over MMELS and the validation of the AC processors in this site are described in Tavares et al. (2021).

The sentinel-2 MSI images were downloaded using the Python package *sentinelsat* (Valgur et al., 2019), processed using the Python package for ACOLITE, and then post-processed in *R* (R Core Team, 2021). In total, 142 images were processed for the region (36 in the wet season and 62 in the dry season); the mean cloud cover was around ∼ 50% for each lagoon, so a maximum cloud cover of 75% was defined. For cloud and cloud shadow screening, we tested FMask (version 4.5) (Qiu et al., 2019) and Sen2Cor (version 2.5.5) (Müller-Wilm et al., 2016), but both showed unsatisfactory results; for this reason, a pre-processing was run using a combination of MNDWI (Xu, 2006) and thresholds for bands 1 (443 nm, aerosols), 3 (560 nm, green) and 5 (705 nm, red-edge), and then the remaining clouds and cloud shadows were removed manually.

To process the imagery, all bands were upscaled to 60 m (20 m bands aggregated to 3 × 3 pixels and 10 m bands aggregated to 6 × 6 pixels) to reduce noise in the remote sensing data. All processing was carried out in the *R* environment (R Core Team, 2021) with package *terra* (Hijmans, 2021).

2.3. Water quality algorithms

To retrieve *chla*, the semi-analytical NIR-red ratio algorithm (Gons et al., 2002, 2005) was employed, as previously validated in Tavares et al. (2021) ($n = 49$, $r^2 = 0.78$, RMSE = 36.2 mg m^{-3}). In this algorithm, chla is estimated based on water absorption and backscattering. It assumes that the absorption in the red-edge spectrum is dominated by water, and in the red spectrum it is due to chla and water combined. The backscattering coefficient is assumed to be wavelength-independent and is calculated from radiance in the NIR region as:

$$b_b = 1.61 \times \frac{\pi R_{rs}(783)}{0.082 - 0.6\pi R_{rs}(783)} \tag{1}$$

and *chla* as:

$$chla = \frac{\frac{R_{rs}(705)}{R_{rs}(665)} \times (a_w(705) + b_b) - a_w(665) - b_b^{1.67}}{0.0141} \tag{2}$$

where $a_w(665) = 0.4$ m^{-1} and $a_w(705) \approx 0.7$ m^{-1} (Buiteveld et al., 1994) are approximated values of water absorption coefficients in the red and red-edge bands, respectively.

The coloured dissolved organic matter absorption coefficient (aCDOM) at 400 nm was used as a proxy for organic matter inputs from the watershed (allochthonous source), as well as to infer light limitation of primary productivity. To retrieve aCDOM(400), a semi-empirical algorithm validated in MMELS (Lima Filho et al., 2022) was employed ($n = 29$, $r^2 = 0.65$, RMSE = 0.30 m^{-1}). This algorithm establishes a log ∼ log relationship between aCDOM and a band ratio, with one band in the NIR spectrum, where CDOM absorption is very weak but present, and the effects of other water constituents are minimised (water absorption is fixed), and the other in the blue spectrum, where CDOM absorption is very strong. It is calculated as:

$$\text{aCDOM}(400) = \exp\left[1.08 + 0.43\log(R_{rs}(740)/R_{rs}(490))\right] \tag{3}$$

2.4. *Environmental data*

To assess the drivers of short-term phytoplankton dynamics, we evaluated the impact of meteorological and hydrodynamic forcings over the system. Information on the tide was provided by the Navy Oceanographic Center (CHN) as water level data from Maceió Harbour (9°40.968’S, 35°43.424’W), located 9 km from the Mundaú Lagoon inlet. From this data, we calculated the tide at the time of satellite overpass using a fitted sinusoidal function (Brito Jr et al., 2018). Meteorological data were retrieved from a meteorological station located 7.5 km northeast of the Mundaú lagoon centre. This station is maintained by the Instituto Nacional de Meteorologia (INMET), providing hourly meteorological data. We retrieved air temperature, solar radiation, precipitation, and wind speed and direction. River flow data were retrieved from two river gauge stations maintained by the Agência Nacional de Águas (ANA), Fazenda Boa Fortuna, which measures Mundaú river’s daily mean flow at 16 km from the Mundaú lagoon, and Atalaia, which measures Paraíba do Meio river’s daily mean flow at 15 km from the Manguaba lagoon. Unfortunately, no data from the Sumaúma river is available, and only the precipitation over Maceió can be used to estimate its impact on Manguaba lagoon. Figure 3 shows the climatology of precipitation and river flow in MMELS for the study period, highlighting the region’s well-defined wet and dry periods.

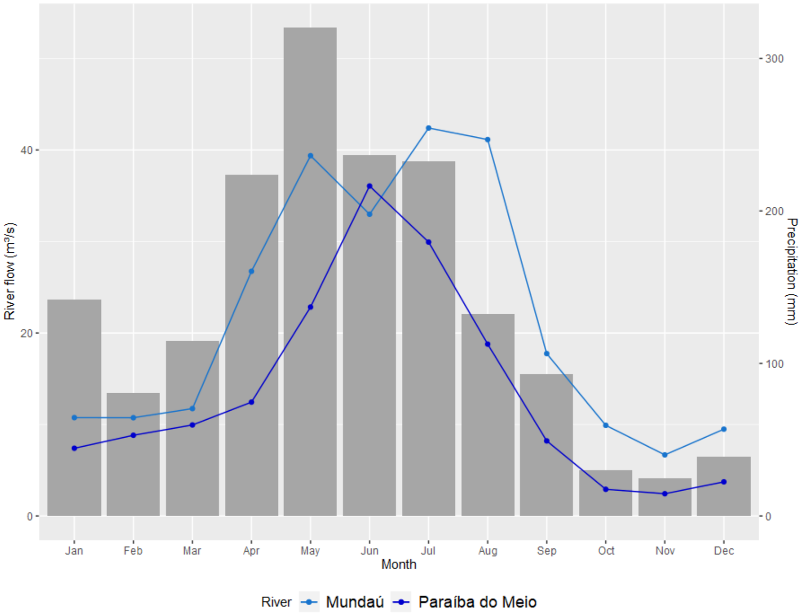

Figure 3: Climatology of precipitation and river inflow to MMELS during 2016–2021.

2.5. Spatiotemporal patterns of chla and drivers

To analyse the resulting rasters of chla concentrations, we calculated the mean values for each pixel for the whole period of analysis, and the wet (May to August) and dry (October to January) periods. From these rasters, we calculated the mean for each lagoon and for the system for these selected periods. We also assessed the correlation between chla and aCDOM for each pixel over the system using Spearman rank correlation ρ, as this relationship may not be linear.

The relationship between chla and environmental drivers was established using a methodology similar to Lins et al. (2018), however, considering a daily scale, for short-term dynamics and fewer images. First, we divided the lagoons into homogeneous spatial groups (HSG) using Ward's minimum variance clustering (Legendre and Legendre, 1998), considering the normalised values of chla and aCDOM in each pixel and 4 clusters in each lagoon, following Lins et al. (2018), using packages *cluster* (Maechler et al., 2021) and *vegan* (Oksanen et al., 2022). For each cluster, we then calculated the monthly means of chla and descriptive statistics over the whole period of analysis.

Then, we assessed the relationship between chla and the environmental data in each cluster for the time series using Canonical Correspondence Analysis (CCA) (Legendre and Legendre, 1998). For this, we calculated each cluster's mean chla and aCDOM in each image, and the mean value of the environmental variables 24h before the satellite overpass (at ~10:30 am, local time). A minimum threshold of 250 pixels for Manguaba and 125 pixels for Mundaú was set to process mean chla and aCDOM in each cluster. For the environmental data, we calculated daily mean solar radiation (*Rad*), temperature (*Temp*), wind speed (*ws*) and direction (*wd*, which was divided into 30°quadrants), as well as wind speed in the x (u_x) and y (u_y) directions, precipitation in the 24h (*P.24h*) and 48h (*P.48h*) before satellite overpass, river flow (Q), and the tide at the time of satellite overpass (*Td.Hour*), tide amplitude (*Td.Amp*) and mean tide (*Td.Mean*) 24h before satellite overpass. Only mean temperature was considered due to a very high correlation between daily maximum, minimum and mean temperatures.

The relationship established with CCA was processed with package *vegan* (Oksanen et al., 2022) and plotted using *ggvegan* (Simpson, 2019). Due to missing pixels and missing data from the meteorological station, 93 data points were available for Manguaba, and 84 data points were available for Mundaú, of the 142 images available.

3. Results

3.1. Means

Figure 4 shows the mean values of chla over MMELS during different periods of the year, and Figure 5 highlights the difference in chla between the wet and dry periods. Manguaba lagoon shows more eutrophic conditions than Mundaú lagoon, with higher values of chla over its western margin, especially in the centre of the lagoon, while in Mundaú, the higher values are closer to the urban area. In both lagoons, during the wet period, the chla values are smaller near the inflow areas, except near the Sumaúma river, and near the point sources of pollution the chla values are higher this season. Table 1 quantifies the calculated mean chla values for the lagoons over different periods of the year.

It shows how chla is always higher in Manguaba lagoon and the months with the higher (March) and lower (September) concentrations.

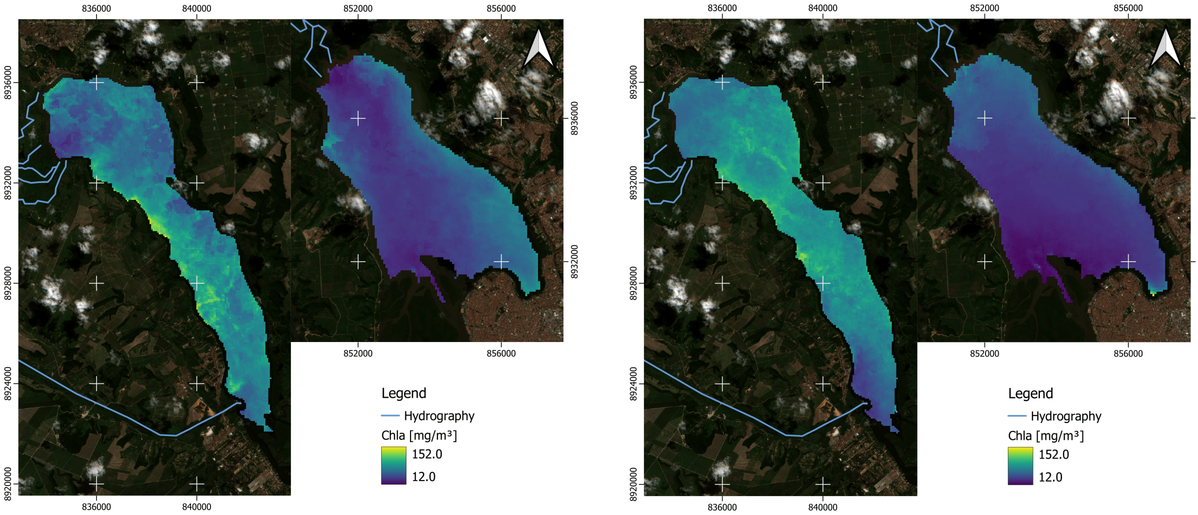

(a) Wet

(b) Dry

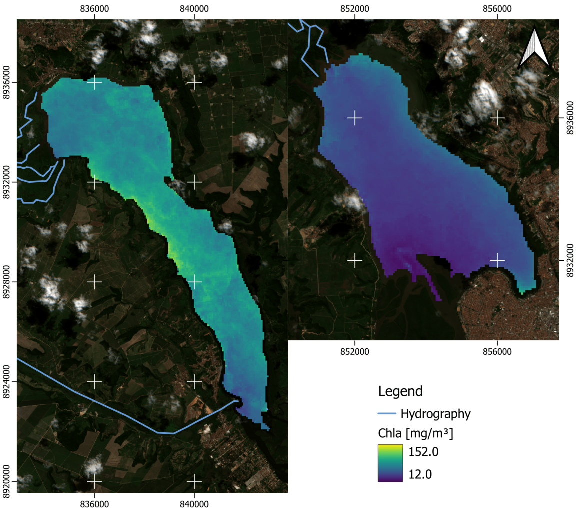

(c) Whole period

Figure 4: Mean values of chlorophyll-*a* concentration in the a) wet and b) dry periods, and c) for all images.

Figure 6 shows the mean values of aCDOM(400) over the whole period. While the aCDOM distribution over the system generally follows that of chla, we can see some differences, notably the similar amplitude of the absorption coefficient in Manguaba and Mundaú lagoons. The urban areas have a significant input of organic matter, but in the southern part of Mundaú, they do not contribute to aCDOM, probably due to the influence of the tides. The relationship between aCDOM and chla is shown spatially using the Spearman correlation coefficient at different periods in Figure 7. Near the Mundaú and Paraíba do Meio inflows, the correlation is low, but it is higher than 0.7 over most of the system,

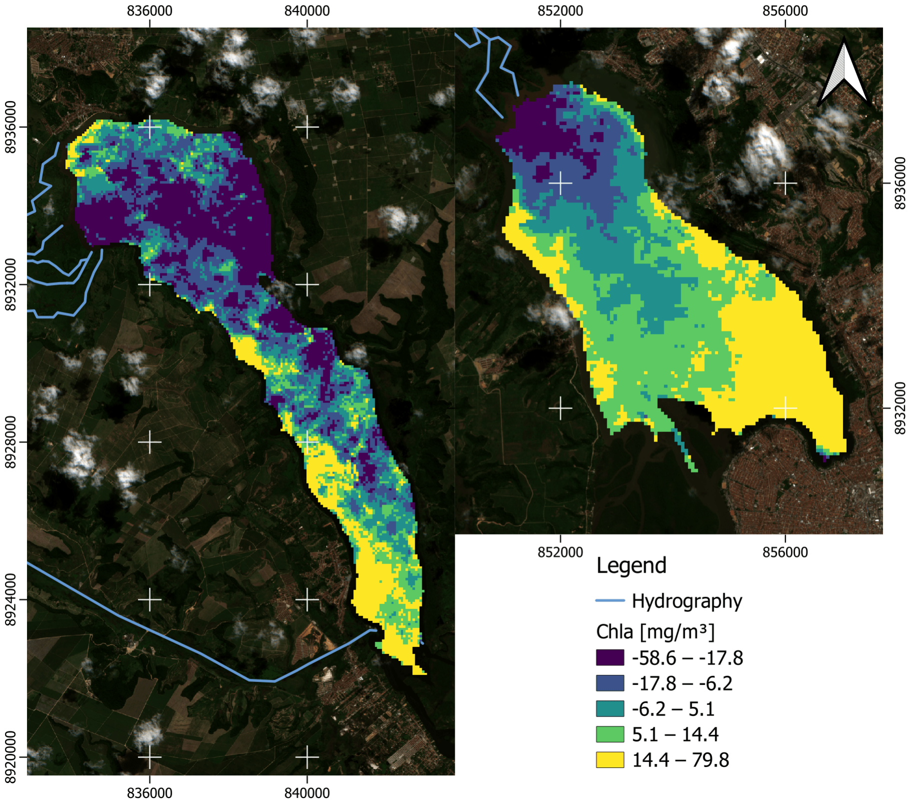

Figure 5: Difference between the mean values of chlorophyll-*a* concentration in the wet and dry periods.

especially in the dry period when the input in the system is low. During the wet period, the correlation map is more dispersed, but the correlation between chla and aCDOM significantly decreases.

3.2. Clusters

Figure 8 shows the clusters divided by Ward's clustering method, considering the time series of chla and aCDOM. As expected, the main drivers of spatial variability are the connecting channels (influence of tides) and the inflows. However, while for Mundaú there is a gradient from the Mundaú river inflow to the channel inlet, with an influence of the point sources of pollution contributing to a different cluster at the eastern margin, where Maceió is, for Manguaba the division resulted in a gradient starting at the centre of the lagoon, with the pixels at the extremes (at the Paraíba do Meio river inflow and at the channel inlet) belonging to the same cluster.

Table 2 shows the descriptive statistics of chla for each cluster and the correlation between chla and aCDOM. In Mundaú, as expected, HSG1 showed the highest values of chla, influenced by the point sources of nutrients and organic matter and more stagnant waters. HSG2 showed intermediate values of chla, with the lowest correlation between chla and aCDOM due to the effect of discharge of the Mundaú river, which carries DOM along with suspended sediments, resulting in light limitation. HSG3 and HSG4 show similar statistics, with lower values of chla in the HSG4 due to the

Table 1: Mean values (and standard deviation), in mg m^{-3}, of the mean chlorophyll-*a* concentration of the pixels in each site during different periods of the year

Site	Whole period	Wet	Dry	March	September
MMELS	67.1 ± 22.1	62.6 ± 20.2	63.6 ± 23.6	118.7 ± 61.0	48.6 ± 12.8
Mundaú	41.8 ± 10.5	45.2 ± 13.5	37.6 ± 11.8	53.6 ± 20.9	46.0 ± 14.4
Manguaba	81.1 ± 12.1	72.2 ± 16.5	78.0 ± 14.3	153.5 ± 44.4	50.0 ± 11.6

stronger influence of the tides.

Table 2: Statistics (in mg m^{-3}) of estimated chla considering the different HSG for each lagoon

Site	Group	Mean	Min	Max	SD	ρ (chla~CDOM)
Mundaú	HSG1	63.5	39.1	86.5	13.6	0.42
	HSG2	48.9	33.9	65.9	10.0	0.25
	HSG3	42.9	29.8	57.2	7.6	0.76
	HSG4	32.6	21.6	40.2	6.2	0.68
Manguaba	HSG1	95.9	54.8	171.8	30.1	0.63
	HSG2	86.1	53.5	158.0	27.0	0.58
	HSG3	79.3	50.1	149.8	25.2	0.31
	HSG4	69.7	45.3	139.1	23.9	0.54

In Manguaba, HSG1 showed the highest values of chla, being less affected by the sediments carried by Paraíba do Meio river and influenced by more stagnant waters due the tides. It also extends to recirculation zones in the northwest and southeast margins, where productivity hotspots are found. The gradient of chla occurs similarly to Mundaú, from HSG1 to HSG4, with HSG4 being the most influenced by the river inflow and tides. However, chla is still high in HSG4, with a contribution from the discharge of the Sumaúma river, with potentially high nutrient content. Interestingly, HSG3 showed the lowest correlation between chla and aCDOM, where there is a relatively low influence of the river inflows. However, we can see from Figure 7 that, despite being in the same group, there is a very different relationship between chla and CDOM in HSG4, with the area near the Paraíba do Meio inflow with a smaller correlation due to light limitation by CDOM and sediment input.

Figure 9 shows the monthly means of chla in each cluster. The two lagoons show distinct patterns, with Mundaú showing a relatively larger variability, especially in HSG 1 and 2. They show higher chla and variability, with higher chla in March, August and October, and lower concentrations in the dry period. Manguaba, on the other hand, shows a more uniform variability across the clusters, with a clear increase in chla in the dry period leading to a distinct peak in March, followed by low variability in the wet period and a minimum in September, as shown in Table 1.

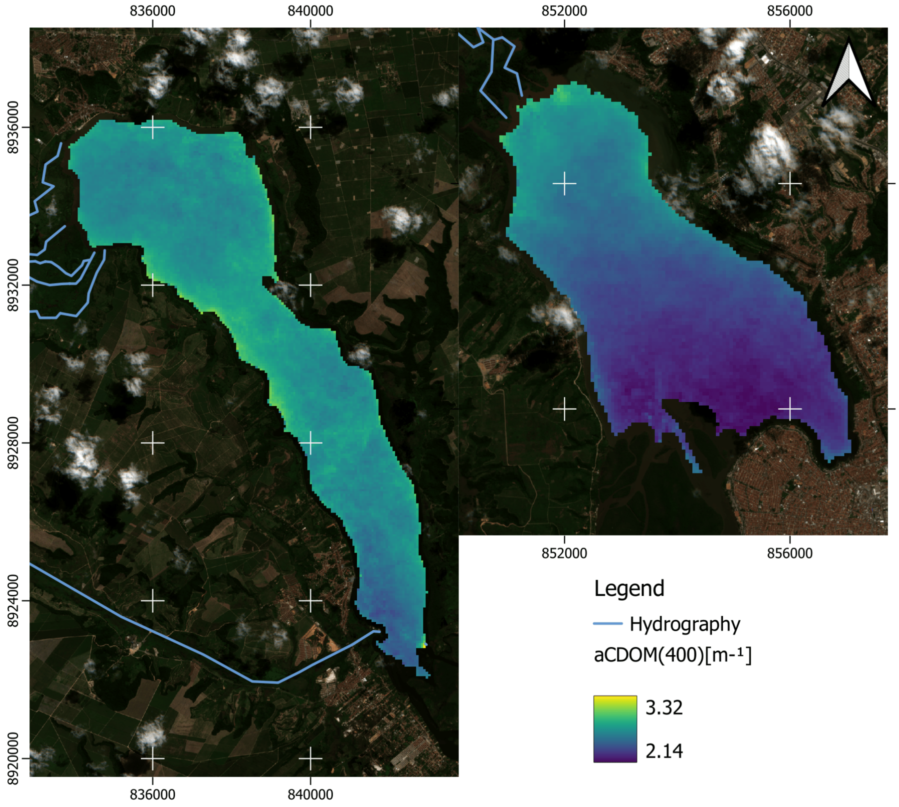

Figure 6: Mean values of aCDOM(400) for the studied period.

3.3. Environmental drivers

Figure 10 shows the plot of the first two axes of the CCA, which explain ~40% of the variability in Mundaú and ~56% in Manguaba lagoon. In both lagoons, the clusters were divided in each plot quadrant, and the aCDOM did not help explain much of the variability in chla. In Mundaú, the chla in HSG1 is mostly influenced by wind, favoured by stagnant waters. It is not correlated to antecedent precipitation, contrary to expectation, but is negatively affected by solar radiation, which is negatively correlated to precipitation. HSG2, being at the discharge area of the Mundaú river, is controlled by river flow and precipitation. The tide is determinant for HSG3 and HSG4, as expected, as this cluster is the most affected by it, with HSG3 being mostly influenced by tide amplitude and wind speeds, which is related to the residence times, and chla in HSG4 being higher with higher temperatures and lower tides at the time of measurement, showing how volatile is this transition area between fresh and seawater.

In Manguaba, the first axis of the CCA explained much more of the chla variability than in Mundaú. Interestingly, the tide affects the clusters differently, with the tide amplitude affecting the HSG1, related to the residence times of these areas, the tide at the time of measurements influencing HSG2 the most, and the 24h mean tide determining HSG3 and HSG4, which are the most affected by the tides in the lower portion of the lagoon. Wind direction also has a determining role in Manguaba, with stronger southerly winds contributing to chla in HSG3 and strong westerly winds

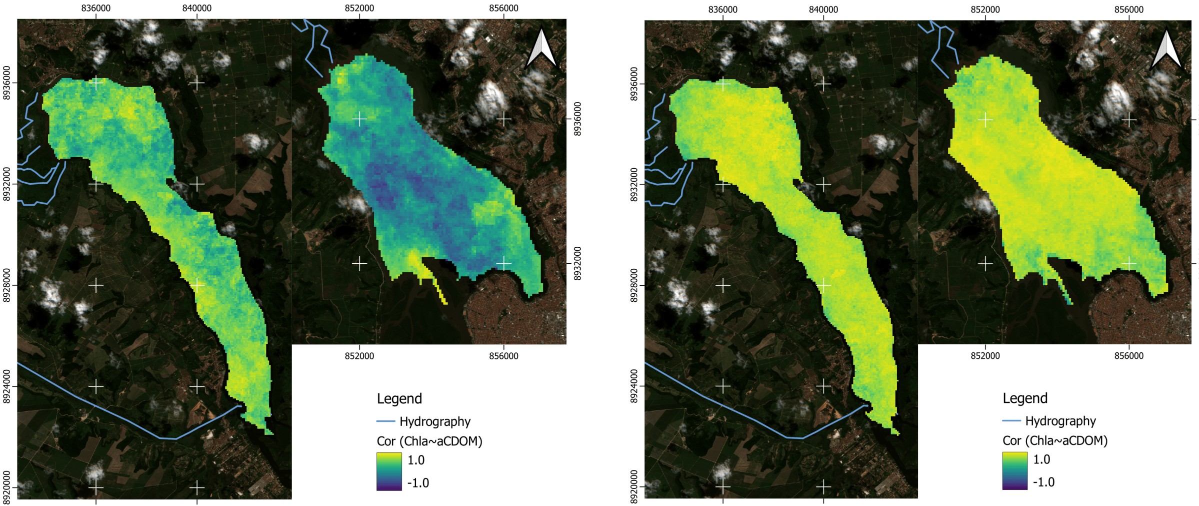

(a) Wet

(b) Dry

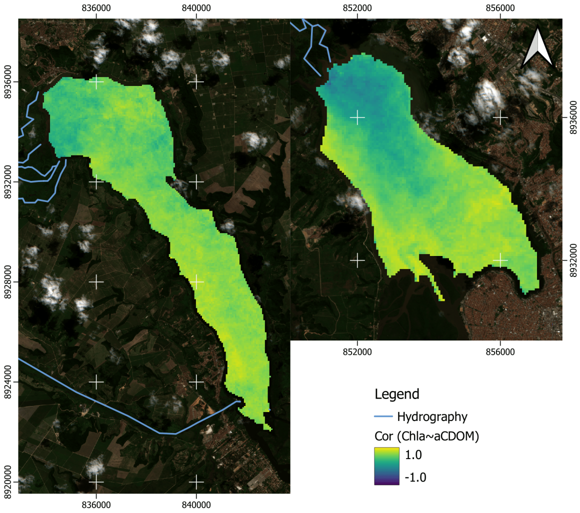

(c) Whole period

Figure 7: Spearman correlation coefficient between chla and aCDOM(400) in the a) wet and b) dry periods, and c) for all images.

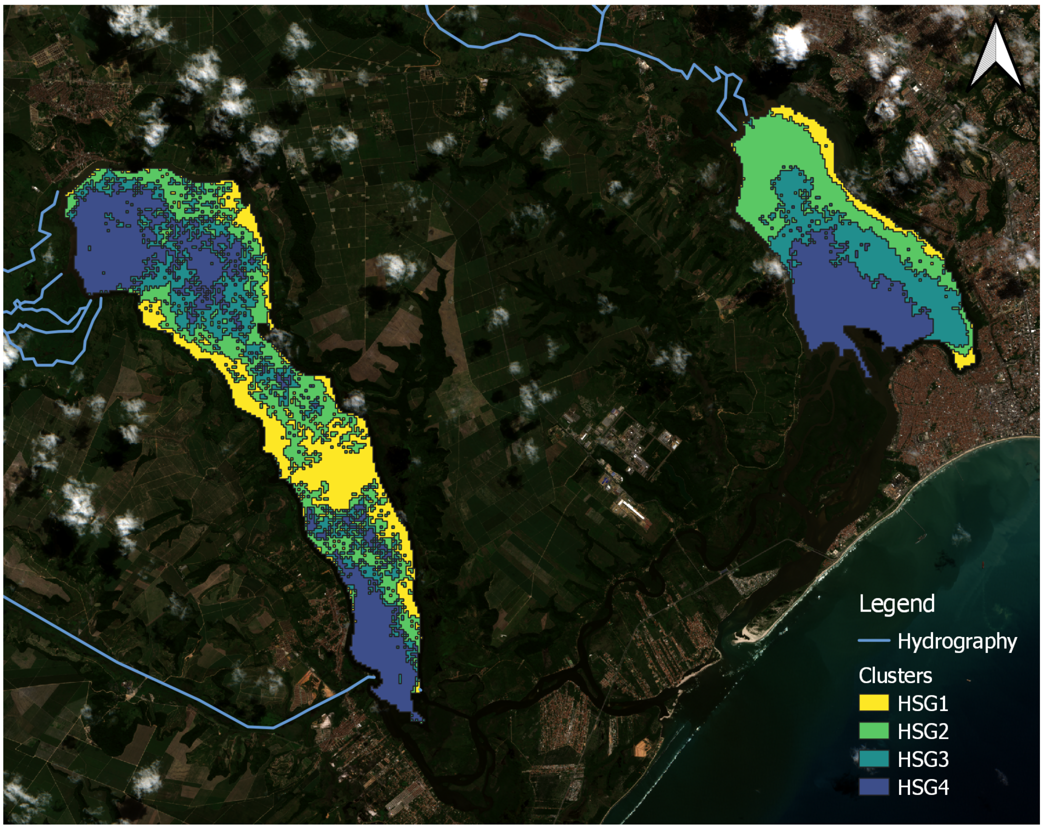

Figure 8: Map of clusters in Manguaba and Mundaú lagoons, considering the time series of chla and aCDOM.

contributing to chla in HSG4, both related to increased water residence times and sediment resuspension. HSG4 is also affected by river flow and 24h-accumulated precipitation, mostly in its southern portion due to the Sumaúma inflow, but HSG1 is the most affected by 48h-accumulated precipitation, probably due to the long residence times, especially when there is a high tide amplitude.

4. Discussion

In this study, we showed the spatial variation of chla over a eutrophic shallow estuarine-lagoon complex. The chla patterns are much more homogeneous in the Mundaú lagoon (Figure 4), with a defined distribution that follows the wet and dry periods. In the Manguaba lagoon, however, the distribution is more complex, with varying patterns reflected in the more chaotic cluster map (Figure 8). Chla is also always higher in Manguaba (Table 1), with a smaller difference between the lagoons in September, at the end of the wet season, and a higher difference in March, when chla is very high in Manguaba.

Our results also highlight the importance of the point sources of pollution in both lagoons, especially in HSG1 in Mundaú and near the mouth of the Sumaúma river in the Manguaba lagoon. Despite previous reports of low sewage

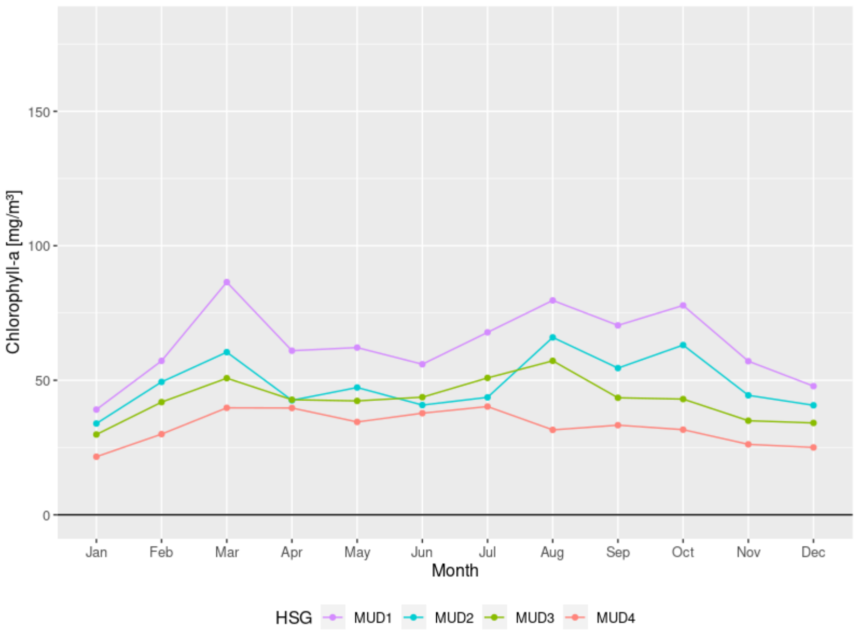

(a) Mundaú lagoon

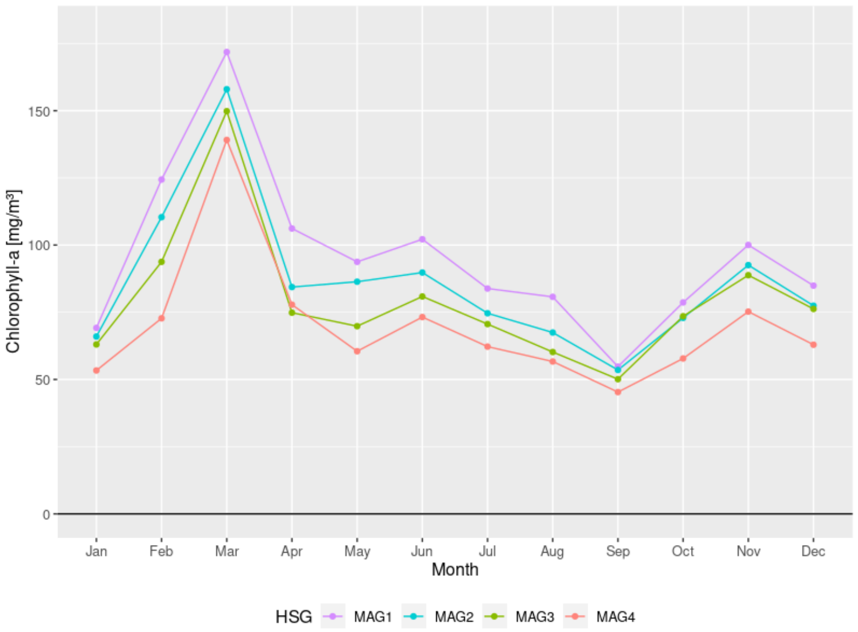

(b) Manguaba lagoon

Figure 9: Monthly means of chla in each cluster in a) Mundaú and b) Manguaba lagoons.

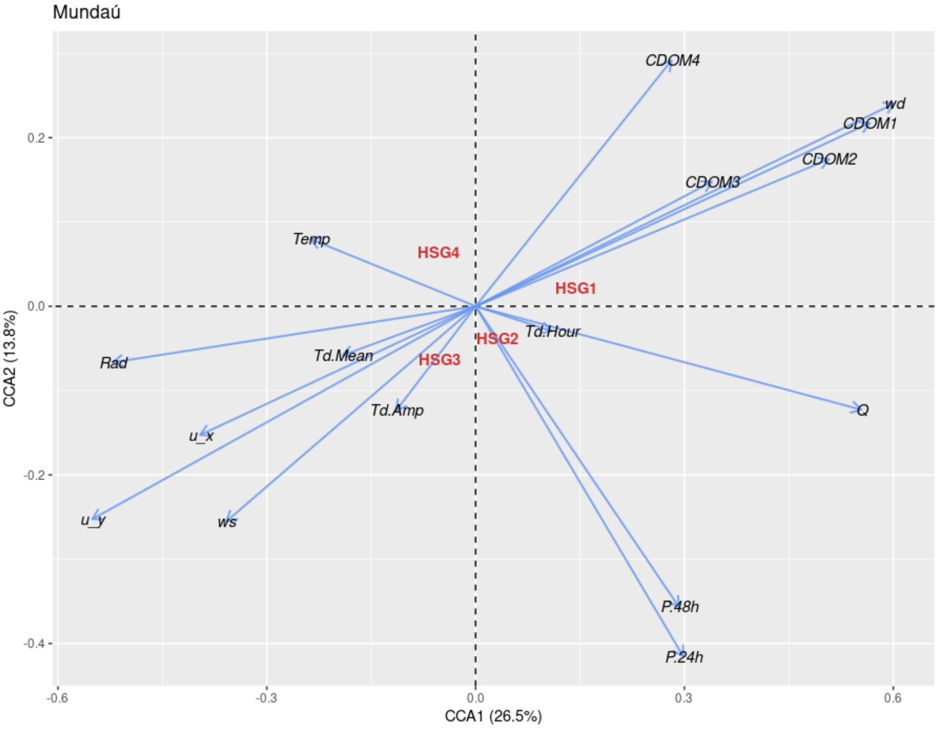

(a) Mundaú lagoon

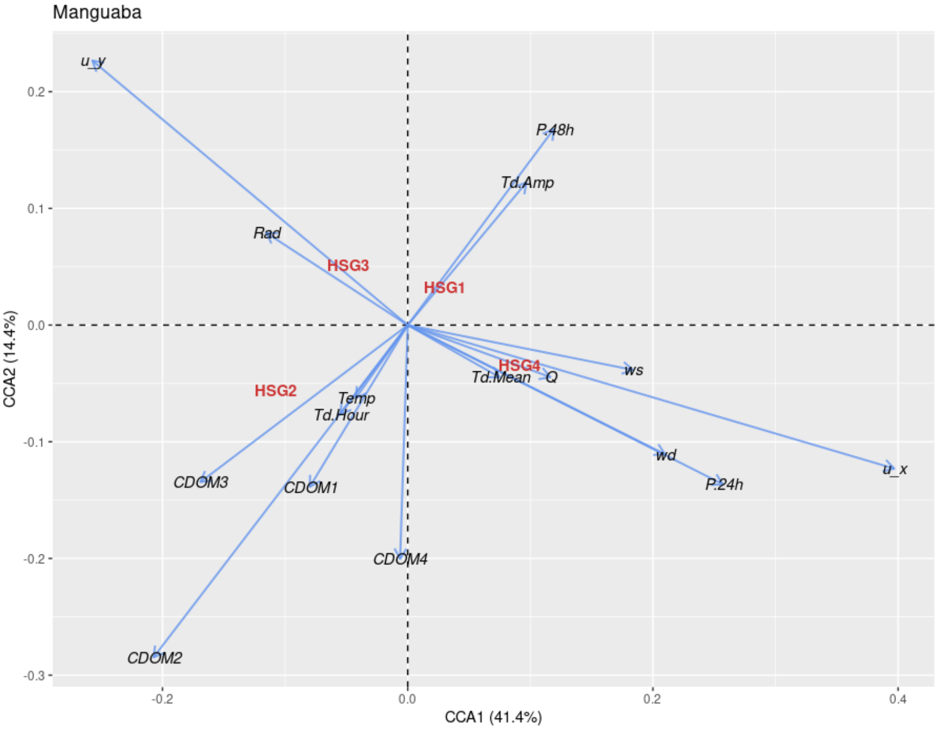

(b) Manguaba lagoon

Figure 10: Plot of the first two axes of the Canonical Correspondence Analysis for a) Mundaú and b) Manguaba lagoons.

discharge into Manguaba lagoon (Costa et al., 2011), we see from Figure 6 that this source of pollution has a large contribution to CDOM, and this can be due to the high population growth observed in this urban area in Marechal Deodoro (growth of 15% between 2011 and 2021), leading to increased discharge of wastewater in Manguaba which, in conjunction with the Sumaúma discharge, causes the high chla concentration.

The effects of CDOM on chla are two-fold: the organic matter generally supplies nutrients that increase production, but CDOM also attenuates light, causing a limitation on primary production (Kelly et al., 2018). This effect is still understudied, but it is understood that it depends on the nutrient:carbon stoichiometry and the chromophoricity of the DOM, *i.e.*, how the DOM interacts with light (Seekell et al., 2015). Our mapping of CDOM does not take these factors into account, only the absorption coefficient, therefore the maps of correlation between chla and aCDOM do not consider the different nutrient content of the different sources of DOM, and how these different inputs of DOM affect the relationship between DOM and primary production (Olson et al., 2020). For example, algal-derived DOC has a low colour intensity, and DOC from wastewater effluent is even less coloured, but has a high nutrient content (Brezonik et al., 2015).

Therefore, it is difficult to accurately quantify the influence of CDOM on chla in these lagoons, but we showed that they are generally correlated (Figure 7), with a very high correlation in the dry season, when possibly most of CDOM in the system is derived from phytoplankton (autochthonous source), as Costa et al. (2011) showed that most of the particulate organic matter (POM) results from phytoplankton mortality. During the wet season, much OM is carried to the lagoons, carrying loads of untreated sewage discharged, especially into the Mundaú lagoon, and fertiliser and nutrient loads from the river watersheds, mainly into the Manguaba lagoon (Costa et al., 2011). In this season, we can see that the relationship between them is more complex and non-linear, notably in the Mundaú lagoon where it is largely negative. In this case, and at the mouth of the Mundaú and Paraíba do Meio rivers in general, it is likely due to light limitation due to the absorption of light by CDOM (Branco and Kremer, 2005), associated with the suspended solids carried by both rivers, but more notably by Mundaú river, as noted in Oliveira and Kjerfve (1993) and Lins et al. (2017).

Another key variable that explains the spatial variation of chla is the water residence times. In eutrophic estuaries, water residence times can be the variable controlling algal biomass (Wainger et al., 2016) and is a driver of chla in MMELS (Lins et al., 2018). Mundaú typically shows a lower residence time (Oliveira and Kjerfve, 1993; Brito Jr et al., 2018; Cunha et al., 2021) for being smaller and receiving more freshwater discharge throughout the year (Figure 3). Mundaú is also more affected by the tides, decreasing the lagoon's water renewal time (Brito Jr et al., 2018). Here we highlight that since this region is close to the Equator, the tide amplitude can be high, up to 2.5 m, thus having a large impact on the variability both of water residence times and in the phytoplankton community, regulating salinity and nutrient availability, which associated with the high turbidity in Mundaú lagoon, may limit primary production (Oliveira and Kjerfve, 1993; Melo-Magalhães et al., 2009), especially in the region of HSG4 (Figure 8). In Manguaba, the water residence times are typically much higher (Cunha et al., 2021), with a very low influence of the tide in the lagoon's salinity (Oliveira and Kjerfve, 1993), with the hydrodynamics dominated by river discharge and wind stress. This, coupled with lower turbidity, allows for the higher chla, and with the characteristics of the phytoplankton community, with a dominance by freshwater cyanobacteria species (Melo-Magalhães et al., 2009) associated with low wind speeds, form the conditions for algal blooms (Vaičiūtė et al., 2021), which are common in this lake.

Compared with the clusters generated by Lins et al. (2018), we highlight that the different periods, different approaches, and, most importantly, the limited spatial coverage from MODIS resulted in the different clusters. That work, however, also showed the longitudinal gradient found in the Mundaú lagoon and indicated a region in the middle of the Manguaba lagoon where chla values were much higher. The time series of chla in each cluster here show a much higher value over the whole year, and the peak we found in March was only observed in Mundaú, while in Lins et al. (2018), the peak in Manguaba was in April–May. The difference in the results can be three-fold: the difference in the methods to retrieve chla, the difference in the spatial coverage of the two sensors, and an actual difference in chla in the system. In Lins et al. (2018), the authors applied a NIR-red model with MODIS Terra and Aqua, with an RMSE = 15.2 mg/m³ and a significant underestimation of chla in the low concentration range, which may partially explain the differences. Here, the RMSE was significantly higher (36.2 mg/m³), with an uncorrected adjacency effect affecting mainly Mundaú, especially the HSG4 (closer to the urban area), that might explain the differences found in this lagoon.

We can also see that the monthly chla concentrations in Lins et al. (2018) follow the region's climatology, with the peak in May observed in Manguaba following the rainfall peak (Figure 3). Here, chla do not directly correlate with the rainy and dry seasons, although this effect is more directly observed in Mundaú (Figure 9), with both lagoons showing a peak in chla in March, when rainfall and river flow are relatively low, resulting in common algal blooms in Manguaba lagoon. This is a result of the sugarcane plantation cycle, as sugarcane crops are widespread over the MMELS watershed, especially in the Sumaúma river basin (Figure 1), with high potential to lower the water quality of waterbodies, and already been investigated in other studies in Brazil (e.g., Barra Bonita reservoir, Tundisi et al., 2008). From September, when the cycle starts, to March–May, when the sugarcane is harvested and processed, the water quality of the rivers is heavily altered by the water use and leaching of the crop fields. Especially in March, water is withdrawn from the rivers to wash ash from the burned leaf in the sugarcane stalks before processing them. The water is returned to the rivers with no additional treatment, carrying a load with high biochemical and chemical oxygen demand in the effluent, rapidly lowering the pH and DO concentrations (Oliveira and Kjerfve, 1993). This leads to the occurrence of algal blooms that affects mostly the Manguaba lagoon, but its effects can also be seen in Mundaú. Unfortunately, the Sumaúma river is not monitored, and therefore we could not quantify its impact on chla in Manguaba lagoon, however, it clearly has a direct effect, as seen by the influence of rainfall in the clusters (Figure 10).

The short-term analysis also allowed for assessing the tides' effect on the system. It is a determinant factor in the whole system, whether by controlling salinity, nutrients, and phytoplankton composition or controlling the water residence times (Melo-Magalhães et al., 2009). The analysis with the CCA showed that different characteristics of the tide have different impacts in the system, as in Manguaba, the region most affected by eutrophication and algal blooms being determined by tide amplitude, whereas near the channel inlet, where fish kill events have been reported, the mean daily tide preceding the event drives chla. The effects of the tide are even more pronounced in the dry season, when the water residence times are higher and chla is higher in the northern and central parts of the lagoon.

5. Conclusions

In this study, we assessed the spatiotemporal patterns of chlorophyll-*a* in a heavily anthropised system using a validated Sentinel-2 MSI-derived time series. We also used a remote sensing-derived series of aCDOM to explore the chla-CDOM relationship and evaluated the impact of environmental forcings on chla. The results quantified the mean chla concentrations in the lagoons between 2016 and 2021, showing that Manguaba is more eutrophic than Mundaú and has a less defined variation along the year, mostly due to the nutrient influx coming from the basin due to sugarcane crops. Mundaú shows a more defined pattern and pronounced variation along the year, affected by the sugarcane crop cycle and by precipitation. The chla maps also clearly showed the impact of the river inflows on the system, which generally tend to decrease chla due to light limitation by CDOM and TSS (which were not quantified) inputs, as well as the point sources of pollution, which increased chla during the wet season.

A clustering technique divided the two lagoons into four homogeneous spatial groups, where in Mundaú they show a distinct longitudinal gradient of chla, while in Manguaba the gradient showed an increase of chla from the extremities to the centre of the lagoon. This most productive cluster, at the centre of the lagoon, included areas of recirculation, highlighting the importance of hydrodynamics and water residence times in this system. A canonical correspondence analysis was applied to determine each cluster's most important drivers of chla. The short-term analysis also allowed for assessing the relative importance of the tides on the system.

Compared to previous works in the system (Oliveira and Kjerfve, 1993; Melo-Magalhães et al., 2009; Lins et al., 2018), our results point to a further degradation of the water quality in the system, with a possible increase in algal bloom events, and fish kill events reported near the Manguaba lagoon. We highlight how remote sensing monitoring should be used as a tool for the management of the system to provide data and knowledge to management plans, such as to prevent fish kill events, although it may lack variables necessary to fully understand the system dynamics (*e.g.*, salinity and water residence times, Wainger et al., 2016), which have to be monitored *in situ*. Further studies in the system should include a model of the Sumaúma river discharge to quantify its effect in Manguaba lagoon, explore water transparency (*e.g.*, Secchi disk depth) effects on phytoplankton, and assess the occurrence of algal blooms in the system (Vaičiūtė et al., 2021), as well as the impact of these algal blooms on CDOM.

Acknowledgements

This research was funded by CAPES (Coordenação de Aperfeiçoamento de Pessoal de Nível Superior) through the project "Qualidade e circulação de água em ecossistemas costeiros: monitoramento e modelagem para tomada de decisão", and by CNPq (Conselho Nacional de Desenvolvimento Científico e Tecnológico) through the scholarship number 140505/2020-2. We also would like to thank Quinten Vanhellemont for providing ACOLITE for free, INMET for the meteorological data and ANA for the river flow data.

References

Amorim, C.A., Moura, A.N., 2021. Ecological impacts of freshwater algal blooms on water quality, plankton biodiversity, structure, and ecosystem functioning. Science of the Total Environment 758, 143605. doi:`10.1016/j.scitotenv.2020.143605`.

Baban, S.M.J., 1996. Trophic classification and ecosystem checking of lakes using remotely sensed information. Hydrological Sciences Journal 41, 939–957. doi:`10.1080/02626669609491560`.

Barbier, E.B., Hacker, S.D., Kennedy, C., Koch, E.W., Stier, A.C., Silliman, B.R., 2011. The value of estuarine and coastal ecosystem services. Ecological Monographs 81, 169–193. doi:`10.1890/10-1510.1`.

Boyer, J.N., Kelble, C.R., Ortner, P.B., Rudnick, D.T., 2009. Phytoplankton bloom status: Chlorophyll *a* biomass as an indicator of water quality condition in the southern estuaries of Florida, USA. Ecological Indicators 9, S56–S67. doi:`10.1016/j.ecolind.2008.11.013`.

Branco, A.B., Kremer, J.N., 2005. The relative importance of chlorophyll and colored dissolved organic matter (CDOM) to the prediction of the diffuse attenuation coefficient in shallow estuaries. Estuaries 28, 643–652. doi:`10.1007/BF02785000.`

Brezonik, P.L., Olmanson, L.G., Finlay, J.C., Bauer, M.E., 2015. Factors affecting the measurement of CDOM by remote sensing of optically complex inland waters. Remote Sensing of Environment 157, 199–215. doi:`10.1016/j.rse.2014.04.033`.

Brito Jr, A.N., Fragoso Jr, C.R., Larson, M., 2018. Tidal exchange in a choked coastal lagoon: A study of Mundaú Lagoon in northeastern Brazil. Regional Studies in Marine Science 17, 133–142. doi:`10.1016/j.rsma.2017.12.005`.

Buiteveld, H., Hakvoort, J., Donze, M., 1994. Optical properties of pure water, in: Ocean Optics XII, pp. 174–183. doi:`10.1117/12.190060`.

Carlson, R.E., 1977. A trophic state index for lakes 1. Limnology and Oceanography 22, 361–369. doi:`10.4319/lo.1977.22.2.0361`.

Costa, T.L., Araújo, M.P., Knoppers, B.A., Carreira, R.S., 2011. Sources and distribution of particulate organic matter of a tropical estuarine-lagoon system from NE Brazil as indicated by lipid biomarkers. Aquatic Geochemistry 17, 1–19. doi:`10.1007/s10498-010-9104-1`.

Courrat, A., Lobry, J., Nicolas, D., Laffargue, P., Amara, R., Lepage, M., Girardin, M., Le Pape, O., 2009. Anthropogenic disturbance on nursery function of estuarine areas for marine species. Estuarine, Coastal and Shelf Science 81, 179–190. doi:`10.1016/j.ecss.2008.10.017`.

Cunha, C.d.L.d.N., Scudelari, A.C., Sant'Ana, D.d.O., Luz, T.E.B., Pinheiro, M.K.d.R., 2021. Effects on circulation and water renewal due to the variations in the river flow and the wind in a Brazilian estuary lagoon complex. Revista Ambiente & Água 16. doi:`doi:10.4136/ambi-agua.2600`.

Fulweiler, R.W., Nixon, S.W., 2012. Net sediment N2 fluxes in a southern New England estuary: variations in space and time. Biogeochemistry 111, 111–124. doi:`10.1007/s10533-011-9660-5`.

Giardino, C., Brando, V., Gege, P., Pinnel, N., Hochberg, E., Knaeps, E., Reusen, I., Doerffer, R., Bresciani, M., Braga, F., Foerster, S., Champollion, N., Dekker, A., 2019. Imaging spectrometry of inland and coastal waters: state of the art, achievements and perspectives. Surveys in Geophysics 40, 401–429. doi:`10.1007/s10712-018-9476-0`.

Gitelson, A.A., Kondratyev, K.Y., 1991. Optical models of mesotrophic and eutrophic water bodies. International Journal of Remote Sensing 12, 373–385. doi:`10.1080/01431169108929659`.

Gons, H.J., Rijkeboer, M., Ruddick, K.G., 2002. A chlorophyll-retrieval algorithm for satellite imagery (Medium Resolution Imaging Spectrometer) of inland and coastal waters. Journal of Plankton Research 24, 947–951. doi:`10.1093/plankt/24.9.947`.

Gons, H.J., Rijkeboer, M., Ruddick, K.G., 2005. Effect of a waveband shift on chlorophyll retrieval from MERIS imagery of inland and coastal waters. Journal of Plankton research 27, 125–127. doi:`10.1093/plankt/fbh151`.

Harmel, T., Chami, M., Tormos, T., Reynaud, N., Danis, P.A., 2018. Sunglint correction of the Multi-Spectral Instrument (MSI)-SENTINEL-2 imagery over inland and sea waters from SWIR bands. Remote Sensing of Environment 204, 308–321. doi:`10.1016/j.rse.2017.10.022`.

Hijmans, R.J., 2021. terra: Spatial Data Analysis. URL: `https://CRAN.R-project.org/package=terra`. r package version 1.4-22.

Kelly, P.T., Solomon, C.T., Zwart, J.A., Jones, S.E., 2018. A framework for understanding variation in pelagic gross primary production of lake ecosystems. Ecosystems 21, 1364–1376. doi:`10.1007/s10021-018-0226-4`.

Legendre, P., Legendre, L., 1998. Numerical Ecology. Elsevier.

Lima Filho, M.C.O., Tavares, M.H., Fragoso Jr., C.R., Lins, R.C., Vich, D.V., 2022. Semi-empirical models for remote estimation of colored dissolved organic matter (CDOM) in a productive tropical estuary. Environmental Monitoring and Assessment (submitted) .

Lins, R.C., Martinez, J.M., Motta-Marques, D., Cirilo, J.A., Fragoso Jr., C.R., 2017. Assessment of chlorophyll-a remote sensing algorithms in a productive tropical estuarine-lagoon system. Remote Sensing 9, 516. doi:`10.3390/rs9060516`.

Lins, R.C., Martinez, J.M., Motta-Marques, D., Cirilo, J.A., Medeiros, P.R.P., Fragoso Jr, C.R., 2018. A multivariate analysis framework to detect key environmental factors affecting spatiotemporal variability of chlorophyll-a in a tropical productive estuarine-lagoon system. Remote Sensing 10, 853. doi:`10.3390/rs10060853`.

Luz, T.E.B., Pinheiro, M.K.d.R., Scudelari, A.C., Cunha, C.d.L.d.N., 2022. Effects of different tidal inlet configurations on the water quality of an estuary lagoon complex in northeastern brazil. Brazilian Journal of Water Resources 27. doi:`10.1590/2318-0331.272220220056`.

Maechler, M., Rousseeuw, P., Struyf, A., Hubert, M., Hornik, K., 2021. cluster: Cluster Analysis Basics and Extensions. URL: `https://CRAN.R-project.org/package=cluster`. r package version 2.1.2 — For new features, see the 'Changelog' file (in the package source).

Matthews, M.W., 2017. Bio-optical modeling of phytoplankton chlorophyll-*a*, in: Mishra, D.R., Ogashawara, I., Gitelson, A.A. (Eds.), Bio-optical Modeling and Remote Sensing of Inland Waters. Elsevier, pp. 157–188. doi:`10.1016/B978-0-12-804644-9.00006-9`.

Melo-Magalhães, E., Medeiros, P., Lira, M., Koening, M., Moura, A., 2009. Determination of eutrophic areas in Mundaú/Manguaba lagoons, Alagoas-Brazil, through studies of the phytoplanktonic community. Brazilian Journal of Biology 69, 271–280. doi:`10.1590/S1519-69842009000200006`.

Mitchell, S.B., Jennerjahn, T.C., Vizzini, S., Zhang, W., 2015. Changes to processes in estuaries and coastal waters due to intense multiple pressures–an introduction and synthesis. Estuarine, Coastal and Shelf Science 156, 1–6. doi:`10.1016/j.ecss.2014.12.027`.

Müller-Wilm, U., Devignot, O., L, P., 2016. Sen2Cor Configuration and User Manual. Technical Report. S2-PDGS-MPC-L2ASUM-V2.5.5, Telespazio VEGA Deutschland GmbH: Darmstadt, Germany.

Oksanen, J., Simpson, G.L., Blanchet, F.G., Kindt, R., Legendre, P., Minchin, P.R., O'Hara, R., Solymos, P., Stevens, M.H.H., Szoecs, E., Wagner, H., Barbour, M., Bedward, M., Bolker, B., Borcard, D., Carvalho, G., Chirico, M., De Caceres, M., Durand, S., Evangelista, H.B.A., FitzJohn, R., Friendly, M., Furneaux, B., Hannigan, G., Hill, M.O., Lahti, L., McGlinn, D., Ouellette, M.H., Ribeiro Cunha, E., Smith, T., Stier, A., Ter Braak, C.J., Weedon, J., 2022. vegan: Community Ecology Package. URL: `https://CRAN.R-project.org/package=vegan`. r package version 2.6-4.

Oliveira, A.M., Kjerfve, B., 1993. Environmental responses of a tropical coastal lagoon system to hydrological variability: Mundaú-Manguaba, Brazil. Estuarine, Coastal and Shelf Science 37, 575–591. doi:`10.1006/ecss.1993.1074`.

Olson, C.R., Solomon, C.T., Jones, S.E., 2020. Shifting limitation of primary production: experimental support for a new model in lake ecosystems. Ecology Letters 23, 1800–1808. doi:`10.1111/ele.13606`.

Orive, E., Elliott, M., de Jonge, V., 2002. Nutrients and eutrophication in estuaries and coastal waters. Springer Netherlands.

Pahlevan, N., Sarkar, S., Franz, B., Balasubramanian, S., He, J., 2017. Sentinel-2 MultiSpectral Instrument (MSI) data processing for aquatic science applications: Demonstrations and validations. Remote Sensing of Environment 201, 47–56.

Qiu, S., Zhu, Z., He, B., 2019. Fmask 4.0: Improved cloud and cloud shadow detection in Landsats 4–8 and Sentinel-2 imagery. Remote Sensing of Environment 231, 111205. doi:`10.1016/j.rse.2019.05.024`.

R Core Team, 2021. R: A Language and Environment for Statistical Computing. R Foundation for Statistical Computing. Vienna, Austria. URL: `https://www.R-project.org/`.

Seekell, D.A., Lapierre, J.F., Ask, J., Bergström, A.K., Deininger, A., Rodríguez, P., Karlsson, J., 2015. The influence of dissolved organic carbon on primary production in northern lakes. Limnology and Oceanography 60, 1276–1285. doi:`10.1002/lno.10096`.

Simpson, G.L., 2019. ggvegan: 'ggplot2' Plots for the 'vegan' Package. R package version 0.1-0.

Souza Jr, C.M., Z. Shimbo, J., Rosa, M.R., Parente, L.L., A. Alencar, A., Rudorff, B.F., Hasenack, H., Matsumoto, M., G. Ferreira, L., Souza-Filho, P.W., et al., 2020. Reconstructing three decades of land use and land cover changes in Brazilian biomes with Landsat archive and Earth Engine. Remote Sensing 12, 2735. doi:`10.3390/rs12172735`.

Tavares, M.H., Lins, R.C., Harmel, T., Fragoso Jr, C.R., Martínez, J.M., Motta-Marques, D., 2021. Atmospheric and sunglint correction for retrieving chlorophyll-a in a productive tropical estuarine-lagoon system using sentinel-2 msi imagery. ISPRS Journal of Photogrammetry and Remote Sensing 174, 215–236. doi:`10.1016/j.isprsjprs.2021.01.021`.

Tundisi, J., Matsumura-Tundisi, T., Abe, D., 2008. The ecological dynamics of Barra Bonita (Tietê River, SP, Brazil) reservoir: implications for its biodiversity. Brazilian Journal of Biology 68, 1079–1098. doi:`10.1590/S1519-69842008000500015`.

Vaičiūtė, D., Bučas, M., Bresciani, M., Dabulevičienė, T., Gintauskas, J., Mėžinė, J., Tiškus, E., Umgiesser, G., Morkūnas, J., De Santi, F., Bartoli, M., 2021. Hot moments and hotspots of cyanobacteria hyperblooms in the Curonian Lagoon (SE Baltic Sea) revealed via remote sensing-based retrospective analysis. Science of The Total Environment 769, 145053. doi:`10.1016/j.scitotenv.2021.145053`.

Valgur, M., Kersten, J., Delucchi, L., Baier, G., unnic Malte, Staniewicz, S., Kinyanjui, L.K., Bahr, V., Salembier, P., martinber, Keller, G., dwlsalmeida, Castro, C., Raspopov, A., 2019. sentinelsat/sentinelsat: v0.13 (v0.13). URL: `https://doi.org/10.5281/zenodo.2629555`. zenodo.

Vanhellemont, Q., 2019. Adaptation of the dark spectrum fitting atmospheric correction for aquatic applications of the Landsat and Sentinel-2 archives. Remote Sensing of Environment 225, 175–192. doi:`10.1016/j.rse.2019.03.010`.

Vanhellemont, Q., Ruddick, K., 2018. Atmospheric correction of metre-scale optical satellite data for inland and coastal water applications. Remote Sensing of Environment 216, 586–597. doi:`10.1016/j.rse.2018.07.015`.

Wainger, L., Yu, H., Gazenski, K., Boynton, W., 2016. The relative influence of local and regional environmental drivers of algal biomass (chlorophyll-a) varies by estuarine location. Estuarine, Coastal and Shelf Science 178, 65–76. doi:`10.1016/j.ecss.2016.05.024`.

Xu, H., 2006. Modification of normalised difference water index (NDWI) to enhance open water features in remotely sensed imagery. International Journal of Remote Sensing 27, 3025–3033.

Zhang, Y., Zhou, L., Zhou, Y., Zhang, L., Yao, X., Shi, K., Jeppesen, E., Yu, Q., Zhu, W., 2020. Chromophoric dissolved organic matter in inland waters: present knowledge and future challenges. Science of The Total Environment , 143550doi:`10.1016/j.scitotenv.2020.143550`.

Capítulo 5

Impacto da correção do efeito de *cool-skin* sobre as tendências da temperatura superficial da água e o balanço de calor de lagos de três grandes lagoas rasas subtropicais

Matheus Henrique Tavares
David da Motta Marques
Carlos Ruberto Fragoso Jr.

Artigo a ser submetido.

Impact of cool-skin effect correction on lake surface water temperature trends and heat budget of three large shallow subtropical lakes

Matheus Henrique Tavares[a,*], David Motta-Marques[a], Carlos Ruberto Fragoso Jr.[b]

[a] *Instituto de Pesquisas Hidráulicas, Universidade Federal do Rio Grande do Sul, 91501-970 Porto Alegre, Brazil*
[b] *Centro de Tecnologia, Universidade Federal de Alagoas, 57072–970 Maceió, Brazil*

Abstract

The cool-skin effect affects the estimation of lake surface water temperatures (LSWT) by thermal infrared sensors due to air-water heat interactions at thin superficial water, which emits thermal radiation (radiometric temperature), causing a negative bias in estimations of bulk surface temperatures (kinetic temperature). The opposite is true for lake-atmosphere heat exchange, when only this thin superficial water layer interacts with the air above the water. When not considering this effect, studies of the impacts of climate change on lake surface water temperature and of lake heat fluxes, which depend on this variable, might substantially under or overestimate changes, although these still need to be quantified. In this study, we first validated two empirical cool-skin correction models, originally developed for oceanic waters, for the MODIS surface temperature product in lake Mangueira, a subtropical shallow Brazilian lake, using ancillary meteorological reanalysis data. The bias between the MODIS-derived LSWT and the *in situ* water temperature was 0.5°C, and both models partially corrected for this, reducing bias to -0.2°C. The model developed by Minnett et al. (2011), which is simpler and depends only on wind speed, showed the best metrics. Despite not being developed for inland waters, the model showed a good performance with reanalysis wind speed data, and it was selected in this study as the best method of correction for the cool-skin effect and applied thereafter. Subsequently, we also assessed the impact of this correction on lake surface water temperature warming and heat balance trends of lake Mangueira and two other nearby large shallow lakes between 2000 and 2022. The effects on the computation of warming rates caused differences around 5%, ranging from 0% to 0.19°C dec^{-1} (26%), with the skin (non-corrected) T_w generally underestimated trends. In terms of trends of $\overline{T_w}$, the results were expressive for Patos Lagoon, with a difference of 0.09°C dec^{-1} (14%). For the computation of lake heat budget, relatively high values for water evaporation, of 7 $\sim$ 9% (oscillating between 2 and 4 W m^{-2} over the period), and high differences in the sensible heat flux, of up to 55%. These differences reflected on generally smaller trends for the heat budget terms when using bulk T_w, with the highest differences being 0.8 W m^{-2} dec^{-1} for Patos Lagoon. Since the cool-skin has an inverse relationship with wind speed, the differences can be even greater in the heat budget of larger, sheltered lakes.

Keywords: Lake surface water temperature, skin effects, thermal infrared remote sensing, lake-atmosphere interactions

---

[*] Correspondence author.
Email address: `tavaresmatheush@gmail.com` (Matheus Henrique Tavares)

Manuscript to be submitted to Journal of Geophysical Research: Atmospheres *March 27, 2023*

1. Introduction

Water temperature is a key physical variable in lentic ecosystems, regulating many processes and metabolic reactions, and is the most directly impacted by climate change (Woolway et al., 2020). These changes include increasing air temperatures and solar radiation (O'Reilly et al., 2015) and variation in surface wind speeds (Woolway et al., 2019), with impacts such as warming temperatures (Livingstone, 2003; Schneider and Hook, 2010; O'Reilly et al., 2015), modified heat exchange and thermal stratification (Lee et al., 2012; Fink et al., 2014; Zhong et al., 2016; Woolway and Merchant, 2018), phenology (Deng et al., 2014), and primary production (O'Reilly et al., 2003).

However, as temperature data are quite scarce, with field monitoring generally at few locations and low frequency, remote sensing data has been increasingly used in studies of climate change impacts on lakes (Schneider and Hook, 2010; O'Reilly et al., 2015; Woolway and Merchant, 2018; Toffolon et al., 2020). Using remote sensing, temperatures are obtained using thermal sensors (in the thermal infrared – TIR – spectral range) aboard satellites (Minnett et al., 2019). Although these estimates have lower accuracy than field measurements, caused by factors such as atmospheric correction (Jiménez-Muñoz et al., 2010), emissivity uncertainty (Wenyao et al., 1987) and adjacency effect (Torgersen et al., 2001), they have the advantage of being spatialised measurements, limited only by the different sensor resolutions, and provide a consistent data for investigating the effects of climate change on aquatic ecosystems on a global scale (Schneider and Hook, 2010; O'Reilly et al., 2015).

A significant limitation of measuring water temperature with thermal infrared sensors is that they measure water's radiometric temperature, *i.e.*, the radiation emitted by the water, according to Planck's law, differing from the kinetic temperature measured by a thermometer. The thermal radiation is emitted at a very thin superficial thermal layer ($\sim$10–20 μm), which is, in most conditions, thinner than the superficial layer interacting with the atmosphere (Wong and Minnett, 2018). Due to the air-water heat interactions, mostly the net flux of long-wave (including thermal) radiation and turbulent (conductive and evaporation) heat fluxes from water to air (Schluessel et al., 1990), this superficial layer, termed the skin layer, is generally colder than the layer of water immediately below. This difference in temperature, which is measured by thermal radiometers but not by thermometers, which measure bulk temperatures, is termed the cool-skin effect and affects the estimation of lake surface water temperatures (LSWT) by TIR sensors aboard satellites, causing a negative bias in estimations of bulk surface temperatures in the order of 0.1 to 1.0°C (Schluessel et al., 1990; MacCallum and Merchant, 2012; Wilson et al., 2013; Alappattu et al., 2017; Prats et al., 2018).

The cool-skin effect has been extensively studied in ocean waters (Robinson et al., 1984; Schluessel et al., 1990; Fairall et al., 1996a; Donlon et al., 2002; Minnett et al., 2011; Alappattu et al., 2017), however, few studies have investigated how this affects measurements of LSWT by radiometers (Oppenheimer, 1997; Wilson et al., 2013; Prats et al., 2018). Many models have been developed to quantify the cool-skin effect on ocean waters, both empirical (Donlon et al., 2002; Alappattu et al., 2017) and deterministic (Fairall et al., 1996b), primarily as a function of wind speed as it regulates both turbulent mixing and net heat flux, as well as air renovation, with stronger winds resulting in thinner cool-skin layer depth and thus lower temperature difference (Fairall et al., 1996a; Donlon et al., 2002). In inland waters, however, studies were limited to investigating the cool-skin effect (Wilson et al., 2013), with Riffler et al. (2015) applying an empirical cool-skin model developed by Minnett et al. (2011) and Prats et al. (2018) assessing the application of a deterministic model to correct for this effect. In this sense, more studies are necessary to assess whether the ocean models can be applied to inland waters.

Additionally, although thermal sensors only measure LSWT, this parameter is critical for understanding the exchange of heat and gases with the atmosphere (Minnett et al., 2019). Climate change has affected the heat exchange between lakes and the atmosphere (emission of long-wave radiation and latent and sensible heat fluxes) (Fink et al., 2014; Zhong et al., 2016). To accurately calculate these fluxes, it is necessary to know the water temperature at the surface layer, which under most conditions is equal to the skin temperature (Oppenheimer, 1997). Oppenheimer (1997) showed that using bulk temperatures to calculate lake latent and sensible heat fluxes resulted in an overestimation of approximately 10%. Cool-skin correction has been shown to improve estimations of air-sea interactions, which are used, for example, in numerical weather prediction (Brodeau et al., 2017; Zhong et al., 2019).

Therefore, the importance of understanding the cool-skin effect for studies of LSWT is two-fold: to accurately determine bulk temperatures when measuring radiometric temperatures, for example, for understanding lake warming rates using remote sensing data, and to accurately determine skin temperatures, when computing lake-atmosphere interactions from bulk temperatures. In this study, we assessed both the occurrence and correction of the cool-skin effect in retrieving LSWT from remote sensing data and its result in studies of climate change impacts on lakes. To achieve this, we first validated two empirical cool-skin correction models, originally developed for oceanic waters, for the MODIS LST product in a monitored subtropical shallow lake using ancillary meteorological reanalysis data. Subsequently, we assessed the impact of this correction on LSWT warming and heat balance trends of this and two other nearby large shallow lakes 22-yr long time series.

2. Methods

2.1. Study area

The study area Brazil's three largest natural lakes (Figure 1): lake Mangueira, lake Mirim, which is partially in Uruguayan territory, and the Patos Lagoon. They are all shallow lakes located in the southernmost state in Brazil, Rio Grande do Sul, resulting from an ancient depression in the coastline enclosed by sand beaches that resulted from the combined actions of wind and ocean currents (Schwarzbold and Schäfer, 1984). The climate in the region is subtropical (Cfa in Köppen's classification), with a mean annual temperature of ∼ 18°C and rainfall ranging from 1,100 mm to 1,600 mm (Kottek et al., 2006), evenly distributed throughout the year, with slightly higher rainfall in winter and drier periods in the summer.

Lake Mangueira is the smaller and the southernmost of the three lakes, with an area of 800 km^2, located in the narrow strip of land between the Atlantic Ocean and lake Mirim. It has an elongated shape, with a length of 90 km and width of 3 to 11.5 km (mean width of 8.3 m), mean depth of 2.6 m, and maximum depth of 7.5 m. It has a small

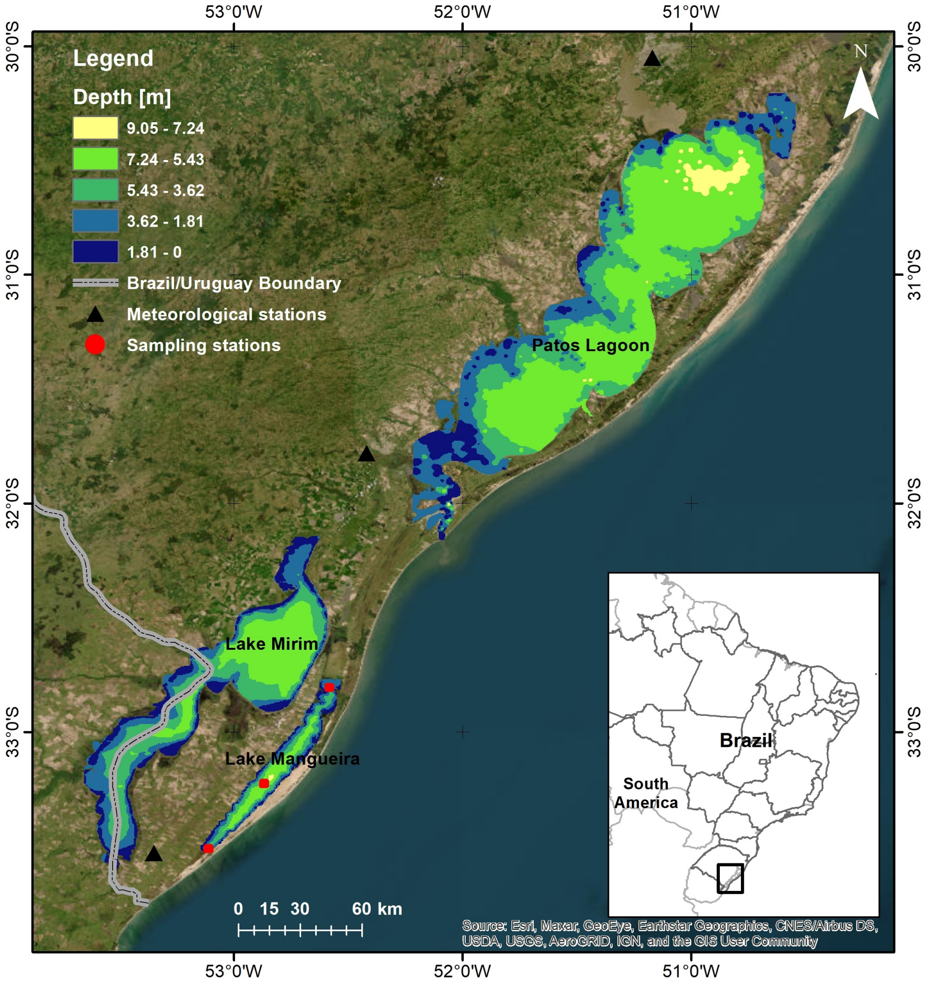

Figure 1: Map of the study area, showing the Patos Lagoon, lake Mirim and lake Mangueira, the sampling stations in lake Mangueira, and the location of the meteorological stations.

watershed, and the main water use is rice irrigation, the main economic activity in the region. Lake Mangueira is the only monitored site with measured temperature data used in this study, further described in Section 2.4.

Lake Mirim is the largest freshwater lake in the region, with an area of 4,000 km^2. It is 200 km along the major axis and 30 km wide on average (maximum width of 43.7 km), with a maximum depth of 10 m and average depth of 4.5 m. Besides ecological importance, it has political and economic significance for being on the Brazil-Uruguay border and its waters supplying the local population and irrigating rice fields.

The Patos Lagoon is the world's largest choked lagoon, with a surface area of approximately 10,000 km^2, 260 km in length in its major axis, maximum width of 60 km, and mean width of 40 km. It is a shallow lagoon with a mean depth of 5 m (maximum depth of 8.5 m), and its waters are generally brackish only in its estuarine region since the effect of the tides is softened by the narrow outlet channel. Here, the estuarine region of the Patos Lagoon was not considered due to the influence of tides and the ocean in the water temperature, as well as the Casamento lake due to the shallowness of Abreu bank, which connects it to the main waterbody and can dry out in periods of low water levels.

All three lakes are shallow and have an elongated shape, with their major axis in the NNE-SSW direction, coincident with the dominant wind direction. In this flat region, winds can be strong and are one of the main drivers of hydrodynamics, especially in lake Mangueira and during low flow periods in the other lakes, producing mixing and preventing stratification longer than a few days during the summer (Fragoso Jr et al., 2011; Munar et al., 2019). In this sense, the warm layer effect was considered negligible for the three lakes, and only the cool-skin effect was considered.

2.2. *MODIS data processing*

MODIS Terra (launched on December 1999) and MODIS Aqua (launched on May 2002) daily LST products (version 6.1) with a nominal spatial resolution of 1 km (actual 0.927 km) at nadir (MOD11A1 and MYD11A1) were obtained for the period from March 2000 (July 2002 for Aqua) to February 2022 from NASA's Application for Extracting and Exploring Analysis Ready Samples (AppEEARS, `https://appeears.earthdatacloud.nasa.gov/`). The MODIS/Terra LST data are recorded at approximately 10:30 a.m. local time, while MODIS/Aqua data are recorded at approximately 1:30 p.m. local time. For nighttime data we only used the observations from Terra, which overpass the study areas at approximately 10:30 p.m. local time.

MODIS LST product derives the temperature with a split-window algorithm (Wan and Dozier, 1996) based on the differential brightness temperature measurements from its two thermal bands, band 31, centred on 11.03 μm, and band 32, centred on 12.02 μm. Water emissivity is derived from the MODIS Emissivity Library (Zhang, 1999) for each thermal band, and the surface temperature is estimated with calibrated coefficients depending on sensor viewing zenith angle, surface air temperature and atmospheric water vapour content.

The MODIS data were processed for the three study areas according to the data quality flag recorded in the quality control (QC) band. Only pixels with errors within 1°C or marked as good data quality (QC = 0, 1, 5, 65) were used, and the remaining pixels were discarded. LSWT data were then aggregated to a 2x2 pixels ($\sim$ 1.8×1.8 km) grid to reduce noise in the remote sensing product. The aggregation was limited to 2 pixels due to the narrowness of lake Mangueira. An inward (negative) buffer of 1 km was used for Mangueira and 2 km for lake Mirim and Patos Lagoon to remove mixed land-water pixels and reduce the adjacency effect.

Processing was carried out in the *R* environment (R Core Team, 2021) with package *terra* (Hijmans, 2021).

2.3. *Cool-skin correction*

We tested two empirical models developed for oceanic waters to correct the cool-skin effect in the remote sensing-derived temperatures. The first model was developed by Minnett et al. (2011) (hereafter named M11), which quantifies this effect based on wind speed and has already been applied to inland waters (Riffler et al., 2015). This model results from a re-calibration of older models based on an exponential function of wind speed (Donlon et al., 2002; Horrocks et al., 2003; Gentemann and Minnett, 2008), and the cool-skin effect is estimated as:

$$T_{skin} = -0.13 - 0.724\exp(-0.35u_{10}) \tag{1}$$

where T_{skin} is the cool-skin effect, and u_{10} is the wind speed measured at 10 m.

The second and more recent model was developed by Alappattu et al. (2017) (hereafter named A17), which parameterises the cool-skin effect into three sub-models, which are functions of the net long-wave radiation flux (R_{lw}, the difference between the incident long-wave radiation and the radiation emitted by the water surface), the time of the day at which the measurement is taken (h), and wind speed. The model also split the wind speed correction step into two models, one for wind speeds up to 4 m s^{-1} and the other for $u > 4$ m s^{-1}, calculating the cool-skin effect as:

$$T_{u>4} = 0.035u_{10}^2 - 0.24u_{10} + 0.85 \tag{2}$$

$$T_{u<4} = -0.0037u_{10} + 0.35 \tag{3}$$

$$T_{hour} = 0.11\sin(10.35h + 0.67) \tag{4}$$

$$T_{lw} = 0.002R_{lw} - 0.15 \tag{5}$$

$$T_{skin} = T_u + T_{hour} + T_{lw} \tag{6}$$

The net long-wave radiation flux is calculated as the difference between the incident long-wave radiation (J_{lw}^{down}) and the radiation emitted by the water surface (J_{lw}^{w}):

$$R_{lw} = J_{lw}^{\mathrm{down}} - J_{lw}^{\mathrm{w}} = J_{lw}^{\mathrm{down}} - \epsilon\sigma(T_w)^4 \tag{7}$$

where $\epsilon = 0.97$ is the water emissivity, $\sigma = 5.67 \times 10^{-8}$ W m^{-2} K^{-4} is the Planck constant, and T_w is the surface water temperature, in K, derived by MODIS.

Due to the limitation of hourly wind speed and incident long-wave radiation measured *in situ* and the spatialisation of these two variables over the lakes, we used the wind speed data from the ERA5 reanalysis (Hersbach et al., 2020) and incident long-wave radiation data from the ERA5 Land (Muñoz-Sabater et al., 2021). Although these products were not validated, meteorological data from ERA5 have already been used to assess changes in temperature and precipitation in the Amazon forest (Xu et al., 2020) and changes in water vapour over Europe (Yuan et al., 2021), for example, and also other reanalysis products were used as a data source for cool-skin correction and comparison (Riffler et al., 2015; Zhang et al., 2019).

Unidimensional wind velocities (u-v) at 10 m above ground are provided at an hourly frequency on a 0.5×0.5°grid and were downloaded from NCAR's Research Data Archive (`https://rda.ucar.edu/datasets/ds633.0/`) and processed for the three lakes. The J_{lw}^{down} data is supplied at an hourly frequency on a 0.1×0.1°grid, and were downloaded from Copernicus's Climate Data Store (`https://cds.climate.copernicus.eu/cdsapp#!/dataset/reanalysis-era5-land`) and processed for the three lakes. First, wind speed in each grid point were calculated ($u = \sqrt{u^2 + v^2}$) and then interpolated on a refined grid using the inverse weighed distance method with a cubic function (*idw* function in package *gstat*, Gräler et al., 2016). The same interpolation was used for the J_{lw}^{down} data. Then, spatialised T_{skin} was calculated for both models, and the LSWT was corrected by adding T_{skin}.

2.4. Validation of MODIS data

Lake Mangueira was selected as the site for validating the cool-skin models. It has already been used for validating MODIS LST data (Tavares et al., 2019), but we conducted a new validation using an incremented measured bulk water temperature dataset. It is monitored by the *Laboratório de Ecotecnologia e Limnologia Aplicada* (Laboratory of Ecotechnology and Applied Limnology) of the Federal University of Rio Grande do Sul (UFRGS) since 2000, with seasonal measurements in three stations spread lengthwise over the lake, as shown in Figure 1. The measurements were made usually in the morning, using a thermometer with a precision of ±0.1°C at a depth of 30–50 cm.

The MODIS water temperature datasets were validated with the *in situ* measured data using matchups with a window of up to 3h between the field measurement and satellite overpass. To obtain the LSWT at the sampling stations, we used a rectangle involving 2×2 pixels at native resolution surrounding each station. In total, we used 118 matchups of *in situ* measured and satellite-derived LSWT. To assess the satellite data, we used bias, the median of errors, the maximum absolute error (Emax) and the root mean squared error (RMSE).

2.5. Meteorological data

To calculate the heat budget of the three lakes, we used the following monthly mean meteorological data: mean air temperature (T_a), relative humidity (RH) and wind speed. While we used the wind speed derived from the ERA5 dataset mentioned above, T_a and RH were retrieved from the three local meteorological stations (Figure 1, from north to south): Porto Alegre (WMO code 83967), Pelotas (83985), and Santa Vitória do Palmar (83997). Due to size of lake Mirim and Patos Lagoon, to represent the climatic forcings over these two lakes, we used the mean of the monthly means at Porto Alegre and Pelotas stations for Patos Lagoon, and the mean of the monthly means at Pelotas and Santa Vitória do Palmar stations for lake Mirim. We used data only at Santa Vitória do Palmar to represent the climatic forcings over lake Mangueira.

To calculate the heat budget, wind speed measured at 10 m was converted to wind at 2 m (Tubelis and Nascimento, 1988):

$$u_2 = u_{10} \times \left(\frac{2}{10}\right)^{1/7} \approx 0.795 u_{10} \tag{8}$$

2.6. Computation of warming trends and heat budget

We compared the trends and heat budget terms calculated with the raw MODIS LSWT data (skin) to those using corrected LSWT data using the best model (bulk), validated in Section 2.4. The seasonal trends calculated with the corrected LSWT have already been estimated by Tavares et al. (2023).

First, we calculated the monthly means of T_w of the entire lakes (lake-average LSWT, $\langle T_w \rangle$) for the period between March 2000 and February 2022 for the three MODIS products: MODIS Terra Day, Terra Night and Aqua Day, and the mean of the three products, $\overline{T_w}$. To calculate the means, we only considered images with a minimum of 70% of valid pixels to avoid artificial spatialisation of water temperature, and monthly means were only calculated for the months with at least 4 valid images. Then, the missing data in the time series of monthly mean $\langle T_w \rangle$ were filled using linear models using as input T_a in the closest station and $\langle T_w \rangle$ derived from the other MODIS products (bias = 0 and RMSE =∼ 0.4°C for all three datasets). In this filling, the Aqua Day time series was also filled from March 2000 to June 2002 to match the length of the Terra series. After processing the time series, we calculated the seasonal (Fall: MAM; Winter: JJA; Spring: SON; Summer: DJF) T_w trends using Sen's slope with the Mann-Kendall (MK) trend analysis and a significance level of 5% and then calculated the absolute and percentage difference between the trends calculated with skin and bulk temperatures.

For computations of the surface heat flux at the water-atmosphere interface, the skin surface temperature must be used, and therefore heat budget computations that employ bulk lake water temperatures generally overestimate the heat exchange (Oppenheimer, 1997). To evaluate this overestimation, we calculated lake heat budget terms on a monthly scale, using $\overline{T_w}$ calculated for each lake, and considering only the terms that depend on T_w: emission of long-wave radiation, and flux of sensible and latent heat (Alcântara et al., 2010). The emission of long-wave radiation is given by equation 7. The flux of sensible heat (conduction) is given by (Large et al., 1997):

$$H = \rho_a C p_a C_s u_2 (T_w - T_a) \tag{9}$$

where $\rho_a = 1.2$ kg m^{-3} is the air density, $Cp_a = 1005$ J kg^{-1} K^{-1} is the specific heat of air, $C_s = 1.1 \times 10^{-3}$ is a coefficient of turbulent heat transfer, and T_a is the mean air temperature.

The flux of latent heat (evaporation) is given by (Large et al., 1997):

$$E = \rho_a Le C_l u_2 0.622 (e_w - RH e_a)/p_a \tag{10}$$

where $Le = 2.264 \times 10^6$ J kg^{-1} is the specific latent heat of vaporisation of water, $C_l = 1.1 \times 10^{-3}$ is a coefficient of turbulent heat transfer, p_a is the atmospheric surface pressure, fixed at 760 mmHg, and e_w e e_{ar} are the saturated vapour pressure at T_w and T_a, respectively, which are approximated by Magnus formula (Raudkivi, 1979):

$$e_{sat}[\text{mmHg}] = 4.596 \exp\left(\frac{17.27T}{237.3 + T}\right) \tag{11}$$

Then, the heat budget terms were aggregated seasonally, and we calculated the absolute and percentage difference between each term for each lake.

Lastly, we also calculated the trends for the seasonal heat budget terms for each lake, using Sen's slope with the Mann-Kendall (MK) trend analysis and a significance level of 5%.

3. Results

Table 1 shows the metrics calculated for the MODIS LSWT data validated at lake Mangueira and with the cool-skin correction by models M11 and A17. We observe a bias of -0.5°C for the raw MODIS data, caused by the cool-skin effect, and that this effect is partially corrected by both models M11 and A17, reducing bias to -0.2°C and the median of errors from -0.4°C to nearly 0. Model M11 also marginally improved the RMSE and Emax, showing the best metrics, although the differences in the results between models M11 and A17 were very small. Therefore, due to simplicity and results, model M11 was selected in this study as the best correction method for the cool-skin effect and applied in the following sections.

Table 1: Metrics (in °C) for the validation of MODIS data without correction and correction with models developed by Minnett et al. (2011) (M11) and Alappattu et al. (2017) (A17). 118 match-ups were used, with a window of time of up to 3h between *in situ* measurements and satellite overpass

Data	**Bias**	**Emax**	**Median**	**RMSE**
No correction	-0.5	4.2	-0.4	1.1
M11	-0.2	3.9	-0.1	1.0
A17	-0.2	4.0	-0.1	1.1

The difference between the seasonal means calculated for the raw and corrected (using model M11) LSWT data showed a mean value close to 0.30°C, with little seasonal variation or among MODIS products, and with the smaller differences found for T_wN ($\overline{T_{skin}}$ = 0.28°C), as in the nighttime winds are stronger, and with the larger differences found in lake Mirim ($\overline{T_{skin}}$ = 0.32°C), the most inland of the lakes, where winds are slightly weaker.

Table 2 shows the difference in the trends calculated for the bulk and skin MODIS LSWT for each season and each lake. We note a few very large percentage differences caused by low warming trends and, therefore, with low statistical significance (Gray et al., 2018). Considering only the significant trends, the differences are around 5%, ranging from 0% for the yearly trends for T_wD for lake Mangueira to 0.19°C dec^{-1} (26%) for T_wA for the Patos Lagoon in spring, a considerably high difference. The skin MODIS LSWT generally resulted in lower warming trends, although exceptions occurred. In terms of trends of T_w mean, which indicates the general seasonal warming rates of the lakes and are significant only in spring (except for the yearly trends for lake Mangueira), the results are also only expressive for Patos Lagoon, with a difference of 0.09°C dec^{-1} (14%).

Table 3 shows the mean heat budget terms calculated with the bulk (corrected for the cool-skin) and skin T_w for each lake for the period between March 2000 and February 2022. We note a very small difference in the emission of long-wave radiation, around 0.5%, higher values for water evaporation, of 7 $\sim$ 9%, and high differences in the sensible heat flux, the smaller heat budget term, of up to 55%. Since the emission of long-wave radiation is much larger than the other two terms, the difference in the total heat budget calculated here is small, up to 1.6% for Patos Lagoon. Figure 2 shows these differences for each season for the study period, totalling 88 seasons. The variation in J_{lw} is nearly constant over the whole period, and because of this, the sum of the three terms is as well, in percentage difference. The absolute difference of the sum of the three terms, however, shows a marked seasonality, as for all three terms, the dependency on T_w enhances the differences when winds are weaker, *i.e.*, in fall and winter, especially due to differences in lake evaporation, which mostly oscillates between 2 and 4 W m^{-2} over the period, with a mean of 3.3 W m^{-2} (8.8%) in fall and of 2.1 W m^{-2} (11.1%) in winter, and in the summer when lake evaporation is higher, with a mean of 3.8 W m^{-2} (6.9%). The percentage difference shows peaks for latent and especially sensible heat, occurring mainly when the

Table 2: Absolute (percentage) difference in the trends, in °C dec^{-1} (%) calculated for the bulk (corrected with model M11) and skin T_w. The reference trends were calculated with the corrected bulk temperatures, available in Tavares et al. (2023). Values in bold indicate significant trends

Season	**Lake**	**Terra Day**	**Terra Night**	**Aqua Day**	**T_w mean**
Autumn	**Patos**	-0.01 (-4.2)	-0.05 (-323.1)	0.01 (14.7)	0.00 (1.7)
	Mirim	0.01 (16.0)	-0.01 (-168.6)	0.01 (10.3)	-0.02 (-48.0)
	Mang.	0.02 (10.7)	-0.02 (-10.3)	-0.01 (-27.3)	-0.02 (-17.2)
Winter	**Patos**	0.03 (13.7)	0.03 (59.6)	-0.04 (-36.9)	0.01 (76.1)
	Mirim	0.00 (-4.4)	0.00 (7.2)	-0.01 (-8.6)	0.00 (5.1)
	Mang.	0.09 (226.4)	0.04 (18.7)	-0.14 (-63.0)	-0.03 (-20.8)
Spring	**Patos**	**0.10 (14.7)**	**0.02 (2.0)**	**0.19 (26.0)**	**0.09 (13.9)**
	Mirim	**-0.02 (-6.0)**	**0.00 (0.4)**	**0.08 (10.7)**	**0.01 (1.5)**
	Mang.	**0.01 (3.0)**	0.02 (4.7)	**-0.01 (-2.6)**	**-0.01 (-1.1)**
Summer	**Patos**	**0.05 (14.6)**	0.00 (1.0)	-0.01 (-7.8)	0.01 (3.3)
	Mirim	-0.01 (-4.5)	-0.03 (-12.2)	-0.04 (-103.3)	0.00 (-1.9)
	Mang.	**-0.03 (-10.3)**	**-0.03 (-7.6)**	0.00 (-1.2)	0.02 (5.0)
Year	**Patos**	**0.05 (16.7)**	**0.01 (2.1)**	**0.04 (20.0)**	0.03 (13.6)
	Mirim	-0.02 (-8.56)	**0.00 (-1.7)**	0.02 (12.5)	0.01 (2.4)
	Mang.	**0.00 (0.0)**	**-0.01 (-3.8)**	-0.01 (-8.4)	**-0.02 (-8.0)**

difference between T_w and T_a is small.

Table 4 shows the trends of each heat budget term for each lake in each season. There are some expressive differences in the trends, generally higher for the skin T_w, with the larger variation found for the Patos Lagoon and in the fall and winter, when wind speeds are lower. Considering only the significant trends (which, as occurred with the temperature trends, are concentrated in spring), the differences are smaller, with the highest differences found for the sum of the three terms, of up to 0.8 W m^{-2} dec^{-1} for Patos Lagoon. We can also see that the trends are only significant in a few cases when using the skin T_w, especially in fall, due to higher trends.

4. Discussion

4.1. Cool-skin correction

Despite the incremented dataset, the validation of raw MODIS LSWT data showed the same metrics reported in the previous study in lake Mangueira (Tavares et al., 2019), with a bias of -0.5°C and RMSE of 1.1°C. The methods of cool-skin correction developed by ocean waters partially corrected for this bias, with the model developed by Minnett et al. (2011) and by Alappattu et al. (2017) improving all metrics. Besides not being developed for inland waters, these models depend on hourly, site-specific input data, especially wind speeds, which are difficult to obtain, especially for

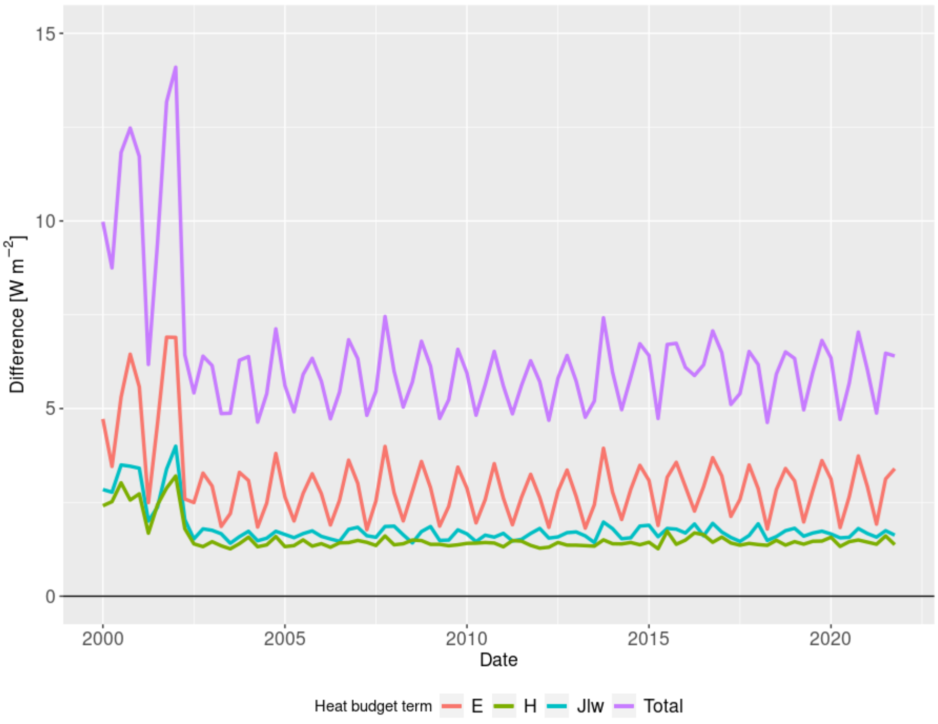

(a) Absolute

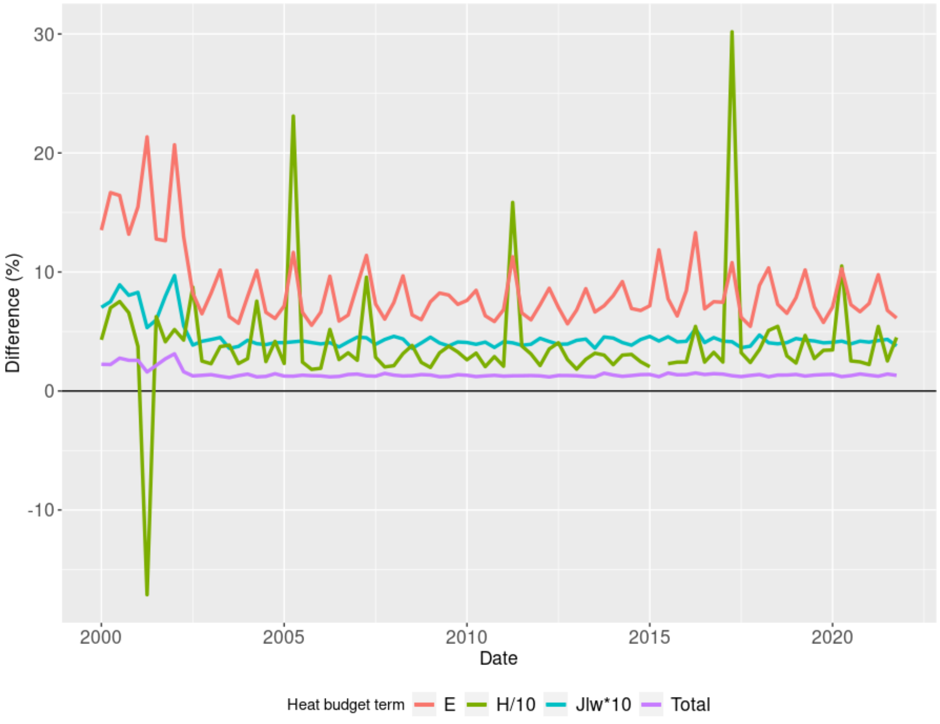

(b) Percentage

Figure 2: a) Absolute and b) percentage difference in the seasonal heat budget terms calculated with the bulk and skin T_w. The values were calculated as the mean of the terms for the three lakes. In b) the differences in H were divided by 10, and the differences in J_{lw} were multiplied by 10 to improve visualisation. One H data point was omitted for resulting in a difference of over 1000%.

Table 3: Long-term mean of the terms of lake heat budget (in W m^{-2}) calculated with the bulk and skin T_w. Percentage differences were calculated in relation to the lake heat budget calculated with the skin T_w

Lake	Term	bulk T_w	skin T_w	Diff (%)
Patos	J_{lw}	405.4	403.5	0.5
	H	3.2	1.4	54.8
	E	40.3	36.8	8.7
	Total	448.9	441.8	1.6
Mirim	J_{lw}	400.5	398.6	0.5
	H	4.8	3.3	30.8
	E	33.6	30.7	8.6
	Total	438.9	432.7	1.4
Mang.	J_{lw}	398.3	396.7	0.4
	H	6.1	4.7	23.2
	E	39.8	37.1	6.7
	Total	444.2	438.5	1.3

*J_{lw} = emission of longwave radiation; H = flux of sensible heat; E = flux of latent heat

large water bodies such as the lakes studied here, where a considerable spatial variation can occur (Minnett et al., 2019). The ERA5 wind speed data used here were robust enough to improve the accuracy of the remote sensing-derived LSWT data, even though this data has not been, to our knowledge, validated in Brazil, and other reanalysis datasets have already been used in studies of cool-skin effect in ocean and inland waters (Riffler et al., 2015; Zhang et al., 2019). More accurate sources of wind data can further enhance the quality of cool-skin correction, but the ERA5 data could be a dependable source of wind speed data for large-scale correction of remote sensing-derived LSWT.

The models showed very similar metrics, despite having different parameterisations. However, when inspecting them, the two models provide very similar results for wind speeds up to 3 m s^{-1} but diverge for stronger winds, which are common in the region, when model A17 estimates higher T_{skin}. The addition of the other submodels (using the hour of the day and net long-wave radiation) slightly reduces this overcorrection compared to model M11, which results in close estimations of T_{skin}. A limiting factor for model A17 is the source of incident long-wave radiation, the ERA5 Land (Muñoz-Sabater et al., 2021), which does not have grid points over water bodies and, therefore, the data over the lake depends on the spatial interpolation of the surrounding land grid points, impairing its quality. This significantly affects the ability of the submodel to correct for the cool-skin effect, although its overall effect is limited when compared with the wind speed effect on T_{skin}, but *in situ* J_{lw}^{down} data will likely enhance the model, correcting for the still negative bias found here.

The cool-skin was not completely removed using the models, which can be a limitation of the models, as they were

Table 4: Seasonal trends of each heat budget term (in W m^{-2} dec^{-1}) calculated with the bulk and skin T_w

Season		**Fall**			**Winter**			**Spring**			**Summer**		
Term		**Patos**	**Mirim**	**Mang.**	**Patos**	**Mirim**	**Mang.**	**Patos**	**Mirim**	**Mang.**	**Patos**	**Mirim**	**Mang.**
bulk T_w	J_{lw}	0.7	0.3	0.4	-0.1	-0.2	-0.7	**2.0**	**2.9**	**2.8**	1.5	1.5	1.8
	H	0.7	-0.4	**-0.8**	0.2	0.0	-0.6	0.7	1.2	0.8	-0.2	-0.5	-0.7
	E	3.1	1.3	1.9	0.2	0.5	0.1	2.5	**4.0**	**4.2**	0.4	-0.4	1.4
	Total	3.0	0.5	1.9	1.0	0.0	-1.5	**7.5**	**6.8**	**7.1**	2.0	1.6	1.9
skin T_w	J_{lw}	1.2	0.3	0.6	0.9	0.0	-0.6	**3.2**	**3.2**	**2.7**	2.1	2.0	1.8
	H	**1.0**	0.1	**-0.8**	0.5	0.1	-0.4	1.2	1.3	0.7	0.1	-0.1	-0.7
	E	**4.4**	2.5	1.9	0.8	0.4	0.1	2.8	**4.3**	**4.1**	1.7	0.6	1.2
	Total	**6.1**	2.3	2.0	3.3	0.4	-1.0	**8.3**	**7.5**	**7.0**	3.8	2.2	2.1

*J_{lw} = emission of longwave radiation; H = flux of sensible heat; E = flux of latent heat

developed for ocean waters, or as Wilson et al. (2013) asserted, it is not possible to correct for this effect in inland waters using solely wind speed, as the other effects have higher importance than in ocean waters. They found, for example, a large variation of the skin effect during weak winds (from -1 to +1°C, from Lake Tahoe buoys), which is due to dominant convective heat exchange (Fairall et al., 1996a; Donlon et al., 2002) and the possible formation of a warm layer. This effect occurs when there is a large $T_a - T_w$ difference and thermal stratification occurs (Zhang et al., 2019), which rarely occurs in lake Mangueira, but adds a positive bias in the skin temperature, masking the cool-skin effect. A few validation data points showed an overestimation of T_w by MODIS, suggesting that this effect might be relevant during low wind speeds (although less pronounced than what was found by Wilson et al. 2013 in Lake Tahoe), and the cool-skin could be stronger than the bias of 0.5°C observed here, as seen in other studies (Crosman and Horel, 2009; Liu et al., 2015).

Other limiting factors on the validation of MODIS-derived LSWT are the intrapixel variation, which can be considerable in lake Mangueira due to its narrowness, and the water temperature variability between the *in situ* measurement and satellite overpass (limited to 3h), although the diel variation of temperature in the lake is relatively low, of around 0.7°C (Tavares et al., 2023). Furthermore, the formation of a warm layer could also impair the validation of the cool-skin correction, as discussed above, and limitations in the remote estimation of LSWT add further uncertainty in the data, including instrument calibration (Hulley et al., 2011), noise, atmospheric correction, and emissivity uncertainty (Li et al., 2013), resulting in the almost invariant RMSE. All in all, due to the simplicity of the model M11, it is recommended over the model A17, and further testing is required for its application over inland waters. Additional discussion on the accuracy of remote sensing-derived LSWT is provided in Prats et al. (2018) and Tavares et al. (2019), for example.

4.2. *Effects on warming trends and heat budget*

We observe that the impact of cool-skin correction was generally limited, with most differences of ~ 5%, when considering only the significant trends, but expressive in a few cases, especially in the Patos Lagoon, when differences were up to 0.19°C dec^{-1} (26%). As expected, the trends deviated less during nighttime, when winds are stronger, and T_{skin} is smaller. The spatial variability in T_{skin} could be a key factor in the differences in the trends, as the results showed a gradient in the differences from the largest (Patos Lagoon) to the smallest (lake Mangueira) lake, suppressing the effect of wind speeds, as winds are weaker in the more inland lake Mirim (Tavares et al., 2023). The effect in the trends, therefore, can be more relevant in large, sheltered lakes (*e.g.*, Lake Tahoe, Wilson et al., 2013), but we acknowledge that the length of the series here is short (22 yrs) for a more robust analysis of the trends, especially considering that the trends in spring and summer are around 0.5 and 0.3°C dec^{-1}, respectively, considerably lower than the threshold of 1°C dec^{-1} stipulated by Gray et al. (2018) for robust trend estimation of LSWT series shorter than 30 yrs. The effect on longer series should be further investigated, but it might be lower than what we found here using MODIS-derived data.

To our knowledge, this is the study to assess the impact of skin correction on the calculation of warming trends of LSWT. A few studies have estimated trends with a fixed bias correction (*e.g.*, Liu et al. 2015), however, such an approach does not correct for the small trend differences we found as cool-skin depends on spatiotemporal wind speeds, *i.e.*, it has monthly, seasonal and interannual variation, for example, due to atmospheric stilling (Woolway et al., 2019), impacting the trends. Other studies have indicated such impact; Pareeth et al. (2017), for example, suggested that one possible reason for the different trends they calculated for Italian alpine lakes, compared with Riffler et al. (2015), could be the lack of cool-skin correction, as Riffler et al. (2015) applied the model M11. Other studies, for example those that use LSWT derived from the Along Track Scanning Radiometer (MacCallum and Merchant, 2012; Woolway and Merchant, 2018) without cool-skin correction, may also have underestimated epilimnetic warming rates.

While the use of bulk (*i.e.*, cool-skin corrected) LSWT is necessary for robust estimation of epilimnetic warming rates, to calculate lake heat flux the opposite is required, as the interaction of water-atmosphere occurs at the very thin superficial thermal layer (Wong and Minnett, 2018) where the skin temperatures are estimated by thermal infrared sensors (Minnett et al., 2019). Here we showed that using bulk temperatures can substantially overestimate surface heat fluxes, with the effects on lake evaporation being the most important, with differences up to 20% (7 W m^{-2}), mainly in fall and winter, when winds are weaker, generally ranging between 8–12% (2–4 W m^{-2}). Zhang et al. (2019), for example, found an overestimation of 18% in the latent heat flux in the South China Sea when using bulk temperatures, where the application of the COARE algorithm to correct for the cool-skin effect initially reduced it to 8.5%. Similarly, on a sensitivity analysis, Brodeau et al. (2017) reported that the cool-skin correction could impact up to 10% in air-sea heat fluxes. For inland waters, Oppenheimer (1997) found similar results, with an overestimation of nearly 10% in both latent and sensible heat fluxes in a crater lake, however, in this case resulting from a bias of -1.5°C, much higher than what we found in lake Mangueira. The differences in the latent heat fluxes, however, were similar, but for sensible heat flux we found much higher overestimation, with a mean value up to 55% for the Patos Lagoon.

Studies that employ lake models (*e.g.*, General Lake Model) or that use heat flux equating with *in situ* measured water surface kinetic temperatures to estimate surface heat fluxes generally do not consider the cool-skin effect (*e.g.*, Fink et al. 2014; Woolway et al. 2018), which results in overestimation of heat fluxes and possibly underestimating heat budget trends, as found here in most cases. The phenomenon of atmospheric stilling, reported in the Northern Hemisphere and related to accelerated lake warming (Woolway et al., 2019), potentially enhances the overestimation of heat fluxes, although it may also induce the formation of stronger warm layers, as it results in stronger thermal stratification. Cool-skin correction or reparametrisation of heat flux equations considering bulk temperatures (Oppenheimer, 1997) will help reduce this overestimation, although other processes, such as the formation of the warm layer, will still influence the heat budget calculations.

We highlight that winds in our study area are strong and, for the three shallow lakes, produce mixing and drive the hydrodynamics during most of the year (Fragoso Jr et al., 2011; Munar et al., 2018). Conversely, for lakes where winds are weaker, the cool-skin effect is more pronounced (Wilson et al., 2013), and, therefore, the difference in trends and heat budget can be even more expressive, especially in lakes where wind speed can have a high spatial variability.

4.3. Considerations on heat fluxes

Here we showed that the use of bulk or skin T_w impacts the estimation of the heat budget terms, especially of latent heat flux, which is of substantial importance as it is a major form of lake heat and water loss. However, we also have to consider that we only analysed the sensibility of the equations to the cool-skin correction, but the equating itself and the precision of the other variables, such as air temperature and especially wind speed, a reanalysis product, should also be taken into account. Furthermore, since the remote sensing-derived LSWT data had many missing data, mostly due to cloud cover, we calculated the heat flux on a monthly scale (Alcântara et al., 2010), which increases uncertainty. Other assumptions, such as a fixed coefficient of heat transfer (which depends on wind speed, for example Garfinkel et al. 2011) and atmospheric pressure, also impact the estimations.

The estimated heat budget terms (Table S1) and trends are relatively homogeneous for all three lakes, with the most significant trends concentrated in spring, as expected since it is when the higher warming rates are found (Tavares et al., 2023). Across all seasons, the trends were generally positive, except for lake Mangueira in a few cases. Also using monthly means of MODIS-derived LSWT, Alcântara et al. (2010) found monthly latent heat fluxes of 20–120 W m^{-2} for a large reservoir in Central Brazil, roughly in the same order of magnitude as our results, considering that this region has very marked seasons, with monthly mean relative humidity varying between 45–80% over the year. The annual mean and seasonal variation of the heat budget is also in the same order of magnitude as those calculated by Munar et al. (2019), modelling lake Mirim's heat budget using a hydrodynamic-water quality coupled model, finding (with bulk temperatures) an annual mean of 51.1 W m^{-2} for the latent heat flux, and of 6.7 W m^{-2} for the sensible heat flux. The overestimation, compared to our computations, probably arise from a large LSWT bias (1.45°C in relation to MODIS-derived LSWT), which has been shown in other studies (Heiskanen et al., 2015). Also modelling lake heat budgets, Woolway et al. (2018) showed that the relative contribution of latent heat can represent more than 90% of total turbulent lake heat loss, with a larger contribution at the tropics and decreasing with latitude mostly due to decreased evaporation. Our results agree with these findings with a relatively larger contribution of E, as it ranged from 89% in lake Mangueira to 96% in Patos Lagoon, the latter being due to its large surface area and strong winds (Woolway et al., 2018), enhancing evaporation.

To our knowledge, only Fink et al. (2014) calculated trends of the lake heat budget terms to assess the observed warming trend of 0.46°C dec^{-1} in Lake Constance using lake modelling. The authors found a mean of 42.6 W m^{-2} for E and 14.6 W m^{-2} for H, with trends of 2.7 and -0.3 W m^{-2} dec^{-1}, respectively. The results diverge from what we found here for H, possibly for being deep and in a much colder region, where the difference between T_w and T_a is more significant, but for E the results are similar, indicating a similar magnitude of this increase despite the different geographic and morphological characteristics. The rates found here for evaporation can have a significant effect on reducing water level, which in turn can decrease water clarity and further enhance surface heating (Rose et al., 2016). All in all, the results found here help to further understand the warming rates in these three large subtropical shallow lakes (Tavares et al., 2023).

5. Conclusion

In this study, we validated two empirical cool-skin correction models, originally developed for oceanic waters, for the MODIS surface temperature product in lake Mangueira, a subtropical shallow Brazilian lake, using ancillary meteorological reanalysis data. Subsequently, we also assessed the impact of this correction on lake surface water temperature warming and heat balance trends of lake Mangueira and two other nearby large shallow lakes between 2000 and 2022. The bias between the MODIS-derived LSWT and the *in situ* water temperature was 0.5°C, caused by the cool-skin effect, and both models partially corrected for this effect, reducing bias to -0.2°C and the median of errors from -0.4°C to nearly 0. The model developed by Minnett et al. (2011), which is simpler and depends only on wind speed, also marginally improved the RMSE and Emax, showing the best metrics by a slight margin. Despite not being developed for inland waters, the model showed a good performance with reanalysis wind speed data, and it was selected in this study as the best method of correction for the cool-skin effect, applied in the following tests.

The effects of this correction on the computation of warming rates caused differences of around 5%, ranging from 0% to 0.19°C dec^{-1} (26%), a considerably high difference. The skin (non-corrected) T_w generally underestimated trends. In terms of trends of $\overline{T_w}$, the results were only expressive for Patos Lagoon, with a difference of 0.09°C dec^{-1} (14%). For the computation of lake heat budget, when the use of bulk water temperatures causes overestimation of the heat fluxes, we observed a very small difference in the emission of long-wave radiation (~0.5%), higher values for water evaporation, of $7 \sim 9\%$ (oscillating between 2 and 4 W m^{-2} over the period), and high differences in the sensible heat flux, the smaller heat budget term, of up to 55%, resulting in a small difference in the sum of the three terms (since J_{lw} is much larger than the other two terms), with the larger difference being of 1.6% for Patos Lagoon. These differences reflected on generally smaller trends for the heat budget terms when using bulk T_w, with the highest differences found for the sum of the three terms, of up to 0.8 W m^{-2} dec^{-1} for Patos Lagoon. We also observed, in a few cases, that trends were only significant when using the skin T_w, especially in fall, due to the higher trends. These differences can be even greater in the heat budget of larger, sheltered lakes.

Acknowledgements

This work was carried out with the support of CNPq, Conselho Nacional de Desenvolvimento Científico e Tecnológico - Brazil through the scholarship number 140505/2020-2. We would like to thank NASA for MODIS imagery, NOAA/ECMWF for the ERA5 Reanalysis data, and INMET for the meteorological data. We are also grateful to the Global Lake Ecological Observatory Network (GLEON: `www.gleon.org`) and the network with Institut de Recherche pour le Développement (IRD) Montpellier for joint lake science and modeling development.

References

Alappattu, D.P., Wang, Q., Yamaguchi, R., Lind, R.J., Reynolds, M., Christman, A.J., 2017. Warm layer and cool skin corrections for bulk water temperature measurements for air-sea interaction studies. Journal of Geophysical Research: Oceans 122, 6470–6481. doi:`10.1002/2017JC012688`.

Alcântara, E.H., Stech, J.L., Lorenzzetti, J.A., Bonnet, M.P., Casamitjana, X., Assireu, A.T., de Moraes Novo, E.M.L., 2010. Remote sensing of water surface temperature and heat flux over a tropical hydroelectric reservoir. Remote Sensing of Environment 114, 2651–2665.

Brodeau, L., Barnier, B., Gulev, S.K., Woods, C., 2017. Climatologically significant effects of some approximations in the bulk parameterizations of turbulent air–sea fluxes. Journal of Physical Oceanography 47, 5–28. doi:`10.1175/JPO-D-16-0169.1`.

Crosman, E.T., Horel, J.D., 2009. MODIS-derived surface temperature of the Great Salt Lake. Remote Sensing of Environment 113, 73–81.

Deng, J., Qin, B., Paerl, H.W., Zhang, Y., Ma, J., Chen, Y., 2014. Earlier and warmer springs increase cyanobacterial (Microcystis spp.) blooms in subtropical Lake Taihu, China. Freshwater Biology 59, 1076–1085. doi:`10.1111/fwb.12330`.

Donlon, C., Minnett, P., Gentemann, C., Nightingale, T., Barton, I., Ward, B., Murray, M., 2002. Toward improved validation of satellite sea surface skin temperature measurements for climate research. Journal of Climate 15, 353–369. doi:`10.1175/1520-0442(2002)015<0353:TIVOSS>2.0.CO;2`.

Fairall, C.W., Bradley, E.F., Godfrey, J.S., Wick, G.A., Edson, J.B., Young, G.S., 1996a. Cool-skin and warm-layer effects on sea surface temperature. Journal of Geophysical Research: Oceans 101, 1295–1308.

Fairall, C.W., Bradley, E.F., Rogers, D.P., Edson, J.B., Young, G.S., 1996b. Bulk parameterization of air-sea fluxes for tropical ocean-global atmosphere coupled-ocean atmosphere response experiment. Journal of Geophysical Research: Oceans 101, 3747–3764. doi:`10.1029/95JC03205`.

Fink, G., Schmid, M., Wahl, B., Wolf, T., Wüest, A., 2014. Heat flux modifications related to climate-induced warming of large European lakes. Water Resources Research 50, 2072–2085. doi:`10.1002/2013WR014448`.

Fragoso Jr, C.R., Marques, D.M.M., Ferreira, T.F., Janse, J.H., van Nes, E.H., 2011. Potential effects of climate change and eutrophication on a large subtropical shallow lake. Environmental Modelling & Software 26, 1337–1348.

Garfinkel, C.I., Molod, A., Oman, L., Song, I.S., 2011. Improvement of the GEOS-5 AGCM upon updating the air-sea roughness parameterization. Geophysical Research Letters 38. doi:`10.1029/2011GL048802`.

Gentemann, C.L., Minnett, P.J., 2008. Radiometric measurements of ocean surface thermal variability. Journal of Geophysical Research: Oceans 113. doi:`10.1029/2007JC004540`.

Gray, D.K., Hampton, S.E., O'Reilly, C.M., Sharma, S., Cohen, R.S., 2018. How do data collection and processing methods impact the accuracy of long-term trend estimation in lake surface-water temperatures? Limnology and Oceanography: Methods 16, 504–515. doi:`10.1002/lom3.10262`.

Gräler, B., Pebesma, E., Heuvelink, G., 2016. Spatio-temporal interpolation using gstat. The R Journal 8, 204–218. URL: `https://journal.r-project.org/archive/2016/RJ-2016-014/index.html`.

Heiskanen, J.J., Mammarella, I., Ojala, A., Stepanenko, V., Erkkilä, K.M., Miettinen, H., Sandström, H., Eugster, W., Leppäranta, M., Järvinen, H., Vesala, T., Nordbo, A., 2015. Effects of water clarity on lake stratification and lake-atmosphere heat exchange. Journal of Geophysical Research: Atmospheres 120, 7412–7428. doi:`10.1002/2014JD022938`.

Hersbach, H., Bell, B., Berrisford, P., Hirahara, S., Horányi, A., Muñoz-Sabater, J., Nicolas, J., Peubey, C., Radu, R., Schepers, D., Simmons, A., Soci, C., Abdalla, S., Abellan, X., Balsamo, G., Bechtold, P., Biavati, G., Bidlot, J., Bonavita, M., Chiara, G.D., Dahlgren, P., Dee, D., Diamantakis, M., Dragani, R., Flemming, J., Forbes, R., Fuentes, M., Geer, A., Haimberger, L., Healy, S., Hogan, R.J., Hólm, E., Janisková, M., Keeley, S., Laloyaux, P., Lopez, P., Lupu, C., Radnoti, G., de Rosnay, P., Rozum, I., Vamborg, F., Villaume, S., Thépaut, J.N., 2020. The ERA5 global reanalysis. Quarterly Journal of the Royal Meteorological Society 146, 1999–2049. doi:`10.1002/qj.3803`.

Hijmans, R.J., 2021. terra: Spatial Data Analysis. URL: `https://CRAN.R-project.org/package=terra`. r package version 1.4-22.

Horrocks, L.A., Candy, B., Nightingale, T.J., Saunders, R.W., O'Carroll, A., Harris, A.R., 2003. Parameterizations of the ocean skin effect and implications for satellite-based measurement of sea-surface temperature. Journal of Geophysical Research: Oceans 108. doi:`10.1029/2002JC001503`.

Hulley, G.C., Hook, S.J., Schneider, P., 2011. Optimized split-window coefficients for deriving surface temperatures from inland water bodies. Remote Sensing of Environment 115, 3758–3769.

Jiménez-Muñoz, J.C., Sobrino, J.A., Mattar, C., Franch, B., 2010. Atmospheric correction of optical imagery from MODIS and Reanalysis atmospheric products. Remote Sensing of Environment 114, 2195–2210.

Kottek, M., Grieser, J., Beck, C., Rudolf, B., Rubel, F., 2006. World map of the Köppen-Geiger climate classification updated. Meteorologische Zeitschrift 15, 259–263.

Large, W.G., Danabasoglu, G., Doney, S.C., McWilliams, J.C., 1997. Sensitivity to surface forcing and boundary layer mixing in a global ocean model: Annual-mean climatology. Journal of Physical Oceanography 27, 2418–2447. doi:`10.1175/1520-0485(1997)027<2418:STSFAB>2.0.CO;2`.

Lee, H.W., Kim, E.J., Park, S.S., Choi, J.H., 2012. Effects of climate change on the thermal structure of lakes in the asian monsoon area. Climatic Change 112, 859–880.

Li, Z.L., Tang, B.H., Wu, H., Ren, H., Yan, G., Wan, Z., Trigo, I.F., Sobrino, J.A., 2013. Satellite-derived land surface temperature: Current status and perspectives. Remote Sensing of Environment 131, 14–37.

Liu, G., Ou, W., Zhang, Y., Wu, T., Zhu, G., Shi, K., Qin, B., 2015. Validating and mapping surface water temperatures in Lake Taihu: Results from MODIS land surface temperature products. IEEE Journal of Selected Topics in Applied Earth Observations and Remote Sensing 8, 1230–1244.

Livingstone, D.M., 2003. The warming of lake Tahoe. Climatic Change 57, 205–225.

MacCallum, S.N., Merchant, C.J., 2012. Surface water temperature observations of large lakes by optimal estimation. Canadian Journal of Remote Sensing 38, 25–45.

Minnett, P., Alvera-Azcárate, A., Chin, T., Corlett, G., Gentemann, C., Karagali, I., Li, X., Marsouin, A., Marullo, S., Maturi, E., et al., 2019. Half a century of satellite remote sensing of sea-surface temperature. Remote Sensing of Environment 233, 111366. doi:`10.1016/j.rse.2019.111366`.

Minnett, P.J., Smith, M., Ward, B., 2011. Measurements of the oceanic thermal skin effect. Deep Sea Research Part II: Topical Studies in Oceanography 58, 861–868. doi:`10.1016/j.dsr2.2010.10.024`.

Munar, A.M., Cavalcanti, J.R., Bravo, J.M., Fan, F.M., Motta-Marques, D.M.L., Fragoso Jr, C.R., 2018. Coupling large-scale hydrological and hydrodynamic modeling: Toward a better comprehension of watershed-shallow lake processes. Journal of Hydrology 564, 424–441.

Munar, A.M., Cavalcanti, J.R., Bravo, J.M., Motta-Marques, D., Fragoso Jr., C.R., 2019. Assessing the large-scale variation of heat budget in poorly gauged watershed shallow lake system using a novel integrated modeling approach. Journal of Hydrology 575, 244–256. doi:`10.1016/j.jhydrol.2019.05.025`.

Muñoz-Sabater, J., Dutra, E., Agustí-Panareda, A., Albergel, C., Arduini, G., Balsamo, G., Boussetta, S., Choulga, M., Harrigan, S., Hersbach, H., et al., 2021. ERA5-Land: A state-of-the-art global reanalysis dataset for land applications. Earth System Science Data 13, 4349–4383.

Oppenheimer, C., 1997. Ramifications of the skin effect for crater lake heat budget analysis. Journal of Volcanology and Geothermal Research 75, 159–165. doi:`10.1016/S0377-0273(96)00037-6`.

O'Reilly, C.M., Alin, S.R., Plisnier, P.D., Cohen, A.S., McKee, B.A., 2003. Climate change decreases aquatic ecosystem productivity of Lake Tanganyika, Africa. Nature 424, 766–768.

O'Reilly, C.M., Sharma, S., Gray, D.K., Hampton, S.E., Read, J.S., Rowley, R.J., Schneider, P., Lenters, J.D., McIntyre, P.B., Kraemer, B.M., et al., 2015. Rapid and highly variable warming of lake surface waters around the globe. Geophysical Research Letters 42, 10–773.

Pareeth, S., Bresciani, M., Buzzi, F., Leoni, B., Lepori, F., Ludovisi, A., Morabito, G., Adrian, R., Neteler, M., Salmaso, N., 2017. Warming trends of perialpine lakes from homogenised time series of historical satellite and in-situ data. Science of the Total Environment 578, 417–426. doi:`10.1016/j.scitotenv.2016.10.199`.

Prats, J., Reynaud, N., Rebière, D., Peroux, T., Tormos, T., Danis, P.A., 2018. LakeSST: Lake Skin Surface Temperature in French inland water bodies for 1999–2016 from Landsat archives. Earth System Science Data 10, 727–743.

R Core Team, 2021. R: A Language and Environment for Statistical Computing. R Foundation for Statistical Computing. Vienna, Austria. URL: `https://www.R-project.org/`.

Raudkivi, A.J., 1979. Hydrology. Pergamon, Oxford, England.

Riffler, M., Lieberherr, G., Wunderle, S., 2015. Lake surface water temperatures of European Alpine lakes (1989–2013) based on the Advanced Very High Resolution Radiometer (AVHRR) 1 km data set. Earth System Science Data 7, 1–17. doi:`10.5194/essd-7-1-2015`.

Robinson, I., Wells, N., Charnock, H., 1984. The sea surface thermal boundary layer and its relevance to the measurement of sea surface temperature by airborne and spaceborne radiometers. International Journal of Remote Sensing 5, 19–45.

Rose, K.C., Winslow, L.A., Read, J.S., Hansen, G.J., 2016. Climate-induced warming of lakes can be either amplified or suppressed by trends in water clarity. Limnology and Oceanography Letters 1, 44–53. doi:`10.1002/lol2.10027`.

Schluessel, P., Emery, W.J., Grassl, H., Mammen, T., 1990. On the bulk-skin temperature difference and its impact on satellite remote sensing of sea surface temperature. Journal of Geophysical Research: Oceans 95, 13341–13356.

Schneider, P., Hook, S.J., 2010. Space observations of inland water bodies show rapid surface warming since 1985. Geophysical Research Letters 37.

Schwarzbold, A., Schäfer, A., 1984. Gênese e morfologia das lagoas costeoras do Rio Grande do Sul-Brasil. Amazoniana: Limnologia et Oecologia Regionalis Systematis Fluminis Amazonas 9, 87–104.

Tavares, M.H., Cardoso, M.A., Motta-Marques, D., Fragoso Jr, C.R., 2023. High warming rates in spring in three large shallow subtropical lakes in southern Brazil detected with MODIS imagery. Submitted to Science of the Total Environment .

Tavares, M.H., Cunha, A.H.F., Motta-Marques, D., Ruhoff, A.L., Cavalcanti, J.R., Fragoso Jr, C.R., Bravo, J.M., Munar, A.M., Fan, F.M., Rodrigues, L.H.R., 2019. Comparison of methods to estimate lake-surface-water temperature using Landsat 7 ETM+ and MODIS imagery: case study of a large shallow subtropical lake in Southern Brazil. Water 11, 168.

Toffolon, M., Piccolroaz, S., Calamita, E., 2020. On the use of averaged indicators to assess lakes' thermal response to changes in climatic conditions. Environmental Research Letters 15, 034060. doi:`10.1088/1748-9326/ab763e`.

Torgersen, C.E., Faux, R.N., McIntosh, B.A., Poage, N.J., Norton, D.J., 2001. Airborne thermal remote sensing for water temperature assessment in rivers and streams. Remote Sensing of Environment 76, 386–398.

Tubelis, A., Nascimento, F.J.L., 1988. Meteorologia descritiva; fundamentos e aplicações brasileiras. Nobel.

Wan, Z., Dozier, J., 1996. A generalized split-window algorithm for retrieving land-surface temperature from space. IEEE Transactions on Geoscience and Remote Sensing 34, 892–905.

Wenyao, L., Field, R., Gantt, R., Klemas, V., 1987. Measurement of the surface emissivity of turbid waters. Remote Sensing of Environment 21, 97–109.

Wilson, R.C., Hook, S.J., Schneider, P., Schladow, S.G., 2013. Skin and bulk temperature difference at Lake Tahoe: A case study on lake skin effect. Journal of Geophysical Research: Atmospheres 118, 10–332. doi:`10.1002/jgrd.50786`.

Wong, E.W., Minnett, P.J., 2018. The response of the ocean thermal skin layer to variations in incident infrared radiation. Journal of Geophysical

Research: Oceans 123, 2475–2493. doi:`10.1002/2017JC013351`.

Woolway, R.I., Kraemer, B.M., Lenters, J.D., Merchant, C.J., O'Reilly, C.M., Sharma, S., 2020. Global lake responses to climate change. Nature Reviews Earth & Environment 1, 388–403. doi:`10.1038/s43017-020-0067-5`.

Woolway, R.I., Merchant, C.J., 2018. Intralake heterogeneity of thermal responses to climate change: A study of large Northern Hemisphere lakes. Journal of Geophysical Research: Atmospheres 123, 3087–3098.

Woolway, R.I., Merchant, C.J., Van Den Hoek, J., Azorin-Molina, C., Nõges, P., Laas, A., Mackay, E.B., Jones, I.D., 2019. Northern Hemisphere atmospheric stilling accelerates lake thermal responses to a warming world. Geophysical Research Letters 46, 11983–11992. doi:`10.1029/2019GL082752`.

Woolway, R.I., Verburg, P., Lenters, J.D., Merchant, C.J., Hamilton, D.P., Brookes, J., de Eyto, E., Kelly, S., Healey, N.C., Hook, S., et al., 2018. Geographic and temporal variations in turbulent heat loss from lakes: A global analysis across 45 lakes. Limnology and Oceanography 63, 2436–2449. doi:`10.1002/lno.10950`.

Xu, X., Jia, G., Zhang, X., Riley, W.J., Xue, Y., 2020. Climate regime shift and forest loss amplify fire in amazonian forests. Global Change Biology 26, 5874–5885. doi:`10.1111/gcb.15279`.

Yuan, P., Hunegnaw, A., Alshawaf, F., Awange, J., Klos, A., Teferle, F.N., Kutterer, H., 2021. Feasibility of ERA5 integrated water vapor trends for climate change analysis in continental Europe: An evaluation with GPS (1994–2019) by considering statistical significance. Remote Sensing of Environment 260, 112416. doi:`10.1016/j.rse.2021.112416`.

Zhang, H., Babanin, A.V., Liu, Q., Ignatov, A., 2019. Cool skin signals observed from Advanced Along-Track Scanning Radiometer (AATSR) and in situ SST measurements. Remote Sensing of Environment 226, 38–50. doi:`10.1016/j.rse.2019.03.035`.

Zhang, Y., 1999. MODIS UCSB Emissivity Library. `https://icess.eri.ucsb.edu/modis/EMIS/html/em.html`. Acessed on November 22nd 2017.

Zhong, Y., Notaro, M., Vavrus, S.J., 2019. Spatially variable warming of the Laurentian Great Lakes: an interaction of bathymetry and climate. Climate Dynamics 52, 5833–5848. doi:`10.1007/s00382-018-4481-z`.

Zhong, Y., Notaro, M., Vavrus, S.J., Foster, M.J., 2016. Recent accelerated warming of the Laurentian Great Lakes: Physical drivers. Limnology and Oceanography 61, 1762–1786. doi:`10.1002/lno.10331`.

Capítulo 6

Altas taxas de aquecimento na primavera em três grandes lagoas rasas subtropicais no sul do Brasil detectadas com imagens MODIS

Matheus Henrique Tavares
Maria Angélica Cardoso
David da Motta Marques
Carlos Ruberto Fragoso Jr.

Artigo a ser submetido.

High spring warming rates in three large subtropical shallow lakes in southern Brazil detected with MODIS imagery

Matheus H. Tavares[a,*], Maria Angélica Cardoso[a], David Motta-Marques[a], Carlos Ruberto Fragoso Jr.[b]

[a]*Instituto de Pesquisas Hidráulicas, Universidade Federal do Rio Grande do Sul, 91501-970 Porto Alegre, Brazil*
[b]*Centro de Tecnologia, Universidade Federal de Alagoas, 57072–970 Maceió, Brazil*

Abstract

Air temperature increase impacts on lake surface water temperature (LSWT) have been well documented in deep northern lakes, however, these impacts are less understood in the southern hemisphere, especially in shallow lakes. In this study, we assessed seasonal warming rates of three large shallow lakes in southern Brazil using a 22-year time series of meteorological data and LSWT derived from MODIS imagery. We found high regional warming of lake water concentrated in spring (mean trend of 0.5°C dec^{-1}) and, to a lesser extent, in summer (0.3°C dec^{-1}), with agreement between the air and water temperature trends, as well as substantial shortening of the cold season and increase of maximum and minimum air temperatures in these two seasons. Data also showed an overall homogeneity of the warming rates but with notable spatial differences that may result from the tributaries' temperature, discharge, or water clarity variability. The high warming rates found here are comparable to those found in deep northern lakes, but with distinguished changes and processes involved in the heating. The warming is stronger in early spring, resulting, for example, in earlier start of phytoplankton phenology, and the spatial differences in the warming can have additional ecological impacts such as changes in thermal habitat suitability.

Keywords: Lake surface water temperature, shallow lakes, warming rates, remote sensing, MODIS

---

[*] Correspondence author.
Email address: `tavaresmatheush@gmail.com` (Matheus H. Tavares)

Manuscript to be submitted to Science of the Total Environment *March 27, 2023*

1. Introduction

Water temperature is a key physical variable in lentic ecosystems, regulating many processes and metabolic reactions, and is the most directly impacted by climate change (Woolway et al., 2020). These changes include increasing air temperatures and solar radiation (O'Reilly et al., 2015) and variation in surface wind speeds (Woolway et al., 2019a), with impacts such as warming temperatures (Livingstone, 2003; Schneider and Hook, 2010; O'Reilly et al., 2015), modified heat exchange and thermal stratification (Lee et al., 2012; Fink et al., 2014; Zhong et al., 2016; Woolway and Merchant, 2018), phenology (Deng et al., 2014) and primary production (O'Reilly et al., 2003).

Studies conducted in the northern hemisphere showed that the current rate of warming temperatures is unprecedented (Woolway et al., 2017) in both meteorological drivers and lake responses (Schmid and Köster, 2016; Zhong et al., 2016; Woolway et al., 2019a), however much less attention is paid to lakes in the southern hemisphere. A few studies have explored the yearly warming rates in lakes with different geographic and climatic characteristics (O'Reilly et al., 2015; Piccolroaz et al., 2020), but none, to our knowledge, have focused on the impacts of recent warming on Southern lakes, especially shallow lakes.

Additionally, recent studies have shown that to understand these impacts better, yearly warming rates are insufficient, as the trends have different seasonal or monthly magnitudes, which can be masked when analysing yearly means (Winslow et al., 2017; Woolway et al., 2017; Kelleher et al., 2021). It is especially important when considering that lower trends may be estimated with significant differences from their true value for shorter or less consistent water temperature series (Gray et al., 2018), and that different strength among seasonal trends can have deep effects in lake ecosystems (Winslow et al., 2017).

Furthermore, it has already been shown that besides seasonal or monthly differences, spatial differences are also relevant (Woolway and Merchant, 2018; Toffolon et al., 2020; Calamita et al., 2021), and differential water warming can have additional effects on lake ecosystems such as variability in thermal habitat suitability (Halverson et al., 2021; Hansen, 2021). Regular temporal time series of *in situ* measured temperatures are essential to understand lake response to warming temperatures, however remote sensing techniques can complement this monitoring by providing spatially-resolved lake surface water temperatures (LSWT), which can be applied to understanding the spatial differences in water warming (Woolway and Merchant, 2018). These differences have been mostly related to summer warming and thermal stratification of deep lakes (Woolway and Merchant, 2018; Zhong et al., 2019), and Toffolon et al. (2020) indicated that shallower lakes have a more homogeneous response to warming temperatures, especially in the summer, but this has to be further explored.

This study aims to assess the impacts of climate variability in the LSWT of three subtropical shallow lakes in southern Brazil, taking advantage of the spatial and temporal capabilities of the MODIS sensors, aboard the Aqua and Terra satellites, using a 22-year time series to investigate *a)* the seasonal warming rates and *b)* how different parts of these lakes respond to climate change.

2. Methods

2.1. Study area

The study area contains Brazil's three largest natural lakes (Figure 1): lake Mangueira, lake Mirim, which is partially in Uruguayan territory, and the Patos Lagoon. They are all shallow lakes located in the southernmost state in Brazil, Rio Grande do Sul, resulting from an ancient depression in the coastline enclosed by sand beaches that resulted from the combined actions of wind and ocean currents (Schwarzbold and Schäfer, 1984). The climate in the region is subtropical (Cfa in Köppen's classification), with mean annual temperature of ∼ 18°C and rainfall ranging from 1,100 mm to 1,600 mm (Kottek et al., 2006), evenly distributed throughout the year, with slightly higher rainfall in winter and drier periods in the summer. Table 1 shows lake characteristics, and meteorological and water temperature means calculated for the study period.

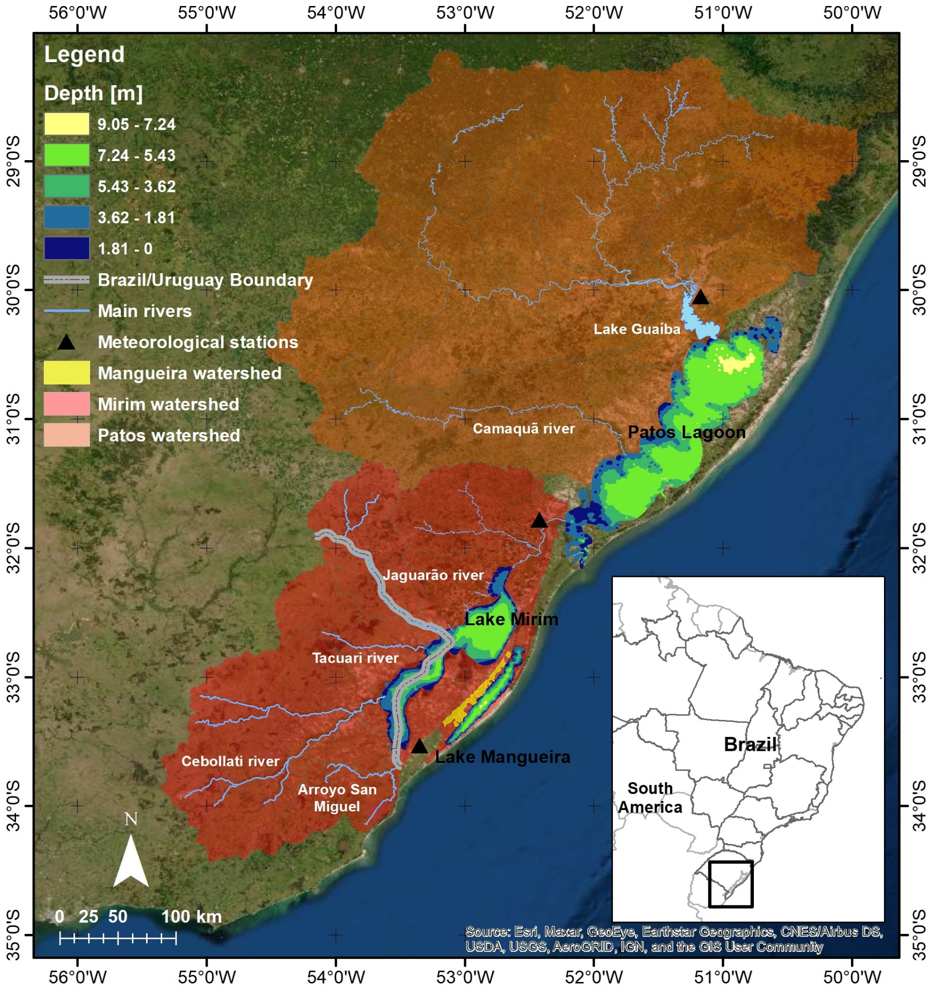

Figure 1: Map of the study area, showing the Patos lagoon, lake Mirim and lake Mangueira, their watersheds, and the location of the meteorological stations.

This region contains three Ramsar sites: Lagoa do Peixe, a brackish lagoon located between Patos Lagoon and the Atlantic Ocean, the Taim Ecological Station, a freshwater wetland with diverse ecosystems located north of lake Mangueira, and the Bañados del Este, a large wetland complex comprised of fresh and brackish water located southwest of lake Mirim. They all harbour high biodiversity and are important zones of wintering and staging for migratory birds.

Table 1: Lake characteristics and long-term monthly means (standard deviation) of the meteorological and LSWT data for each lake/station for the study period (2000-2022)

Parameter	**Patos/Porto Alegre**	**Mirim/Pelotas**	**Mangueira/Santa Vitória**
Latitude	-31.2°	-32.8°	-33.2°
Longitude	-51.4°	-53.2°	-52.8°
Area [km^2]	10,000	4,000	800
Perimeter [km]	1,200	740	272
Mean depth [m]	5.0	4.5	2.6
Maximum depth [m]	8.5	10.0	7.5
Fetch [NNE, km]	168.9	90.4	50.7
Mean air temperature [°C]	20.0 (4.0)	18.2 (4.1)	17.2 (4.2)
Maximum air temperature [°C]	25.7 (4.2)	23.5 (4.1)	22.2 (4.4)
Minimum air temperature [°C]	16.0 (3.8)	14.3 (4.0)	13.4 (4.0)
Precipitation [mm/month]	125.9 (64.7)	119.3 (72.3)	102.6 (70.2)
Radiation [hours of sunlight]	6.0 (1.7)	6.5 (1.6)	6.3 (1.7)
Relative humidity [%]	76.7 (4.8)	82.5 (3.9)	80.0 (4.6)
Wind speed [m/s]	4.8 (0.6)	4.1 (0.5)	4.6 (0.5)
Water temperature (mean) [°C]	19.8 (4.0)	18.9 (4.5)	18.5 (4.3)
Water temperature (Terra Day) [°C]	19.6 (4.0)	18.6 (4.5)	18.4 (4.4)
Water temperature (Aqua Day) [°C]	20.7 (4.3)	20.0 (4.9)	19.2 (4.4)
Water temperature (Terra Night) [°C]	19.1 (3.8)	18.0 (4.2)	17.8 (4.2)
Diel temperature range [°C]	0.4 (0.7)	0.6 (0.7)	0.7 (0.6)

Lake Mangueira is the smaller and the southernmost of the three lakes, with an area of 800 km^2, located in the narrow strip of land between the Atlantic Ocean and lake Mirim. It has an elongated shape, with a length of 90 km and width of 3 to 11.5 km (mean width of 8.3 m), mean depth of 2.6 m, and maximum depth of 7.5 m. It is a seepage lake with a small watershed (area of 400 km^2), and its water flows to the Taim wetland, which then flows to lake Mirim. The main water use is rice irrigation, the leading economic activity in the region.

Lake Mirim is the largest freshwater lake in the region, with an area of 4,000 km^2. It is 200 km long along the major axis and 30 km wide on average (maximum width of 44 km), with a maximum depth of 10 m and an average depth of 4.5 m. Besides ecological importance, it has political and economic significance for being on the Brazil-Uruguay border, serving as water supply for the local population and for irrigating rice fields. Unlike lake Mangueira, it has a large watershed, with a surface area of 58,400 km^2, almost equally divided between Uruguay and Brazil, and with Jaguarão, Cabollati, and Tacuari rivers as main tributaries. Lake Mirim is connected, at its northernmost tip, to the Patos Lagoon through the São Gonçalo Channel, discharging into the estuarine region of the lagoon.

The Patos Lagoon is the world's largest choked lagoon, with a surface area of approximately 10,000 km^2, 260 km in length in its major axis, a maximum width of 60 km, and a mean width of 40 km. It is a shallow lagoon with a mean depth of 5 m (maximum depth of 8.5 m). Its waters are generally brackish only in its estuarine region since the effect of the tides is softened by the narrow outlet channel, and the lagoon is mostly composed of freshwater coming from its large watershed (approximately 120,000 km^2, not considering lake Mirim's watershed), comprised of the rivers Caí, Gravataí, Taquari, and Jacuí, whose delta forms lake Guaíba, which flows into the northwest part of the Patos Lagoon, and the Camaquã river. Here, the estuarine region of the Patos Lagoon was not considered due to the influence of tides and the ocean in the water temperature, nor was the Casamento lake due to the shallowness of Abreu bank, which connects it to the main waterbody and can dry out in periods of low water levels.

All three lakes are shallow and have an elongated shape, with their major axis in the NNE-SSW direction, coincident with the dominant wind direction. In this flat region, wind can be strong and is one of the main drivers of hydrodynamics, especially in lake Mangueira and during low flow periods in the other lakes, producing mixing and preventing longer periods of stratification during summer, although it occurs ephemerally (Fragoso Jr et al., 2011; Munar et al., 2019).

2.2. Data sources and processing

2.2.1. MODIS data processing

MODIS Terra (launched on December 1999) and MODIS Aqua (launched on May 2002) daily LST products (version 6.1) with a nominal spatial resolution of 1 km (actual 0.927 km) at nadir (MOD11A1 and MYD11A1) were obtained for the period from March 2000 (July 2002 for Aqua) to February 2022 from NASA's Application for Extracting and Exploring Analysis Ready Samples (AppEEARS, `https://appeears.earthdatacloud.nasa.gov/`). The MODIS/Terra LST data are recorded at approximately 10:30 a.m. local time, while MODIS/Aqua data are recorded at approximately 1:30 p.m. local time. For nighttime data we only used the observations from Terra, which overpass the study areas at approximately 10:30 p.m. local time.

MODIS LST product derives the temperature with a split-window algorithm (Wan and Dozier, 1996) based on the differential brightness temperature measurements from its two thermal bands, band 31, centred on 11.03 μm, and band 32, centred on 12.02 μm. Water emissivity is derived from the MODIS Emissivity Library (Zhang, 1999) for each thermal band, and the surface temperature is estimated with calibrated coefficients depending on sensor viewing zenith angle, surface air temperature and atmospheric water vapour content.

The MODIS data were processed for the three study areas according to the data quality flag recorded in the quality control (QC) band. Only pixels with errors within 1°C or marked as good data quality (QC = 0, 1, 5, 65) were used, and the remaining pixels were discarded. LSWT data were then aggregated to a 2x2 pixels (~ 1.8×1.8 km) grid to reduce noise in the remote sensing product. The aggregation was limited to 2 pixels due to the narrowness of lake Mangueira. An inward (negative) buffer of 1 km was used for Mangueira and 2 km for lake Mirim and Patos Lagoon to remove mixed land-water pixels and reduce the adjacency effect.

Processing was carried out in the *R* environment (R Core Team, 2021) with package *terra* (Hijmans, 2021).

Cool-skin correction. To correct for the cool-skin effect in the remote sensing-derived temperatures (Wilson et al., 2013), we applied the empirical model developed by Minnett et al. (2011) for oceanic waters, which quantifies this effect based on wind speed, and has already been applied to inland waters (Riffler et al., 2015). This model was validated in lake Mangueira (Tavares et al., 2023, $n = 118$, bias = -0.2°C, RMSE = 1.0°C), reducing bias in 0.3°C and improving all metrics. In this model, the cool-skin effect is estimated as follows:

$$T_{skin} = -0.13 - 0.724 \exp(-0.35u) \tag{1}$$

where T_{skin} is the temperature difference resulting from the cool-skin effect, and u is the wind speed measured at 10 m.

Due to the limitation of hourly wind speed and the spatialisation of these two variables over the lakes, we used wind speed data from the ERA5 reanalysis (Hersbach et al., 2020). Although this product was not validated, meteorological data from ERA5 have already been used, for example, to assess changes in temperature and precipitation in the Amazon forest (Xu et al., 2020) and changes in water vapour over Europe (Yuan et al., 2021), and other reanalysis products were used in studies of climate change impacts over lakes (Piccolroaz et al., 2020; Toffolon et al., 2020).

Unidimensional wind velocities (u_x–u_y) at 10 m above ground are provided at an hourly frequency on a 0.5×0.5°grid and were downloaded from NCAR's Research Data Archive (`https://rda.ucar.edu/datasets/ds633.0/`) and processed for the three lakes. First, wind speed in each grid point was calculated ($u = \sqrt{u_x^2 + u_y^2}$) and then interpolated on a refined grid using the inverse weighed distance method with a cubic function (*idw* function in package *gstat*, Gräler et al., 2016). Then, spatialised T_{skin} was calculated using equation 1, and the LSWT in each pixel was corrected by adding T_{skin}.

2.2.2. Meteorological data

Meteorological data, comprising of mean (T_a med), maximum (T_a max) and minimum (T_a min) air temperature, relative humidity (RH), and solar radiation (Rad, in hours of sunlight) were retrieved from the three local meteorological stations (Figure 1, from north to south): Porto Alegre (WMO code 83967), Pelotas (83985) and Santa Vitória do Palmar (83997), to represent the climatic forcings over the Patos Lagoon, lake Mirim and lake Mangueira, respectively. Due to a lack of consistent monitoring and to maintain coherence, we used wind speed data from the ERA5 reanalysis, calculating the daily means over each lake.

2.3. Data analysis

To analyse data, we calculated the monthly means of LSWT and meteorological data for the three lakes and three stations. To be consistent with seasons, the years were accounted for by starting in austral Fall (March, April, and May) and ending in Summer (December, January, and February). Furthermore, as all three stations had no data collected in 1987, we analysed the meteorological data for the period between March 2000 and February 2022 as well as starting in 1988 (except for Pelotas, which had continuous data collection starting in 1996) to investigate long-term climate change patterns. The LSWT data was explored data spatially and temporally, analysing the intralake variation of temperature for the period from 2002 to 2022 (due to the launching date of the Aqua satellite) and conducting a temporal analysis of lake-averaged water temperatures ($\langle T_w \rangle$) starting in 2000.

The monthly means of the meteorological data were calculated considering a minimum of 25 daily observations. A linear model was developed for each variable using data from the other two meteorological stations to fill in missing data. For the LSWT data, we calculated the monthly mean pixels values for each dataset, Aqua ($\langle T_w \rangle$A), Terra Day ($\langle T_w \rangle$D), and Terra Night ($\langle T_w \rangle$N), considering only images with a minimum of 70% of valid pixels to avoid artificial spatialisation of water temperature, and monthly means were only calculated for the months with at least four valid images. The spatial LSWT monthly mean ($\overline{T_w}$) was then calculated as the mean value of these three datasets, and $\langle T_w \rangle$ was calculated for the mean as well as each dataset (consisting of 4 time series of $\langle T_w \rangle$) and filled using linear models (the Aqua Day time series was), using as input T_a in the closest station and $\langle T_w \rangle$ derived from the other MODIS products (bias = 0 and RMSE =~ 0.4°C for all three datasets). In this filling, the Aqua Day time series was also filled from March 2000 to June 2002 to match the length of the Terra series.

After processing the time series, we calculated the monthly and seasonal (Fall: MAM; Winter: JJA; Spring: SON; Summer: DJF) trends using Sen's slope with the Mann-Kendall (MK) trend analysis and a significance level of 5% for $\langle T_w \rangle$, the meteorological time series, and for the seasonal means of each pixel in each lake to assess intralake differences.

We also used the warming efficiency introduced by Toffolon et al. (2020), a simple index to assess the relationship between air and water temperature variations in time:

$$\eta = \frac{\Delta \langle T_w \rangle}{\Delta T_a} \tag{2}$$

where $\Delta \langle T_w \rangle$ and ΔT_a are the seasonal variation of lake averaged water and air temperatures, respectively.

While in Toffolon et al. (2020) the authors considered different periods of air and LSWT warming, here we only assessed η to assess seasonal warming (*e.g.*, for warming during the summer). A value of $\eta = 1$ indicates that the lake surface water warmed/cooled exactly as much as air temperatures during a certain period of time, for $\eta > 1$ the lake showed increased warming/cooling than air, and $\eta < 1$ indicates reduced lake response in comparison to air temperatures. For lake Mangueira, T_a was taken as the measurement at Santa Vitória do Palmar station, while for lake Mirim it was considered as the mean of T_a at Santa Vitória do Palmar and Pelotas stations, and for Patos Lagoon as the mean of T_a at Pelotas and Porto Alegre stations.

Following Toffolon et al. (2020), we examined the spatial temperature differences between the hottest and coldest years in the series. The five hottest and coldest years of each season were selected regionally, and the differences were calculated for both water (pixel by pixel, the difference between the mean hottest and mean coldest years in the series) and air temperatures.

We also assessed whether the air and water temperatures are influenced by the El Niño-Southern Oscillation (ENSO) variability during the study period. The ENSO was assessed using the Oceanic Niño Index (ONI Index; three-month running mean of ERSST.v5 SST anomalies in the Niño 3.4 region). These data were obtained from the National Oceanographic and Atmospheric Administration (NOAA) website (`https://origin.cpc.ncep.noaa.gov/products/analysis_monitoring/ensostuff/ONI_v5.php`), considering the 12-months-mean value (March–February) of the ONI index. The periods of La Niña comprised the years 2000, 2007, 2008, 2010, 2011, 2020, and 2021, while periods of El Niño comprised the years 2002, 2004, 2009, and 2015.

To further assess significant changes in the regional climate, we calculated the temperature indices developed by the WMO/WCRP/JCOMM Expert Team on Climate Change Detection and Indices (Karl et al., 1999; Peterson et al., 2001), which are standardised indices to detect changes in the climate extremes. Here we calculated the trends in selected temperature indices, in addition to the yearly 20°C crossing date, widely used in limnological studies (*e.g.*, Winslow et al., 2017):

- SU – Number of summer days: Annual count of days when TX (daily maximum temperature) > 25°C (trend in days per decade)
- TR – Number of tropical nights: Annual count of days when TN (daily minimum temperature) > 20°C (trend in days per decade)
- TXx – Hottest day: Maximum value of TX in each month (trend in °C per decade)
- TNx – Warmest night: Maximum value of TN in each month (trend in °C per decade)
- TXn – Coldest day: Minimum value of TX in each month (trend in °C per decade)
- TNn – Coldest night: Minimum value of TN in each month (trend in °C per decade)
- DTR: mean Diurnal Temperature Range (TX - TN) in each month (trend in °C per decade)
- ETR: Extreme Temperature Range (TXx - TNn) in each month (trend in °C per decade)
- Fall (start) and Spring (end) 20°C crossing date, and length of season when $T_a < 20$°C (trend in days per decade); since summer occurs before winter in a calendar year in the southern hemisphere, we considered the season where temperatures are <20°C to account for this variability in a single year. They were calculated using a moving average of 10 days to minimise the effects of cold and warm fronts, which are common in the region

These indices are based on daily air temperature data, and missing data in series were linearly interpolated. Regular Mann-Kendall trend analysis was employed for the yearly data, and for the monthly indices, the seasonal Mann-Kendall trend analysis was applied, both with a significance level of 5%.

3. Results

3.1. Temporal analysis

Table 2 shows the trends calculated for each lake and its closest meteorological station for each season for the 22-year period. It shows significant and high warming trends of T_w in the austral spring, of 0.5°C dec^{-1} for lakes Mangueira and Mirim and 0.6°C dec^{-1} for Patos Lagoon, with the trends consistent across all MODIS products. In spring, the results show higher a increment in T_w in comparison to T_a. In summer, the opposite was found, with higher warming trends of T_a, especially in the region of lake Mangueira, and lower trends of T_w, of ~0.3°C dec^{-1}. Trends in fall and winter were found to be low and not significant. Other results are the consistent increase in the minimum air temperatures (trends close to 1°C dec^{-1} throughout the year) and decreased relative humidity (up to -2% dec^{-1} in fall) in the region of lake Mangueira, and relative increase in solar radiation, especially in the northern part of the Patos Lagoon in summer.

Table 2: Seasonal trends (unit per decade) of the meteorological and LSWT data for each lake/station. Significant trends are in bold

Season	**Fall**			**Winter**			**Spring**			**Summer**		
Variable	**Patos**	**Mirim**	**Mang.**	**Patos**	**Mirim**	**Mang.**	**Patos**	**Mirim**	**Mang.**	**Patos**	**Mirim**	**Mang.**
T_a **med**	0.1	0.0	0.2	0.0	-0.1	0.0	0.4	0.3	0.4	0.4	0.3	**0.5**
T_a **max**	0.2	0.5	0.4	0.2	0.3	-0.1	0.5	0.4	0.2	**0.7**	**0.6**	**0.5**
T_a **min**	0.0	-0.3	**0.7**	-0.2	-0.4	0.6	0.3	0.2	**1.0**	0.2	0.0	**0.8**
u	0.0	0.0	0.0	0.0	0.0	0.0	0.1	**0.1**	0.1	0.0	0.0	0.0
RH	-1.1	-0.8	**-2.2**	-0.9	0.1	**-1.0**	-0.1	0.4	-0.8	-0.7	1.2	-0.8
Rad	0.1	0.4	0.4	0.1	0.1	0.1	0.3	-0.1	-0.1	**0.6**	0.0	0.1
Terra Day	0.2	0.0	0.1	0.2	-0.1	0.0	**0.7**	**0.4**	**0.4**	**0.3**	0.3	**0.3**
Terra Night	0.0	0.0	0.2	0.0	-0.1	-0.2	**0.8**	**0.5**	0.5	0.2	0.3	**0.3**
Aqua Day	0.1	-0.1	0.0	-0.1	-0.1	-0.2	**0.7**	**0.8**	**0.5**	0.2	0.0	0.2
$\langle\overline{T_w}\rangle$	0.1	0.0	0.1	0.0	0.0	-0.2	**0.6**	**0.5**	**0.5**	0.3	0.3	0.3

Table 3 shows the climate indices calculated for each station. These results evidence the warming trends observed in the region, reinforced by considering a longer period of time, showing a consistent increase of temperature extremes, with an increasing number of days with mean temperatures over 25°C (over 12 days dec^{-1} for both Pelotas and Porto Alegre stations) and of both maximum and minimum T_a max in the region, as well as increase of both maximum and minimum T_a min in the region of lake Mangueira. Interestingly, it also shows an increase in the daily temperature range in Pelotas station, while a decrease was observed in the southerly Santa Vitória station.

It is also clear that the length of the cold season decreased, with a rate of -11.7 days dec^{-1} in both Pelotas and Santa Vitória stations between 2000 and 2021, which is caused mainly by an earlier ending of the cold season, with the spring

Table 3: Trends of the climate indices calculated at each meteorological station. Significant trends are in bold

Index	**Porto Alegre**		**Pelotas**		**Sta. Vitória**	
	2000-	1988-	2000-	1996-	2000-	1988-
SU [days decade^{-1}]	**12.5**	**8.2**	**12.5**	**14.0**	**7.1**	3.3
TR [days decade^{-1}]	7.5	**6.4**	0.0	1.0	**11.6**	**6.7**
TXx [°C decade^{-1}]	**0.6**	**0.4**	0.5	**0.7**	0.2	0.2
TNx [°C decade^{-1}]	0.1	**0.3**	0.0	0.0	**0.7**	**0.4**
TXn [°C decade^{-1}]	**0.4**	**0.4**	**0.4**	**0.4**	0.2	**0.3**
TNn [°C decade^{-1}]	0.3	**0.6**	-0.1	-0.2	**0.9**	**0.6**
DTR [°C decade^{-1}]	0.2	-0.1	**0.5**	**0.5**	**-0.5**	**-0.3**
ETR [°C decade^{-1}]	0.3	-0.2	0.8	**1.0**	-0.6	**-0.4**
Fall 20°C crossing date [days decade^{-1}]	4.8	3.6	2.2	5.5	2.1	4.2
Spring 20°C crossing date [days decade^{-1}]	2.0	-5.3	-6.0	-1.5	-10.8	-4.8
Length of cold season* [days decade^{-1}]	-4.3	-10.0	-11.7	-6.9	**-11.7**	**-10.0**

*season where mean air temperatures <20°C

starting up to almost 11 days dec^{-1} earlier in Santa Vitória station. Similar results were found for the northerly Porto Alegre station, however, for the period between 2000 and 2021 the trends are slightly divergent, which can be caused by many missing data in the station in 2002 (affecting more directly the trend calculated for the shorter time series), and by the wider variation in the ending of the season in this region (see Figure 2).

This decrease in the length of the cold season is observed year by year in the region in Figure 2. There is considerable dispersion in the dates of the ending of the season, which are mostly a result of the wide variation in the dates for the Porto Alegre station, reflected in the variation of the length of the season. Despite that, there is an agreement in the trends, as observed in Table 3. The observed effect of ENSO in the cold season was mild, although El Niño appears to delay the start of the cold season, while La Niña years present the later dates of the ending of the season.

To further explore the air and water temperature trends, in Figure 3 we show the monthly trends for the three lakes and meteorological stations and their mean. There is agreement across both air and water temperatures, and they also agree with each other (Pearson's $r = 0.72$), with warming concentrated in September and December, that is, the transition between seasons. The monthly trends shed light on the smaller trends found in spring for T_a, in relation to $\langle\overline{T_w}\rangle$, with water and air trends in September of 0.75 and 0.9°C decade^{-1}, respectively, but much lower values in October and November for T_a, while for $\langle\overline{T_w}\rangle$ the values remain relatively high, of 0.3 and 0.6°C decade^{-1}, respectively. In the summer, T_a trends are slightly higher, as seen in Table 2.

For fall and winter, the trends mostly fluctuate around 0, especially for $\langle\overline{T_w}\rangle$, probably due to low statistical

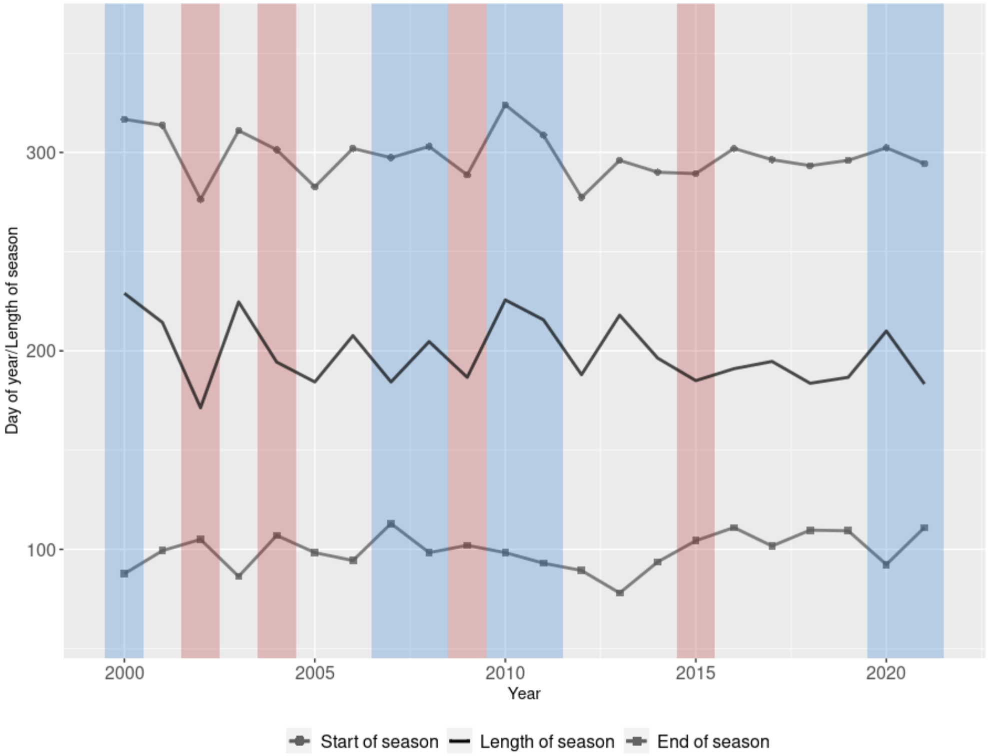

Figure 2: Mean start, end, and length of the cold season in the study area from 2000 to 2021. Blue bars denote the La Niña years, and red bars denote the occurrence of El Niño.

significance, except for the T_a trends in March and April, when they are of -0.4 and 0.5°C decade^{-1}, respectively.

Table 4 shows the seasonal mean warming efficiency and trends for each lake. There is a yearly pattern of higher warming efficiency in spring or winter and decreasing values from summer through fall, where the lowest η are found. Winter has high warming efficiency (*i.e.*, water cools more than air) due to a combination of meteorological factors, mostly the higher precipitation, which reduces solar radiation and increases water levels. η was also high in Spring for both Mirim and Mangueira and considerably lower for the Patos Lagoon. The trends calculated for η were not significant except for the summer in lake Mirim, but they indicate a regional tendency of increasing in spring and diminishing in summer.

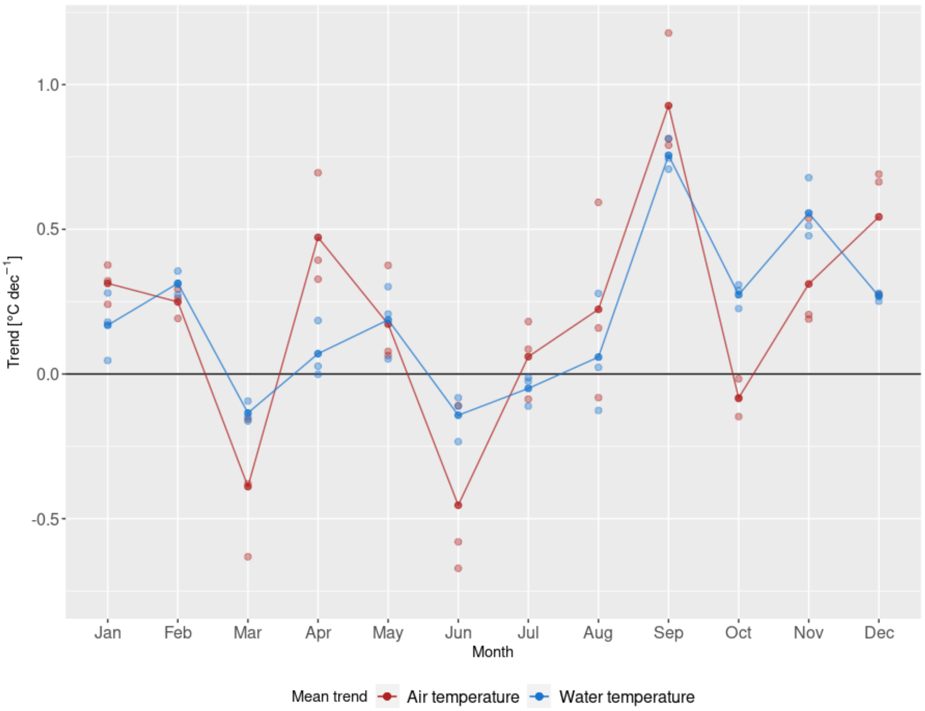

Figure 3: Trends of monthly mean air and water temperatures ($\langle\overline{T_w}\rangle$) in the study area.

Table 4: Seasonal mean warming efficiency and trend

Lake	**Variable**	**Fall**	**Winter**	**Spring**	**Summer**
Patos	η [°C °C^{-1}]	0.83	1.14	1.01	1.03
	Trend [decade^{-1}]	0.01	0.01	0.03	-0.03
Mirim	η [°C °C^{-1}]	1.03	1.20	1.21	1.09
	Trend [decade^{-1}]	0.00	-0.01	0.04	**-0.08**
Mangueira	η [°C °C^{-1}]	0.99	1.12	1.17	1.00
	Trend [decade^{-1}]	0.04	-0.01	0.06	-0.06

3.2. Spatial analysis

Figure 4 shows the seasonal trends for the period between March 2002 and February 2022. The trends reflect the spatial variability in warming seen in Table 2, with the exact trends calculated for each lake and season except for spring, when trends are slightly lower for Mirim and higher for Patos, which is owed to the different time windows and statistical power. For the pixels in Figure 4, only trends for spring (in all three lakes) and the higher summer trends are significant.

The higher trends are found in spring, especially in eastern Patos Lagoon, and central and southern lake Mirim.

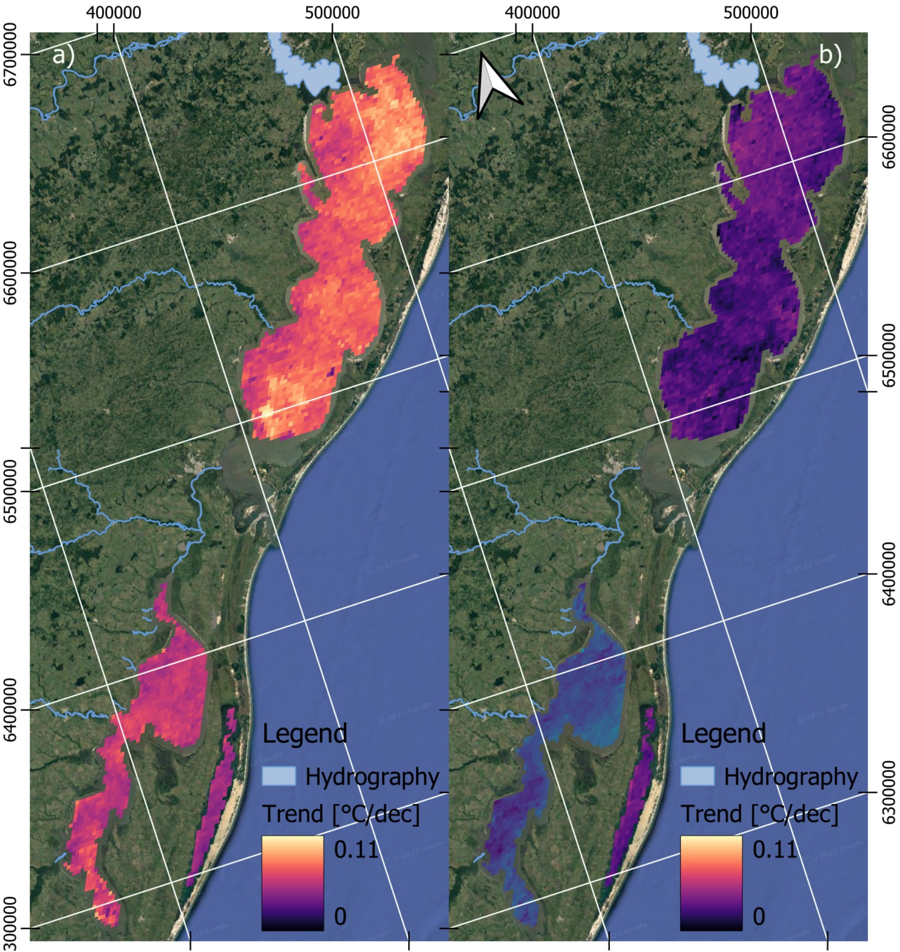

Figure 4: LSWT trends for lakes Mangueira, Mirim and Patos Lagoon in *a)* Spring, and *b)* Summer. Trends were calculated for the period between March 2002 and February 2022.

Trends are also high in the summer in the western margin of lake Mangueira, in the southeastern part of the wider area in lake Mirim, and the lake Guaíba inflow area in the Patos Lagoon. Figure 4 also shows that the inflows have a significant impact on the local trends, predominantly in spring, whether it is increasing, as Jaguarão and Tacuari rivers in lake Mirim, or decreasing the trends, as the major inflows of Patos Lagoon (*i.e.*, lake Guaíba and the Camaquã river) and the Cebollati river in lake Mirim and. In summer, this is slightly different, as, for example, lake Guaíba seemly enhances the warming in Patos Lagoon. Besides this, warming rates are roughly spatially uniform for the three lakes.

Figure 5 also helps to visualise the possible interannual variation in the temperature in the lakes for the two seasons with the higher T_w warming rates, spring and summer. It shows that the difference between the warmest and coldest year in the time series (defined regionally) for each season varies substantially, with spring showing a wider amplitude in T_a (resulting mostly from a large variation in September), but $\langle \overline{T_w} \rangle$ varying roughly the same amount as in summer, with smaller variability in T_a.

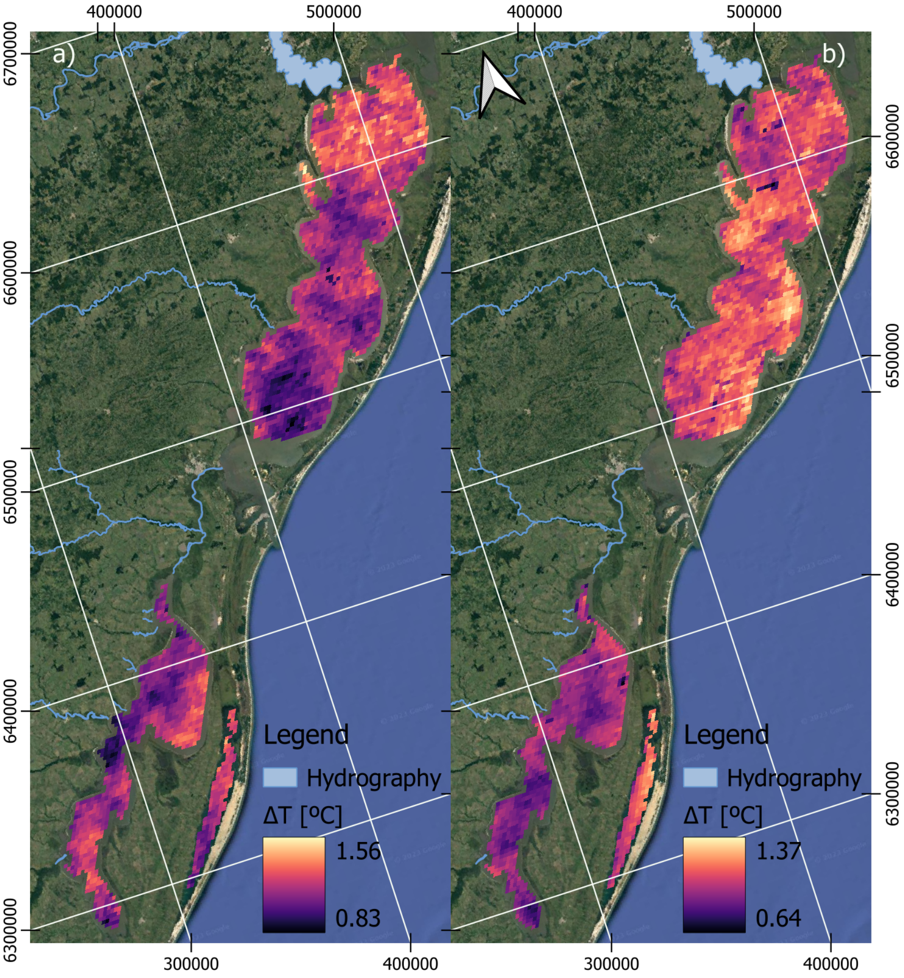

Figure 5: Mean LSWT differences between the five hottest and coldest years in *a)* Spring (September, October, and November) and *b)* Summer (December, January, and February). For spring, the hottest years were 2012, 2014, 2017, 2019, and 2021, and the coldest years were 2003, 2010, 2011, 2015, and 2016, and for summer, the hottest years were 2006, 2009, 2013, 2015, and 2016, and the coldest years were 2003, 2004, 2008, 2011, and 2019.

We can also see the impact of the inflows in the differences, with waters from lake Guaíba and Camaquã showing a higher variability of temperature differences in spring, as well as Cebollati river in lake Mirim and a small impact from arroio Pastoreio in Mangueira. In comparison, the area of discharge of Jaguarão and Tacuari rivers shows much smaller variability, and this variability contrasts with that found for summer, as found for the water warming rates, indicating a relationship between the interannual river temperature variability and the trends.

4. Discussion

4.1. Temporal analysis

Our results show a regional trend of reduced duration of the cold season, with an earlier start of the spring and warmer summer temperatures, especially maximum air temperatures, as reinforced by the climate indices and indicated in previous studies (Cordeiro et al., 2016). As a result, water temperature showed high warming trends in spring for all three lakes, especially in September due to high air warming in this month. In this season, we also found higher warming in T_w compared to T_a, resulting from the lower T_a warming rates in October and November. In the summer, the observed impact on water temperatures was reduced. The trends were only significant in the spring due to the limited length (22 years) of the time series and weaker trends in the other seasons (Gray et al., 2018). Water temperature warming in the summer, however, may also be high and important, as observed in the trends of air temperatures, but the extension of the series limits a more robust analysis (Schneider and Hook, 2010; Gray et al., 2018). Trends in fall and winter were not significant and close to zero, although they showed considerable monthly variation, especially for air temperatures (Figure 3), diverging from other studies (Woolway et al., 2019b). The climate indices also indicate that these are long-term changes and have been intensifying in the last 20 years, notably the reduction of the duration of the cold season, as well as the aforementioned increase of maximum air temperatures.

Despite the variable time span of the analysis, the warming trends in spring and summer observed here are similar to other studies on shallow lakes, and comparable to trends estimated for deeper lakes. Li et al. (2019) found modelled warming rates of 0.4–0.6°C dec^{-1} for spring in four large subtropical, low-altitude shallow lakes in China between 1979 to 2017, with similar trends in the summer. The trends were also homogeneous for all four lakes, and the warming was attributed to solar brightening and increased air temperatures. Shinohara et al. (2021) found, for a temperate turbid shallow lake in Japan, trends of 0.7°C dec^{-1} in March and May (corresponding to September and November in the southern hemisphere), with similar trends in the summer. Other studies also found higher LSWT warming in spring than in summer (Schmid and Köster, 2016). Woolway et al. (2017) also found higher spring warming on 20 Central European lakes between 1961 and 2010, with warming concentrated on late spring (0.6°C dec^{-1}) and similar rates of summer warming (0.5°C dec^{-1}), related to increased thermal stratification. Winslow et al. (2017), on the other hand, found cooling air temperature trends between February and May (corresponding to August and November), with low water temperature warming rates in this part of the year for six shallow and small temperate lakes in the USA over a 35-year period. Higher warming rates were found between September and December. In similarity, the authors also found a high correlation between air and water temperature rates and trends of shortened cold season, with a more pronounced trend of Fall 20°C crossing date, of 5.3 days dec^{-1}.

The high warming rates of air temperature observed in our study area resulted in even higher warming of water temperatures, and the warming efficiency calculated for each season can facilitate understanding the reason for this (Toffolon et al., 2020). We observed high η in winter (*i.e.*, water cools more than air) in all three lakes due to a combination of meteorological factors, mostly lower solar radiation and high precipitation (Table S1), which further reduces solar radiation and increases water levels. As a result, T_w is only slightly higher than T_a in this season, boosting the water warming in September due to high air warming trends. Higher spring η (found in Mirim and Mangueira) can be a result of this lower $T_w - T_a$ difference (reduces heat loss from conduction and evaporation), and the lower η in Patos Lagoon is likely due to its higher thermal inertia.

Other relevant factors in the high spring warming rates are morphometry and water transparency. Studies have shown the influence of lake morphometry on warming (Ptak et al., 2018; González-Ávila et al., 2021; Xie et al., 2022), and the elongated shape and low depth of the three lakes contribute to the homogeneous, high warming rates in response to warming temperatures (Toffolon et al., 2020). Furthermore, spring is the season with the strongest winds (Table S1), and a slight tendency of increase was also observed. This, in conjunction with sediment resuspension (Crossetti et al., 2014) and earlier spring, associated with earlier phytoplankton phenology (*e.g.*, Deng et al., 2014), starting in September (Fragoso Jr et al., 2011), decreases water clarity (which can include the tributary rivers), and has been shown to enhance the effects of warming of lake waters (Rose et al., 2016).

Due to the excess lake water warming in spring, summer warming rates of $\langle \overline{T_w} \rangle$ were considerably lower than T_a, especially in December when higher air trends were found. We can see that except for Patos Lagoon, η is lower in summer than in spring and even shows a tendency of decrease of 8% dec^{-1} for lake Mirim (Table 4). Reported trends of summer warming are, however, generally more pronounced in deep lakes, where air temperature warming induces higher thermal stratification, reducing the water mass that exchanges heat with the atmosphere and further amplifying LSWT warming (Woolway and Merchant, 2018; Woolway et al., 2019a; Zhong et al., 2019; Toffolon et al., 2020; Calamita et al., 2021). Woolway and Merchant (2018), for example, found summer warming rates of 1.1°C dec^{-1} for the deepest and 0.6°C dec^{-1} for the shallowest regions of Lake Huron, in Northern America, and similar trends for other large northern lakes. Here, for the three warm polymictic shallow lakes, thermal stratification lasts only one or two days in lake Mangueira (Fragoso Jr et al., 2011) and potentially for longer in the other two lakes, having a mild impact on the T_w warming, which is further discussed in Section 4.2.

The trends in other meteorological variables also contribute to lower summer lake water temperature warming compared to air temperature. Relative humidity, for example, showed a divergent trend in the Pelotas station, increasing in both spring and summer while it decreased in the other two meteorological stations. This is likely a result of its location, being at the centre of the three lakes, and therefore the RH increases as a result of increased evaporation due to the warming of LSWT (especially in lake Mirim, with trends of increased latent heat flux of 4.3 W m^{-2} in this period, Tavares et al. 2023), whereas RH in the other two stations decreases as a result of consistent warming of mean, maximum and minimum air temperatures. This, associated with the excess warming in spring (resulting in enlarged $T_w - T_a$ difference), amplify lake heat loss via turbulent heat flux (Fink et al., 2014; Zhong et al., 2016; Tavares et al., 2023), contributing to lower warming rates. It should also be noted that the trends in heat loss via turbulent heat flux were much higher in spring (Tavares et al., 2023), due to the strong winds (Table S1) and enhanced $T_w - T_a$ differences, and without this increased source of heat loss, the trends in this season could be even higher.

ENSO events have considerable impacts on the meteorological conditions in the region, with El Niño associated with higher precipitation (Cai et al., 2020) and La Niña associated with droughts and colder weather, especially late fall, winter, and spring (Cordeiro et al., 2016). Here, the observed effects of ENSO in the cold season were mild (Figure 2), although El Niño appears to delay the start of the cold season, while La Niña years present some of the later ending dates and longer cold seasons. The coldest years in the region were also La Niña years (Figure S1).

4.2. Spatial analysis

In spite of the more limited time span of the series, the MODIS imagery provides a suitable dataset to examine not only the mean warming rates but also how warming varies spatially. We see that the seasonal trends were generally homogeneous in the region for the three lakes, with a few exceptions (Figure 4). This homogeneity has been shown, for example, by Toffolon et al. (2020), which, while not calculating warming rates directly, showed that Lake Eire had a more homogeneous response to differential warming compared to the remaining larger, much deeper Laurentian Great Lakes. Here, this homogeneity also results from the lakes' morphometry (Ptak et al., 2018; González-Ávila et al., 2021), as discussed above.

In spring and, to some extent, in summer, trends are slightly different near the major river discharge areas. The higher warming rates near the Jaguarão and Tacuari inflow areas in lake Mirim, and the opposite effect caused by the Cebollati river, is likely a result of more consistent heat input by the former rivers, having a local effect on the trends. Vinnå et al. (2017) showed similar results, although the authors modelled deep, thermally stratified lakes, finding substantial impact of tributaries on lake warming, with a dampening effect more pronounced in the hypolimnion. Jaguarão and Tacuari have much similar behaviour regarding water discharge and temperature, differing from Cebollati, which has a larger, more southwestern basin (Munar et al., 2018, 2019). Although Munar et al. (2019) showed that the Cebollati river has a much larger impact on lake Mirim's heat budget (despite minimal contribution to the overall lake heat budget), it is primarily owed to the higher discharge, being higher than the combined discharge of Jaguarão and Tacuari rivers in some years.

The same behaviour is observed for lake Guaíba and Camaquã river discharges in the Patos Lagoon in the summer, as trends near the Camaquã discharge area are consistently inferior than in most of Patos Lagoon, but near the Guaíba discharge they are higher than the mean warming rates in this season. In lake Mangueira this effect is much reduced, owing to its much smaller watershed and thus, tributaries' discharge contribution. When comparing the seasonal trends with the differences between the hottest and coldest years of spring and summer (Figure 5), we see that river discharges have sharper or dampened temperature differences, and this is reflected in the local warming rates: rivers with a more consistent heat input, *i.e.*, lower temperature difference between the hottest and coldest years in the time series, generally increase the warming trends. The opposite is found in the river discharge areas with the largest temperature differences, where lower-than-mean warming rates are found. River turbidity may also be relevant when considering river discharge variations (Rose et al., 2016), as already discussed above. Although it was not further investigated here, this suggests that river temperature (or river discharge) increase can have a strong local, long-term effect on LSWT, and can be even more pronounced in smaller lakes.

In brief, here we showed local spatial warming rate differences owed to tributary rivers. These spatial differences can have substantial ecological impacts, as discussed in other studies, such as shifting species distribution and phenology of ecosystem processes (Fragoso Jr et al., 2011; Deng et al., 2014; Halverson et al., 2021; Hansen, 2021).

5. Conclusion

In this study, we assessed the warming trends of three large shallow lakes in southern Brazil using a 22-year time series of local meteorological data and LSWT derived from MODIS imagery. We focused on the seasonal scale, analysing both temporal and spatial warming rates. Despite local differences, we found high warming of LSWT in the region concentrated in spring and, to a lesser extent, in summer, with a considerable agreement between the air and water temperature trends. Trends in meteorological forcings and climate indices show long-term warming with a substantial shortening of the cold season and increasing maximum and minimum air temperatures in spring and summer.

The remote sensing-derived data also showed an overall homogeneity of the warming rates, likely resulting from the morphology of the shallow lakes, but with notable spatial differences that may be a result of variability in the tributaries (Vinnå et al., 2017).

Despite the different time span of the analysis, the high warming rates found here are comparable to those found in deep northern lakes but with distinguished changes and processes involved in the heating. The warming is stronger in early spring, resulting in earlier start of phytoplankton phenology (Fragoso Jr et al., 2011), and the spatial differences in the warming can have other ecological impacts, such as shifting species distribution (Halverson et al., 2021; Hansen, 2021). We recommend further studies on the warming in the region, assessing changes in water clarity (Rose et al., 2016), impacts of temperature increase on the tributaries, and using modelling to further understand the processes that resulted in the observed high warming trends.

Acknowledgements

This work was carried out with the support of CNPq, Conselho Nacional de Desenvolvimento Científico e Tecnológico - Brazil through the scholarship number 140505/2020-2. We would like to thank NASA for MODIS imagery, NOAA/ECMWF for the ERA5 Reanalysis data, and INMET for the meteorological data. We are also grateful to the Global Lake Ecological Observatory Network (GLEON: `www.gleon.org`) and the network with Institut de Recherche pour le Développement (IRD) Montpellier for joint lake science and modeling development.

References

Cai, W., McPhaden, M.J., Grimm, A.M., Rodrigues, R.R., Taschetto, A.S., Garreaud, R.D., Dewitte, B., Poveda, G., Ham, Y.G., Santoso, A., et al., 2020. Climate impacts of the El Niño–Southern Oscillation on South America. Nature Reviews Earth & Environment 1, 215–231. doi:10.1038/s43017-020-0040-3.

Calamita, E., Piccolroaz, S., Majone, B., Toffolon, M., 2021. On the role of local depth and latitude on surface warming heterogeneity in the Laurentian Great Lakes. Inland Waters 11, 208–222. doi:`10.1080/20442041.2021.1873698`.

Cordeiro, A.P.A., Berlato, M.A., Fontana, D.C., Alves, R.d.C.M., 2016. Tendências climáticas das temperaturas do ar no estado do rio grande do sul, sul do brasil. Revista Brasileira de Geografia Física 9, 868–880.

Crossetti, L.O., Schneck, F., Freitas-Teixeira, L.M., Motta-Marques, D., 2014. The influence of environmental variables on spatial and temporal phytoplankton dissimilarity in a large shallow subtropical lake (Lake Mangueira, southern Brazil). Acta Limnologica Brasiliensia 26, 111–118. doi:`10.1590/S2179-975X2014000200002`.

Deng, J., Qin, B., Paerl, H.W., Zhang, Y., Ma, J., Chen, Y., 2014. Earlier and warmer springs increase cyanobacterial (Microcystis spp.) blooms in subtropical Lake Taihu, China. Freshwater Biology 59, 1076–1085. doi:`10.1111/fwb.12330`.

Fink, G., Schmid, M., Wahl, B., Wolf, T., Wüest, A., 2014. Heat flux modifications related to climate-induced warming of large European lakes. Water Resources Research 50, 2072–2085. doi:`10.1002/2013WR014448`.

Fragoso Jr, C.R., Marques, D.M.M., Ferreira, T.F., Janse, J.H., van Nes, E.H., 2011. Potential effects of climate change and eutrophication on a large subtropical shallow lake. Environmental Modelling & Software 26, 1337–1348.

González-Ávila, I., Tavares, M.H., Chalegre, C.L.B., Munar, A.M., Fragoso, C.R., Motta-Marques, D., Ruhoff, A., 2021. Southern coastal subtropical shallow lakes skin temperature driven by climatic and non-climatic factors. Environmental Monitoring and Assessment 193, 1–16. doi:`10.1007/s10661-021-08895-5`.

Gray, D.K., Hampton, S.E., O'Reilly, C.M., Sharma, S., Cohen, R.S., 2018. How do data collection and processing methods impact the accuracy of long-term trend estimation in lake surface-water temperatures? Limnology and Oceanography: Methods 16, 504–515. doi:`10.1002/lom3.10262`.

Gräler, B., Pebesma, E., Heuvelink, G., 2016. Spatio-temporal interpolation using gstat. The R Journal 8, 204–218. URL: `https://journal.r-project.org/archive/2016/RJ-2016-014/index.html`.

Halverson, G.H., Lee, C.M., Hestir, E.L., Hulley, G.C., Cawse-Nicholson, K., Hook, S.J., Bergamaschi, B.A., Acuña, S., Tufillaro, N.B., Radocinski, R.G., Rivera, G., Sommer, T.R., 2021. Decline in thermal habitat conditions for the endangered delta smelt as seen from Landsat satellites (1985–2019). Environmental Science & Technology 56, 185–193. doi:`https://doi.org/10.1021/acs.est.1c02837`.

Hansen, G.J., 2021. Novel thermal habitat in lakes. Nature Climate Change 11, 470–471. doi:`10.1038/s41558-021-01067-w`.

Hersbach, H., Bell, B., Berrisford, P., Hirahara, S., Horányi, A., Muñoz-Sabater, J., Nicolas, J., Peubey, C., Radu, R., Schepers, D., Simmons, A., Soci, C., Abdalla, S., Abellan, X., Balsamo, G., Bechtold, P., Biavati, G., Bidlot, J., Bonavita, M., Chiara, G.D., Dahlgren, P., Dee, D., Diamantakis, M., Dragani, R., Flemming, J., Forbes, R., Fuentes, M., Geer, A., Haimberger, L., Healy, S., Hogan, R.J., Hólm, E., Janisková, M., Keeley, S., Laloyaux, P., Lopez, P., Lupu, C., Radnoti, G., de Rosnay, P., Rozum, I., Vamborg, F., Villaume, S., Thépaut, J.N., 2020. The ERA5 global reanalysis. Quarterly Journal of the Royal Meteorological Society 146, 1999–2049. doi:`10.1002/qj.3803`.

Hijmans, R.J., 2021. terra: Spatial Data Analysis. URL: `https://CRAN.R-project.org/package=terra`. r package version 1.4-22.

Karl, T.R., Nicholls, N., Ghazi, A., 1999. Clivar/GCOS/WMO workshop on indices and indicators for climate extremes workshop summary, in: Weather and Climate Extremes. Springer, pp. 3–7.

Kelleher, C.A., Golden, H.E., Archfield, S.A., 2021. Monthly river temperature trends across the US confound annual changes. Environmental Research Letters 16, 104006. doi:`10.1088/1748-9326/ac2289`.

Kottek, M., Grieser, J., Beck, C., Rudolf, B., Rubel, F., 2006. World map of the Köppen-Geiger climate classification updated. Meteorologische Zeitschrift 15, 259–263.

Lee, H.W., Kim, E.J., Park, S.S., Choi, J.H., 2012. Effects of climate change on the thermal structure of lakes in the asian monsoon area. Climatic Change 112, 859–880.

Li, X., Peng, S., Deng, X., Su, M., Zeng, H., 2019. Attribution of lake warming in four shallow lakes in the middle and lower Yangtze River Basin. Environmental Science & Technology 53, 12548–12555. doi:`10.1021/acs.est.9b03098`.

Livingstone, D.M., 2003. The warming of lake Tahoe. Climatic Change 57, 205–225.

Minnett, P.J., Smith, M., Ward, B., 2011. Measurements of the oceanic thermal skin effect. Deep Sea Research Part II: Topical Studies in

Oceanography 58, 861–868. doi:10.1016/j.dsr2.2010.10.024.

Munar, A.M., Cavalcanti, J.R., Bravo, J.M., Fan, F.M., Motta-Marques, D.M.L., Fragoso Jr, C.R., 2018. Coupling large-scale hydrological and hydrodynamic modeling: Toward a better comprehension of watershed-shallow lake processes. Journal of Hydrology 564, 424–441.

Munar, A.M., Cavalcanti, J.R., Bravo, J.M., Motta-Marques, D., Fragoso Jr., C.R., 2019. Assessing the large-scale variation of heat budget in poorly gauged watershed shallow lake system using a novel integrated modeling approach. Journal of Hydrology 575, 244–256. doi:10.1016/j.jhydrol.2019.05.025.

O'Reilly, C.M., Alin, S.R., Plisnier, P.D., Cohen, A.S., McKee, B.A., 2003. Climate change decreases aquatic ecosystem productivity of Lake Tanganyika, Africa. Nature 424, 766–768.

O'Reilly, C.M., Sharma, S., Gray, D.K., Hampton, S.E., Read, J.S., Rowley, R.J., Schneider, P., Lenters, J.D., McIntyre, P.B., Kraemer, B.M., et al., 2015. Rapid and highly variable warming of lake surface waters around the globe. Geophysical Research Letters 42, 10–773.

Peterson, T., Folland, C., Gruza, G., Hogg, W., Mokssit, A., Plummer, N., 2001. Report on the activities of the working group on climate change detection and related rapporteurs. Citeseer.

Piccolroaz, S., Woolway, R.I., Merchant, C.J., 2020. Global reconstruction of twentieth century lake surface water temperature reveals different warming trends depending on the climatic zone. Climatic Change 160, 427–442. doi:10.1007/s10584-020-02663-z.

Ptak, M., Sojka, M., Choiński, A., Nowak, B., 2018. Effect of environmental conditions and morphometric parameters on surface water temperature in polish lakes. Water 10, 580. doi:10.3390/w10050580.

R Core Team, 2021. R: A Language and Environment for Statistical Computing. R Foundation for Statistical Computing. Vienna, Austria. URL: https://www.R-project.org/.

Riffler, M., Lieberherr, G., Wunderle, S., 2015. Lake surface water temperatures of European Alpine lakes (1989–2013) based on the Advanced Very High Resolution Radiometer (AVHRR) 1 km data set. Earth System Science Data 7, 1–17. doi:10.5194/essd-7-1-2015.

Rose, K.C., Winslow, L.A., Read, J.S., Hansen, G.J., 2016. Climate-induced warming of lakes can be either amplified or suppressed by trends in water clarity. Limnology and Oceanography Letters 1, 44–53. doi:10.1002/lol2.10027.

Schmid, M., Köster, O., 2016. Excess warming of a Central European lake driven by solar brightening. Water Resources Research 52, 8103–8116. doi:WileyOnlineLibrary.

Schneider, P., Hook, S.J., 2010. Space observations of inland water bodies show rapid surface warming since 1985. Geophysical Research Letters 37.

Schwarzbold, A., Schäfer, A., 1984. Gênese e morfologia das lagoas costeiras do Rio Grande do Sul-Brasil. Amazoniana: Limnologia et Oecologia Regionalis Systematis Fluminis Amazonas 9, 87–104.

Shinohara, R., Tanaka, Y., Kanno, A., Matsushige, K., 2021. Relative impacts of increases of solar radiation and air temperature on the temperature of surface water in a shallow, eutrophic lake. Hydrology Research 52, 916–926. doi:10.2166/nh.2021.148.

Tavares, M.H., Motta-Marques, D., Fragoso Jr, C.R., 2023. Impact of cool-skin effect correction on lake surface water temperature trends and heat budget of three large shallow subtropical lakes. Submitted to Journal of Geophysical Research: Atmospheres .

Toffolon, M., Piccolroaz, S., Calamita, E., 2020. On the use of averaged indicators to assess lakes' thermal response to changes in climatic conditions. Environmental Research Letters 15, 034060. doi:10.1088/1748-9326/ab763e.

Vinnå, L.R., Wüest, A., Zappa, M., Fink, G., Bouffard, D., 2017. Tributaries affect the thermal response of lakes to climate change. Hydrology and Earth System Sciences 22, 31. doi:10.5194/hess-22-31-2018.

Wan, Z., Dozier, J., 1996. A generalized split-window algorithm for retrieving land-surface temperature from space. IEEE Transactions on Geoscience and Remote Sensing 34, 892–905.

Wilson, R.C., Hook, S.J., Schneider, P., Schladow, S.G., 2013. Skin and bulk temperature difference at Lake Tahoe: A case study on lake skin effect. Journal of Geophysical Research: Atmospheres 118, 10–332. doi:10.1002/jgrd.50786.

Winslow, L.A., Read, J.S., Hansen, G.J., Rose, K.C., Robertson, D.M., 2017. Seasonality of change: Summer warming rates do not fully represent effects of climate change on lake temperatures. Limnology and Oceanography 62, 2168–2178. doi:10.1002/lno.10557.

Woolway, R.I., Dokulil, M.T., Marszelewski, W., Schmid, M., Bouffard, D., Merchant, C.J., 2017. Warming of Central European lakes and their response to the 1980s climate regime shift. Climatic Change 142, 505–520. doi:10.1007/s10584-017-1966-4.

Woolway, R.I., Kraemer, B.M., Lenters, J.D., Merchant, C.J., O'Reilly, C.M., Sharma, S., 2020. Global lake responses to climate change. Nature Reviews Earth & Environment 1, 388–403. doi:`10.1038/s43017-020-0067-5`.

Woolway, R.I., Merchant, C.J., 2018. Intralake heterogeneity of thermal responses to climate change: A study of large Northern Hemisphere lakes. Journal of Geophysical Research: Atmospheres 123, 3087–3098.

Woolway, R.I., Merchant, C.J., Van Den Hoek, J., Azorin-Molina, C., Nõges, P., Laas, A., Mackay, E.B., Jones, I.D., 2019a. Northern Hemisphere atmospheric stilling accelerates lake thermal responses to a warming world. Geophysical Research Letters 46, 11983–11992. doi:`10.1029/2019GL082752`.

Woolway, R.I., Weyhenmeyer, G.A., Schmid, M., Dokulil, M.T., de Eyto, E., Maberly, S.C., May, L., Merchant, C.J., 2019b. Substantial increase in minimum lake surface temperatures under climate change. Climatic Change 155, 81–94. doi:`https://doi.org/10.1007/s10584-019-02465-y`.

Xie, C., Zhang, X., Zhuang, L., Zhu, R., Guo, J., 2022. Analysis of surface temperature variation of lakes in China using MODIS land surface temperature data. Scientific Reports 12, 1–13. doi:`10.1038/s41598-022-06363-9`.

Xu, X., Jia, G., Zhang, X., Riley, W.J., Xue, Y., 2020. Climate regime shift and forest loss amplify fire in amazonian forests. Global Change Biology 26, 5874–5885. doi:`10.1111/gcb.15279`.

Yuan, P., Hunegnaw, A., Alshawaf, F., Awange, J., Klos, A., Teferle, F.N., Kutterer, H., 2021. Feasibility of ERA5 integrated water vapor trends for climate change analysis in continental Europe: An evaluation with GPS (1994–2019) by considering statistical significance. Remote Sensing of Environment 260, 112416. doi:`10.1016/j.rse.2021.112416`.

Zhang, Y., 1999. MODIS UCSB Emissivity Library. `https://icess.eri.ucsb.edu/modis/EMIS/html/em.html`. Acessed on November 22nd 2017.

Zhong, Y., Notaro, M., Vavrus, S.J., 2019. Spatially variable warming of the Laurentian Great Lakes: an interaction of bathymetry and climate. Climate Dynamics 52, 5833–5848. doi:`10.1007/s00382-018-4481-z`.

Zhong, Y., Notaro, M., Vavrus, S.J., Foster, M.J., 2016. Recent accelerated warming of the Laurentian Great Lakes: Physical drivers. Limnology and Oceanography 61, 1762–1786. doi:`10.1002/lno.10331`.

Capítulo 7

Conclusão

Esta tese teve como objetivos avaliar os padrões de variação espaço-temporal de parâmetros da qualidade da água em dois conjuntos de lagoas costeiras rasas. Como conclusões, responde-se às questões científicas propostas neste trabalho, na primeira parte, para as lagunas tropicais rasas:

— *Qual a melhor combinação de algoritmos de correção atmosférica e estimativa de concentração de clorofila-a num complexo de lagunas tropicais rasas eutróficas? Há variação no desempenho dos algoritmos entre as lagunas do complexo? O resultado obtido confirma o que é esperado de acordo com a literatura?*

No Capítulo 3, foi validado um conjunto de processador de correção atmosférica e algoritmo de clorofila-*a* para todo o complexo utilizando imagens do Sentinel-2 MSI. O processador com melhores resultados foi o ACOLITE que, embora não tenha sido o que apresentou os melhores resultados gerais de correção atmosférica, mostrou a melhor correção da razão de bandas do vermelho e infravermelho próximo (*red edge*), utilizado no algoritmo de clorofila-*a*. Também foi mostrado a necessidade de correção do efeito de *sunglint* para acurada estimativa da reflectância da água por sensores orbitais sem inclinação para remoção deste efeito, em especial nos trópicos, onde o ângulo zenital solar geralmente é alto, e de efeitos de adjacência, que não foi corrigido nesta área de estudo pela limitação de algoritmos para esta tarefa. A validação de algoritmos mostrou que vários algoritmos utilizando razões de bandas do vermelho e infravermelho próximo tiveram resultados semelhantes, porém o modelo semi-analítico criado por Gons et al. (2002) foi o que se mostrou mais robusto para as duas lagunas, e este modelo calibrado com dados medidos em campo mostrou os melhores resultados. Os resultados, em geral, corroboram o que é encontrado na literatura, com o ACOLITE sendo um confiável algoritmo de correção atmosférica em águas interiores turvas, assim como algoritmos de razão de bandas, em que o algoritmo de Gons et al. (2002) mostrou-se recomendável para águas dominadas por fitoplâncton, como as da laguna Manguaba, embora os erros tenham sido relativamente altos, principalmente na Mundaú em que fitoplâncton não é dominante e as águas são mais afetadas por efeito de adjacência da área urbana de Maceió.

— *Quais são os padrões de variação espaço-temporal do fitoplâncton nestas lagoas? Quais são as forçantes que mais influenciam nestes padrões?*

No Capítulo 4, utilizando a série do Sentinel-2 MSI para o período de 2016 a 2021, foram mapeados os padrões espaciais de clorofila-*a* na duas lagunas, durante todo o período e apenas nos períodos seco e chuvoso, mostrando como a Manguaba é mais eutrófica do que a Mundaú e com uma variação menos definida ao longo do ano, afetada principalmente pela afluência de nutrientes da bacia devido ao plantio e coleita de cana-de-açúcar. A Mundaú mostrou um padrão mais definido, com variação afetada tanto pelo ciclo da cana quanto pela precipitação e vazão dos rios. Durante a estação chuvosa a afluência dos rios tributários geralmente causa uma redução de clorofila-*a* na sua área de deságue devido à limitação da luz por CDOM e sólidos suspensos, enquanto que a chuva aumenta a clorofila-*a* nas áreas afetadas pelos lançamentos de esgoto e águas pluviais. A divisão das lagunas em grupos homogêneos possibilitou uma análise temporal de cada grupo, assim como a definição das principais forçantes ambientais utilizando a técnica de análise da correspondência canônica (CCA). Isto permitiu visualizar a importância da hidrodinâmica e tempo de residência no sistema, destacando zonas de recicurlação na laguna Manguaba e sua elevada produtividade, a influência do ciclo da cana na clorofila-*a*, e como as marés influenciam na renovação ou aprisionamento da água no sistema. Comparado a estudos mais antigos, este trabalho mostrou uma aparente piora na qualidade da água no complexo, com provável aumento de florações de algas, além de registrados eventos de mortandade de peixes nos canais próximos à Manguaba.

Na segunda parte, para as lagoas subtropicais costeiras rasas, foram respondidas as seguintes perguntas:

— *Algoritmos de correção de* cool-skin *desenvolvidos para águas oceânicas podem ser utilizados em águas continentais com ganho significativo de precisão? Qual o impacto desta correção em estudos de mudanças climáticas em lagos?*

No Capítulo 5, em conjunto com dados meteorológicos de produtos de reanálise, os dois algoritmos de correção de *cool-skin* testados aqui melhoraram a acurácia dos dados MODIS na lagoa Mangueira, com redução do viés do produto de -0,5 para -0,2°C e a mediana dos erros de -0,4°C para quase 0, além de uma pequena melhora no RMSE e no erro máximo utilizando o modelo mais simples, que depende apenas da velocidade do vento, mostrando que estes modelos também funcionam em águas continentais, embora o viés não tenha sido totalmente corrigido. O impacto observado nos cálculos das tendências de temperatura das três grandes lagoas costeiras foi de cerca de 5%, variando de 0 a 26% na maior diferença (de 0,19°C dec^{-1}), bastante significativa, e mostrando que o produto não-corrigido tende a subestimar as tendências. Analisando a variação no cálculo do balanço de calor destas lagoas, em que a temperatura correta a ser utilizada é com o efeito de *cool-skin*, a sua não inclusão causa uma superestimativa dos fluxos, especialmente no cálculo da evaporação da água, de 7∼9%, e de calor sensível, chegando a até 55%. Esta variação também impactou o cálculo das tendências destes termos de balanço de calor no período, de até 0,8 W $m^{-2}dec^{-1}$ na Lagoa do Patos.

— *Qual o impacto das mudanças climáticas na temperatura superficial de um conjunto de lagoas subtropicais costeiras rasas? Quais são as forçantes que explicam essa variação?*

No Capítulo 6, utilizando uma série de 22 anos de dados de temperatura superficial corrigidas do efeito de *cool-skin*, se verificou que os impactos nestas lagoas são uma alta taxa de aquecimento regional observada na primavera, de 0,5°C dec^{-1}, e em menor escala de aquecimento no verão, de 0,3°C dec^{-1}. Nota-se concordância entre as tendências de temperatura da água e do ar, observadas nas estações meteorológicas na região, além do reflexo destes aumentos em outras variáveis como a umidade relativa. Este aumento na primavera se deve principalmente à uma clara tendência de antecipação do fim do inverno e início da primavera, e rápida resposta das lagoas rasas à esta tendência. Esta tendência de aquecimento também foi observada de forma espacial, mostrando uma geral homogeneidade nas tendências, mas algumas diferenças claras nas áreas de afluência dos rios tributários, que não foram avaliados neste estudo mas provavelmente se devem a variação da temperatura ou vazão destes rios afluentes, ou à variação na turbidez da água.

Este trabalho utilizou produtos validados de sensoriamento remoto para avaliar como forçantes na bacia hidrográfica, no clima, e no próprio corpo hídrico impactam a estrutura e funcionamento destes sistemas de maneira espacializada. Nota-se que os resultados observados aqui estão de acordo com os estressores mapeados por Jenny et al. (2020) na América do Sul, mostrando que os processos de poluição por fontes pontuais e difusas têm deteriorado a qualidade da água de lagos e lagunas, e como a tendência de aquecimento também causa modificação no funcionamento destes corpos hídricos. Os produtos validados aqui poderão, no futuro, serem utilizadas para estudos integrados dos impactos climáticos e não climáticos na comunidade fitoplanctônica destes corpos hídricos de maneira espacializada.

Referências

Adrian, R., O'Reilly, C. M., Zagarese, H., Baines, S. B., Hessen, D. O., Keller, W., Livingstone, D. M., Sommaruga, R., Straile, D., Donk, E. V., Weyhenmeyer, G. A., e Winderl, M. (2009). Lakes as sentinels of climate change. *Lymnology and Oceanography*, 54(6):2283–2297.

Alappattu, D. P., Wang, Q., Yamaguchi, R., Lind, R. J., Reynolds, M., e Christman, A. J. (2017). Warm layer and cool skin corrections for bulk water temperature measurements for air-sea interaction studies. *Journal of Geophysical Research: Oceans*, 122(8):6470–6481.

Amorim, C. A. e Moura, A. N. (2021). Ecological impacts of freshwater algal blooms on water quality, plankton biodiversity, structure, and ecosystem functioning. *Science of the Total Environment*, 758:143605.

Barbosa, C. C. F., Novo, E. M. L. M., e Martins, V. S. (2019). *Introdução ao sensoriamento remoto de sistemas aquáticos: princípios e aplicações*, volume 1. Instituto Nacional de Pesquisas Espaciais.

Barnes, W. L., Pagano, T. S., e Salomonson, V. V. (1998). Prelaunch characteristics of the Moderate Resolution Imaging Spectroradiometer (MODIS) on EOS-AM1. *IEEE Transactions on Geoscience and Remote Sensing*, 36(4):1088–1100.

Brezonik, P. L., Olmanson, L. G., Finlay, J. C., e Bauer, M. E. (2015). Factors affecting the measurement of CDOM by remote sensing of optically complex inland waters. *Remote Sensing of Environment*, 157:199–215.

Bridgewater, P. e Kim, R. E. (2021). The ramsar convention on wetlands at 50. *Nature Ecology & Evolution*, 5(3):268–270.

Brodeau, L., Barnier, B., Gulev, S. K., e Woods, C. (2017). Climatologically significant effects of some approximations in the bulk parameterizations of turbulent air–sea fluxes. *Journal of Physical Oceanography*, 47(1):5–28.

Buiteveld, H., Hakvoort, J., e Donze, M. (1994). Optical properties of pure water. Em *Ocean Optics XII*, volume 2258, pgs. 174–183.

Bulgarelli, B. e Zibordi, G. (2018). On the detectability of adjacency effects in ocean color remote sensing of mid-latitude coastal environments by SeaWiFS, MODIS-A, MERIS, OLCI, OLI and MSI. *Remote Sensing of Environment*, 209:423–438.

Carslaw, D. C. e Ropkins, K. (2012). openair — an r package for air quality data analysis. *Environmental Modelling & Software*, 27–28(0):52–61.

Cavalcanti, J. R., da Motta-Marques, D. M. L., e Fragoso Jr, C. R. (2016). Process-based modeling of shallow lake metabolism: Spatio-temporal variability and relative importance of individual processes. *Ecological Modelling*, 323:28–40.

Cole, J. J., Prairie, Y. T., Caraco, N. F., McDowell, W. H., Tranvik, L. J., Striegl, R. G., Duarte, C. M., Kortelainen, P., Downing, J. A., Middelburg, J. J., et al. (2007). Plumbing the global carbon cycle: integrating inland waters into the terrestrial carbon budget. *Ecosystems*, 10(1):172–185.

Coll, C., Caselles, V., Valor, E., e Niclòs, R. (2012). Comparison between different sources of atmospheric profiles for land surface temperature retrieval from single channel thermal infrared data. *Remote Sensing of Environment*, 117:199–210.

Crossetti, L. O., Schneck, F., Freitas-Teixeira, L. M., e Motta-Marques, D. (2014). The influence of environmental variables on spatial and temporal phytoplankton dissimilarity in a large shallow subtropical lake (Lake Mangueira, southern Brazil). *Acta Limnologica Brasiliensia*, 26(2):111–118.

Dall'Olmo, G., Gitelson, A. A., e Rundquist, D. C. (2003). Towards a unified approach for remote estimation of chlorophyll-a in both terrestrial vegetation and turbid productive waters. *Geophysical Research Letters*, 30(18).

Dall'Olmo, G. e Gitelson, A. A. (2005). Effect of bio-optical parameter variability on the remote estimation of chlorophyll-a concentration in turbid productive waters: experimental results. *Applied Optics*, 44(3):412–422.

Dean, W. E. e Gorham, E. (1998). Magnitude and significance of carbon burial in lakes, reservoirs, and peatlands. *Geology*, 26(6):535–538.

Deng, J., Qin, B., Paerl, H. W., Zhang, Y., Ma, J., e Chen, Y. (2014). Earlier and warmer springs increase cyanobacterial (Microcystis spp.) blooms in subtropical Lake Taihu, China. *Freshwater Biology*, 59(5):1076–1085.

Doerffer, R. e Schiller, H. (2007). The MERIS Case 2 water algorithm. *International Journal of Remote Sensing*, 28(3–4):517–535.

Donlon, C., Minnett, P., Gentemann, C., Nightingale, T., Barton, I., Ward, B., e Murray, M. (2002). Toward improved validation of satellite sea surface skin temperature measurements for climate research. *Journal of Climate*, 15(4):353–369.

Dörnhöfer, K. e Oppelt, N. (2016). Remote sensing for lake research and monitoring–recent advances. *Ecological Indicators*, 64:105–122.

Dugdale, S. J. (2016). A practitioner's guide to thermal infrared remote sensing of rivers and streams: recent advances, precautions and considerations. *Wiley Interdisciplinary Reviews: Water*, 3(2):251–268.

Elzhov, T. V., Mullen, K. M., Spiess, A.-N., e Bolker, B. (2016). *minpack.lm: R Interface to the Levenberg-Marquardt Nonlinear Least-Squares Algorithm Found in MINPACK, Plus Support for Bounds*. R package version 1.2-1.

Fairall, C., Bradley, E. F., Godfrey, J., Wick, G., Edson, J. B., e Young, G. (1996a). Cool-skin and warm-layer effects on sea surface temperature. *Journal of Geophysical Research: Oceans*, 101(C1):1295–1308.

Fairall, C. W., Bradley, E. F., Rogers, D. P., Edson, J. B., e Young, G. S. (1996b). Bulk parameterization of air-sea fluxes for tropical ocean-global atmosphere coupled-ocean atmosphere response experiment. *Journal of Geophysical Research: Oceans*, 101(C2):3747–3764.

Fink, G., Schmid, M., Wahl, B., Wolf, T., e Wüest, A. (2014). Heat flux modifications related to climate-induced warming of large European lakes. *Water Resources Research*, 50(3):2072–2085.

Fragoso Jr, C. R., Motta-Marques, D. M., Collischonn, W., Tucci, C. E., e van Nes, E. H. (2008). Modelling spatial heterogeneity of phytoplankton in Lake Mangueira, a large shallow subtropical lake in South Brazil. *Ecological Modelling*, 219(1-2):125–137.

Friedman, D. (1969). Infrared characteristics of ocean water (1.5–15 μ). *Applied Optics*, 8(10):2073–2078.

Gege, P. (2017). Radiative transfer theory for inland waters. Em Mishra, D. R., Ogashawara, I., e Gitelson, A. A., editores, *Bio-optical Modeling and Remote Sensing of Inland Waters*, pgs. 25–67. Elsevier.

Gitelson, A. A., Dall'Olmo, G., Moses, W., Rundquist, D. C., Barrow, T., Fisher, T. R., Gurlin, D., e Holz, J. (2008). A simple semi-analytical model for remote estimation of chlorophyll-a in turbid waters: Validation. *Remote Sensing of Environment*, 112(9):3582–3593.

Gitelson, A. A., Gritz, Y., e Merzlyak, M. N. (2003). Relationships between leaf chlorophyll content and spectral reflectance and algorithms for non-destructive chlorophyll assessment in higher plant leaves. *Journal of Plant Physiology*, 160(3):271–282.

Gitelson, A. A. e Kondratyev, K. Y. (1991). Optical models of mesotrophic and eutrophic water bodies. *International Journal of Remote Sensing*, 12(3):373–385.

Gons, H. J., Auer, M. T., e Effler, S. W. (2008). Meris satellite chlorophyll mapping of oligotrophic and eutrophic waters in the Laurentian Great Lakes. *Remote Sensing of Environment*, 112(11):4098–4106.

Gons, H. J., Rijkeboer, M., e Ruddick, K. G. (2002). A chlorophyll-retrieval algorithm for satellite imagery (Medium Resolution Imaging Spectrometer) of inland and coastal waters. *Journal of Plankton Research*, 24(9):947–951.

Gons, H. J., Rijkeboer, M., e Ruddick, K. G. (2005). Effect of a waveband shift on chlorophyll retrieval from MERIS imagery of inland and coastal waters. *Journal of Plankton research*, 27(1):125–127.

González-Ávila, I., Tavares, M. H., Chalegre, C. L. B., Munar, A. M., Fragoso, C. R., Motta-Marques, D., e Ruhoff, A. (2021). Southern coastal subtropical shallow lakes skin temperature driven by climatic and non-climatic factors. *Environmental Monitoring and Assessment*, 193(4):1–16.

Gordon, H. R. (2019). *Physical principles of ocean color remote sensing.* University of Miami.

Gordon, H. R. e Wang, M. (1994). Retrieval of water-leaving radiance and aerosol optical thickness over the oceans with SeaWiFS: a preliminary algorithm. *Applied Optics*, 33(3):443–452.

Griffin, C. G., Finlay, J. C., Brezonik, P. L., Olmanson, L., e Hozalski, R. M. (2018). Limitations on using CDOM as a proxy for DOC in temperate lakes. *Water Research*, 144:719–727.

Grolemund, G. e Wickham, H. (2011). Dates and times made easy with lubridate. *Journal of Statistical Software*, 40(3):1–25.

Guillevic, P., Göttsche, F., Nickeson, J., Hulley, G., Ghent, D., Yu, Y., Trigo, I., Hook, S., Sobrino, J., Remedios, J., et al. (2018). Land Surface Temperature product validation best practice protocol. version 1.1. Em Guillevic, P., Göttsche, F., Nickeson, J., e Román, M., editores, *Good Practices for Satellite-Derived Land Product Validation*, pg. 58. Land Product Validation Subgroup (WGCV/CEOS).

Günthel, M., Donis, D., Kirillin, G., Ionescu, D., Bizic, M., McGinnis, D. F., Grossart, H.-P., e Tang, K. W. (2019). Contribution of oxic methane production to surface methane emission in lakes and its global importance. *Nature Communications*, 10(1):1–10.

Halverson, G. H., Lee, C. M., Hestir, E. L., Hulley, G. C., Cawse-Nicholson, K., Hook, S. J., Bergamaschi, B. A., Acuña, S., Tufillaro, N. B., Radocinski, R. G., Rivera, G., e Sommer, T. R. (2021). Decline in thermal habitat conditions for the endangered delta smelt as seen from Landsat satellites (1985–2019). *Environmental Science & Technology*, 56(1):185–193.

Handcock, R. N., Torgersen, C. E., Cherkauer, K. A., Gillespie, A. R., Tockner, K., Faux, R. N., e Tan, J. (2012). Thermal infrared remote sensing of water temperature in riverine landscapes. *Fluvial Remote Sensing for Science and Management*, 12:85–113.

Hansen, G. J. (2021). Novel thermal habitat in lakes. *Nature Climate Change*, 11(6):470–471.

Harmel, T., Chami, M., Tormos, T., Reynaud, N., e Danis, P.-A. (2018). Sunglint correction of the Multi-Spectral Instrument (MSI)-SENTINEL-2 imagery over inland and sea waters from SWIR bands. *Remote Sensing of Environment*, 204:308–321.

Heiskanen, J. J., Mammarella, I., Ojala, A., Stepanenko, V., Erkkilä, K.-M., Miettinen, H., Sandström, H., Eugster, W., Leppäranta, M., Järvinen, H., Vesala, T., e Nordbo, A. (2015). Effects of water clarity on lake stratification and lake-atmosphere heat exchange. *Journal of Geophysical Research: Atmospheres*, 120(15):7412–7428.

Hijmans, R. J. (2021). *terra: Spatial Data Analysis.* R package version 1.4-22.

Hulley, G. C., Hook, S. J., e Schneider, P. (2011). Optimized split-window coefficients for deriving surface temperatures from inland water bodies. *Remote Sensing of Environment*, 115(12):3758–3769.

Janssen, A. B., Hilt, S., Kosten, S., de Klein, J. J., Paerl, H. W., e Van de Waal, D. B. (2021). Shifting states, shifting services: Linking regime shifts to changes in ecosystem services of shallow lakes. *Freshwater Biology*, 66(1):1–12.

Jansson, M., Bergström, A.-K., Blomqvist, P., e Drakare, S. (2000). Allochthonous organic carbon and phytoplankton/bacterioplankton production relationships in lakes. *Ecology*, 81(11):3250–3255.

Jenny, J.-P., Anneville, O., Arnaud, F., Baulaz, Y., Bouffard, D., Domaizon, I., Bocaniov, S. A., Chèvre, N., Dittrich, M., Dorioz, J.-M., et al. (2020). Scientists' warning to humanity: Rapid degradation of the world's large lakes. *Journal of Great Lakes Research.*

Jensen, J. R. (2009). *Remote sensing of the environment: An earth resource perspective.* Pearson Education, 2ª edição.

Ji, Z.-G. (2017). *Hydrodynamics and water quality: modeling rivers, lakes, and estuaries.* John Wiley & Sons.

Jiménez-Muñoz, J. e Sobrino, J. (2006). Error sources on the land surface temperature retrieved from thermal infrared single channel remote sensing data. *International Journal of Remote Sensing*, 27(05):999–1014.

Jiménez-Muñoz, J. C. e Sobrino, J. A. (2003). A generalized single-channel method for retrieving land surface temperature from remote sensing data. *Journal of Geophysical Research*, 108:D22.

Kay, J. E., Kampf, S. K., Handcock, R. N., Cherkauer, K. A., Gillespie, A. R., e Burges, S. J. (2005). Accuracy of lake and stream temperatures estimated from thermal infrared images. *JAWRA Journal of the American Water Resources Association*, 41(5):1161–1175.

Kelleher, C. A., Golden, H. E., e Archfield, S. A. (2021). Monthly river temperature trends across the US confound annual changes. *Environmental Research Letters*, 16(10):104006.

Kelly, P. T., Solomon, C. T., Zwart, J. A., e Jones, S. E. (2018). A framework for understanding variation in pelagic gross primary production of lake ecosystems. *Ecosystems*, 21:1364–1376.

Kraemer, B. M., Anneville, O., Chandra, S., Dix, M., Kuusisto, E., Livingstone, D. M., Rimmer, A., Schladow, S. G., Silow, E., Sitoki, L. M., Tamatama, R., Vadeboncoeur, Y., e McIntyre, P. B. (2015). Morphometry and average temperature affect lake stratification responses to climate change. *Geophysical Research Letters*, 42(12):4981–4988.

Kraemer, B. M., Mehner, T., e Adrian, R. (2017). Reconciling the opposing effects of warming on phytoplankton biomass in 188 large lakes. *Scientific Reports*, 7(1):1–7.

Kutser, T., Verpoorter, C., Paavel, B., e Tranvik, L. J. (2015). Estimating lake carbon fractions from remote sensing data. *Remote Sensing of Environment*, 157:138–146.

Le, C., Li, Y., Zha, Y., Sun, D., Huang, C., e Lu, H. (2009). A four-band semi-analytical model for estimating chlorophyll-a in highly turbid lakes: The case of Taihu Lake, China. *Remote Sensing of Environment*, 113(6):1175–1182.

Lee, H. W., Kim, E. J., Park, S. S., e Choi, J. H. (2012). Effects of climate change on the thermal structure of lakes in the asian monsoon area. *Climatic Change*, 112:859–880.

Lee, Z., Shang, S., Hu, C., Du, K., Weidemann, A., Hou, W., Lin, J., e Lin, G. (2015). Secchi disk depth: A new theory and mechanistic model for underwater visibility. *Remote Sensing of Environment*, 169:139–149.

Lenters, J. D., Kratz, T. K., e Bowser, C. J. (2005). Effects of climate variability on lake evaporation: Results from a long-term energy budget study of Sparkling Lake, northern Wisconsin (USA). *Journal of Hydrology*, 308(1–4):168–195.

Li, Z.-L., Tang, B.-H., Wu, H., Ren, H., Yan, G., Wan, Z., Trigo, I. F., e Sobrino, J. A. (2013). Satellite-derived land surface temperature: Current status and perspectives. *Remote Sensing of Environment*, 131:14–37.

Lins, R. C., Martinez, J.-M., Motta-Marques, D., Cirilo, J. A., Medeiros, P. R. P., e Fragoso Jr, C. R. (2018). A multivariate analysis framework to detect key environmental factors affecting spatiotemporal variability of chlorophyll-a in a tropical productive estuarine-lagoon system. *Remote Sensing*, 10(6):853.

Livingstone, D. M. (2003). The warming of lake Tahoe. *Climatic Change*, 57(1):205–225.

MacCallum, S. N. e Merchant, C. J. (2012). Surface water temperature observations of large lakes by optimal estimation. *Canadian Journal of Remote Sensing*, 38(1):25–45.

Marchetto, A. (2021). *rkt: Mann-Kendall Test, Seasonal and Regional Kendall Tests*. R package version 1.6.

Masuda, K., Takashima, T., e Takayama, Y. (1988). Emissivity of pure and sea waters for the model sea surface in the infrared window regions. *Remote Sensing of Environment*, 24(2):313–329.

Matthews, M. W. (2017). Bio-optical modeling of phytoplankton chlorophyll-a. Em Mishra, D. R., Ogashawara, I., e Gitelson, A. A., editores, *Bio-optical Modeling and Remote Sensing of Inland Waters*, pgs. 157–188. Elsevier.

Melo-Magalhães, E., Medeiros, P., Lira, M., Koening, M., e Moura, A. (2009). Determination of eutrophic areas in Mundaú/Manguaba lagoons, Alagoas-Brazil, through studies of the phytoplanktonic community. *Brazilian Journal of Biology*, 69(2):271–280.

Minnett, P., Alvera-Azcárate, A., Chin, T., Corlett, G., Gentemann, C., Karagali, I., Li, X., Marsouin, A., Marullo, S., Maturi, E., et al. (2019). Half a century of satellite remote sensing of sea-surface temperature. *Remote Sensing of Environment*, 233:111366.

Minnett, P. J., Smith, M., e Ward, B. (2011). Measurements of the oceanic thermal skin effect. *Deep Sea Research Part II: Topical Studies in Oceanography*, 58(6):861–868.

Mishra, S. e Mishra, D. (2014). A novel remote sensing algorithm to quantify phycocyanin in cyanobacterial algal blooms. *Environmental Research Letters*, 9(11):114003.

Moritz, S. e Bartz-Beielstein, T. (2017). imputeTS: Time Series Missing Value Imputation in R. *The R Journal*, 9(1):207–218.

Moses, W. J., Gitelson, A. A., Berdnikov, S., e Povazhnyy, V. (2009). Satellite estimation of chlorophyll-a concentration using the red and NIR bands of MERIS—the Azov sea case study. *IEEE Geoscience and Remote Sensing Letters*, 6(4):845–849.

Moses, W. J., Sterckx, S., Montes, M. J., De Keukelaere, L., e Knaeps, E. (2017). Atmospheric correction for inland waters. Em Mishra, D. R., Ogashawara, I., e Gitelson, A. A., editores, *Bio-optical Modeling and Remote Sensing of Inland Waters*, pgs. 69–100. Elsevier.

Mouw, C. B., Greb, S., Aurin, D., DiGiacomo, P. M., Lee, Z., Twardowski, M., Binding, C., Hu, C., Ma, R., Moore, T., et al. (2015). Aquatic color radiometry remote sensing of coastal and inland waters: Challenges and recommendations for future satellite missions. *Remote sensing of environment*, 160:15–30.

Neil, C., Spyrakos, E., Hunter, P. D., e Tyler, A. N. (2019). A global approach for chlorophyll-a retrieval across optically complex inland waters based on optical water types. *Remote Sensing of Environment*, 229:159–178.

O'Farrell, I., Sánchez, M. L., Schiaffino, M. R., Izaguirre, I., Huber, P., Lagomarsino, L., e Yema, L. (2021). Human impacted shallow lakes in the Pampean plain are ideal hosts for cyanobacterial harmful blooms. *Environmental Pollution*, 288:117747.

Oleksy, I. A., Jones, S. E., e Solomon, C. T. (2021). Hydrologic setting dictates the sensitivity of ecosystem metabolism to climate variability in lakes. *Ecosystems*, pgs. 1–18.

Oliveira, A. M. e Kjerfve, B. (1993). Environmental responses of a tropical coastal lagoon system to hydrological variability: Mundaú-Manguaba, Brazil. *Estuarine, Coastal and Shelf Science*, 37(6):575–591.

Olson, C. R., Solomon, C. T., e Jones, S. E. (2020). Shifting limitation of primary production: experimental support for a new model in lake ecosystems. *Ecology Letters*, 23(12):1800–1808.

Oppenheimer, C. (1997). Ramifications of the skin effect for crater lake heat budget analysis. *Journal of Volcanology and Geothermal Research*, 75(1-2):159–165.

O'Reilly, C. M., Alin, S. R., Plisnier, P.-D., Cohen, A. S., e McKee, B. A. (2003). Climate change decreases aquatic ecosystem productivity of Lake Tanganyika, Africa. *Nature*, 424:766–768.

O'Reilly, C. M., Sharma, S., Gray, D. K., Hampton, S. E., Read, J. S., Rowley, R. J., Schneider, P., Lenters, J. D., McIntyre, P. B., Kraemer, B. M., et al. (2015). Rapid and highly variable warming of lake surface waters around the globe. *Geophysical Research Letters*, 42(24):10–773.

O'Reilly, J. E., Maritorena, S., Mitchell, B. G., Siegel, D. A., Carder, K. L., Garver, S. A., Kahru, M., e McClain, C. (1998). Ocean color chlorophyll algorithms for SeaWiFS. *Journal of Geophysical Research: Oceans*, 103(C11):24937–24953.

Ottlé, C. e Stoll, M. (1993). Effect of atmospheric absorption and surface emissivity on the determination of land surface temperature from infrared satellite data. *International Journal of Remote Sensing*, 14(10):2025–2037.

Pahlevan, N., Mangin, A., Balasubramanian, S. V., Smith, B., Alikas, K., Arai, K., Barbosa, C., Bélanger, S., Binding, C., Bresciani, M., Giardino, C., Gurlin, D., Fan, Y., Harmel, T., Hunter, P., Ishikaza, J., Kratzer, S., Lehmann, M. K., Ligi, M., Ma, R., Martin-Lauzer, F.-R., Olmanson, L., Oppelt, N., Pan, Y., Peters, S., Reynaud, N., Carvalho, L. A. S., Simis, S., Spyrakos, E., Steinmetz, F., Stelzer, K., Sterckx, S., Tormos, T., Tyler, A., Vanhellemont, Q., e Warren, M. (2021). ACIX-Aqua: A global assessment of atmospheric correction methods for Landsat-8 and Sentinel-2 over lakes, rivers, and coastal waters. *Remote Sensing of Environment*, 258:112366.

Pahlevan, N., Sarkar, S., Franz, B., Balasubramanian, S., e He, J. (2017). Sentinel-2 MultiSpectral Instrument (MSI) data processing for aquatic science applications: Demonstrations and validations. *Remote Sensing of Environment*, 201:47–56.

Pahlevan, N., Smith, B., Schalles, J., Binding, C., Cao, Z., Ma, R., Alikas, K., Kangro, K., Gurlin, D., Hà, N., Matsushita, B., Moses, W., Greb, S., Lehmann, M. K., Ondrusek, M., Oppelt, N., e Stumpf, R. (2020). Seamless retrievals of chlorophyll-a from Sentinel-2 (MSI) and Sentinel-3 (OLCI) in inland and coastal waters: A machine-learning approach. *Remote Sensing of Environment*, pg. 111604.

Pereira, L. (2023). Paraigera ou algoa de sal (lagoa fluvial). Em *BiblioAtlas - Biblioteca de Referências do Atlas Digital da América Lusa*. `http://lhs.unb.br/atlas/Paraigeira_ou_Algoa_de_Sal_(lagoa_fluvial)`.

Perry, E. M. e Moran, M. S. (1994). An evaluation of atmospheric corrections of radiometric surface temperatures for a semiarid rangeland watershed. *Water resources research*, 30(5):1261–1269.

Pi, X., Luo, Q., Feng, L., Xu, Y., Tang, J., Liang, X., Ma, E., Cheng, R., Fensholt, R., Brandt, M., et al. (2022). Mapping global lake dynamics reveals the emerging roles of small lakes. *Nature Communications*, 13(1):5777.

Piccolroaz, S., Toffolon, M., e Majone, B. (2013). A simple lumped model to convert air temperature into surface water temperature in lakes. *Hydrology and Earth System Sciences*, 17:3323–3338.

Pierce, D. (2021). *ncdf4: Interface to Unidata netCDF (Version 4 or Earlier) Format Data Files.* R package version 1.19.

Prats, J., Reynaud, N., Rebière, D., Peroux, T., Tormos, T., e Danis, P.-A. (2018). LakeSST: Lake Skin Surface Temperature in French inland water bodies for 1999–2016 from Landsat archives. *Earth System Science Data*, 10(2):727–743.

Ptak, M., Sojka, M., Choiński, A., e Nowak, B. (2018). Effect of environmental conditions and morphometric parameters on surface water temperature in polish lakes. *Water*, 10(5):580.

Purkis, S. J. e Klemas, V. V. (2011). *Remote sensing and global environmental change.* John Wiley & Sons.

R Core Team (2017). *R: A Language and Environment for Statistical Computing.* R Foundation for Statistical Computing, Vienna, Austria.

Richardson, D. C., Melles, S. J., Pilla, R. M., Hetherington, A. L., Knoll, L. B., Williamson, C. E., Kraemer, B. M., Jackson, J. R., Long, E. C., Moore, K., Rudstam, L. G., Rusak, J. A., Saros, J. E., Sharma, S., Strock, K. E., Weathers, K. C., e Wigdahl-Perry, C. R. (2017). Transparency, geomorphology and mixing regime explain variability in trends in lake temperature and stratification across Northeastern North America (1975–2014). *Water*, 9(6):442.

Riffler, M., Lieberherr, G., e Wunderle, S. (2015). Lake surface water temperatures of European Alpine lakes (1989–2013) based on the Advanced Very High Resolution Radiometer (AVHRR) 1 km data set. *Earth System Science Data*, 7(1):1–17.

Robinson, I., Wells, N., e Charnock, H. (1984). The sea surface thermal boundary layer and its relevance to the measurement of sea surface temperature by airborne and spaceborne radiometers. *International Journal of Remote Sensing*, 5(1):19–45.

Rose, K. C., Winslow, L. A., Read, J. S., e Hansen, G. J. (2016). Climate-induced warming of lakes can be either amplified or suppressed by trends in water clarity. *Limnology and Oceanography Letters*, 1(1):44–53.

Schaeffer, B. A., Loftin, K. A., Stumpf, R. P., e Werdell, P. J. (2015). Agencies collaborate, develop a cyanobacteria assessment network. *Eos, Earth and Space Science News*, 96.

Schluessel, P., Emery, W. J., Grassl, H., e Mammen, T. (1990). On the bulk-skin temperature difference and its impact on satellite remote sensing of sea surface temperature. *Journal of Geophysical Research: Oceans*, 95(C8):13341–13356.

Schmid, M. e Köster, O. (2016). Excess warming of a Central European lake driven by solar brightening. *Water Resources Research*, 52(10):8103–8116.

Schneider, P. e Hook, S. J. (2010). Space observations of inland water bodies show rapid surface warming since 1985. *Geophysical Research Letters*, 37(22).

Schott, J. R. (2007). *Remote sensing: the image chain approach.* Oxford University Press; 2nd edition.

Schwarzbold, A. e Schäfer, A. (1984). Gênese e morfologia das lagoas costeiras do Rio Grande do Sul-Brasil. *Amazoniana: Limnologia et Oecologia Regionalis Systematis Fluminis Amazonas*, 9(1):87–104.

Seekell, D. A., Lapierre, J.-F., Ask, J., Bergström, A.-K., Deininger, A., Rodríguez, P., e Karlsson, J. (2015). The influence of dissolved organic carbon on primary production in northern lakes. *Limnology and Oceanography*, 60(4):1276–1285.

Sobrino, J. A., Jiménez-Muñoz, J. C., e Paolini, L. (2004). Land surface temperature retrieval from Landsat TM 5. *Remote Sensing of Environment*, 90(4):434–440.

Sobrino, J. A., Jiménez-Muñoz, J. C., Soria, G., Romaguera, M., Guanter, L., Moreno, J., Plaza, A., e Martinez, P. (2008). Land surface emissivity retrieval from different VNIR and TIR sensors. *IEEE Transactions on Geoscience and Remote Sensing*, 46(2):316–327.

Spyrakos, E., O'Donnell, R., Hunter, P. D., Miller, C., Scott, M., Simis, S. G., Neil, C., Barbosa, C. C., Binding, C. E., Bradt, S., Bresciani, M., Dall'Olmo, G., Giardino, C., Gitelson, A. A., Kutser, T., Li, L., Matsushita, B., Martinez-Vicente, V., Matthew, M. W., Ogashawara, I., Ruiz-Verdú, A., Schalles, J. F., Tebbs, E., Zhang, Y., e Tyler, A. N. (2018). Optical types of inland and coastal waters. *Limnology and Oceanography*, 63(2):846–870.

Toffolon, M., Piccolroaz, S., e Calamita, E. (2020). On the use of averaged indicators to assess lakes' thermal response to changes in climatic conditions. *Environmental Research Letters*, 15(3):034060.

Topp, S. N., Pavelsky, T. M., Jensen, D., Simard, M., e Ross, M. R. (2020). Research trends in the use of remote sensing for inland water quality science: Moving towards multidisciplinary applications. *Water*, 12(1):169.

Tranvik, L. J., Downing, J. A., Cotner, J. B., Loiselle, S. A., Striegl, R. G., et al. (2009). Lakes and reservoirs as regulators of carbon cycling and climate. *Limnology and Oceanography*, 54(6part2):2298–2314.

Tundisi, J. G. e Tundisi, T. M. (2016). *Limnologia.* Oficina de Textos.

Valgur, M., Kersten, J., Delucchi, L., Baier, G., unnic Malte, Staniewicz, S., Kinyanjui, L. K., Bahr, V., Salembier, P., martinber, Keller, G., dwlsalmeida, Castro, C., e Raspopov, A. (2019). *sentinelsat/sentinelsat: v0.13 (v0.13).* Zenodo.

Wan, Z. e Dozier, J. (1996). A generalized split-window algorithm for retrieving land-surface temperature from space. *IEEE Transactions on Geoscience and Remote Sensing*, 34(4):892–905.

Wenyao, L., Field, R., Gantt, R., e Klemas, V. (1987). Measurement of the surface emissivity of turbid waters. *Chinese Journal of Oceanology and Limnology*, 5(4):363–369.

Wetzel, R. G. (2001). *Limnology: lake and river ecosystems*. Elsevier Academic Press.

Wickham, H., François, R., Henry, L., e Müller, K. (2022). *dplyr: A Grammar of Data Manipulation*. R package version 1.0.9.

Williamson, C. E., Dodds, W., Kratz, T. K., e Palmer, M. E. (2008). Lakes and streams as sentinels of environmental change in terrestrial and atmospheric processes. *Frontiers in Ecology and the Environment*, 6(5):247–254.

Wilson, R. C., Hook, S. J., Schneider, P., e Schladow, S. G. (2013). Skin and bulk temperature difference at Lake Tahoe: A case study on lake skin effect. *Journal of Geophysical Research: Atmospheres*, 118(18):10–332.

Winslow, L. A., Read, J. S., Hansen, G. J., Rose, K. C., e Robertson, D. M. (2017). Seasonality of change: Summer warming rates do not fully represent effects of climate change on lake temperatures. *Limnology and Oceanography*, 62(5):2168–2178.

Wong, E. W. e Minnett, P. J. (2018). The response of the ocean thermal skin layer to variations in incident infrared radiation. *Journal of Geophysical Research: Oceans*, 123(4):2475–2493.

Woolway, R. I., Jones, I. D., Maberly, S. C., French, J. R., Livingstone, D. M., Monteith, D. T., Simpson, G. L., Thackeray, S. J., Andersen, M. R., Battarbee, R. W., et al. (2016). Diel surface temperature range scales with lake size. *PLoS One*, 11(3):e0152466.

Woolway, R. I., Kraemer, B. M., Lenters, J. D., Merchant, C. J., O'Reilly, C. M., e Sharma, S. (2020). Global lake responses to climate change. *Nature Reviews Earth & Environment*, 1(8):388–403.

Woolway, R. I. e Merchant, C. J. (2018). Intralake heterogeneity of thermal responses to climate change: A study of large Northern Hemisphere lakes. *Journal of Geophysical Research: Atmospheres*, 123(6):3087–3098.

Woolway, R. I., Merchant, C. J., Van Den Hoek, J., Azorin-Molina, C., Nõges, P., Laas, A., Mackay, E. B., e Jones, I. D. (2019). Northern Hemisphere atmospheric stilling accelerates lake thermal responses to a warming world. *Geophysical Research Letters*, 46(21):11983–11992.

Woolway, R. I., Verburg, P., Lenters, J. D., Merchant, C. J., Hamilton, D. P., Brookes, J., de Eyto, E., Kelly, S., Healey, N. C., Hook, S., et al. (2018). Geographic and temporal variations in turbulent heat loss from lakes: A global analysis across 45 lakes. *Limnology and Oceanography*, 63(6):2436–2449.

Yang, W., Matsushita, B., Chen, J., Fukushima, T., e Ma, R. (2010). An enhanced three-band index for estimating chlorophyll-a in turbid case-II waters: case studies of Lake Kasumigaura, Japan, and Lake Dianchi, China. *IEEE Geoscience and Remote Sensing Letters*, 7(4):655–659.

Yang, Z., Zhang, M., Shi, X., Kong, F., Ma, R., e Yu, Y. (2016). Nutrient reduction magnifies the impact of extreme weather on cyanobacterial bloom formation in large shallow Lake Taihu (China). *Water Research*, 103:302–310.

Zhang, Y. (1999). MODIS UCSB Emissivity Library. `https://icess.eri.ucsb.edu/modis/EMIS/html/em.html`. Acessed on November 22nd 2017.

Zhang, Y., Zhou, L., Zhou, Y., Zhang, L., Yao, X., Shi, K., Jeppesen, E., Yu, Q., e Zhu, W. (2020). Chromophoric dissolved organic matter in inland waters: present knowledge and future challenges. *Science of The Total Environment*, pg. 143550.

Zhong, Y., Notaro, M., e Vavrus, S. J. (2019). Spatially variable warming of the Laurentian Great Lakes: an interaction of bathymetry and climate. *Climate Dynamics*, 52(9):5833–5848.

Anexos

ANEXO A

Ambiente de processamento

Para o desenvolvimento deste trabalho, todo o processamento foi realizado em ambiente *R* (R Core Team, 2017), utilizando os seguintes pacotes:

- *dplyr* (Wickham et al., 2022): para programação funcional e manipulação de dados
- *imputeTS* (Moritz e Bartz-Beielstein, 2017): para preenchimento de falhas em séries temporais
- *lubridate* (Grolemund e Wickham, 2011): para manipulação de datas e horas
- *minpack.lm* (Elzhov et al., 2016): para implementação do método dos mínimos quadrados não-linear
- *ncdf4* (Pierce, 2021): para manipulação de dados NetCDF
- *openair* (Carslaw e Ropkins, 2012): para graficar diagramas de Taylor
- *rkt* (Marchetto, 2021): para análise de Mann-Kendall de tendência de séries temporais
- *terra* (Hijmans, 2021): para manipulação de dados espaciais

Além destes pacotes, parte do processamento também foi realizado em *Python* em função da disponibilidade de bibliotecas. A biblioteca *sentinelsat* (Valgur et al., 2019) foi utilizada para download das imagens Sentinel-2 MSI, e o ACOLITE e o SeaDAS (este apenas para Linux), processadores atmosféricos, são escritos em Python. O GRS, outro processador atmosférico, também é escrito em Python, porém foi seu processamento foi realizado diretamente pelo Tristan Harmel. Os demais processadores, o C2RCC, o iCOR e o Sen2Cor, estão disponíveis e foram utilizados no SNAP (*Sentinel Application Platform*), software da ESA para geoprocessamento. Por último, o software ArcGIS foi utilizado para confecção de mapas e criação de arquivos e operações vetorais, e o QGIS foi utilizado para visualização, criação de imagens e remoção de pixels nuvem com o plugin Serval (`https://plugins.qgis.org/plugins/Serval/`).

ANEXO B

Material suplementar dos capítulos

Supplementary Material: Atmospheric and sunglint correction for retrieving chlorophyll-*a* in a productive tropical estuarine-lagoon system using Sentinel-2 MSI imagery

Table S1: Metrics calculated for each atmospheric correction algorithm between *in situ* and satellite-derived water reflectance for Band 2 (blue band) (values in bold represent the best result in each case)

Metric	**Raw**	**Aco**	**Aco-SG**	**C2RCC**	**C2X**	**GRS-AC**	**GRS-SG**	**iCOR**	**S2C**
r^2	0.01	0.04	**0.14**	0.12	0.12	0.13	**0.14**	0.01	-0.01
Slope	0.25	0.42	0.52	0.42	0.43	0.35	**0.55**	0.31	0.23
Bias	5.71	1.90	1.57	0.79	1.32	1.46	**1.17**	2.25	2.41
MAE	5.71	1.95	1.63	1.60	1.60	1.74	**1.53**	2.28	2.45
RMSE	0.0809	0.0198	0.0132	**0.0083**	0.0103	0.0114	0.0124	0.0256	0.0293

Table S2: Metrics calculated for each atmospheric correction algorithm between *in situ* and satellite-derived water reflectance for Band 3 (green band) (values in bold represent the best result in each case)

Metric	**Raw**	**Aco**	**Aco-SG**	**C2RCC**	**C2X**	**GRS-AC**	**GRS-SG**	**iCOR**	**S2C**
r^2	0.28	0.30	**0.34**	-0.02	0.14	0.31	**0.36**	0.29	0.24
Slope	0.66	0.76	0.75	0.08	0.46	**0.82**	0.78	0.78	0.80
Bias	2.32	1.40	1.21	0.70	**1.11**	1.24	**1.09**	1.47	1.51
MAE	2.32	1.50	1.38	1.69	1.48	1.40	**1.34**	1.53	1.60
RMSE	0.0488	0.0213	0.0158	0.0203	0.0165	0.0186	**0.0140**	0.0235	0.0268

Table S3: Metrics calculated for each atmospheric correction algorithm between *in situ* and satellite-derived water reflectance for Band 4 (red band) (values in bold represent the best result in each case)

Metric	**Raw**	**Aco**	**Aco-SG**	**C2RCC**	**C2X**	**GRS-AC**	**GRS-SG**	**iCOR**	**S2C**
r^2	0.23	0.30	0.42	0.37	**0.48**	0.28	**0.46**	0.30	0.20
Slope	0.55	0.69	0.80	0.75	0.76	0.67	**0.85**	0.67	0.62
Bias	2.41	1.59	1.25	0.65	**1.08**	1.41	1.12	1.60	1.65
MAE	2.42	1.65	**1.41**	1.78	**1.38**	1.53	**1.39**	1.66	1.73
RMSE	0.0346	0.0187	0.0125	0.0121	**0.0098**	0.0164	0.0113	0.0190	0.0216

Table S4: Metrics calculated for each atmospheric correction algorithm between *in situ* and satellite-derived water reflectance for Band 5 (red-edge band) (values in bold represent the best result in each case)

Metric	**Raw**	**Aco**	**Aco-SG**	**C2RCC**	**C2X**	**GRS-AC**	**GRS-SG**	**iCOR**	**S2C**
r^2	0.45	0.47	**0.50**	-0.01	0.35	0.46	**0.51**	0.46	0.42
Slope	0.65	0.73	0.76	0.04	0.51	0.76	0.79	0.79	**0.84**
Bias	1.81	1.42	1.16	0.37	**1.10**	1.34	**1.12**	1.46	1.59
MAE	1.87	1.56	**1.42**	2.82	1.51	1.51	**1.43**	1.59	1.71
RMSE	0.0294	0.0207	**0.0166**	0.0310	0.0174	0.0199	**0.0166**	0.0228	0.0281

Table S5: Metrics calculated for each atmospheric correction algorithm between *in situ* and satellite-derived water reflectance for Band 6 (NIR) (values in bold represent the best result in each case)

Metric	**Raw**	**Aco**	**Aco-SG**	**C2RCC**	**C2X**	**GRS-AC**	**GRS-SG**	**iCOR**	**S2C**
r^2	0.27	0.33	**0.57**	0.01	0.42	0.27	**0.57**	0.30	0.22
Slope	0.52	0.61	**0.71**	0.08	0.51	0.60	**0.72**	0.60	0.58
Bias	3.29	2.29	1.64	0.33	**1.23**	1.95	1.45	2.21	2.12
MAE	3.30	2.36	1.78	3.30	1.70	2.12	**1.66**	2.33	2.30
RMSE	0.0280	0.0175	0.0097	0.0151	**0.0089**	0.0157	**0.0086**	0.0171	0.0179

Table S6: Metrics calculated for each atmospheric correction algorithm between *in situ* and satellite-derived water reflectance for Band 7 (NIR) (values in bold represent the best result in each case)

Metric	**Raw**	**Aco**	**Aco-SG**	**C2RCC**	**C2X**	**GRS-AC**	**GRS-SG**	**iCOR**	**S2C**
r^2	0.24	0.30	**0.53**	0.01	0.42	0.24	**0.53**	0.28	0.21
Slope	0.60	0.66	**0.76**	0.09	0.56	0.63	**0.76**	0.65	0.61
Bias	3.70	2.58	1.87	0.36	**1.37**	2.26	1.72	2.64	2.43
MAE	3.70	2.62	1.98	3.16	**1.78**	2.38	1.88	2.69	2.55
RMSE	0.0306	0.0197	0.0114	0.0141	**0.0091**	0.0181	0.0105	0.0205	0.0199

Table S7: Metrics calculated for each atmospheric correction algorithm between *in situ* and satellite-derived water reflectance for Band 8A (NIR) (values in bold represent the best result in each case)

Metric	**Raw**	**Aco**	**Aco-SG**	**C2RCC**	**C2X**	**GRS-AC**	**GRS-SG**	**iCOR**	**S2C**
r^2	0.00	0.03	0.30	0.06	**0.39**	-0.01	0.26	0.01	-0.01
Slope	0.23	0.37	**0.60**	0.11	0.42	0.25	0.55	0.25	0.15
Bias	5.91	4.03	2.54	0.31	**1.19**	3.15	2.20	4.02	3.31
MAE	5.91	4.05	2.66	3.72	**1.87**	3.38	2.44	4.08	3.54
RMSE	0.0267	0.0180	0.0086	0.0072	**0.0044**	0.0159	0.0074	0.0178	0.0165

Table S8: Spectral angle mapper (°) for Aco-SG, C2X and GRS-SG considering only bands 4 and 5 (Space I), bands 4, 5, and 6 (Space II, with the bands used in BI), and bands 4, 5 and 7 (Space III, with the bands used in 2SAR)

Algorithm	**Space I**	**Space II**	**Space III**
Aco-SG	4.3	7.0	8.8
C2X	0.7	0.7	2.0
GRS-SG	1.3	2.3	4.9

Table S9: Intercept, Slope and r^2 of the linear regression between measured *chla* and the ratio $R_{rs}(705)/R_{rs}(665)$

Subset	**Reflectance data**	**Intercept**	**Slope**	r^2
MMELS	**In situ**	-55.1	93.0	0.92
	Aco-SG	-78.5	106.2	0.78
	C2X	-84.4	101.8	0.55
	GRS-SG	-42.9	72.9	0.64
Mundaú	**In situ**	-48.3	86.4	0.74
	Aco-SG	-9.8	38.7	0.07
	C2X	70.2	-31.4	0.13
	GRS-SG	-8.9	37.2	0.05
Manguaba	**In situ**	-59.7	95.4	0.88
	Aco-SG	-89.4	113.0	0.69
	C2X	-81.5	108.7	0.70
	GRS-SG	-13.2	59.9	0.31

Table S10: Metrics calculated for SeaDAS applying the NIR-SWIR switching method (NIR-SWIR) and the iterative NIR-signal removal method (Iterative NIR).

Method		**NIR-SWIR**	**Iterative NIR**
r^2	MMELS	0.25	0.47
	MUD	0.49	0.61
	MAG	0.04	0.31
Slope	MMELS	0.74	0.71
	MUD	0.96	0.85
	MAG	0.33	0.44
nBias	MMELS	0.73	0.79
	MUD	0.76	1.07
	MAG	0.69	0.50
nMAE	MMELS	1.80	1.83
	MUD	1.69	1.48
	MAG	2.09	2.50
RMSE	MMELS	0.0236	0.0131
	MUD	0.0165	0.0107
	MAG	0.0308	0.0158
SAM	MMELS	26.2°	8.0°
	MUD	14.3°	5.86°
	MAG	81.4°	13.52°

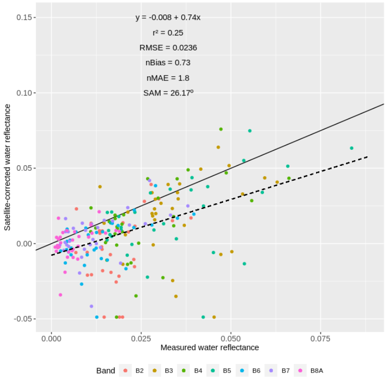

Figure S1: Comparison of the *in situ* with satellite-derived water reflectance corrected by SeaDAS applying the NIR-SWIR switching method.

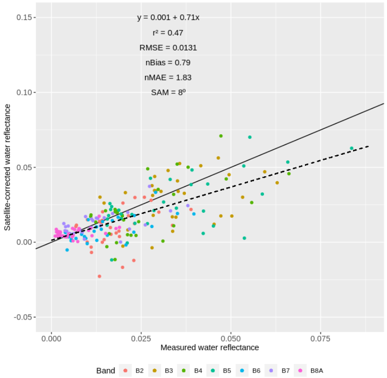

Figure S2: Comparison of the *in situ* with satellite-derived water reflectance corrected by SeaDAS applying the iterative NIR-signal removal method.

Table S11: Metrics for the chlorophyll-*a* retrieved with algorithms (mean of the 100 runs) using *in situ* measured reflectance (values in bold represent the best result in each case)

Subset	**Model**	**Dataset**	r^2	**Bias (mg/m^3)**	**RMSE (mg/m^3)**	**nRMSE (%)**
MMELS	2BRL	calibration	0.92	0.0	15.7	23.5
		validation	0.92	0.4	16.4	25.2
		global	0.92	0.1	16.1	24.1
	2BQR	calibration	0.93	0.0	15.1	22.5
		validation	0.92	0.5	16.4	25.1
		global	0.93	0.2	15.7	23.5
	2SAR	calibration	**0.96**	-3.3	12.5	18.6
		validation	**0.96**	-2.9	12.6	19.2
		global	**0.96**	-3.2	12.5	18.8
	3BR	calibration	**0.96**	0.0	11.2	16.8
		validation	**0.96**	0.0	11.4	17.2
		global	**0.96**	0.0	11.3	16.9
	BI	calibration	**0.96**	0.0	**11.0**	**16.4**
		validation	**0.96**	0.0	**11.0**	**16.9**
		global	**0.96**	0.0	**11.0**	**16.5**
	MDN	calibration	NA	NA	NA	NA
		validation	NA	NA	NA	NA
		global	0.93	-21.7	28.6	42.8
	NDCI	calibration	0.92	0.0	16.1	24.0
		validation	0.91	0.5	17.0	26.1
		global	0.92	0.2	16.5	24.7
	OC2	calibration	0.61	-5.8	38.7	57.7
		validation	0.53	-4.2	47.7	73.2
		global	0.57	-5.3	42.6	63.8
Mundaú	2BRL	calibration	0.74	0.0	9.8	30.8
		validation	0.74	-0.2	10.3	31.7
		global	0.74	0.0	10.1	31.4
	2BQR	calibration	0.74	0.0	9.8	30.6
		validation	0.73	0.0	10.8	33.3
		global	0.74	0.0	10.2	31.9
	2SAR	calibration	**0.82**	0.1	**8.3**	**25.9**
		validation	**0.79**	0.1	**9.1**	**28.0**
		global	**0.81**	0.1	**8.6**	**26.8**
	3BR	calibration	0.73	0.0	10.0	31.5
		validation	0.73	-0.1	10.6	32.8
		global	0.73	-0.1	10.3	32.2
	BI	calibration	0.75	0.0	10.7	30.4
		validation	0.73	-0.2	11.3	32.4
		global	0.74	-0.1	11.0	31.5
	MDN	calibration	NA	NA	NA	NA
		validation	NA	NA	NA	NA
		global	0.67	-14.8	18.9	58.9
	NDCI	calibration	0.75	0.0	9.7	30.4
		validation	0.73	-0.1	10.5	32.4
		global	0.74	0.0	10.1	31.5
	OC2	calibration	0.23	-4.1	17.4	54.6
		validation	0.09	-4.3	20.7	63.9
		global	0.16	-4.2	18.7	58.4
Manguaba	2BRL	calibration	0.88	0.0	20.4	19.2
		validation	0.88	0.6	21.6	20.3
		global	0.88	0.2	21.0	19.7
	2BQR	calibration	0.89	0.0	19.2	18.0
		validation	0.88	0.7	20.9	19.7
		global	0.89	0.2	20.0	18.8
	2SAR	calibration	**0.95**	-3.9	14.7	13.8
		validation	**0.95**	-3.7	15.1	14.2
		global	**0.95**	-3.8	14.9	14.0
	3BR	calibration	**0.96**	0.0	12.1	11.4
		validation	**0.96**	0.2	12.4	11.8
		global	**0.96**	0.1	12.2	11.4
	BI	calibration	**0.97**	0.0	**10.8**	**10.2**
		validation	**0.97**	0.2	**11.2**	**10.6**
		global	**0.97**	0.1	**11.0**	**10.3**
	MDN	calibration	NA	NA	NA	NA
		validation	NA	NA	NA	NA
		global	0.90	-29.5	36.7	34.4
	NDCI	calibration	0.90	0.0	19.1	17.9
		validation	0.89	0.6	20.6	19.4
		global	0.89	0.2	19.8	18.6
	OC2	calibration	0.67	-4.6	34.5	32.4
		validation	0.56	-4.1	42.9	40.4
		global	0.62	-4.4	37.9	35.6

Table S12: Metrics for the chlorophyll-*a* retrieved with algorithms (mean of the 100 runs) using Sentinel-2 MSI images corrected using ACOLITE with sunglint correction (values in bold represent the best result in each case)

Subset	**Model**	**Dataset**	r^2	**Bias (mg/m^3)**	**RMSE (mg/m^3)**	**nRMSE (%)**
MMELS	**2BRL**	calibration	**0.79**	0.0	**25.0**	**35.7**
		validation	**0.77**	0.4	**26.0**	**37.8**
		global	**0.78**	0.1	**25.5**	**36.3**
	2BQR	calibration	**0.80**	0.0	**24.0**	**34.1**
		validation	**0.78**	0.4	**25.7**	**37.3**
		global	**0.80**	0.1	**24.8**	**35.3**
	2SAR	calibration	**0.79**	0.4	**24.8**	**35.2**
		validation	**0.75**	2.2	**30.2**	**43.2**
		global	**0.77**	1.0	**27.2**	**38.7**
	3BR	calibration	**0.80**	0.0	**23.7**	**33.4**
		validation	**0.79**	-0.1	**25.4**	**36.5**
		global	**0.80**	-0.5	**24.5**	**34.8**
	BI	calibration	0.62	0.0	33.0	46.7
		validation	0.68	0.3	36.5	52.9
		global	0.63	0.1	35.2	50.0
	MDN	calibration	NA	NA	NA	NA
		validation	NA	NA	NA	NA
		global	0.48	-22.4	45.4	64.6
	NDCI	calibration	**0.81**	0.0	**23.5**	**33.3**
		validation	**0.78**	0.3	**25.3**	**36.7**
		global	**0.81**	0.1	**24.3**	**34.5**
	OC2	calibration	0.43	-11.1	45.4	64.3
		validation	0.29	-1.1	51.2	72.6
		global	0.33	-7.6	47.3	67.1
Mundaú	2BRL	calibration	0.10	0.0	20.1	66.5
		validation	0.22	0.0	23.2	78.1
		global	0.10	0.0	21.6	71.8
	2BQR	calibration	0.26	0.0	18.1	60.1
		validation	0.22	0.9	24.0	81.5
		global	0.17	0.3	20.8	69.2
	2SAR	calibration	0.17	-3.0	20.8	69.6
		validation	**0.23**	-3.6	24.5	82.3
		global	0.10	-3.3	23.3	77.5
	3BR	calibration	0.10	0.0	20.0	66.9
		validation	0.19	-1.6	22.9	78.8
		global	0.07	-0.5	21.5	71.7
	BI	calibration	0.08	0.0	20.2	68.2
		validation	0.17	-0.1	23.1	75.4
		global	0.06	-0.0	21.6	71.7
	MDN	calibration	NA	NA	NA	NA
		validation	NA	NA	NA	NA
		global	0.07	-5.0	24.5	81.5
	NDCI	calibration	0.26	0.0	18.2	60.9
		validation	0.22	0.3	23.5	78.5
		global	0.18	0.1	20.5	68.3
	OC2	calibration	**0.40**	-3.8	**16.7**	**56.2**
		validation	0.22	-3.6	**23.9**	**79.2**
		global	**0.29**	-3.7	**19.8**	**65.8**
Manguaba	**2BRL**	calibration	**0.67**	0.0	**26.3**	**24.0**
		validation	**0.70**	-0.6	**29.1**	**27.5**
		global	0.69	-0.2	**27.6**	**25.4**
	2BQR	calibration	**0.68**	0.0	**25.8**	**23.6**
		validation	**0.68**	-1.4	31.1	29.2
		global	0.67	-0.5	**28.1**	**25.8**
	2SAR	calibration	**0.69**	-0.8	**25.6**	**23.3**
		validation	**0.70**	-2.4	31.2	29.1
		global	0.67	-1.3	**27.3**	**25.2**
	3BR	calibration	**0.73**	0.0	**24.7**	**22.5**
		validation	**0.69**	0.9	**27.0**	**25.6**
		global	**0.72**	0.3	**25.9**	**23.8**
	BI	calibration	0.32	0.0	37.3	34.0
		validation	0.50	4.1	48.7	46.0
		global	0.31	1.5	43.2	39.6
	MDN	calibration	NA	NA	NA	NA
		validation	NA	NA	NA	NA
		global	0.21	-39.1	58.9	54.1
	NDCI	calibration	**0.68**	0.0	**26.0**	**23.7**
		validation	**0.67**	-1.1	**31.3**	**29.5**
		global	0.67	-0.4	**28.3**	**26.0**
	OC2	calibration	0.58	-4.3	30.1	27.5
		validation	0.37	-0.5	42.5	40.0
		global	0.49	-3.0	35.5	32.6

Table S13: Metrics for the chlorophyll-*a* retrieved with algorithms (mean of the 100 runs) using Sentinel-2 MSI images corrected using C2X (values in bold represent the best result in each case)

Subset	**Model**	**Dataset**	r^2	**Bias (mg/m^3)**	**RMSE (mg/m^3)**	**nRMSE (%)**
MMELS	2BRL	calibration	0.54	0.0	35.6	51.2
		validation	0.55	-0.8	39.1	56.8
		global	0.55	-0.3	37.0	52.6
	2BQR	calibration	**0.62**	0.0	**32.6**	**46.8**
		validation	**0.61**	2.0	**36.6**	**52.9**
		global	**0.62**	0.7	34.2	48.7
	2SAR	calibration	0.55	0.2	35.3	50.6
		validation	0.56	1.4	37.9	55.0
		global	0.56	0.6	36.4	51.8
	3BR	calibration	0.58	0.0	33.8	48.9
		validation	0.58	-1.1	**37.0**	**52.5**
		global	0.59	-0.4	35.1	50.0
	BI	calibration	0.58	0.0	34.2	49.0
		validation	0.59	-0.2	**36.7**	**53.1**
		global	0.59	-0.1	35.2	50.1
	MDN	calibration	NA	NA	NA	NA
		validation	NA	NA	NA	NA
		global	0.32	-4.9	45.3	64.4
	NDCI	calibration	**0.63**	0.0	**31.9**	**45.8**
		validation	**0.62**	2.0	**35.3**	**51.2**
		global	**0.64**	0.7	**33.3**	**47.3**
	OC2	calibration	0.20	-17.0	53.0	72.1
		validation	0.11	1.1	64.4	101.0
		global	0.17	-16.3	59.4	86.6
Mundaú	2BRL	calibration	0.16	0.0	19.3	64.0
		validation	0.18	0.7	22.3	76.2
		global	0.13	0.2	20.6	68.7
	2BQR	calibration	0.19	0.0	18.9	62.9
		validation	0.11	0.7	23.8	81.7
		global	0.11	0.2	21.0	70.0
	2SAR	calibration	0.07	-1.9	21.2	70.6
		validation	0.13	-2.4	23.3	78.2
		global	0.06	-2.1	22.2	74.1
	3BR	calibration	0.07	0.0	20.1	66.8
		validation	0.23	-0.2	22.1	74.4
		global	0.03	-0.1	21.2	73.4
	BI	calibration	0.06	0.0	20.4	67.7
		validation	0.11	0.0	21.7	79.1
		global	0.04	0.0	39.1	72.2
	MDN	calibration	NA	NA	NA	NA
		validation	NA	NA	NA	NA
		global	0.18	18.3	48.1	160.0
	NDCI	calibration	0.20	0.0	18.8	62.6
		validation	0.11	0.7	23.9	82.2
		global	0.12	0.2	21.0	69.9
	OC2	calibration	**0.54**	-2.7	**14.6**	**48.4**
		validation	**0.33**	-3.7	21.5	72.4
		global	**0.41**	-3.0	**17.6**	**58.6**
Manguaba	**2BRL**	calibration	0.71	0.0	25.4	23.3
		validation	**0.66**	0.7	**27.8**	**25.8**
		global	**0.70**	0.2	**26.5**	**24.3**
	2BQR	calibration	**0.71**	0.0	**25.0**	**22.9**
		validation	0.65	0.1	28.5	26.5
		global	**0.70**	0.0	**26.6**	**24.4**
	2SAR	calibration	0.62	-2.6	29.6	27.1
		validation	0.56	-2.8	32.3	29.7
		global	0.61	-2.7	31.2	28.6
	3BR	calibration	0.64	0.0	27.8	25.5
		validation	0.64	0.5	30.0	28.0
		global	0.65	0.2	29.0	26.6
	BI	calibration	0.60	0.0	29.8	27.3
		validation	0.56	0.7	33.0	30.6
		global	0.59	0.2	31.3	28.8
	MDN	calibration	NA	NA	NA	NA
		validation	NA	NA	NA	NA
		global	0.55	-27.2	42.4	38.9
	NDCI	calibration	**0.71**	0.0	**25.1**	**23.0**
		validation	0.65	0.2	28.5	26.5
		global	**0.70**	0.1	**26.6**	**24.4**
	OC2	calibration	0.39	-6.8	37.5	34.4
		validation	0.21	-13.7	66.4	61.2
		global	0.17	-9.3	50.8	46.6

Table S14: Metrics for the chlorophyll-*a* retrieved with algorithms (mean of the 100 runs) using Sentinel-2 MSI images corrected using GRS with sunglint correction (values in bold represent the best result in each case)

Subset	**Model**	**Dataset**	r^2	**Bias (mg/m^3)**	**RMSE (mg/m^3)**	**%RMSE (%)**
MMELS	2BRL	calibration	0.66	0.0	31.1	45.2
		validation	0.64	-1.2	36.5	51.3
		global	0.64	-0.4	33.5	47.7
	2BQR	calibration	0.68	0.0	29.9	43.5
		validation	0.58	-0.4	39.2	55.0
		global	0.63	-0.1	33.9	48.2
	2SAR	calibration	**0.76**	-0.5	**25.9**	**37.7**
		validation	**0.73**	-1.0	**30.8**	**42.9**
		global	**0.75**	-0.7	**28.0**	**39.8**
	3BR	calibration	0.65	0.0	31.0	45.2
		validation	0.71	-1.1	32.9	45.7
		global	0.67	-0.4	32.0	45.5
	BI	calibration	0.66	0.0	31.0	45.1
		validation	0.63	-0.7	36.0	50.5
		global	0.64	-0.2	33.1	47.1
	MDN	calibration	NA	NA	NA	NA
		validation	NA	NA	NA	NA
		global	0.38	-14.7	46.5	66.1
	NDCI	calibration	0.68	0.0	30.1	43.7
		validation	0.61	-0.9	37.8	53.1
		global	0.64	-0.3	33.4	47.5
	OC2	calibration	0.23	-13.8	49.2	72.1
		validation	0.15	-19.8	59.0	80.4
		global	0.18	-15.8	53.2	75.7
Mundaú	2BRL	calibration	0.12	0.0	20.2	66.6
		validation	0.21	-0.3	24.0	82.0
		global	0.05	-0.1	21.9	73.0
	2BQR	calibration	**0.36**	0.0	**17.0**	**56.5**
		validation	0.21	-0.3	**23.1**	**79.7**
		global	**0.23**	-0.1	**19.7**	**65.7**
	2SAR	calibration	0.20	-2.8	20.6	67.5
		validation	**0.24**	-2.4	24.5	84.5
		global	0.09	-2.7	22.7	75.6
	3BR	calibration	0.10	0.0	19.7	66.0
		validation	0.21	-1.5	**24.1**	**79.2**
		global	0.06	-0.5	21.8	72.5
	BI	calibration	0.12	0.0	20.2	66.8
		validation	0.18	0.3	23.6	80.8
		global	0.06	0.1	21.7	72.4
	MDN	calibration	NA	NA	NA	NA
		validation	NA	NA	NA	NA
		global	0.04	-5.7	25.0	83.4
	NDCI	calibration	**0.35**	0.0	**17.2**	**56.9**
		validation	0.21	-0.1	23.4	80.8
		global	**0.22**	0.0	**20.0**	**66.6**
	OC2	calibration	**0.32**	-3.9	18.2	60.4
		validation	0.19	-3.5	23.9	79.7
		global	**0.21**	-3.8	20.8	69.3
Manguaba	2BRL	calibration	0.33	0.0	38.4	35.4
		validation	0.38	1.0	43.4	40.4
		global	0.31	0.4	41.0	37.7
	2BQR	calibration	0.41	0.0	36.3	33.4
		validation	0.29	0.2	46.9	43.8
		global	0.31	0.1	41.3	37.9
	2SAR	calibration	**0.61**	-1.2	**29.5**	**27.2**
		validation	**0.55**	-2.3	**33.2**	**31.0**
		global	**0.59**	-1.6	**31.2**	**28.7**
	3BR	calibration	0.38	0.0	36.5	33.4
		validation	0.40	2.8	44.1	41.7
		global	0.35	1.0	40.1	36.8
	BI	calibration	0.32	0.0	38.9	35.8
		validation	0.36	0.0	42.6	39.6
		global	0.31	0.0	40.7	37.4
	MDN	calibration	NA	NA	NA	NA
		validation	NA	NA	NA	NA
		global	0.06	-23.3	60.2	55.3
	NDCI	calibration	0.38	0.0	37.0	34.1
		validation	0.31	-1.3	48.0	45.0
		global	0.31	-0.5	42.1	38.6
	OC2	calibration	0.22	-7.9	42.8	39.3
		validation	0.11	-5.5	53.7	49.6
		global	0.13	-7.0	47.9	43.9

Supplementary Material: Impact of cool-skin effect correction on lake surface water temperature trends and heat budget of three large shallow subtropical lakes

Table S1: Seasonal means of heat budget terms (in W m^{-2}) for the three lakes

Term	**Lake**	**Fall**	**Winter**	**Spring**	**Summer**
J_{lw}	Patos	411.4	377.4	401.5	431.4
	Mirim	406.1	369.0	396.8	430.2
	Mang.	403.9	368.4	394.5	426.5
H	Patos	5.9	2.4	2.0	2.5
	Mirim	5.9	1.6	5.1	6.6
	Mang.	6.7	3.8	7.1	6.6
E	Patos	41.4	21.7	40.6	57.5
	Mirim	32.7	15.0	34.2	52.5
	Mang.	38.9	20.0	41.1	59.2

Supplementary Material: High warming rates in spring in three large shallow subtropical lakes in southern Brazil detected with MODIS imagery

Table S1: Seasonal means of water temperature and meteorological variables for each lake. For the Patos Lagoon, the seasonal means of meteorological variables are calculated as the mean of the values measured in Porto Alegre and Pelotas stations, and for lake Mirim, as the mean of Pelotas and Santa Vitória do Palmar stations

Season	**Fall**			**Winter**			**Spring**			**Summer**		
Variable	**Pts**	**Mir**	**Man**	**Pts**	**Mir**	**Man**	**Pts**	**Mir**	**Man**	**Pts**	**Mir**	**Man**
$\langle \overline{T_w} \rangle$	20.9	19.9	19.5	14.6	13.0	12.9	19.1	18.3	17.9	24.4	24.2	23.6
T_{air} **med**	19.7	18.4	18.1	14.2	12.7	12.1	18.7	17.1	16.4	23.9	22.7	22.2
T_{air} **max**	25.2	23.7	23.2	19.7	17.7	16.9	24.0	22.0	21.4	29.6	27.9	27.5
T_{air} **min**	15.9	14.7	14.4	10.4	9.0	8.7	14.7	13.3	12.6	19.7	18.5	18.1
Prec	115.2	119.2	120.5	125.3	109.4	103.9	134.1	107.4	90.1	114.9	106.9	95.7
Rad	5.9	6.1	5.9	4.8	5.0	4.7	6.3	6.5	6.5	8.1	8.2	8.1
RH	81.5	82.8	81.2	83.1	84.6	83.9	78.3	80.2	79.0	75.7	77.3	75.7
$\boldsymbol{u}$	4.6	3.8	4.5	4.6	3.9	4.5	5.2	4.3	4.9	4.9	4.0	4.6

Table S2: Spearman correlation between the mean seasonal trends and LSWT and depth for each lake

Lake	**Dataset**	**Fall**	**Winter**	**Spring**	**Summer**	**Yearly**
Patos	Temperature	-0.23	-0.18	-0.26	-0.18	0.33
	Depth	0.21	-0.17	0.25	0.13	0.40
Mirim	Temperature	-0.33	-0.27	-0.47	0.02	0.03
	Depth	-0.30	0.35	0.04	0.14	0.25
Mangueira	Temperature	-0.01	-0.09	0.58	0.15	0.25
	Depth	0.26	0.00	0.08	-0.08	0.10

a Mangueira

b Mirim

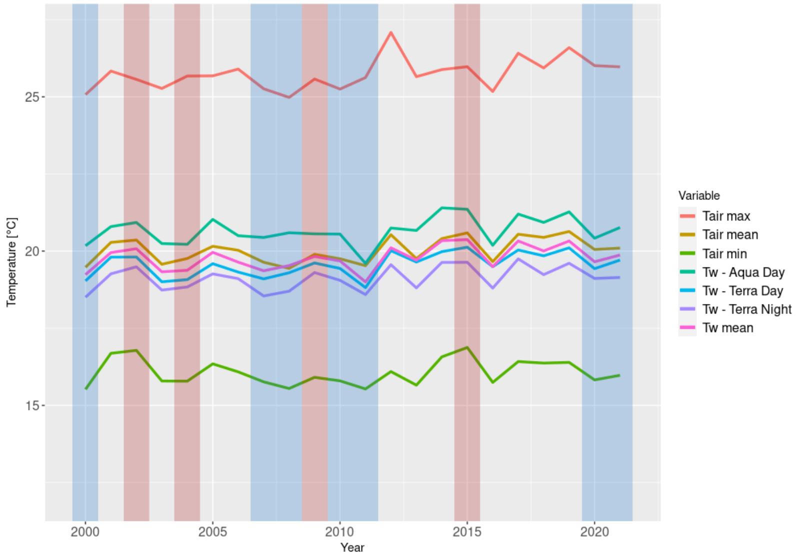

c Patos

Figure S1: Yearly mean air and water temperatures for the three lakes, and ENSO events. Blue denotes the La Niña years, and red denotes the occurrence of El Niño.

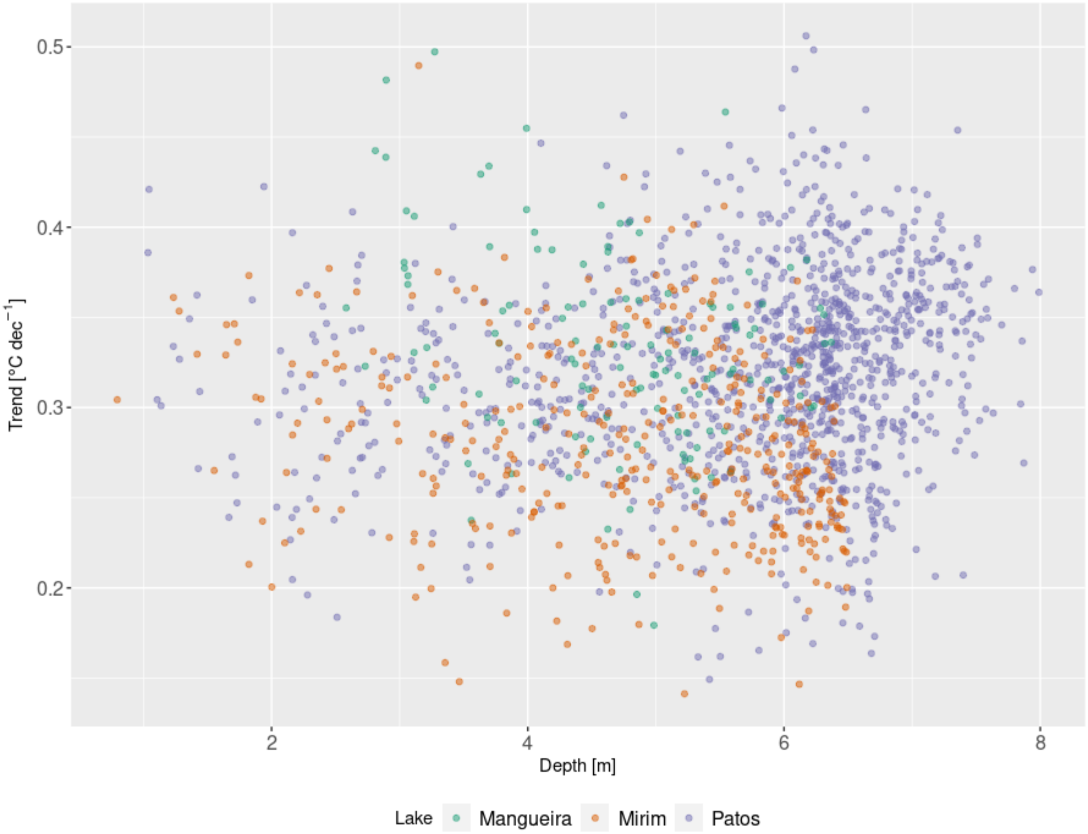

Figure S2: Relationship between summer trend (Sen's slope for seasonal Mann-Kendall) and depth for the three lakes. Only pixels with p-value>0.25 are displayed.